



**Department of Electrical and Electronic Engineering Communication
Research Group**

**Design of Millimeter-wave Dielectric Resonator Antennas
for Off/On-Body Applications**

By:

Tarek S. M. Abdou

**Department of Electronic and Electrical Engineering
University of Sheffield**

A thesis submitted in partial fulfilment of the requirements for the degree of Doctor of
Philosophy

2024

Dedicated to:

To the souls of my **mother** and my **father**, may Allah have a mercy on them.

To my family, brothers, sisters, and Friends.

Acknowledgements

I want to extend my heartfelt gratitude to my supervisor, Dr. Salam Khamas whose steadfast and boundless support has been an indispensable pillar throughout my journey of pursuing a PhD. It is with immense appreciation that I acknowledge his continuous encouragement and the illuminating ideas he has shared, as without them, the realization of this thesis would have undoubtedly remained beyond reach. Also, I would like to acknowledge the use of the National Millimetre-Wave Facility and thank Steve Marsden for his support with the measurements.

Publications

Journal

1. Abdou TS, Saad R, Khamas SK. A Circularly Polarized mmWave Dielectric-Resonator-Antenna Array for Off-Body Communications. *Applied Sciences*. 2023 Feb 3;13(3):2002 (Chapter 3)
2. Abdou, T.S.; Khamas, S.K. A Multiband Millimeter-Wave Rectangular Dielectric Resonator Antenna with Omnidirectional Radiation Using a Planar Feed. *Micromachines* 2023, 14, 1774. <https://doi.org/10.3390/mi14091774> (Chapter 4)

Conference papers

1. Abdou TS, Khamas SK. A mmWave Circularly Polarized Wristwatch Dielectric Resonator Antenna for Off-Body Communications. *International Workshop on Antenna Technology (iWAT)*, 2022 May 16 (pp. 168-171). IEEE. (Chapter 2)
2. Abdou TS, Khamas SK. A Low-profile Wide Bandwidth Circularly Polarized Dielectric Resonator Antenna for mmWave Off-Body Applications. *17th European Conference on Antennas and Propagation (EuCAP)*, 2023 Mar 26 (pp. 1-5). IEEE. (Chapter 2)
3. Abdou TS, Khamas SK. Millimeter Wave Dielectric Resonator Antenna for Off-Body Communications with Grooved GP. *International Workshop on Antenna Technology (iWAT)*, 2023 May 15 (pp. 1-4). IEEE. (Chapter 2)
4. Abdou TS, Khamas SK. Omnidirectional Cylindrical Dielectric Resonator Antenna for Off & On Body Communications. *18th European Conference on Antennas and Propagation (EuCAP)*, 2024. (Chapter 5)

List of Acronyms and Abbreviations

AR	Axial Ratio
BAN	Body Area Network
BCN	Body Centric Network
CP	Circular polarization
CPW	Coplanar waveguide
DRA	Dielectric Resonator Antenna
EBG	Electromagnetic band-gap
IoT	Internet of Things
ISM	Industrial, scientific and medical
LHCP	Left-hand circular polarization
mmWave	Millimetre wave
MPA	Microstrip patch antenna
RHCP	Right-hand circular polarization
SAR	Specific absorption rate
UWB	Ultra-Wideband
WLAN	Wireless Lan Area Network
WBAN	Wireless body-area networks
WPAN	Wireless personal area networks
WSN	Wireless sensor networks

Abstract

Dielectric Resonator Antennas (DRAs) possess several advantageous characteristics, including high radiation efficiency, wide bandwidth, and compact size, making them versatile for a range of applications, such as body area networks (BAN). This research introduces innovative millimetre wave (mmWave) DRA designs tailored for on/off-body communication needs. Among these designs are a wideband circularly polarised (CP) rectangular DRA with dual dielectric layers, enhancing robustness and radiation, and a low-profile CP DRA that addresses feed alignment challenges through a second ground plane and groove placement. Besides, a mmWave circularly polarised, wristwatch DRA is proposed as a potential candidate for off-body applications in the 24-34GHz frequency range. Additionally, a novel 28 GHz CP rectangular DRA array has been designed, which exhibits impressive performance metrics, including a 29% impedance bandwidth, 13% axial-ratio bandwidth, and 13.7 dBic broadside gain at 28 GHz. Furthermore, the study presents a novel millimeter-wave rectangular DRA (RDRA) with an omnidirectional pattern. The degenerate TE_{121}/TE_{211} modes were excited at 28.5 GHz with an overall internal electromagnetic field distribution that was similar to that of the HEM_{218} mode of a cylindrical DRA. A unique feature is the use of a planar feed network to achieved the omnidirectional radiation, not previously reported. The antenna also supports multiband operation with diverse radiation patterns for on/off-body communications. The research also introduces innovative millimeter-wave cylindrical and hemispherical DRAs that provide broadside and omnidirectional patterns at different frequency bands, using a planar feed network. It's worth noting that the impact of the human body's presence has been investigated by using CST. The proposed designs were validated through measurements, demonstrating good agreement with simulations.

Table of Contents

Acknowledgements	ii
Publications	iii
List of Acronyms and Abbreviations.....	iv
Abstract.....	v
List of Figures.....	ix
List of Tables.....	xiii
Chapter 1	1
Introduction and Literature Review.....	1
1.1 Dielectric Resonator Antenna	1
1.2 Overview of Body Centric Networks (BCN) Applications.....	3
1.2.1 Millimetre-wave on-body and off-body communication.....	4
1.2.2 Next-to-Body Devices in the Era of 5G.....	6
1.2.3 Interaction between the Antennas and Human Body.....	7
1.2.4 Specific Absorption Rate (SAR).....	8
1.3 Body-Centric Antennas.....	9
1.3.1 Textile Body-Centric Antennas.....	9
1.3.2 Non-textile Body-Centric Antennas	11
1.3.3 Circular Polarised Body-Centric Antennas.....	12
1.3.4 Challenges in on/off-body communication were addressed through the designs of DRAs.....	13
1.3.5 Body-Centric Dielectric Resonator Antenna	14
1.3.6 Body-Centric Array Antenna.....	15
1.4 Millimetre-wave DRA Arrays.....	16
1.5 Multi Band and Omnidirectional Pattern	17
1.6 Definition of the Research Problem	19
1.7 The Goals and Objectives of the Thesis.....	20
1.8 Research Contributions	21
1.9 Thesis Outline	21
Chapter 2	23
Low-profile Circularly Polarized Rectangular Dielectric Resonator Antennas for mmWave Off-Body Applications.....	23
2.1 Introduction.....	23
2.1.1 Dielectric Waveguide Mode	24
2.2 Supported Modes of a Rectangular DRA.....	25
2.3 Fabrication and Measurements Procedures.....	31
2.3.1 Reflection Coefficient Measurements.....	31
2.3.2 Far-field Measurements.....	31
2.4 Two layered Dielectric Resonator Antenna for mmWave with removable customized holder.....	32
2.4.1 Considered Single DRA Elements.....	32
2.5 Dielectric Resonator Antenna with Grooved GP	45

2.6	A Wristwatch Dielectric Resonator Antenna	54
2.7	Conclusion	60
Chapter 3		62
A Circularly Polarized mmWave Dielectric-Resonator-Antenna Array for Off-Body Communications		62
3.1	Introduction.....	62
3.2	Design Methodology.....	63
3.3	A Single DRA Element.....	63
3.3.1	The DRA Height.....	65
3.3.2	Single DRA Next to a Human Body.....	68
3.4	Broadside DRA Array.....	71
3.4.1	Array Factor.....	71
3.5	2×2 DRA Array.....	77
3.5.2	Array Next to a Human Body.....	82
3.5.3	Specific Absorption Rate (SAR) of the DRA Array	86
3.6	Measurements.....	87
3.7	Conclusion.....	93
Chapter 4		94
A Multi-Band Millimeter-Wave Rectangular Dielectric Resonator Antenna with Omnidirectional Radiation Using a Planar-Feed.....		94
4.1	Introduction.....	94
4.2	Antenna Configuration.....	96
4.3	Supported Modes of the Proposed DRA	97
4.4	Design of the Slot Aperture Feed.....	99
4.4.1	Square Ring-slot Feed.....	99
4.4.2	Rectangular Ring-slot Feed	103
4.4.3	The Ground Plane Size and the Dielectric Constants	106
4.4.4	DRA Performance Next to a Human Body.....	108
4.5	Measured Results	111
4.6	Conclusion	117
Chapter 5		119
Dual Band mmWave Cylindrical and Hemispherical DRAs for Off & On Body Communications		119
5.1	Introduction.....	119
5.2	Dual Band Cylindrical DRA	121
5.2.1	Theoretical Framework of CDRA	121
5.2.2	Design of a Dual Band CDRA.....	123
5.2.3	Shape of the Feeding Slot	124
5.2.4	The Impact of the CDRA Height on Reflection Coefficient.....	129
5.2.5	Ground Plane Size and Effective Permittivity Impact on Reflection Coefficient	130
5.2.6	CDRA Next to a Human Tissue.....	131
5.2.7	Analysis of the Specific Absorption Rate.....	134

5.3	Measurements of the Cylindrical DRA	136
5.4	Dual Band Hemispherical DRA.....	139
5.4.1	Geomtry of the Hemispherical DRA	139
5.5	HDRA Design.....	141
5.5.1	Radius of the HDRA.....	142
5.5.2	HDRA Next to the Human Tissue.	145
5.6	Hemispherical DRA Measurements.....	148
5.7	Conclusion.	152
Chapter 6	154
Conclusion and future work	154
6.1	Conclusion	154
6.2	Future work.....	157
References	158

List of Figures

Figure 1-1 Various geometries of DR antennas.....	2
Figure 2-1 Chapter review.....	24
Figure 2-2 The rectangular DRA placed on the ground plane.....	25
Figure 2-3 (a) MATLAB code for TE ₁₁₃ at 22.7GHz (b) Magnetic field of the TE ₁₁₃ , at 23.4GHz (c) Magnetic field of the TE ₁₁₇ , at 23.3GHz (d) Magnetic field of the TE ₁₁₉ , at 23.6GHz.....	28
Figure 2-4 The current density of the feed network (a) TE ₁₁₃ , (b) TE ₁₁₇ , and (c) TE ₁₁₉	29
Figure 2-5 $ S_{11} $ of rectangular DRAs excited in the TE ₁₁₃ , TE ₁₁₇ and TE ₁₁₉ resonance modes.....	29
Figure 2-6 The variation of the return losses as a function of the dielectric constant.....	30
Figure 2-7 Geometric of single DRA.....	32
Figure 2-8 Stub length's effects on DRA return losses.....	33
Figure 2-9 Geometry of the proposed layered DRA.....	34
Figure 2-10 Reflection coefficient of a single and two-layer DRAs.....	35
Figure 2-11 Gain and axial ratio of a single and two-layer DRAs.....	36
Figure 2-12 Radiation pattern of a single and two-layer DRAs.....	36
Figure 2-13 The proposed layered DRA above the body phantom.....	37
Figure 2-14 $ S_{11} $ a layered DRA placed next to a phantom.....	38
Figure 2-15 Gain and axial ratio of a two-layer DRA placed next to a body phantom.....	38
Figure 2-16 The SAR of the proposed DRA with various input power levels for a 1g tissue; (a) 15 dBm, (b) 18 dBm.....	39
Figure 2-17 The SAR of the proposed DRA with various input power levels for a 10g tissue; (a) 15 dBm, (b) 18 dBm,.....	39
Figure 2-18 The relation of the SAR with the Ground plane size.....	40
Figure 2-19 Prototype of the proposed antenna (a) RDRA with the dielectric coat, (b) Removable custom holder, (c) Feed network with two pieces of adhesive copper tape and the custom holder, (d) proposed antenna with the removable holder, (e) the proposed antenna.....	41
Figure 2-20 Measured and simulated $ S_{11} $ of the layered DRA.....	41
Figure 2-21 The measured gain of the layered DRA.....	42
Figure 2-22 The measured axial ratio of the layered DRA.....	42
Figure 2-23 The measured far field patterns of the layered DRA at 24GHz.....	43
Figure 2-24 Magnetic field distribution inside the layered DRA.....	44
Figure 2-25 Geometry of the proposed DRA.....	45
Figure 2-26 The proposed DRA above the body phantom.....	46
Figure 2-27 $ S_{11} $ of CP DRA placed next to a phantom.....	47
Figure 2-28 Gain and axial ratio of a CP DRA placed next to a body phantom.....	47
Figure 2-29 The SAR of the proposed DRA with various input power levels for a 1g tissue; (a) 15 dBm, (b) 18 dBm.....	48
Figure 2-30 The SAR of the proposed DRA with various input power levels for a 10g tissue; (a) 15 dBm, (b) 18 dBm,.....	48
Figure 2-31 a) centered DRA, b) DRA shifted to the left by 25 μm . c) DRA shifted towards top by 25 μm , d) DRA shifted to the bottom by 25 μm	49
Figure 2-32 $ S_{11} $ of DRA for various misaligned positions.....	49
Figure 2-33 Gain and AR of DRA for various misaligned positions.....	50
Figure 2-34 The prototyped DRA (a) back view (b) Top view of feed network with grooved ground plane (c) Assembled DRA.....	51
Figure 2-35 The measured and simulated $ S_{11} $ of the CP DRA on a grooved ground plane.....	51
Figure 2-36 The measured gain of the CP DRA on a grooved ground plane.....	52
Figure 2-37 The simulated and measured Normalized radiation patterns at 28GHz for a CP DRA above a grooved ground plane.....	52
Figure 2-38 The measured axial ratio of the CP DRA on a grooved ground plane.....	53
Figure 2-39 The proposed wristwatch DRA a) Oblique view b) Top view.....	54
Figure 2-40 The wristwatch DRA on the equivalent wrist.....	55
Figure 2-41 $ S_{11} $ of a wristwatch DRA in free space with different ground plane sizes.....	55
Figure 2-42 Gain of a wristwatch DRA in free space using different ground plane size.....	56

Figure 2-43 Axial Ratio of wristwatch DRA in free space with different ground plane sizes.....	56
Figure 2-44 Far field pattern of wristwatch DRA in free space at 28GHz; a) E- plane and b) H- plane.	57
Figure 2-45 $ S_{11} $ of DRA on-wrist with different ground plane sizes.....	57
Figure 2-46 Gain of on-wrist DRA with different ground plane sizes.....	58
Figure 2-47 Axial ratio of on-wrist DRA with different ground plane sizes.	58
Figure 2-48 Far field pattern of the on-wrist DRA at 28GHz; a) E- plane and b) H- plane.	59
Figure 3-1 Antenna configuration a) top view b) front view c) back view.....	63
Figure 3-2. Reflection coefficient of various height of the DRA	65
Figure 3-3. Gain of DRA with various heights.....	65
Figure 3-4. Axial ratio of DRA with various heights.	66
Figure 3-5. E- Plane and b) H- Plane radiation patterns of the proposed DRA at 28 GHz.....	67
Figure 3-6. A single DRA element above the body phantom.	68
Figure 3-7. $ S_{11} $ of a DRA in free space and placed next to a phantom.	69
Figure 3-8. Axial ratio of a DRA placed in free space and next to a phantom.	70
Figure 3-9. Gain of a DRA placed in free space and next to a phantom.....	70
Figure 3-10. The radiation pattern for 2-elements at 28GHz.....	73
Figure 3-11. Reflection coefficients of various DRA arrays.	74
Figure 3-12. Gain of various DRA arrays.....	74
Figure 3-13. Directivity of various DRA arrays.	75
Figure 3-14. Radiation pattern of various DRA arrays at 28GHz. (a) E-plane. (b) H-plane	76
Figure 3-15. The array's gain and bandwidth as a function of the number of elements.....	76
Figure 3-16. Configuration of the proposed DRA array antenna (a) Top view, (b) 3D view, and (c) Feed network	78
Figure 3-17. $ S_{11} $ of the DRA arrays for various separation distances (d_s).	78
Figure 3-18. AR of the DRA arrays using various separation distances (d_s) between the DRAs.....	79
Figure 3-19. Gain of the DRA arrays using various separation distances (d_s) between the DRAs.....	80
Figure 3-20. Radiation pattern of the DRA arrays using various separation distances (d_s) between the DRAs. ...	80
Figure 3-21. Directivity of the DRA arrays using various separation distances (d_s) between the DRAs.....	81
Figure 3-22. S-parameter values of feeding network.....	81
Figure 3-23. Cross section view of a DRA array next to the body phantom.	83
Figure 3-24. Reflection coefficient of a DRA array in free space and placed next to a phantom.....	83
Figure 3-25. Axial ratio of a DRA array placed in free space and next to a body phantom.	84
Figure 3-26. Gain of a DRA array operating in free space and next to a body phantom.	85
Figure 3-27. Surface current distribution on the DRA array's ground plane at 28 GHz.	86
Figure 3-28. SAR of the DRA array for a 1 g tissue and input power of (a) 15 dBm, (b) 18 dBm, (c) 20 dBm ..	86
Figure 3-29. SAR of the DRA array for a 10 g tissue and input power of (a) 15 dBm, (b) 18 dBm, (c) 20 dBm.	87
Figure 3-30. The array prototype a) Back view of the feed network b) Top view of the feed network c) Assembled DRA array d) Measurements system.	88
Figure 3-31. The simulated and measured $ S_{11} $ of the DRA array.	89
Figure 3-32. The simulated and measured gain of the DRA array.	90
Figure 3-33. The simulated and measured gain of the DRA array.	90
Figure 3-34. Simulated and measured radiation patterns across the CP bandwidth of the DRA array.....	91
Figure 4-1. The proposed omnidirectional DRA; (a) Ground plane with an etched ring-slot, (b) Bottom view, (c) Side view	95
Figure 4-2. Magnetic field distributions inside the proposed isolated DRA at $z=0$ when $a = b = 3.8$ mm and $h = 1.7$ mm; (a) TE_{111} mode at 17.5GHz, (b) TE_{121}^x mode at 28.5GHz, (c) TE_{121}^x at 28.5GHz.	98
Figure 4-3. Return losses of the DRA using different sizes of the square-ring feeding slot.....	100
Figure 4-4. The xy plane view of the quasi HEM 21δ internal magnetic field distribution of a square ring-slot fed DRA at 27.7GHz.	100
Figure 4-5. The radiation patterns of square ring-slot fed DRA with arm lengths of $l_{s1}=l_{s2}=2.5$ mm, (a) 16 GHz, (b) 24 GHz (c) and (d) 27.7 GHz.....	101
Figure 4-6. The omnidirectional gain variation at the $\theta=40^\circ$ azimuth plane when a square ring feeding slot is utilized.	102
Figure 4-7. Realized gain and radiation efficiency of the square ring-slot fed DRA.....	103
Figure 4-8. Simulated return losses of the rectangular ring-slot DRA when the longest slot arm's length, l_{s1} , is varied while $l_{s2}=2$ mm.	104

Figure 4-9. The xy plane view of the internal magnetic field distribution inside the rectangular ring-slot fed DRA, which corresponds to the quasi $HEM_{21\delta}$ at 28.5 GHz.	105
Figure 4-10. 3D radiation patterns at the three operating frequency bands; (a) 17.5 GHz, (b) 23 GHz, (c) 28.5 GHz.	105
Figure 4-11. The xy plane view of the electric and magnetic field distributions on the rectangular ring-slot feed structure at 17.5 GHz.	106
Figure 4-12 The xy plane view of the magnetic and electric field distributions on the rectangular ring-slot feed at 28.5 GHz.	106
Figure 4-13. The variation of return losses as a function of the ground plane size.	107
Figure 4-14. The variation of the return losses as a function of the dielectric constant of the DRA	107
Figure 4-15. The proposed rectangular DRA in the proximity of a human body phantom (Chest).	108
Figure 4-16. The variations in return losses when the antenna was placed on the arm, chest, and stomach	109
Figure 4-17. The 3D omnidirectional radiation pattern next to the equivalent tissue at 28.5 GHz when $d=5$ mm.	109
Figure 4-18. The SAR of the proposed DRA with various input power levels for a 1g tissue; (a) 15 dBm, (b) 18 dBm, and (c) 20 dBm.	110
Figure 4-19. The SAR of the proposed DRA with various input power levels for a 10g tissue; (a) 15 dBm, (b) 18 dBm, and (c) 20 dBm.	110
Figure 4-20. Prototype of the proposed antenna (a) Ground plane with a rectangular ring-slot and outlined DRA position, (b) Assembled prototype.	111
Figure 4-21. The measured and simulated return losses for the proposed DRA that is fed using a rectangular ring-slot.	112
Figure 4-22. Normalized radiation patterns of the TE_{111} mode at 17.5 GHz; (a) E-plane, (b) H-plane.	113
Figure 4-23. Normalized radiation patterns of the resonant slot at 23 GHz (a) E-plane, (b) H-plane	114
Figure 4-24. Normalized radiation patterns of the quasi- $HEM_{21\delta}$ mode at 28.5 GHz (a) $\phi=90^\circ$ plane, (b) $\theta=40^\circ$ plane.	114
Figure 4-25. The azimuthal variation of the omnidirectional gain at the $\theta=40^\circ$ plane.	115
Figure 4-26. Measured and simulated gains at the main beam directions for the three resonance modes.	116
Figure 5-1 Cylindrical DRA placed on a ground plane.	122
Figure 5-2 (a) Top view and (b) side view of the proposed CDRA configuration.	124
Figure 5-3 Simulated return loss of cylindrical DRA using elliptical and annular ring-slots.	124
Figure 5-4 The Normalized radiation patterns of CDRA fed using annular and elliptical ring slots. (a) E-field (broadside), (b), H-field (broadside), (c) E-field (omnidirectional) (d) H-field (omnidirectional) (e) $\theta = 41^\circ$	125
Figure 5-5 The omnidirectional gains' variation of CDRA fed using elliptical and annular ring-slots.	126
Figure 5-6 Field distributions of the CDRA a) HEM_{111} at 21.5GHz b) $HEM_{21\delta}$ at 25.5GHz.	127
Figure 5-7 Realized gain and radiation efficiency of the ring-slot fed.	128
Figure 5-8 The variation of return losses as a function of the CDRA height.	129
Figure 5-9. The variation of return losses as a function of the ground plane size.	130
Figure 5-10 The variation of the return losses as a function of the dielectric constant of the CDRA.	131
Figure 5-11. CDRA element above the body phantom.	132
Figure 5-12. The variations of the return losses as a function of the distance between the DRA and human phantom	133
Figure 5-13 Normalized omnidirectional on body at $d = 5$ mm.	133
Figure 5-14 The SAR with input power 18dBm at 21.5GHz	135
Figure 5-15 The SAR with input power 18dBm at 25.5GHz	135
Figure 5-16 CDRA prototype	136
Figure 5-17 Simulated and measured $ S_{11} $ of CDRA.	137
Figure 5-18 Measured and simulated gains at the main beam directions for the two resonance modes.	137
Figure 5-19 Normalised radiation patterns of the resonant slot at 21.5 GHz (a) E-plane, (b) H-plane	138
Figure 5-20 Normalised radiation pattern of CDRA at 25.5 GHz (a) E-plane and (b) $\theta = 41^\circ$	138
Figure 5-21 Geometry of Hemispherical DRA.	140
Figure 5-22 (a) Top view and (b) side view of the HDRA.	141
Figure 5-23 The variation of the return losses as a function of the radius of HDRA.	142
Figure 5-24 The variation of the return losses as a function of the dielectric constant of the HDRA.	143
Figure 5-25 The Normalized radiation pattern of HDRA a) 21.5GHz, b) 25.7GHz.	144
Figure 5-26 Field distributions of the HDRA a) TE_{111} at 21.5GHz b) $TE_{21\delta}$ 25.5GHz.	144

Figure 5-27 The proposed HDRA in the proximity of a human body phantom.	145
Figure 5-28 The variations of the return losses as a function of the distance between the DRA and human phantom	146
Figure 5-29 Normalized omnidirectional on body at $d = 5\text{mm}$	146
Figure 5-30 The SAR with input power 20dBm at 21.5GHz.	147
Figure 5-31 The SAR with input power 20dBm at 25.5GHz	147
Figure 5-32 HDRA prototype.....	149
Figure 5-33 Simulated and measured $ S_{11} $ of HDRA.	149
Figure 5-34 Simulated and measured Gain of HDRA. (you need to indicate θ for each case).....	150
Figure 5-35 Normalised radiation patterns of the resonant slot at 21.5 GHz (a) E-plane, (b) H-plane.	150
Figure 5-36 Normalized radiation pattern at 25.5GHz (a) x - z plane and (b) azimuth-plane.....	151

List of Tables

Table 1-1 Applications of on-body devices. [14]	3
Table 2-1 Dielectric constant and rectangular DRA dimensions' effects on modes	27
Table 2-2 Rectangular DRAs of various dimensions functioning in the resonance modes of TE_{113} , TE_{117} , and TE_{119}	27
Table 2-3 Human body parameters at 24GHz[136].....	37
Table 2-4 Comparison of the layered-DRA performance against that of published counterparts	45
Table 2-5 Comparison of the performance of a DRA on a grooved ground plane with published counterparts ..	54
Table 2-6 Comparison of the performance of the wristwatch DRA against published counterparts	60
Table 3-1. Resonance frequencies of a number of TE modes supported by the used DRA.	64
Table 3-2. Parameters of the proposed single DRA element.	67
Table 3-3. Human body tissue parameters at 28 GHz.	68
Table 3-4. Bandwidth, Gain, and size of various DRA arrays.....	77
Table 3-5. The average SAR for 1g and 10g tissues using input power of 15 dBm, 18 dBm, and 20 dBm.	87
Table 3-6. Comparison of the proposed antenna performance against previously published designs.	92
Table 4-1. Resonance frequencies of the supported TE modes by the proposed DRA.	98
Table 4-2. Human-body-tissue parameters at 28 GHz [157].	108
Table 4-3. Comparison of the proposed on-body antenna's performance against cutting-edge mmWave counterparts	117
Table 5-1 compared results pf annular and elliptical slots.....	128
Table 5-2. Human body tissue parameters at 25.5 GHz.	132
Table 5-3 The averaged SAR for 1g and 10g tissues using input power of 15 dBm, 18 dBm, and 20 dBm at 21.5GHz.....	134
Table 5-4 The averaged SAR for 1g and 10g tissues using input power of 15 dBm, 18 dBm, and 20 dBm at 25.5GHz.....	134
Table 5-5 The averaged SAR for 1g and 10g tissues using input power of 15dBm, 18 dBm, and 20 dBm at 21.5GHz.....	148
Table 5-6 The averaged SAR for 1g and 10g tissues using input power of 15 dBm, 18 dBm, and 20 dBm at 25.5GHz.....	148
Table 6-1 The proposed mm wave DRA for of/ on-body applications.....	156

Chapter 1

Introduction and Literature Review

1.1 Dielectric Resonator Antenna

The dielectric resonator (DR) term has been given to dielectric materials having the capacity to resonate at a specific frequency. Dielectric resonators were first delivered in microwave circuits as oscillators or filters and replaced steel waveguide cavities because of their sizable advantages when mounted on the pinnacle of a metal ground plane as DRAs radiate energy effectively and can function as. Moreover, the DR antenna (DRA) performance is established by proper feed mechanism as well as antenna dimensions and material [1, 2]. DRAs provide a range of significant benefits. Firstly, possess the unique capability to resonate in different shapes, allowing for design flexibility and customization. Additionally, DRAs are lightweight, ensuring ease of integration into compact devices. Also offer temperature stability, maintaining consistent performance across varying environmental conditions. Furthermore, DRAs are cost-effective, making them an affordable choice for wireless communication systems. Another advantage lies in the absence of metallic losses, which results in enhancing the radiation efficiency [3]. Their efficient energy radiation and dual functionality as both resonators and antennas contribute to their widespread use in modern electronic systems [4]. Figure 1-1 illustrates various shapes of DRAs, showcasing the versatility and flexibility in their design. These design considerations significantly impact the radiation characteristics, bandwidth, and efficiency of the DRA, allowing for customization and optimization based on specific application requirements [5, 6].

The size of the DRA is determined with respect to the wavelength $\lambda_0/\sqrt{\epsilon_r}$. where, λ_0 is the free space wavelength and the choice of dielectric material enables lower conduction losses in the DRA. These characteristics make the DRA suitable for both microwave and mmWave applications. Additionally, the DRA stands out due to its ease of fabrication. The DRA can take on different geometrical shapes, including rectangular, cylindrical, and hemispherical configurations, each characterized by their unique dimensions. The rectangular DRA is characterized by three independent geometrical dimensions: width (a), length (b), and height (h). Similarly, cylindrical and hemispherical DRAs have their respective dimensions. Various modes can be generated in DRAs, including Transverse Electric and Magnetic (TEM) mode, Transverse Electric (TE) mode, and Transverse Magnetic (TM) mode. The propagation of these modes is mainly influenced by the DRA's excitation, dimensions, medium, and the point of excitation. [7].



Figure 1-1 Various geometries of DR antennas.

There are several popularly used feeding mechanisms for DRAs, as demonstrated by previous research studies. Aperture coupling involves creating an aperture on the ground plane of the DRA to facilitate electromagnetic energy coupling [8]. Microstrip-line feed, as presented in [9] where the suggested DRA is positioned on top of microstrip line, this technology is appealing because it is inexpensive and simple to fabricate. Moreover, a circularly fed coplanar waveguide (CPW) fed stacked dielectric resonator antenna for use with wireless local area

networks to facilitate internet access [10]. Coaxial-probe feed, where in order to bring proper impedance-matching the coaxial cable height varied and appropriately fine as explored in [11]. Additionally, a rectangular waveguide has been investigated as a low-loss excitation scheme, as reported in [12]. These various feeding mechanisms offer different advantages and characteristics, providing options for designers to choose the most suitable method based on their specific requirements, such as desired radiation patterns, impedance matching, and ease of implementation.

1.2 Overview of Body Centric Networks (BCN) Applications

In recent years, there has been a growing interest in BCN, as evidenced by numerous studies focusing on systems and devices for various applications including personal entertainment, defense, security, gaming, and healthcare [13]. Table 1-1 provides examples of on-body devices along with their respective applications [14]. These advancements highlight the increasing significance of body-centric wireless communication technologies and their potential to revolutionize diverse sectors.

Table 1-1 Applications of on-body devices. [14]

Field	Applications
Health Care	Wearable Thermometer/Breast Cancer Detection/ Oximetry/ Wearable Doppler Unit/ GPS tracker/Endoscopy/Glucose monitoring
Security and Rescue	Life Jacket/ Helmet/ Rain coat/ Trackers/ E-shoes/Fitness bands
Entertainment	LED dress/ Smart watches/ intelligent shoes

Body-centric wireless communications encompass the utilization of implantable and wearable wireless devices, facilitating human-self and human-to-human systems. This field

combines various wireless network concepts, including wireless body-area networks (WBAN), wireless personal area networks (WPAN), and wireless sensor networks (WSN) [15]. Off-body links refer to connections between external nodes located away from the human body and nodes positioned on the human body. Conversely, on-body links involve the reception and transmission of signals along the surface of the human body [16]. These distinctions are crucial in understanding the different modes of communications within body-centric wireless systems.

1.2.1 Millimetre-wave on-body and off-body communication

Millimeter-wave (mmWave) communication has gained significant attention due to its potential to revolutionize wireless communication systems. The need for mmWave communication in on-body and off-body scenarios arises from the demand for high data rates, low latency, and increased connectivity in emerging applications like wearable devices, healthcare monitoring, IoT, and beyond. Millimeter-wave (mmWave) technology refers to wireless communications that operate within the frequency range of 30 GHz to 300 GHz, encompassing wavelengths spanning from 10 to 1 millimeter [17, 18]. At these frequencies, the available bandwidth is significantly wider compared to lower frequency bands. This wide bandwidth allows for the transmission of large amounts of data, enabling high-speed communication crucial for applications that require real-time data transfer, such as healthcare monitoring or augmented reality systems .and can facilitate the development of next-to-body sensor systems equipped with specialized antennas [19]. These systems have wide applications in the healthcare sector, enabling communications, monitoring, and energy assembly and storage [20]. Off/on-body wireless communications have emerged as a well-explored research field with a multitude of applications, developments, and studies. However, operating such systems in the mmWave frequency band presents unique opportunities and challenges. Notably, the mmWave band allows for the development of compact antennas specifically

suitable for off/on-body communications [21]. These antennas offer advantages such as reduced interference and the potential for higher data rates. The mmWave band presents a promising avenue for advancing next-to-body technologies, providing improved performance, and expanding the possibilities for seamless wireless communication in healthcare and other domains [22]. Dielectric Resonator Antennas (DRAs) play a pivotal role in facilitating mmWave communication due to their unique characteristics and advantages over other antenna types in these applications. DRAs operate based on the principle of resonance within a dielectric material, typically a ceramic or composite structure. Their design allows for efficient transmission and reception of mmWave signals [3, 23]. DRAs offer several advantages in millimeter-wave applications. Their compact design allows seamless integration into small devices like wearables or sensors without sacrificing performance. With high radiation efficiency at mmWave frequencies [2]. DRAs ensure minimal signal loss during transmission. Their low-profile nature is essential for on-body applications where space is at a premium. Additionally, the ability to tailor DRAs to specific frequencies within the mmWave spectrum offers flexibility in designing communication systems for diverse applications. Moreover, their robustness against interference from surrounding objects or the human body makes DRAs particularly suitable for on-body communication scenarios [24].

Millimeter-wave Dielectric Resonator Antennas (DRAs) have uniquely tackled challenges in on/off-body communication by enabling miniaturization crucial for wearable devices without compromising efficiency, mitigating signal attenuation caused by the human body or surrounding obstacles, and offering low-profile designs with directional capabilities, ensuring reliable links in on-body scenarios. Their adaptability across various frequencies within the mmWave spectrum allows for flexibility in meeting specific application requirements and regulatory standards, while their seamless integration into devices maintains

high performance, addressing the complex demands of on/off-body communication systems, ultimately enhancing reliability and signal integrity in these challenging environments.

1.2.2 Next-to-Body Devices in the Era of 5G.

The inclusion of higher frequency spectra in the millimeter wave (mm-W) frequency range has been considered due to the demand for high-speed data rates and the limited available spectrum [25]. This necessitates a paradigm shift in component design, new communication architectures, and unique models for mmWave propagation tailored specifically for next-to-body devices. Additionally, blockages and increased propagation path losses in the mmWave range require the organization of cells into smaller macro-cells and pico-cells, accommodating the integration of machine-type and next-to-body devices into the current realm of tablets and smartphones. Exciting developments are expected in terms of data transfer growth, potential core network virtualization at cell edges, and advancements in the Internet of Things (IoT), creating a dense system of interconnected devices [26]. Next-to-body devices offer increasingly attractive solutions across various domains, from consumer electronics to medical and military applications. These devices are also set to play a crucial role in the upcoming fifth-generation (5G) systems. These systems aim to achieve lower outage probabilities and higher bit rates in smaller micro and pico cells, covering larger areas than the fourth-generation (4G) networks. Furthermore, beamforming and beam configurability are expected to ensure spectral and energy efficiencies at both base station and smartphone levels, overcoming the limitations of current 4G systems [27-29]. The integration of next-to-body devices into 5G networks holds great promise for enhanced connectivity, improved performance, and expanded capabilities in future wireless communication systems.

1.2.3 Interaction between the Antennas and Human Body.

To ensure compatibility with the human body shape, BCN antennas require small size, low profile, and lightweight characteristics. Flexibility, wide bandwidth, and high gain are also necessary for the mmWave operation to meet the demands of high data rates [30]. Additionally, low energy consumption is a crucial consideration [31]. Furthermore, the impact of the human presence on such antennas needs to be characterized to ensure optimal performance. Electromagnetic distortions can occur due to absorptions in the lossy tissues of the human body and scattering/reflections from the body surface [32]. Therefore, a comprehensive evaluation of the interaction between wearable antennas and the human body is essential for efficient BCN structures. The presence of a complete ground plane beneath the antenna can minimize interaction with the human body, thereby avoiding significant performance degradation [33]. It is advisable to establish criteria for selecting an appropriate shape for the ground plane, which can enhance antenna robustness against random variations in the body [34].

Additional important key to evaluate the antenna performance is testing the antenna near to the human body, where it has been found that when the antenna is flat, bent, or placed close to the chest, arm, or stomach of a human, it still retains a great gain and efficiency of over 70% [35]. Moreover, the lower edge frequency of the operating band shifts from 2.27 GHz in free space to 2.29, 2.31, and 2.34 GHz on the chest, leg, and arm, respectively [36]. Furthermore, the distance between the antenna and the human tissue need to be taken into account when test the antenna, where it has been observed that, the antenna worked well when placed at a distance of 1 to 6 mm from the surface of the human body, simulating common body-mounted settings, despite experiencing detuning, pattern degradation, and a loss in efficiency in on-body locations with an antenna-body gap of 0 and 1 mm [37]. Hence, it can be noted that testing the antenna in different parts of the human body shows almost the same result with a small shift in the resonance frequencies, therefore, the test of the antenna can be done either in one part of

the human body or different parts. In terms of the distance between the proposed antennas and Investigations into the impact of the human body on Dielectric Resonator Antennas (DRAs) involve experimental setups where DRAs were simulated alongside three layers of the equivalent human body. Positioned at varying distances from the antenna, these models simulate real-world scenarios to analyze the antenna's performance metrics like radiation patterns, impedance, and efficiency. Findings reveal that the human body's presence near DRAs causes a small signal attenuation. Such investigations inform strategies for mitigating these effects, ensuring optimal DRA performance in on-body communication systems despite the presence of the human body.

1.2.4 Specific Absorption Rate (SAR)

SAR is a critical parameter used for evaluating the exposure risk to microwaves and radio frequencies [38]. Researchers and engineers are consistently concerned about the health effects of radiation and the energy absorbed by the human body. Wireless devices have been subjected to SAR evaluation [39]. The SAR varies across different frequencies due to the varying dielectric constants of tissues. SAR values are typically expressed in watts per kilogram (W/kg) for either 1g or 10g of tissue. Two widely used SAR limit methods are those defined by IEEE, which specifies a limit of 1.6W/kg for any 1g of tissue, and International Commission on Non-Ionizing Radiation Protection (ICNIRP), which sets a limit of 2W/kg for any 10g of tissue [39]. In the context of on-body antennas, it is important to note that more investigation and attention are needed regarding the SAR. Array antennas, with their strong fields, can result in SAR values that exceed the recommended levels [40]. This highlights the need for further research and measures to address SAR concerns associated with on-body antennas.

SAR represents the rate at which radio frequency energy is absorbed by the human body tissue [41], which determines the absorbed energy per mass unit according to the following equation [42].

$$\text{SAR} = \sigma \frac{E_i^2}{\rho} \text{ W/kg}$$

where E_i is the strength of the incident electric field, ρ is the tissue's mass density in kg/m^3 , and σ is the tissue's conductivity in S/m .

The specific absorption rate needs to be evaluated to ensure that it is lower than the recommended safety threshold limit according to the Federal Communications Commission (FCC) and ICNIRP standards. However, it is important to note that these SAR guidelines are defined for frequencies up to 10 GHz and 6 GHz for the FCC and ICNIRP, respectively, and have not yet been released for higher frequencies. Since near-field exposure at mmWaves has only become a concern in recent years, these guidelines do not offer any dosimetric information or suggestions that could be applied to near-field exposure at mmWaves [41-43]. However, it is still important to calculate the SAR since the antenna operates next to the human body. According to [41, 42, 44], at 28 GHz, the used space between the antenna and the human body can be maintained at 5 mm with the recommended input powers of 15 dBm, 18 dBm, or 20 dBm.

1.3 Body-Centric Antennas

1.3.1 Textile Body-Centric Antennas.

Due to the desirable features of textile materials such as flexibility, wash ability, and cost-effectiveness, there has been a growing interest in their utilization in wearable and Body Area Network (BAN) applications [45]. Numerous studies have been conducted on wearable textile antennas within BAN as offer flexibility and can be seamlessly integrated into clothing

[45-49]. For instance, microstrip antennas designed for wearable applications have been developed using electric textiles and copper conductive components, with fabric substrate materials made from jeans cotton [45, 46]. A textile end-fire array operating at 60 GHz has been proposed for wireless BAN, while the Yagi-Uda antenna has been studied using an equivalent tissue model representing the human body. The textile substrate's permittivity has been characterized, resulting in maximum measured on-body gain and efficiency of 11.9 dBi and 48.0%, respectively, when the antenna operates within the 57-64 GHz frequency range [47]. In another study focusing on the Industrial, Scientific, and Medical (ISM) communications range of 2.45 GHz to 6 GHz, a multi-band miniature patch antenna has been proposed using various electro-textile substrates [48]. The antenna incorporates a T-shaped slot, with the silk substrate exhibiting a minimum reflection coefficient and an impedance bandwidth of 4.8% at the cost of a specific absorption rate of 32 Peak/f1g W/kg [48]. Additionally, a miniature wearable 2.5 GHz antenna has been suggested, fully implemented using textile materials. The antenna demonstrates a free-space gain of 4.2 dBi, reduced to 3.8 dBi in the on-body scenario. The achieved impedance matching bandwidths are 4.8% in free space and 5.1% on-body [49]. Another study proposed a small ground plane as the main radiator, employing a flexible felt substrate with a permittivity of 1.2. The fabricated antenna offers a wide impedance bandwidth of 20% and remains matched when worn on the body. However, the free-space gain decreases from 1.6 dBi to 1.2 dBi when placed on-body due to human tissue losses [50]. In medical applications, a microstrip rectangular patch antenna has been proposed utilizing different textiles as substrates with varying dielectric constants [51]. Furthermore, an Ultra-Wideband (UWB) antenna has been designed using textile materials for both the substrate and conducting components. The proposed antenna meets the requirements of wide bandwidth, flexibility, wash ability, and compact size. The main radiation characteristics of the antenna design have been presented [52]. Overall, textile materials

enhance the antenna's impedance bandwidth and provide a low dielectric constant, reducing surface wave losses [53]. However, the electromagnetic properties of textiles are influenced by factors such as water exchange with the surroundings, compressibility, density changes under low pressures, porosity, and anisotropy [54]. To mitigate undesired effects, it is crucial to understand how these characteristics impact the antenna's behaviour.

1.3.2 Non-textile Body-Centric Antennas

Millimeter-wave reconfigurable antennas are considered the future of next-generation wireless systems. In the context of 5G networks, a coplanar waveguide (CPW) fed T-shaped millimeter-wave antenna has been proposed by incorporating two variable resistors, the resonant frequency is adjusted to achieve matching within the frequency range of 23-29GHz [55]. Another study introduces a wearable CPW fed antenna backed by a 3×3 cell Flexible Fractal Electromagnetic Bandgap (EBG) surface. This configuration improves the -10 dB bandwidth and gain by 40% and 3 dB, respectively. The measured realized gain without and with EBG on different human body parts are: 7.8 dBi on the chest, 8.1 dBi on the forearm, and 8 dBi on the thigh at 24 GHz [56]. In another research, a flexible circuit board is utilized for millimeter-wave body-centric applications, with an overall antenna size of $14 \times 10.5 \times 1.15$ mm³. The effects of three key elements, namely the feed gap length, the thickness of the air substrate, and the rectangular loop (RL) thickness are investigated to enhance the antenna's performance. The antenna achieves a gain of 12.1 dBi on-body and 10.6 dBi off-body, with a bandwidth of 9.8 GHz. Performance evaluation using a realistic numerical phantom demonstrates excellent performance when the antenna is positioned at a distance of 6 mm from the human body surface. The efficiency experiences a slight drop at on-body distances of 0 and 1 mm [37]. Additionally, 3D printing has been demonstrated for the fabrication of conformal on-body antennas for various wrist-worn wireless telecommunications. The process involves

painting metallic layers and utilizing a single machine to fabricate both the bracelet and the metallic layer, employing a multistep approach [57].

1.3.3 Circular Polarised Body-Centric Antennas

The polarisation of the transmitted antenna is determined by the orientation of the electric field of the electromagnetic plane wave. There are three main types of polarisation: linear, elliptical, and circular. Circular polarisation can be further divided into right-hand circular polarisation (RHCP) and left-hand circular polarisation (LHCP). In RHCP, the thumb points in the direction of wave propagation, while the curled fingers indicate the direction of polarization. LHCP, on the other hand, represents a left-hand circular rotation, which is counter-clockwise [58].

Linearly polarised antennas are commonly utilized in BANs due to their ease of design and fabrication compared to circularly polarized antennas [59]. However, it is acknowledged that circular polarisation provides a more flexible orientation between transmitting and receiving antennas compared to linear polarization. Nevertheless, designing wideband CP antennas that achieve wide axial ratio and impedance bandwidths simultaneously presents a challenge [60]. A novel CP textile antenna has been developed, demonstrating a 3-dB axial-ratio CP bandwidth of approximately 3% [61]. In another study, for body-centric communications, a flexible circularly polarised textile antenna and its conformal antenna array (WCAA) are discussed. The results show an antenna peak gain of 8.5 dBi, a measured bandwidth of 35.1%, and a bandwidth of 17.5% at a 3 dB axial ratio [62]. In the 2.4 GHz Industrial, Scientific, and Medical (ISM) band, a small circularly polarised filtering antenna achieves an axial ratio of 3 dB, >3.5 dBi gain, and -10 dB return loss. It keeps these qualities close to the body, which makes it perfect for off-body communication [63]. Another ISM band design is a compact circularly

polarised off-body antenna that operates in the 5.16–6.13 GHz frequency, the proposed antenna has a high-permittivity substrate reflector for off-body radiation and is coplanar waveguide-fed. It achieves steady radiation, 90% efficiency, a peak gain of 6.22 dBic, and a specific absorption rate (SAR) of 0.131 W/g [64]. Furthermore, a compact CP co-designed filtering antenna has been reported. This design achieves an axial ratio of less than 3 dB and a gain exceeding 5.2 dBi over a bandwidth of approximately 12.2%, with a -10 dB S_{11} bandwidth ranging from 3.77 to 4.26 GHz. The radiation properties and stable impedance of the antenna design have been considered when mounted on various positions of the human body [65].

1.3.4 Challenges in on/off-body communication were addressed through the designs of DRAs.

In the realm of body-centric networks, extensive research has been conducted on microstrip antennas. However, microstrip antennas come with certain limitations. One notable drawback is their narrow bandwidth, which can restrict their performance in dynamic environments. Additionally, its require mounting on less vulnerable parts of the body to avoid issues related to bending and wrinkling. Consequently, exploring alternative options becomes crucial. In this context, DRAs have emerged as a promising alternative [66]. Because the Dielectric Resonator Antenna (DRA) consists entirely of dielectric material, it can achieve minimal losses even when operating at millimeter-wave frequencies, resulting in remarkably high radiation efficiency. These desirable characteristics position the DRA as an excellent choice for contemporary wireless systems [67]. DRAs offer wider bandwidth, increased robustness against body movements, and the flexibility to be mounted on various parts of the body. Investigating the potential of DRAs within body-centric networks, can overcome the limitations associated with microstrip antennas and unlock new possibilities for efficient and reliable wireless communication in wearable devices and on-body applications [68].

1.3.5 Body-Centric Dielectric Resonator Antenna

DRA's have garnered attention in the field of BAN and have been the subject of several studies. One such study proposes and implements a textile wearable broadband DRA [69]. In another investigation, a DRA is introduced in the form of a wearable button structure, utilizing a microstrip feed on an FR4 substrate [70]. Additionally, a compact DRA with a four-line feed for excitation is proposed, resulting in an impedance bandwidth of 11.7% and an AR bandwidth of 3.9% accompanied by a gain of 8.6 dBic [71]. Another compact circularly polarised DRA is suggested, exhibiting respective impedance and AR bandwidths of 66% and 15% in free space. When positioned next to the human body, a ground plane is employed between the antenna and the body [72]. Furthermore, a wearable CP DRA operating in the TE_{183}^y higher-order mode is reported for off-body communications, demonstrating respective impedance and AR bandwidths of 20.7% and 9.6% [68]. In [73] a mmWave circularly polarized DRA is proposed as a wristwatch, exciting the resonance modes of TE_{113} and TE_{115} at 25 GHz and 29 GHz, respectively, in free space. However, when placed on the equivalent wrist, only the TE_{115} resonance mode is excited at 27.5 GHz. Higher-order mode DRA operation offers higher gain at the expense of a narrow bandwidth, which can be addressed through the utilization of a multilayer structure [74]. By incorporating a dielectric coating layer with a relative permittivity of ϵ_{r2} , a transition region is created between the DRA and free space, significantly enhancing the radiation characteristics [74].

Moreover, the designed antenna is supposed to act as a button placed at the shoulders. The antenna/body interaction has been studied by comparing the performance of the off-body DRA with the on-body counterpart that was placed on a rectangular phantom with human dielectric properties. A gain of 5.4 dBi has been accomplished at 5.8 GHz for on-body DRA [75].

Furthermore, a broadband DRA has been proposed for medical applications, where the antenna size has been minimized by incorporating a planar conductive wall as well as a multi-segment dielectric. The antenna has achieved matching over a frequency range of 4.4-9.7 GHz [76]. An alternative study a slot-fed DRA with a modified T-shaped feed line at different resonant modes [77]. The antenna achieved matching from 1.67-6.7 GHz with a gain of 8.7 dBi. A number of studies have been published that address the DRA conformability with respect to the human body. As an example, a curved ground plane with conformal convex and concave DRA has been proposed [78]. In order to avoid performance degradation, analysis of the watchband-like substrate has been considered and user effects were investigated [79]. One of the main concerns of using mmWave DRAs is the assembly and bonding of the antenna to the feed network. In this article, a grooved ground plane has been utilized to address this issue [80].

1.3.6 Body-Centric Array Antenna.

A screen printing was utilized on a flexible substrate to ensure lower costs as well as compatibility with wearable devices, where an optimised 77 GHz array has been demonstrated with a high gain of 11.2 dBi, and to protect the antenna from human body losses a microstrip patch antenna has been utilized due to the presence of a ground plane. The antenna array has three independent beams where it has performed in flat and flexed conditions to detect objects moving in three different directions [81]. An alternative design of a finger ring antenna has been proposed in [82] as a circular phased antenna array for 28 GHz 5G communication systems. The design has been tested in free space and on phantom hand. For on-body results the realized gain of 5 dBi has been observed with impedance bandwidth around 3.5%.

Furthermore, several studies have been reported on CP radiating elements such as printed antennas [83] as well as sequentially rotated CP DRA array [84]. Furthermore, G-shaped monopoles have been utilized in a MIMO antenna with wideband impedance and CP bandwidths [85]. In [86] a dual polarised, multiband four-port decagon shaped flexible MIMO

antenna has been proposed. Another MIMO antenna with wideband impedance and circular polarisation bandwidths has been proposed in [87]. Moreover, various publications have examined the effectiveness of cross-slot feeding to achieve CP radiation by exciting two degenerate DRA resonance modes with equal amplitudes and 90° phase difference with a wide CP bandwidth [73, 88, 89].

1.4 Millimetre-wave DRA Arrays

Dielectric resonator antennas have undergone extensive research over the recent decades [90, 91]. Therefore, DRAs represent ideal candidates for wireless communication systems, especially those that operate in the mmWave band. Traditional microstrip antennas, on the other hand, exhibit substantial surface-wave and ohmic losses at high frequencies, which drastically deteriorate the radiation efficiency [92, 93]. MmWave DRA arrays' have been utilized in a number of research studies [92, 94-99]. For example, a 2×2 DRA array has been fabricated using the substrate integrated technology with a gain of 12.7 dBic together with impedance and CP bandwidths of 16.4% and 1.1%, respectively [92]. An aperture-coupled 2×2 DRA array has been reported when each cylindrical DRA element operates in the $HEM_{11\delta}$ resonance mode, which leads to a gain of 11.43 dBi as well as an impedance bandwidth of 26% [94]. In addition, a monolithic polymer-based DRA array has been proposed using four elements with a realized broadside gain of 10.5 dBi and stable radiation patterns at 60 GHz along with an impedance bandwidth of 12% [95]. Another study has proposed a 1×8 elements grid dielectric resonator antenna array that has a measured impedance bandwidth of 18.3% and a broadside gain of 12 dBi [96]. Moreover, a 2×2 circularly polarized DRA array has been reported at an operating frequency of 30 GHz and a maximum gain of 9.5 dBic with respective impedance and axial ratio bandwidths of 33% and 5% [97]. In order to easily align the individual array elements, a grooved and grounded superstrate has been utilized for a 16 cylindrical DRAs array with

measured impedance bandwidth of 9.8% and a maximum gain of 15.68 dBi at 28.72 GHz [98]. Furthermore, it has been demonstrated that when the DRA elements are joined using dielectric arms, for alignment purposes, the achieved impedance bandwidth and gain are 31% and 9.8 dBi, respectively [99]. From the literature, it can be noted that the highest achieved gain of a mmWave DRA array is 15.68 dBi using 16 linearly polarized DRA elements [98]. However, the increased number of elements is associated with larger antenna size as well as complex feed network. Therefore, arrays of 4 circularly polarized DRA elements address these limitations, albeit with a lower gain [92, 94, 97]. As a result, a compact array with the advantages of higher gain and wider CP bandwidth would be beneficial and has not been reported earlier at the considered frequency range.

1.5 Multi Band and Omnidirectional Pattern

Over recent years, the evolution of mm Wave communication systems has led to more rigorous requirements for antenna designs such as high gain, wide and multi-band operation as well as pattern diversity. DRAs have the potential of addressing these requirements due to well-known advantages such as high radiation efficiency, wide impedance bandwidth and design flexibility. Therefore, mmWave DRAs received an increased research interest with focus on broadside radiation [74, 100-102]. On the other hand, omnidirectional radiation is desired for 5G and Beyond 5G (B5G) communication systems to increase the coverage area in various applications such as on-body communications as well as device-to-device short distance communications [103]. Therefore, several studies have been reported on the design of mmWave omnidirectional antennas [104, 105]. However, an omnidirectional mmWave DRA has not been reported earlier, which is in sharp contrast with the numerous published studies on the design of omnidirectional DRAs at lower frequencies with focus on exciting

specific transverse magnetic (TM) and transverse electric (TE) modes to achieve the required pattern.

For example, an omnidirectional cylindrical DRA was proposed by exciting the $TE_{01\delta}$ and $TM_{01\delta}$ resonance modes at 3.87 GHz and 4.02 GHz, respectively, using a central coaxial probe feed [106]. Besides, a multi-band multi-sense circularly polarized hybrid patch/DRA omnidirectional antenna was reported by exciting the TM_{02} and TM_{011} resonance modes for the patch at 2 GHz and DRA at 2.6 GHz, respectively [107]. In a more recent study, wideband filtering omnidirectional cylindrical DRA has been presented using a hybrid feed that consists of coaxial probe and metallic disk to excite the $TM_{01\delta}$ and TM_{013} DRA resonance modes at 2.19 GHz and 3.37 GHz, respectively [108]. Further, a coaxial probe-fed omnidirectional hemispherical DRA was proposed by exciting the TM_{101} resonance mode at 3.7 GHz [109]. Another probe-fed omnidirectional hemispherical DRA was designed for wireless capsule endoscope system by exciting the $TM_{01\delta}$ and $TE_{01\delta}$ resonance modes for multi polarization at 2.45 GHz [110]. Moreover, a probe-fed omnidirectional rectangular DRA with a square cross section has been designed by exciting the quasi- TM_{011} mode at 2.4 GHz for linear and circular polarizations [111]. Furthermore, innovative rectangular multi-function glass DRAs were reported with the capability of achieving linearly and circularly polarized omnidirectional radiation patterns by exciting the quasi- TM_{011} mode at 2.4 GHz [112]. Similarly, the higher-order degenerate TE_{121}^x and TE_{211}^y modes have been excited at 3.6 GHz, with equal amplitude and phase, to achieve omnidirectional radiation from a rectangular DRA [113, 114]. Subsequently, a multi band probe-fed omnidirectional rectangular DRA was proposed, where the TE_{121}^x and TE_{211}^y resonance modes were excited at 3.5 GHz together with the TE_{141}^x and TE_{411}^y resonance modes at 5.8 GHz [114].

It should be noted that in all the above-mentioned studies, omnidirectional radiation has been attained using a centrally located coaxial feeding-probe to excite the required resonance

modes. On the other hand, owing to their capability of supporting various type of modes when placed above a ground plane, cylindrical DRAs have successfully been utilized recently with planar feed networks to achieve omnidirectional radiation patterns. For example, an omnidirectional cylindrical DRA with a planar feed of shorted microstrip cross has been demonstrated by exciting the $TM_{01\delta}$ and $TM_{011+\delta}$ resonance modes at ~ 2.4 GHz to achieve circular polarization diversity [115]. The first attempt to utilize a ring slot aperture to feed an omnidirectional cylindrical DRA was proposed by exciting the $TM_{01\delta}$ fundamental resonance mode at 2.4 GHz [116]. Furthermore, a pattern diversity cylindrical DRA has been proposed using a meander line-loaded annular slot to excite the $TM_{01\delta}$ mode in combination with a differential strip to excite the $HEM_{11\delta}$ for omnidirectional and broadside radiations, respectively, at 2.4 GHz [117]. Moreover, four linear stubs have been utilized to excite the $TM_{01\delta}$ and $TM_{011+\delta}$ resonance modes of omnidirectional cylindrical DRA to achieve circular polarization at 5.8 GHz [118]. In a more recent study, arced-aperture feeding was employed in the design of a wideband omnidirectional cylindrical DRA by merging the bandwidth of the excited $TM_{01\delta}$ and $TM_{02\delta}$ resonance modes at ~ 5.8 GHz [119].

1.6 Definition of the Research Problem

The large size of a DRA poses a challenge for their on-body use at lower frequencies. However, this limitation can be overcome at mmWave frequencies, where the smaller wavelength allows for more practical antenna designs. In addition, circular polarisation is usually adopted to address orientation issues that can arise with linearly polarised antennas. To mitigate challenges related to body presence and mechanical deformations, the complete ground plane is carried out. Simulation techniques are employed to explore various shapes, including planar and conformal configurations, aiming to enhance antenna performance while maintaining a low profile. Additionally, alignment plays a crucial role at mmWave frequencies, and several

techniques are proposed to address this issue. Moreover, Since the simulated results on the equivalent human tissue closely match those obtained in free space with a separation distance between 1 mm to 5 mm, all measurements were conducted in a free space environment. This research contributes to the design of mmWave antennas suitable for both off/on-body applications, incorporating desirable features such as low profile, high gain, wide bandwidth, and flexible orientation. Furthermore, an omnidirectional mmWave DRA of any shape has not been reported previously, due to the obstacle of using the coaxial-cable feed in the higher frequencies, a planar feed network with a ring slot was used to overcome this problem for the first time in this study.

1.7 The Goals and Objectives of the Thesis

The main objective of this project is to explore innovative designs of a DRA that exhibit enhanced performance for mmWave off/on-body applications. In order to accomplish this primary goal, specific objectives have been established:

- Introduce innovative designs of single-element rectangular DRAs for off-body applications.
- Enhance the gain of the rectangular DRA by increasing the number of elements in the array configuration.
- For on-body in particular the signal needs to travel along the surface of the human body, hence the omnidirectional is needed, explore novel methods to excite the DRA and achieve an omnidirectional radiation pattern, as the traditional probe feeder is impractical mm wave.
- Achieve both broadside and omnidirectional radiation patterns in a single design by incorporating multiple bands. This eliminates the need for a reconfigurable design, as the desired radiation patterns can be achieved without any adjustments or modifications.

1.8 Research Contributions

This research not only delves into the impact of the human body on Dielectric Resonator Antennas (DRAs) for on/off-body communication but also introduces innovative designs to enhance their performance. These designs encompass coated rectangular DRAs, DRAs situated on grooved ground planes, and wristwatch DRAs, all aiming to broaden impedance and axial ratio bandwidths while maintaining high gain within a reduced antenna profile. Moreover, this study explores techniques to improve gain by employing array configurations with multiple elements, ensuring stable high gain across most of the antenna's impedance bandwidth. Additionally, the research investigates unconventional methods to excite DRAs for achieving omnidirectional radiation patterns, a challenge particularly pertinent in mmWave applications where traditional probe feeders are impractical. The incorporation of multiple bands in a single design facilitates both broadside and omnidirectional radiation patterns without necessitating reconfigurable designs, offering versatility in achieving desired radiation patterns without requiring adjustments or modifications. These advancements collectively propel the field forward by not only understanding the interaction of DRAs with the human body but also by introducing innovative designs that optimize their performance for on/off-body communication in millimeter-wave scenarios.

1.9 Thesis Outline

The thesis comprises six Chapters, outlined as follows:

Chapter 1: The first chapter of the thesis provides an introduction, literature review, and an overview of the research contribution. It also outlines the layout and structure of the thesis.

Chapter 2: Explore and analyze various designs of a single-element rectangular DRA to optimise their performance and efficiency for reliable wireless communication in off-body scenarios. The simulated and measured results exhibit strong conformity.

Chapter 3: Investigating and analyzing the rectangular DRA array to enhance gain while maintaining a low profile for off-body applications with CP radiation and high gain. Good agreement between simulated and experimental results.

Chapter 4: Presents a multi-band mmWave DRA designed for off/on-body communications. The antenna achieves broadside and omnidirectional radiation using a planar-feed configuration, allowing for reliable wireless communication across multiple frequency bands. The practical measurements validate and support the simulation results obtained.

Chapter 5: Presents a dual-band mmWave Cylindrical and Hemispherical DRAs designed for off/on-body communications. A close agreement has been achieved between the measurement and simulation results.

Chapter 6: Presenting the key conclusions drawn from the research and offering suggestions for future work that can build upon the findings.

Chapter 2

Low-profile Circularly Polarized Rectangular Dielectric Resonator Antennas for mmWave Off-Body Applications.

2.1 Introduction.

In the fast-growing field of off-body communications, the need for high-performance antennas operating in millimeter-wave (mmWave) frequency bands has grown significantly. These antennas play an important role in enabling efficient wireless communications between various off-body devices [120, 121]. In the framework of off-body communications, novel and new designs of a low-profile wide bandwidth circularly polarised DRA have been proposed for mmWave applications. It is well-known that circularly polarized antennas offer various benefits, including eliminating the need for alignment between transmitting and receiving antennas, thus providing orientation independence, reduced fading, improved coverage, less interference, smaller form factors, and simplified integration. These advantages ensure reliable performance and user safety [122]. The aim of the proposed antenna designs is to address the challenges associated with off-body communications. The low-profile ensures compactness and aesthetic appeal, making it suitable for integration into wearable devices or other off-body applications. Additionally, the antenna's wide bandwidth capability allows communication across a range of mmWave frequencies, enabling compatibility with different systems and standards. Besides, higher gains increase the communication distance. By harnessing the unique properties of the proposed designs, enhanced connectivity and efficiency in various off-body scenarios can be achieved, thereby facilitating the advancement of wireless communication technologies in this domain. The first part of this thesis is focused on the design of efficient off-body mmWave antennas. Therefore, this Chapter presents three different designs of off-body rectangular

DRA. The first proposed antenna is a two-layered rectangular DRA operating at 24 GHz. The second design is a rectangular DRA with a grooved ground plane, for easy alignment and assembly at 28GHz. Finally, a wristwatch mmWave DRA. The chapter review is illustrated in Figure 2-1.

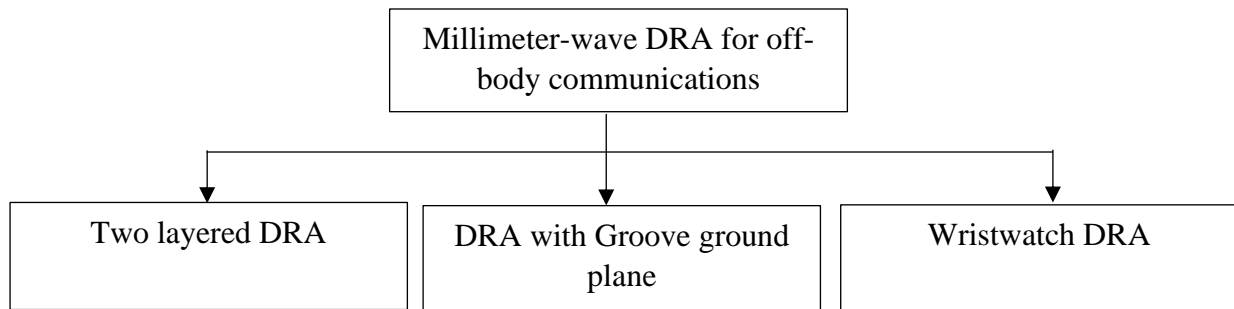


Figure 2-1 Chapter review.

2.1.1 Dielectric Waveguide Mode

DWM typically stands for Dielectric Waveguide Mode, a fundamental concept in electromagnetics and waveguide theory. In a dielectric waveguide, electromagnetic waves propagate through a dielectric medium, guided by the structure's geometry. Dielectric waveguides often consist of a core material with a different dielectric constant surrounded by another material. These guides can transmit waves at microwave or optical frequencies, employed in various communication systems and devices [123]. TE Modes (Transverse Electric): In TE modes, the electric field component is entirely transverse (perpendicular) to the direction of propagation and the waveguide's axis. The subscript abc refers to the mode numbers denoting the variation of the electromagnetic field along the cross-sectional axes of the waveguide. For example, TE_{10} represents a mode with a single half-wave variation along one axis and no variation along the other. TM Modes (Transverse Magnetic) TM modes feature a magnetic field component that is entirely transverse to the direction of propagation and the waveguide's axis. Similar to TE modes, TM modes are characterized by mode numbers denoting variations of the electromagnetic field along the cross-sectional axes of the waveguide. The

orientations of these modes within a waveguide can be illustrated by considering the orientations of the electric and magnetic fields concerning the waveguide's axis. In TE modes, the electric field doesn't have a component along the direction of propagation (parallel to the waveguide axis), while in TM modes, the magnetic field lacks a component along the waveguide's axis [124, 125].

2.2 Supported Modes of a Rectangular DRA.

In terms of the rectangular DRA, the transverse magnetic (TM) mode cannot be excited when the RDRA is mounted on the ground plane. This is due to the fact that the, TM, modes require the E field to be maximum at $z = 0$, which conflicts with the boundary conditions. Additionally, the DRA's size and permittivity affect each TE and TM mode's resonance frequency. Figure 2-2, illustrates a rectangular DRA placed on a ground plane.

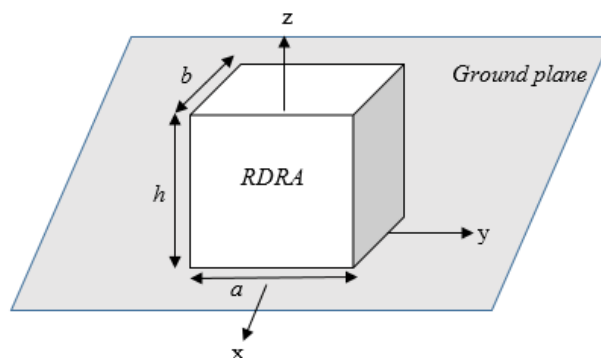


Figure 2-2 The rectangular DRA placed on the ground plane.

The dielectric waveguide model DWM can be utilized in order to calculate the resonance frequency of TE_{mnp} modes of single DRA [126].

$$k_x = \frac{m\pi}{a} \quad (2.1)$$

$$k_y = \frac{n\pi}{b} \quad (2.2)$$

$$k_z \tan\left(\frac{k_z h}{2}\right) = \sqrt{((\epsilon_r - 1)k_0^2 - k_x^2)} \quad (2.3)$$

$$k_x^2 + k_y^2 + k_z^2 = \epsilon_r k_0^2 \quad (2.4)$$

$$k_0 = \frac{2\pi}{\lambda_0} = \frac{2\pi f_0}{c} \quad (2.5)$$

Where c is the speed of the light and λ_0 is the wavelength in free space. Hence the resonance frequency modes can be calculated as:

$$f_0 = \frac{c}{2\pi\epsilon_r} \sqrt{(k_x^2 + k_y^2 + k_z^2)} \quad (2.6)$$

Moreover, the magnetic field distribution of the RDRA can be expressed with respect to the DRA dimensions of a , b and h as:

$$H_z = \frac{(k_z k_x)}{(j\omega\mu_0)} \sin(k_x x) \cos(k_y y) \sin(k_z z) \quad (2.7)$$

$$H_y = \frac{(k_y k_x)}{(j\omega\mu_0)} \sin(k_x x) \sin(k_y y) \cos(k_z z) \quad (2.8)$$

$$H_x = \frac{(k_y^2 + k_z^2)}{(j\omega\mu_0)} \cos(k_x x) \cos(k_y y) \cos(k_z z) \quad (2.9)$$

$$E_x = 0 \quad (2.10)$$

$$E_y = k_z \cos(k_x x) \cos(k_y y) \sin(k_z z) \quad (2.11)$$

$$E_z = -k_y \cos(k_x x) \sin(k_y y) \sin(k_z z) \quad (2.12)$$

In order to investigate the effect of the DRA dimensions and ϵ_r on the resonance frequencies of the mode's equation (2.6) was solved numerically using MATLAB. Examples

were listed in Table 2-1 and compared with CST simulations and the Eigenmode solver of an excited DRA. It is worth noting that the calculated resonance frequencies show slight differences compared to the simulated frequencies due to the presence of the feed network in the simulations.

Table 2-1 Dielectric constant and rectangular DRA dimensions' effects on modes

RDRA size (mm³)	ϵ_r	f_0 GHz (MATLAB)	f_0 GHz Simulated	f_0 GHz Eigen mode solver	Resonance mode
4 x 4 x 5	10	26.6	27	26.63	TE ₁₁₅
5 x 5 x 6	12	26.8	27	26.686	TE ₁₁₇
8 x 5 x 4	15	34.3	35	34.2369	TE ₁₅₅

To demonstrate the significance of the volume of the DRA on the resonance mode, where larger dimensions result in the excitation of higher modes. As shown in Table 2-2, for a given resonance frequency, the DRA dimensions need to be larger to excite a higher-order mode. For instance, the volume of a DRA stimulated in the TE₁₁₉ mode is 7.34 times larger than the volumes required for exciting the TE₁₁₃ mode and 1.8 times larger than the volume needed for exciting the TE₁₁₇ mode, with a permittivity of 9.9 in all three examples.

Table 2-2 Rectangular DRAs of various dimensions functioning in the resonance modes of TE₁₁₃, TE₁₁₇, and TE₁₁₉

The RDRA size (mm)	TE Resonance mode	Resonance frequency (GHz)	Volume (mm ³)
3.5× 3.5× 4	TE ₁₁₃	23.4	49
5×5×8	TE ₁₁₇	23.3	200
6×6×10	TE ₁₁₉	23.6	360

Displayed in Figure 2-3 (a), the MATLAB code provided serves as a demonstrative example. It showcases how the resonant frequency of the excited mode in a Dielectric

Resonator Antenna (DRA) can be accurately calculated by considering the size and relative permittivity of the DRA. The magnetic and the vector fields distribution of modes TE_{113} , TE_{117} , and TE_{119} are illustrated in Figure 2-3 (b-d). The resonance frequencies obtained from MATLAB display slight discrepancies when compared to the simulated frequencies. As mentioned early these differences arise due to the inclusion of the feed network in the simulations, warranting attention

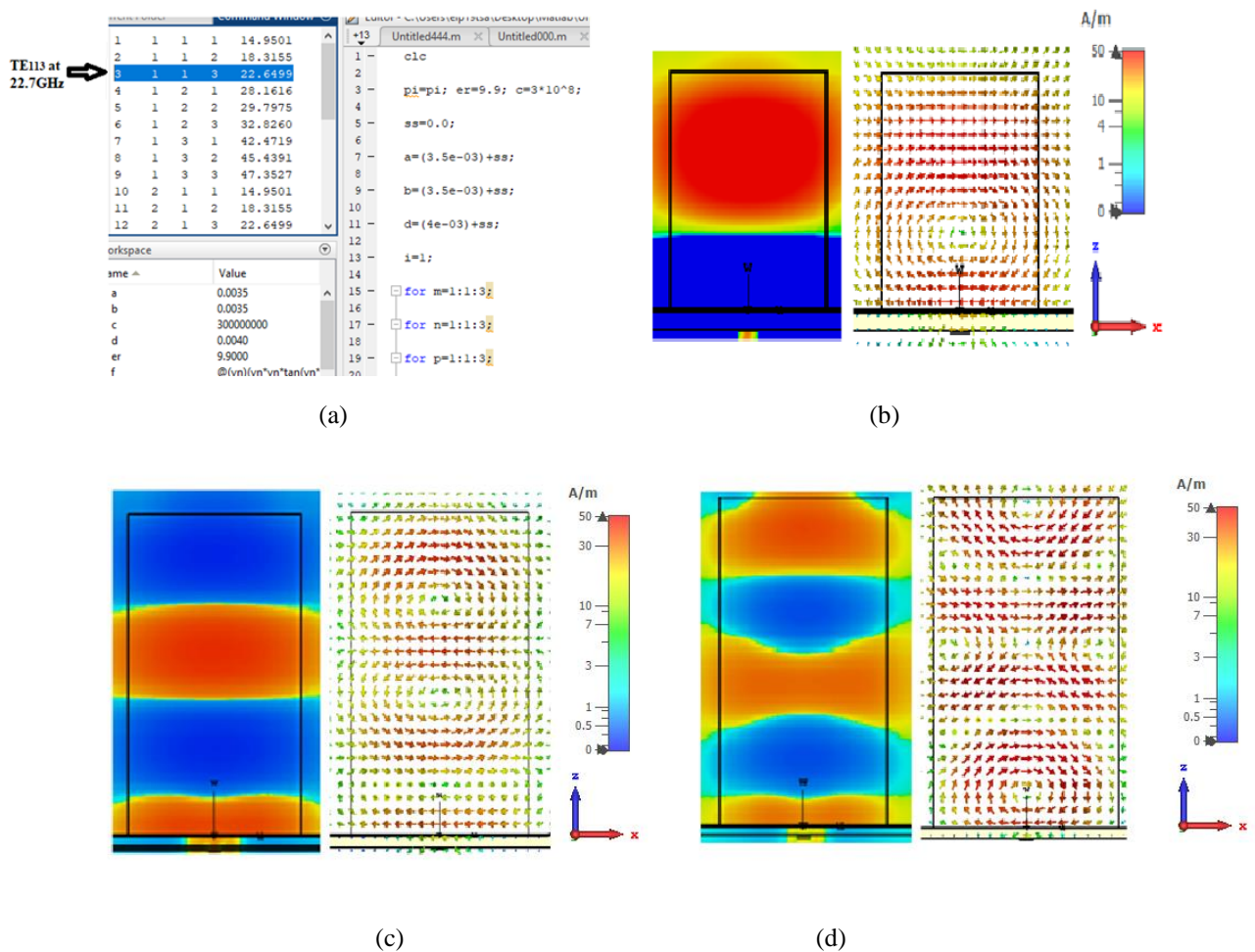


Figure 2-3 (a) MATLAB code for TE_{113} at 22.7GHz (b) Magnetic field of the TE_{113} , at 23.4GHz (c) Magnetic field of the TE_{117} , at 23.3GHz (d) Magnetic field of the TE_{119} , at 23.6GHz.

By leveraging Dielectric Waveguide Modes (DWM), then it, can accurately predict the resonant frequency and the excited mode, as previously explained. However, it's important to note that DWM analysis typically doesn't account for the feed network. Therefore, once the Dielectric Resonator Antenna (DRA) dimensions and relative permittivity (ϵ_r) are specified

based on DWM considerations, Figure 2-4 shows the current density of TE_{113} , TE_{117} , and TE_{119} .

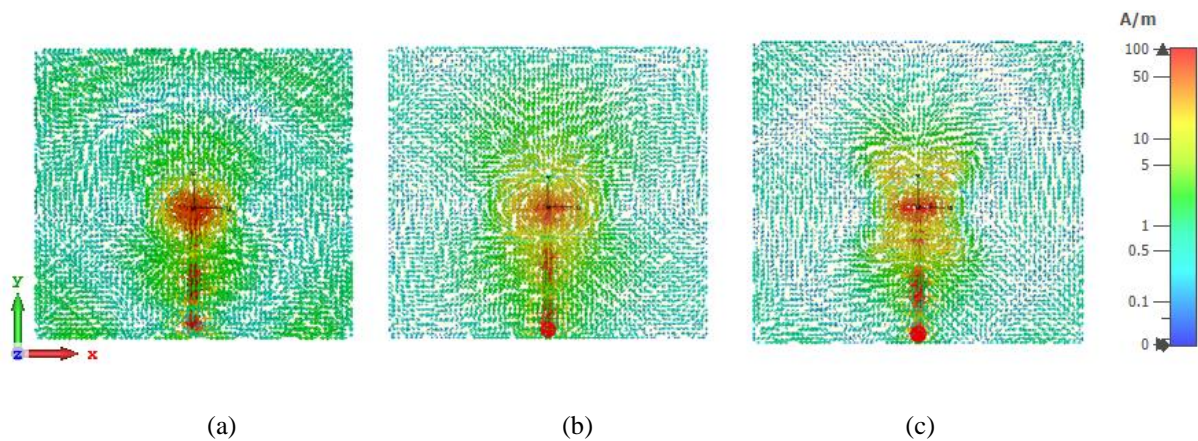


Figure 2-4 The current density of the feed network (a) TE_{113} , (b) TE_{117} , and (c) TE_{119}

The reflection coefficient is in Figure 2-5, where the same feed network was used to excite each DRA. The feed network used in these examples has a length of 25 mm, a width of 27 mm, and a height of 0.3 mm. At the top of the substrate, which has a permittivity of 3.5, there is a ground plane that includes an etched rectangular slot with a width of $w_s = 0.7$ mm and a length of 2 mm, with a microstrip line located at the bottom. It can be noted that the achieved bandwidths for the TE_{113} , TE_{117} , and TE_{119} resonance modes are 5.7%, 2.9%, and 2.6 %, respectively.

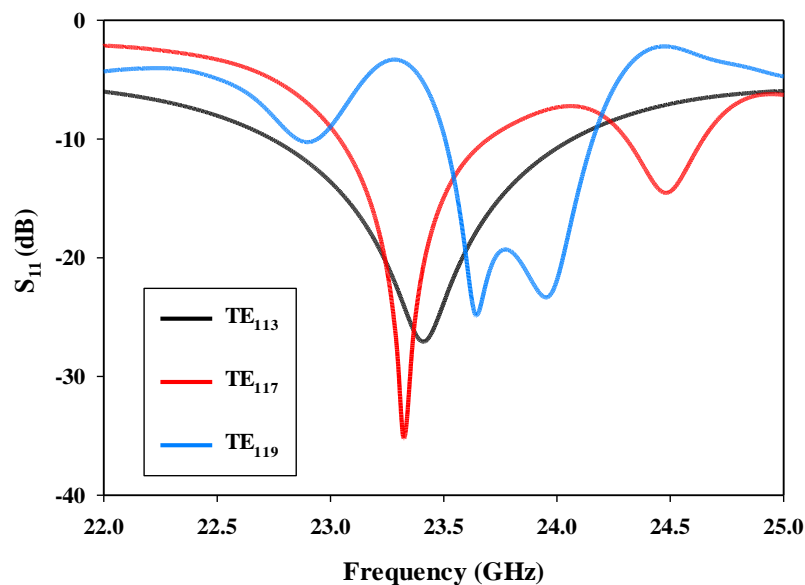


Figure 2-5 $|S_{11}|$ of rectangular DRAs excited in the TE_{113} , TE_{117} and TE_{119} resonance modes.

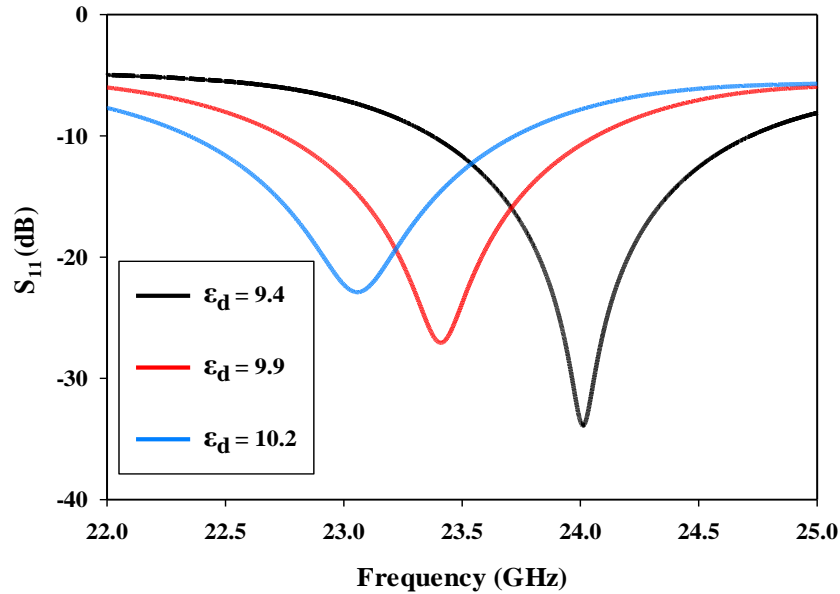


Figure 2-6 The variation of the return losses as a function of the dielectric constant.

As already mentioned, the dielectric permittivity and DRA dimensions are important factors that determine the resonance frequencies of higher-order modes. Therefore, for the case of a RDRA size of $3.5 \text{ mm} \times 3.5 \text{ mm} \times 4 \text{ mm}$, an example of various dielectric constants has been simulated, and their effects on the resonant frequency are illustrated in Figure 2-6, where it can be noted that as long as the permittivity increased, the resonant will be shifted to the lower frequency [127].

The aperture-coupled feed, whether Slot feed or aperture-coupled feed, proves effective in enhancing the activation of a singular mode within the DRA. It serves to minimize interference from unintended electromagnetic waves stemming from the feed line or probes, ensuring a focused excitation in the DRA. Typically, the slot's length measures around half the wavelength ($\lambda/2$) [125]. Moreover, the feeding mechanism within the antenna system, comprising a slot aperture etched onto the ground plane positioned atop the substrate, interacts with the underlying microstrip line. The microstrip line incorporates a length-optimized stub for achieving optimal impedance matching. This strategic configuration allows precise control over the coupling and transmission of electromagnetic signals between the microstrip line and the

radiating structure. By manipulating the current density distribution through this feed network, specific modes are selectively excited within the antenna system, ensuring desired performance while suppressing others. Additionally, this setup enhances resonance and efficiency by directing the signal propagation in a targeted manner, optimizing the overall functionality of the antenna system.

2.3 Fabrication and Measurements Procedures.

This study involves the measurement of several antenna parameters, including the reflection coefficient S_{11} , axial ratio, gain, and radiation patterns. The Alumina DRAs and feed networks were fabricated by T-ceramics [128] and Wrekin [129], respectively. All measurements were carried out using the UKRI National Millimetre-Wave Facility [130], these specific parameters and the procedures employed to measure them are described in this section:

2.3.1 Reflection Coefficient Measurements

The N5245B vector network analyser (VNA) was used to measure the return losses. To begin, the connection of the N5245B VNA was established using suitable 50Ω coaxial cables and connectors, including connector 2.4mm. The calibration procedure is performed to eliminate any potential measurement errors and ensure accurate results.

2.3.2 Far-field Measurements.

The NSI-MI Technologies system was utilized in conducting the far-field measurements. By employing this specialized measurement system, various parameters, including the radiation patterns and gain were accurately measured and visualized. To cover the elevation angle range of $\theta = -90^\circ$ to $\theta = 90^\circ$, the arm of the NSI-MI spherical system was set up to rotate across the upper hemisphere. In order to determine the axial ratio, the right and left-handed electric field components E_R and E_L which are given as [131]:

$$AR = \frac{|E_R| + |E_L|}{|E_R| - |E_L|} \quad (2.13)$$

A reference horn antenna was utilised at the receiving end as part of a comparison method to measure the gain. The DRA's gain could be calculated using the following equation from the measured reference horn's antenna gain.

$$G_{DRA} = G_{Horn} + 10 \log_{10} \left(\frac{P_{DRA}}{P_{Horn}} \right) \quad (2.14)$$

2.4 Two layered Dielectric Resonator Antenna for mmWave with removable customized holder.

2.4.1 Considered Single DRA Elements

The single DRA element in this study is designed for a wireless communication system operating in the 24 GHz frequency. The DRA element is fabricated using a permittivity ceramic material with a permittivity value of $\epsilon_r = 9.9$ and a loss tangent of 0.0001. Its dielectric resonator is shaped as a rectangular structure with an equal length and width $l_1 = w_1 = 6$ mm, and a height of 1.7 mm, making it compact and suitable for integration in small-sized devices. The proposed antenna presents in Figure 2-7.

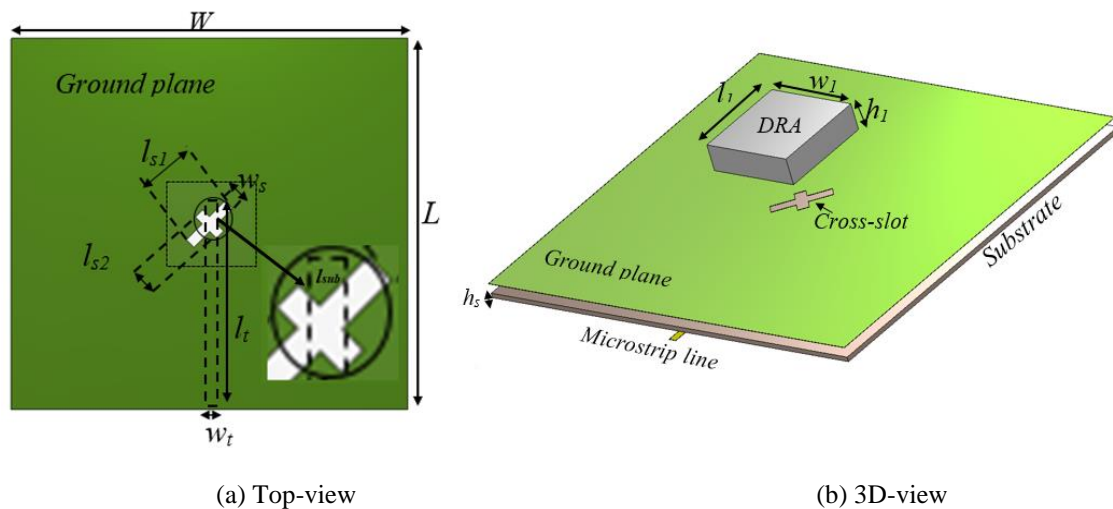


Figure 2-7 Geometric of single DRA

2.4.1.1 Aperture Shapes for Circular Polarization in Antenna Systems

Various aperture shapes, including the cross-slot, spiral, square with gap, annular, and combinations thereof, are employed in antenna systems to achieve Circular Polarization (CP). The selection depends on factors such as the application, operating frequency, and desired polarization characteristics. The cross-slot configuration was selected due to its efficiency in operating at millimeter-wave frequencies [89, 132]

The feed network consists of a Rogers substrate, Ro4003, with a dielectric constant and a loss tangent of 3.5 and 0.0027, respectively. The overall dimensions of the substrate are $L = 25\text{mm}$, $W = 27\text{mm}$ and $h_s = 0.3\text{mm}$. At the top of the substrate, there is a ground plane, which includes an etched cross-slot to ensure proper impedance matching and enhance the antenna's bandwidth, the cross-slot arms have the same width of $w_s = 0.7\text{mm}$ and different lengths of $l_{s1} = 3.7\text{ mm}$ and $l_{s2} = 2\text{ mm}$, where unequal slot arm lengths have been chosen to generate the CP radiation [74]. At the bottom of the substrate, the microstrip line is integrated to efficiently couple energy from the external transmission line to the dielectric resonator, microstrip length is $l_t = 15.5\text{mm}$ width of $w_t = 0.5\text{mm}$. Moreover, optimum matching has been achieved using a microstrip stub with a length of $l_{\text{stub}} = 1.1\text{mm}$. The effect of the length stub on the return loss is demonstrated in Figure 2-8.

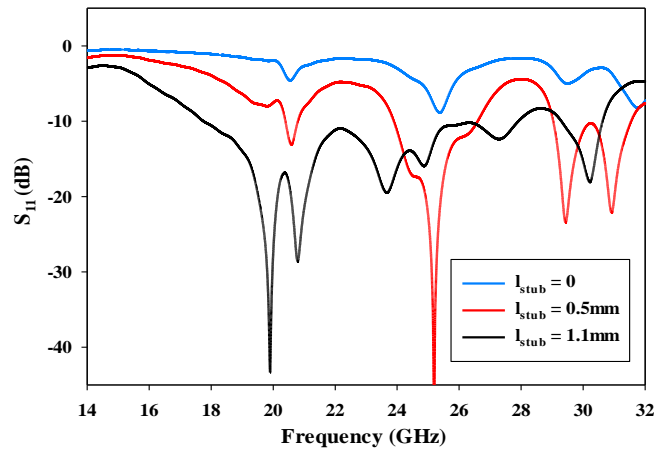


Figure 2-8 Stub length's effects on DRA return losses.

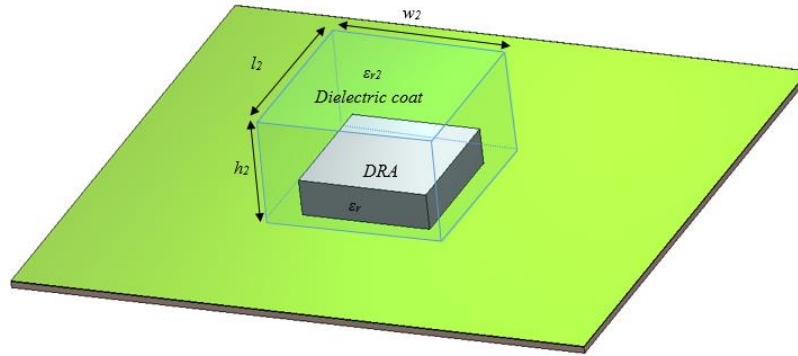


Figure 2-9 Geometry of the proposed layered DRA.

In this section, an outer waterproof dielectric layer used as a dielectric coat for the DRA, which also protects the antenna from wet weather conditions as well as the advantages mentioned earlier. Additionally, a simple removable holder has been designed with a rectangular window that can be used to identify the DRA position precisely. As mentioned earlier, the dielectric waveguide model, DWM, can be utilized to calculate the resonance frequencies for the various modes of a single layer rectangular DRA. However, there is no equivalent model for the layered rectangular DRA. Therefore, the CST Eigenmode solver was utilised to determine the modes' resonance frequencies [89]. Figure 2-9 illustrates the proposed layered DRA, Furthermore, the outer coat layer has been 3D printed using polyimide with respective dielectric constant and loss tangent of 3.5 and $\tan \delta < 0.0027$.

Figure 2-10 illustrates the return losses of the proposed layered antenna before and after adding a dielectric coat, where it can be observed that the presence of the coat has a significant impact on the DRA characteristics. For example, the impedance bandwidth extends from 14 to 30.8 GHz, which corresponds to a -10 dB S_{11} bandwidth of 75%, after adding the coat layer compared to ~ 43% for a single layer DRA. This can be understood by noting the incorporating of a dielectric coating layer, with a relative permittivity of ϵ_{r2} , generates a transition region between the DRA and free space, which improves the radiation characteristics significantly [74].

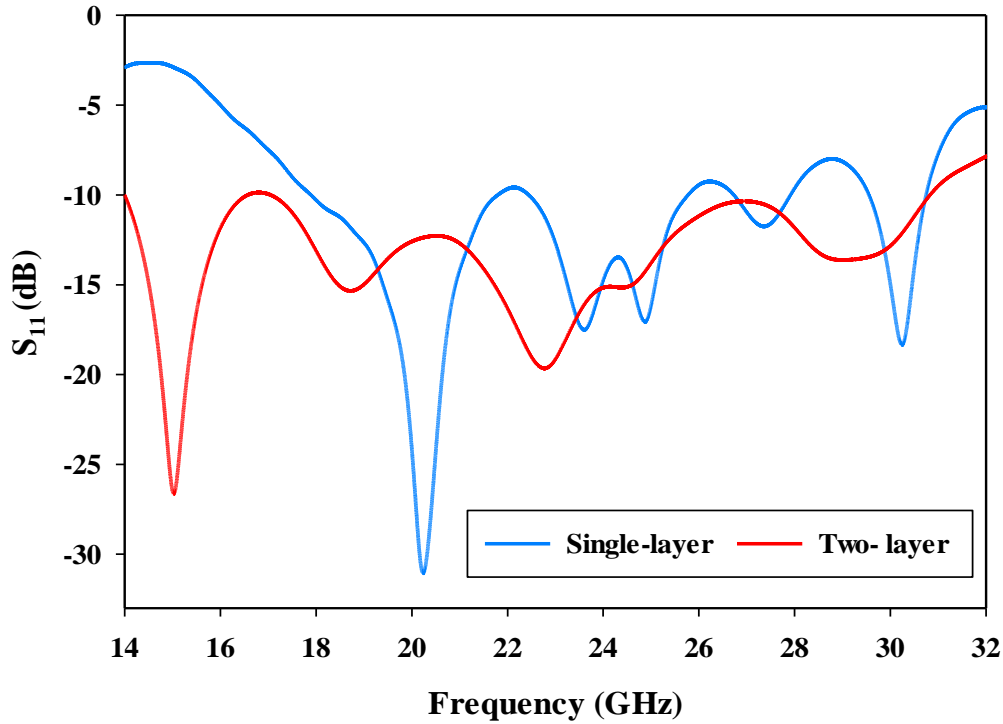


Figure 2-10 Reflection coefficient of a single and two-layer DRAs.

Increasing the dielectric constant has the effect of raising the radiation Q factor, consequently narrowing the antenna bandwidth [133]. Hence, by applying a coating of polyimide with a dielectric constant of 3.5, which is lower than the dielectric constant of the Dielectric Resonator Antenna (DRA), the overall dielectric constant decreases. This reduction in the Q factor results in an increased bandwidth for the antenna. Furthermore, the radiation quality factor can be used to express the antenna impedance bandwidth as follows [133, 134] :

$$BW = \frac{S - 1}{Q_{rad} \sqrt{S}} \quad (2.15)$$

In which S is the maximum desired VSWR value. Where, the radiation Q factor can be calculated as follows using the closed-form formula found in [135] for the stored energy and radiated power of rectangular Dielectric Resonator Antennas (DRAs):

$$Q_{rad} = 2\pi \frac{\text{Stored Energy}}{\text{Radiate Power}} \quad (2.16)$$

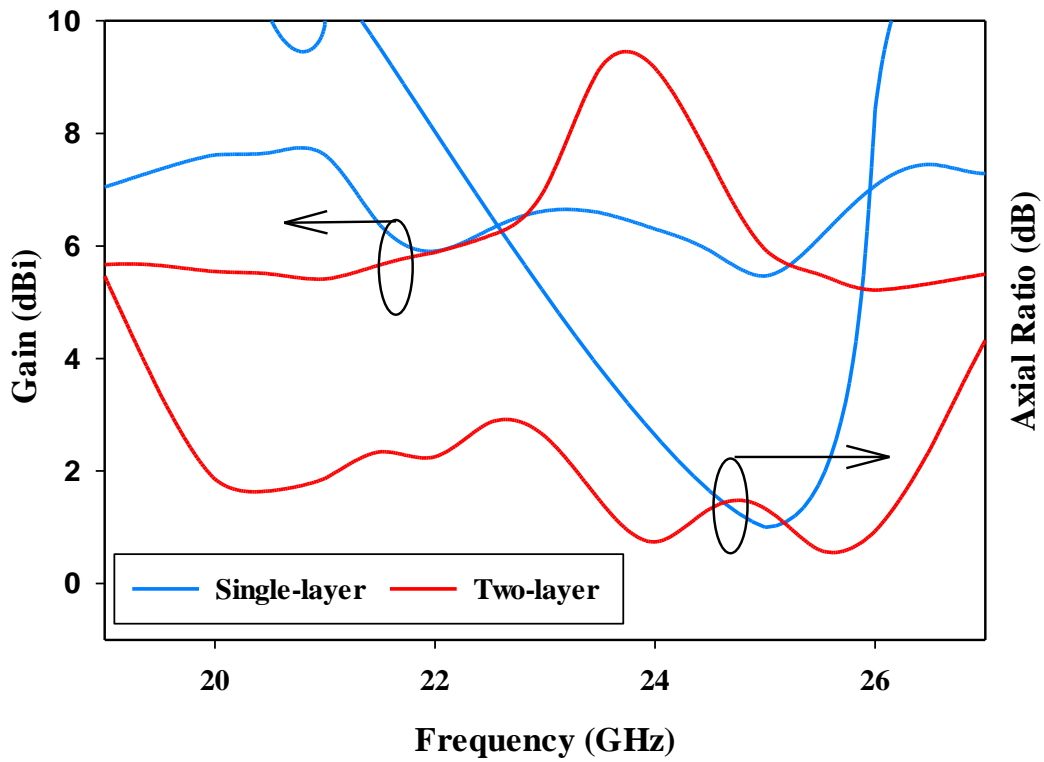


Figure 2-11 Gain and axial ratio of a single and two-layer DRAs

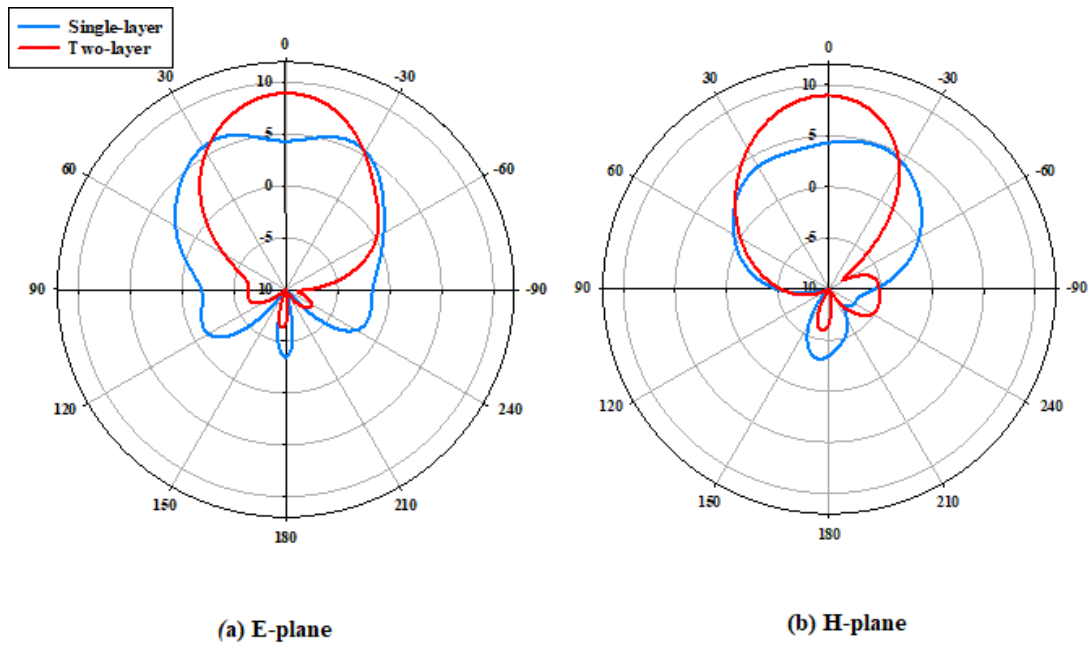


Figure 2-12 Radiation pattern of a single and two-layer DRAs

The broadside gain and axial ratio are illustrated in Figure 2-11, where it can be observed that after adding the coat the maximum gain was enhanced from 6 dBic to 9.16 dBic at 24GHz.

Similarly, the AR bandwidth was improved from ~ 4% to ~ 29% by adding the coat layer. Moreover, the coat serves an additional purpose of protecting the DRA from wet weather and other external factors. Additionally, the direction of the main lobe pattern has improved with the coat as shown in Figure 2-12.

Table 2-3 Human body parameters at 24GHz[136]

	Relative Permittivity	Density (kg/m³)	Conductivity [S/m]	Thickness [mm]
Skin	19	1109	22.8	1
Fat	6.51	911	4.42	2
Muscle	27.4	1090	29.4	10

In order to investigate the impact of the proximity of human body on the antenna's performance, the DRA was mounted on three-layers of human's tissue model. The utilized parameters to simulate the phantom are listed in Table 2-3 and the simulated tissue layers are illustrated in Figure 2-13, using a size of 100 mm × 45 mm × 13 mm³.

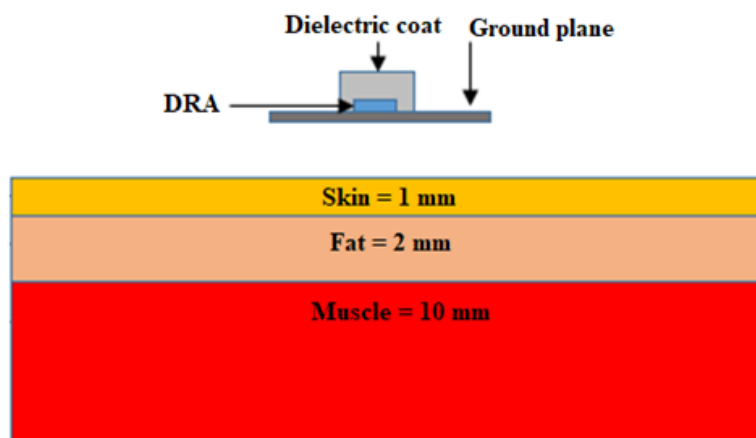


Figure 2-13 The proposed layered DRA above the body phantom

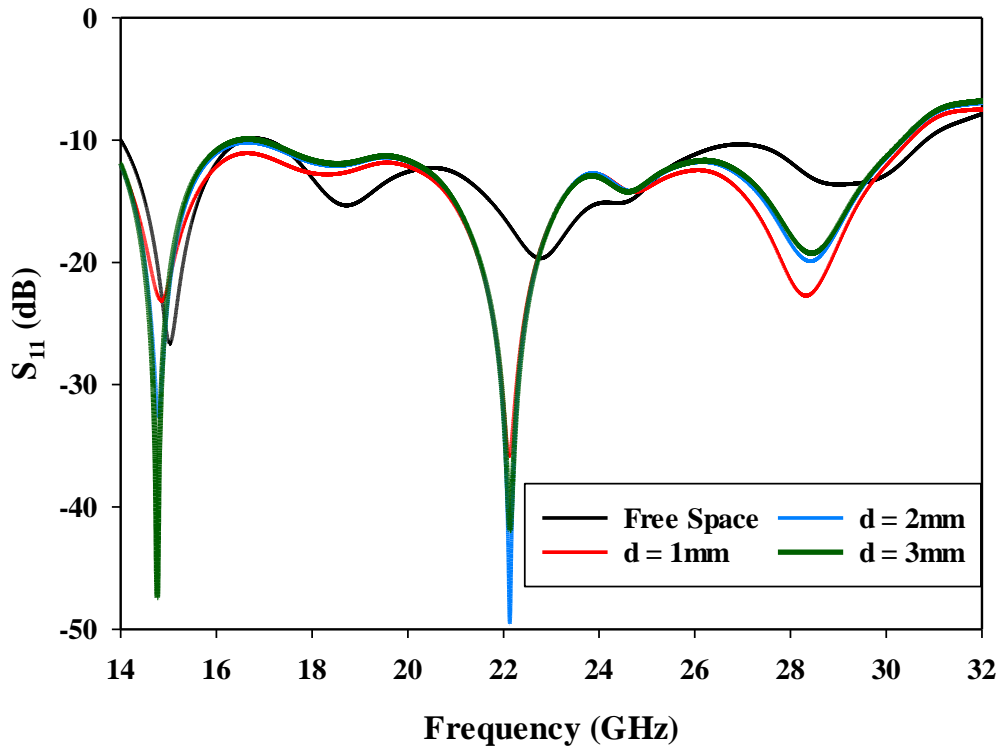


Figure 2-14 $|S_{11}|$ a layered DRA placed next to a phantom.

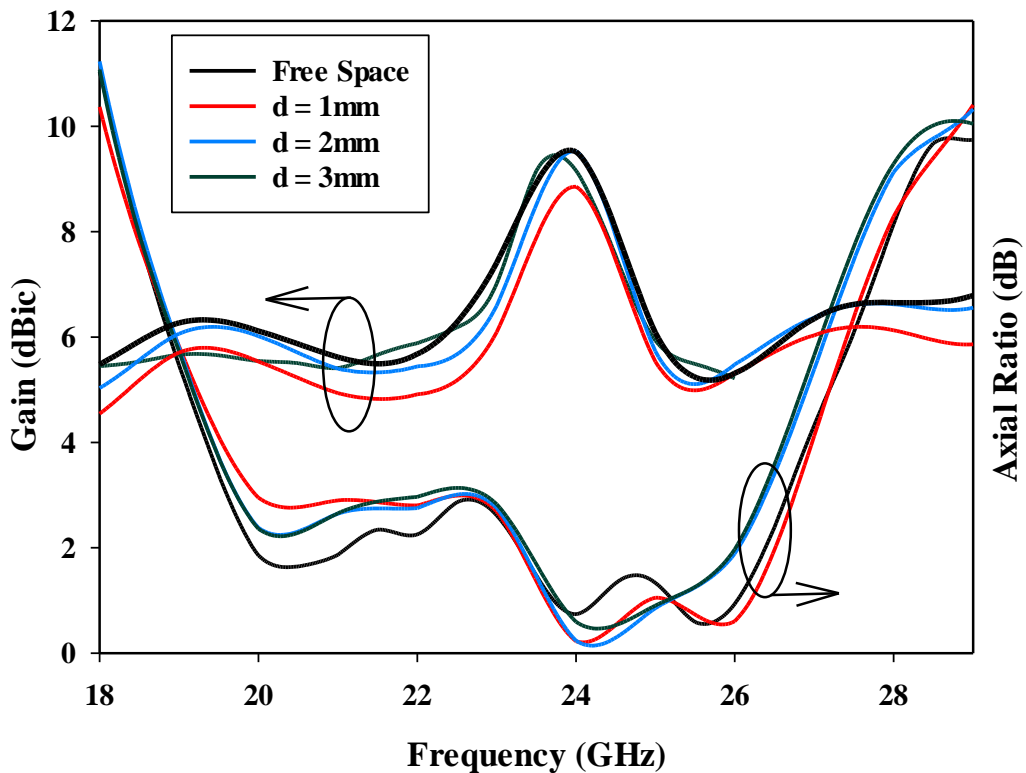


Figure 2-15 Gain and axial ratio of a two-layer DRA placed next to a body phantom.

Figure 2-14 illustrates the return losses when the antenna is placed next to the phantom at various distances of 1mm, 2mm and 3mm. From these results it can be noted that the achieved

impedance bandwidth is $\sim 75\%$ for all the considered distances, which is close to that of a DRA operating in free space. This demonstrates a marginal impact of the human tissue on the impedance bandwidth, which can be attributed to the presence of the ground plane between the antenna and the simulated tissue layers. The same impact was observed for the far field parameters as illustrated in Figure 2-15, where it can be noted that almost identical gain and AR bandwidth has been achieved for various separation distances between the antenna and human tissue.

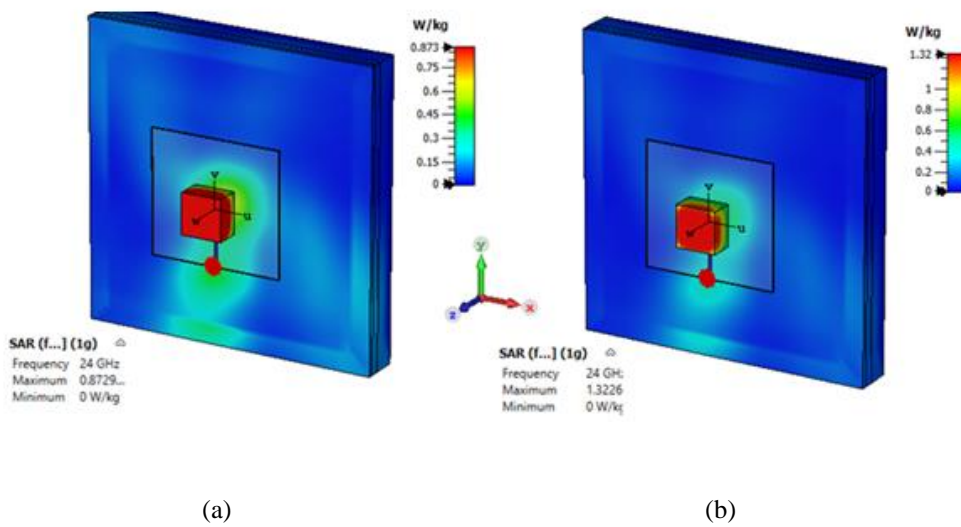


Figure 2-16 The SAR of the proposed DRA with various input power levels for a 1g tissue; (a) 15 dBm, (b) 18 dBm

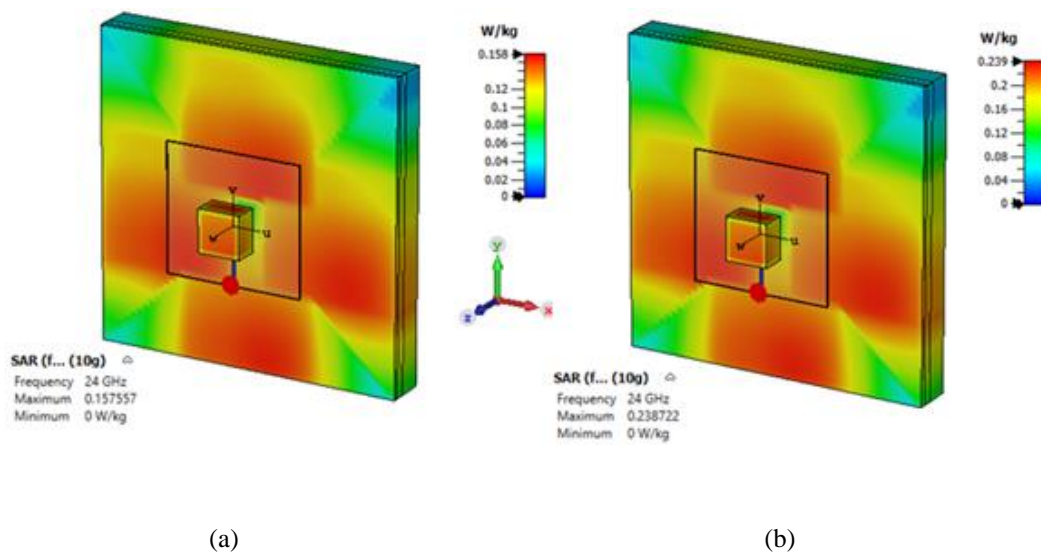


Figure 2-17 The SAR of the proposed DRA with various input power levels for a 10g tissue; (a) 15 dBm, (b) 18 dBm,

The results of the SAR simulations show that the suggested antenna's radiation satisfies the safety standards for 1 g and 10 g tissues, respectively, as shown in Figures 2-16 and 2-17.

2.4.1.2 The SAR as function of the ground plane size.

The investigation delved into assessing the correlation between SAR (Specific Absorption Rate) and ground plane size, exploring dimensions of 15 x 15mm, 25 x 27mm, and 40 x 40mm.

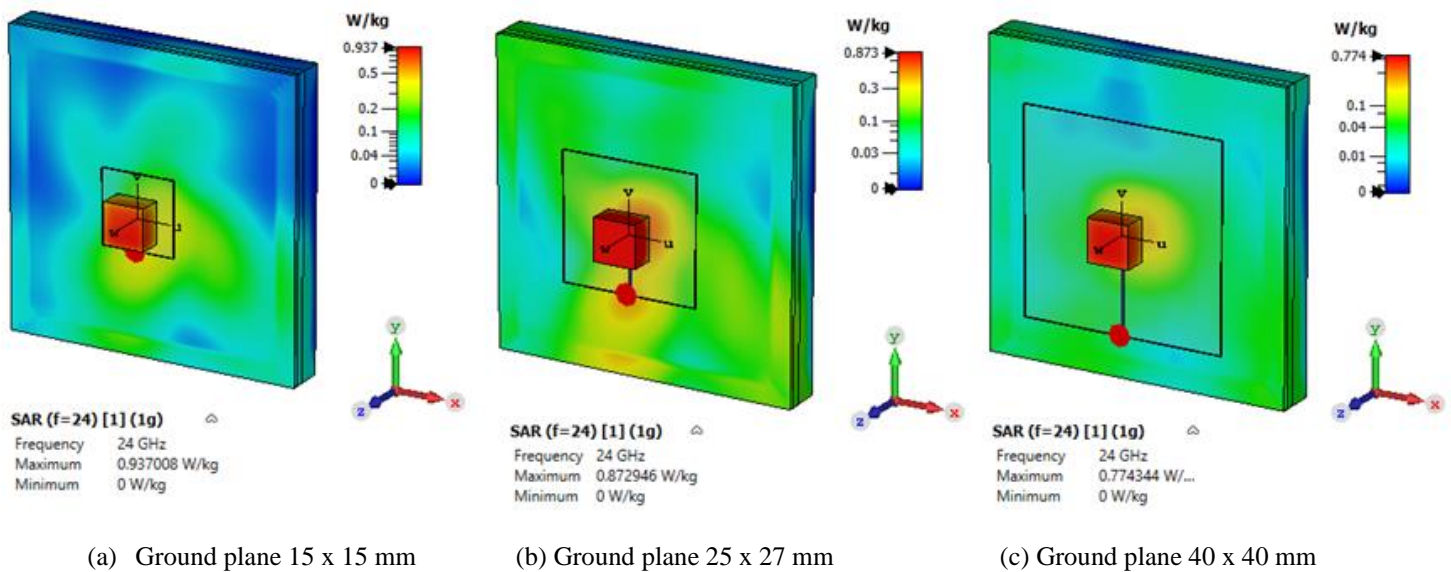


Figure 2-18 The relation of the SAR with the Ground plane size.

The results showcased a descending trend in SAR values with increasing ground plane size: SAR values were measured at 0.9 W/kg, 0.8 W/kg, and 0.7 W/kg for ground plane dimensions of 15 x 15mm, 25 x 27mm, and 40 x 40mm, respectively as shown in figure 2-18. This demonstrates a notable decrease in SAR with larger ground plane sizes, suggesting a potential strategy for mitigating SAR levels in such contexts.

Figure 2-19 presents the DRA prototype for which assembly was simplified by utilizing holder that includes a pocket in which the feed network was inserted. The DRA can then be placed in the precise position, with respect to the feeding slot, with the aid of an extremely thin adhesive copper tape, as shown in Figure 2-19d. Once the DRA is bonded to the feed network,

the holder can be pulled out leaving the prototype shown in Figure 2-19e, which can be measured without any alignment issues.

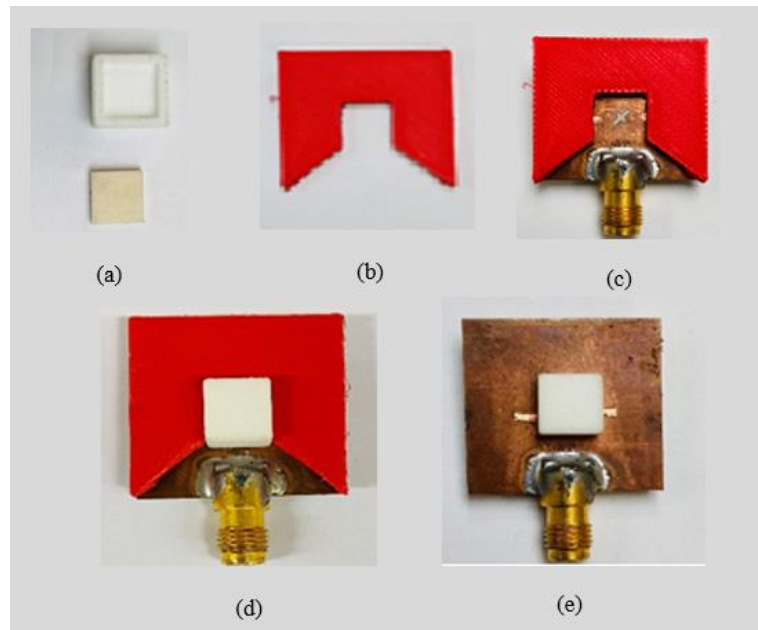


Figure 2-19 Prototype of the proposed antenna (a) RDRA with the dielectric coat, (b) Removable custom holder, (c) Feed network with two pieces of adhesive copper tape and the custom holder, (d) proposed antenna with the removable holder, (e) the proposed antenna

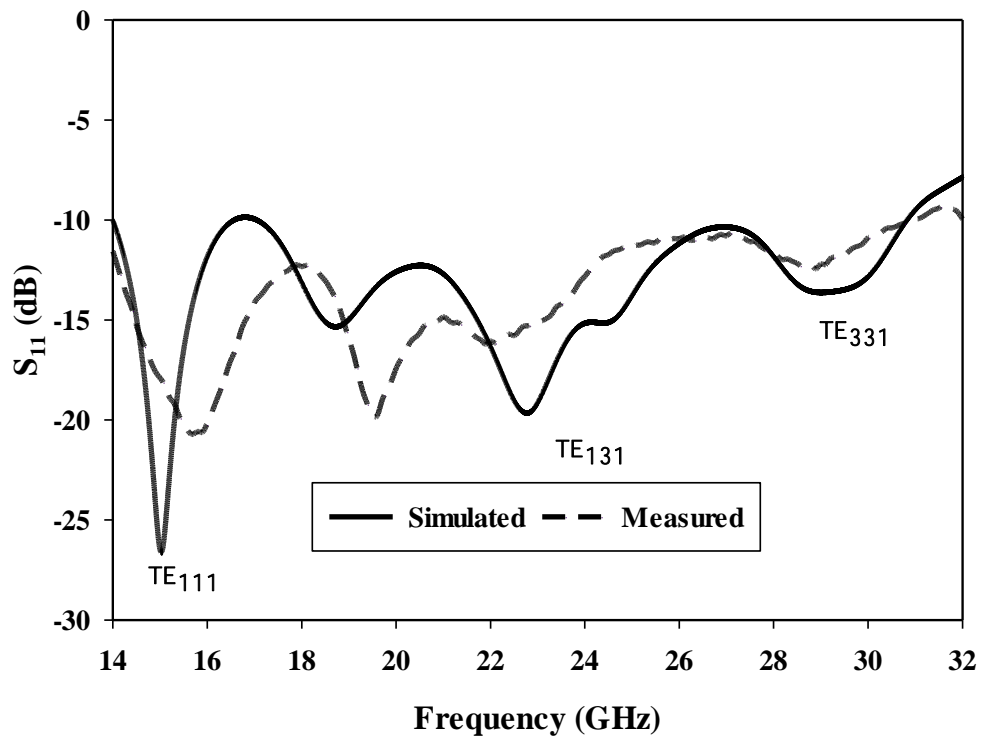


Figure 2-20 Measured and simulated $|S_{11}|$ of the layered DRA.

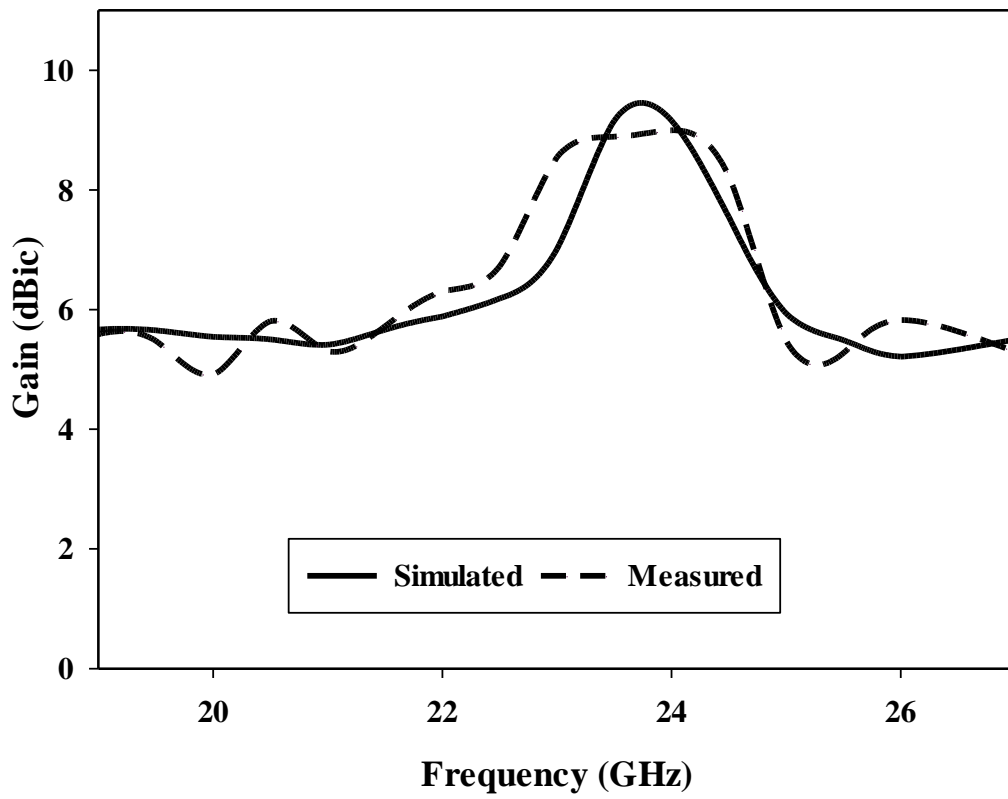


Figure 2-21 The measured gain of the layered DRA.

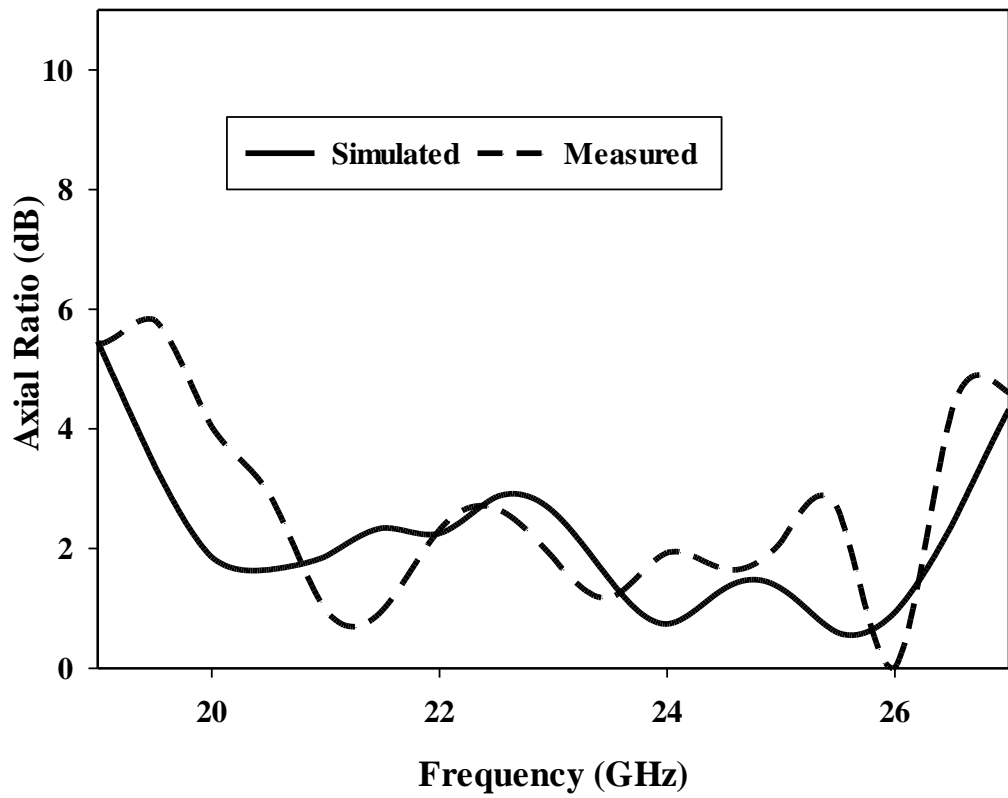


Figure 2-22 The measured axial ratio of the layered DRA

Figure 2-20 demonstrates good agreement between the simulated and measured reflection coefficient, where a bandwidth of 75% has been achieved in both cases. The close agreement between experimental and simulated data confirms the effectiveness of the used alignment procedure. Figures 2-21 presents the simulated and measured gain. From these results, it can be observed that the maximum gain was achieved at 24GHz, where the respective simulated and measured gains are 9.16dBic and 8.91dBic. The simulated and measured CP bandwidths are in reasonable agreement with each other as illustrated in Figure 2-22, where it can be noted that the experimental and simulated AR bandwidths are 26.2% and 29%, respectively. It can be noted that there is a slight drop in the measured CP bandwidth compared to the simulated counterpart and the measured gain has slightly fallen to 8.91dBic. These marginal discrepancies are expected due to the experimental and fabrication tolerances and other factors such as the SMA soldering and any uncertainty in the utilized dielectric permittivity.

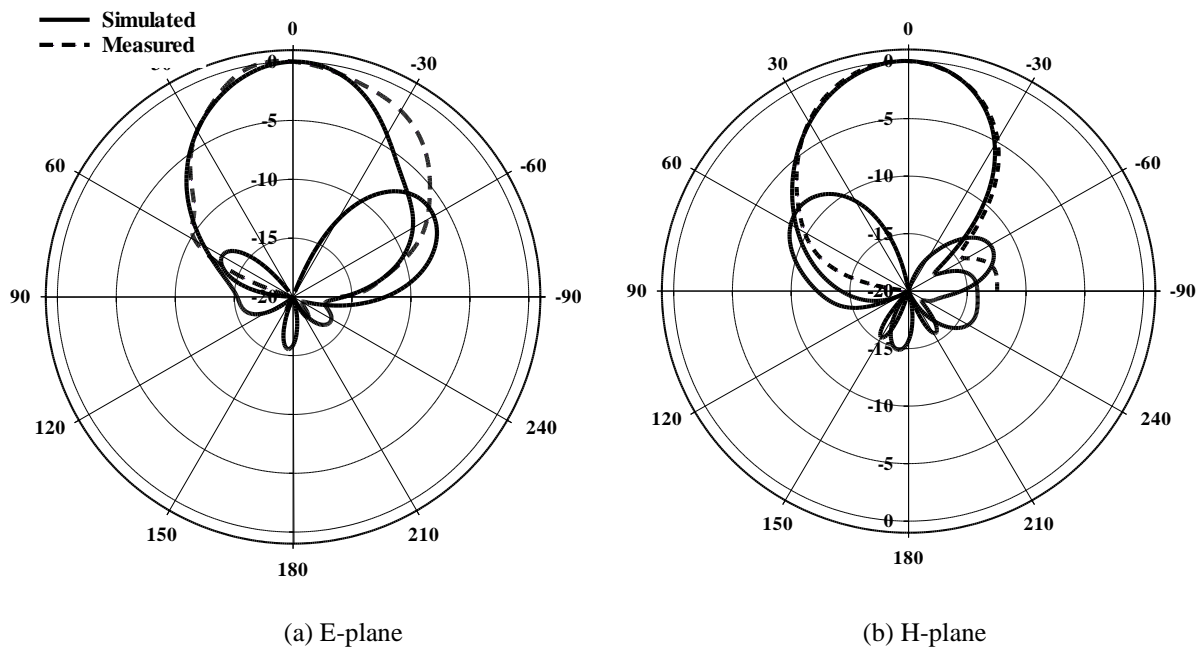


Figure 2-23 The measured far field patterns of the layered DRA at 24GHz.

The E-plane and H-plane radiation patterns were measured at 24GHz as illustrated in Figure 2-23, where it can be noted that close agreement is achieved between simulated and measured far field patterns. the DRA radiates a right-hand circular polarization (RHCP) wave

since E_R is greater than E_L . The magnetic field distribution inside the DRA is presented in Figure 2-24, where it can be noted that the TE_{111} , TE_{131} , and TE_{331} resonance modes were excited at 15 GHz, 24 GHz, and 29.5 GHz respectively.

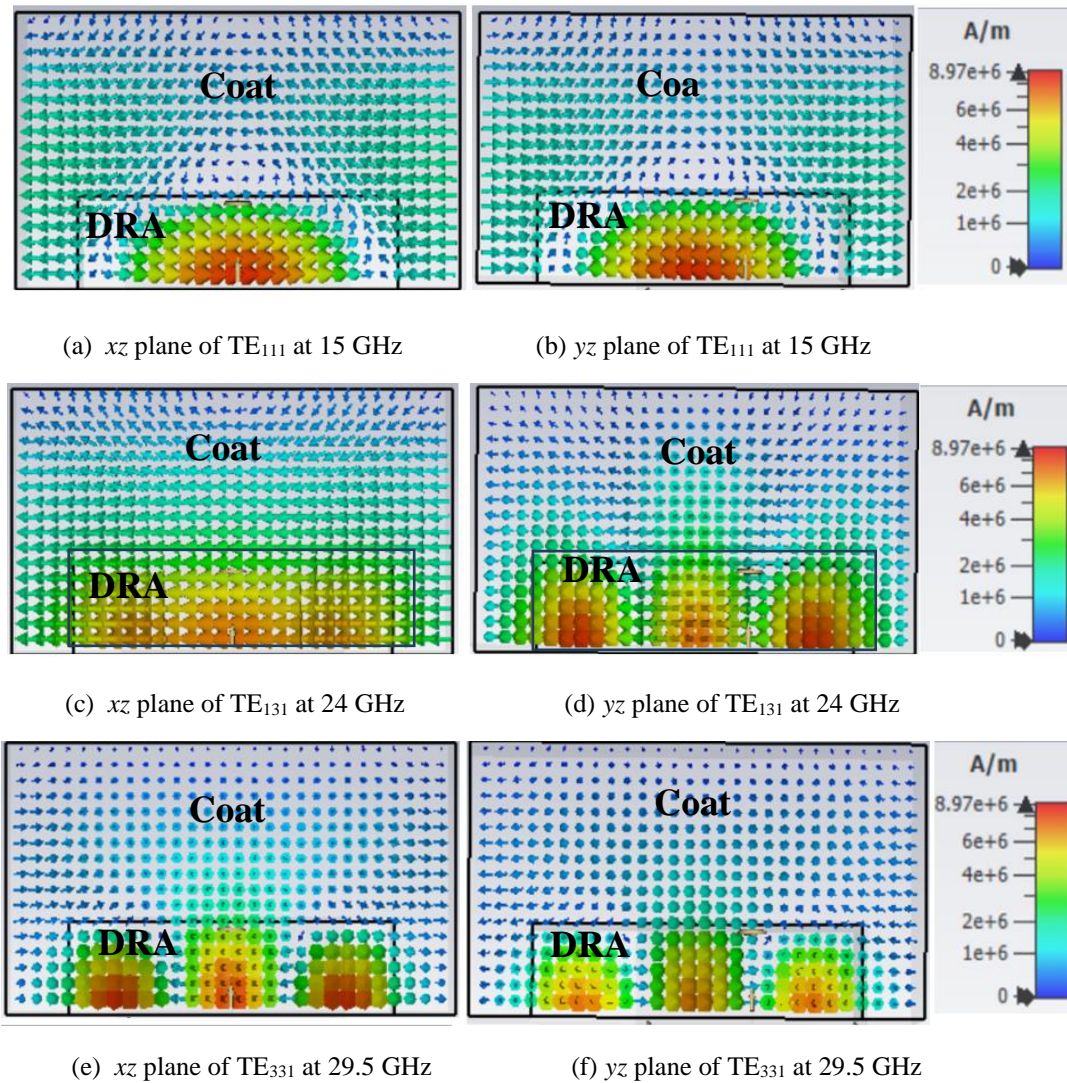


Figure 2-24 Magnetic field distribution inside the layered DRA.

Table 2-4 demonstrates that the proposed DRA offers one of the lowest profiles compared to reported designs, albeit with a considerably wideband operation in terms of impedance matching and axial ratio.

Table 2-4 Comparison of the layered-DRA performance against that of published counterparts

Ref	DRA configuration	DRA dimension (mm)	S ₁₁ BW (%)	Gain (dBic)	AR BW (%)
[71]	Rectangular	5.85 × 5.85 × 4.8	11.7	8.5	3.9
[137]	Modified rectangular	10.2 × 10.27 × 15	66.2	7.5	15
[68]	Rectangular	8 × 12 × 15	20.7	5	9.6
This work	Layered Rectangular	8 × 8 × 5	75	8.91	26.7

2.5 Dielectric Resonator Antenna with Grooved GP

In this DRA design, a grooved ground plane has been utilized to address the alignment issues. Additionally, the designed DRA has been investigated as a potential candidate for off-body communications at the desired frequency of 28GHz.

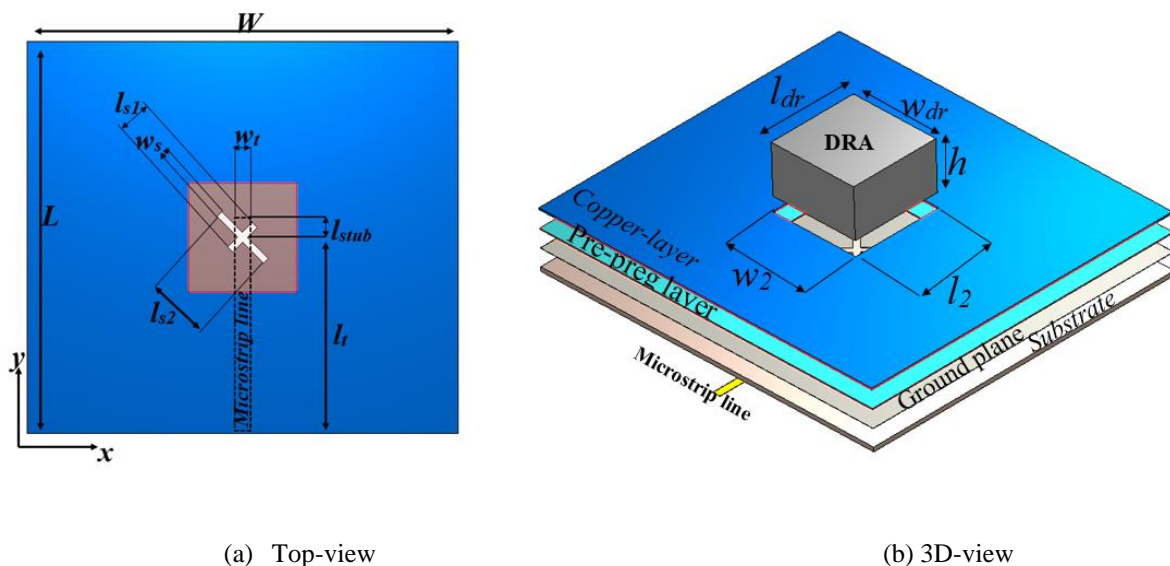


Figure 2-25 Geometry of the proposed DRA.

Figure 2-25 demonstrates the proposed antenna configuration. Once more, the DRA was simulated and fabricated using Alumina with a loss tangent of $\tan \delta < 0.0001$ and a dielectric

constant of $\epsilon_r = 9.9$. The DRA size was determined using the dielectric waveguide model (DWM) as $l_{dr} = w_{dr} = 5.2$ mm and $h = 2.9$ mm [138]. Furthermore, the Rogers substrate, Ro4350B, was used in the feed network, with a loss tangent of $\tan\delta=0.0027$ and a dielectric constant of 3.66. The substrate dimensions are $L = 19$ mm, $W = 21$ mm and $h_s = 0.254$ mm. A microstrip feedline was added at the lower side of the substrate, with a length of $l_t=10.5$ mm and a width $w_t = 0.45$ mm. The cross-slot arms have distinct lengths of $l_{s1} = 1.7$ mm and $l_{s2} = 3.2$ mm with identical widths of $w=0.35$ mm. Additionally, an optimum matching was accomplished by utilizing a microstrip stub with a length of $l_{stub} = 1$ mm. It should be mentioned that a rectangular DRA supports multiple TE_{mnp} resonance modes when placed above a metal ground plane. The modes' resonance frequencies can be determined using the DWM. It should be noted that the aforementioned DRA dimensions support the TE_{111} , TE_{113} and TE_{133} resonance modes at 25 GHz, 27 GHz and 30 GHz, respectively. The second ground plane has square cavity is bigger than the DRA by $50\mu\text{m}$, $l_2 = w_2 = 5.25$ mm. The modelled layers of the human body tissue are illustrated in Figure 2-26 using a size of $45 \times 45 \times 13$ mm³, where the thickness of the skin is 1mm, fat 2mm, and muscle 10mm, the utilized parameters to simulate the phantom are according to [136] at 28GHz.

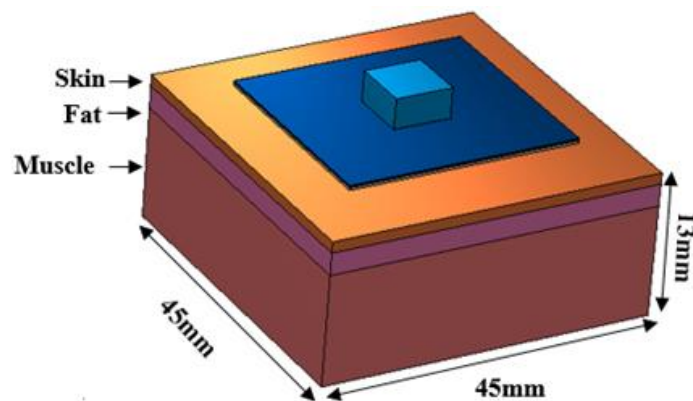


Figure 2-26 The proposed DRA above the body phantom.

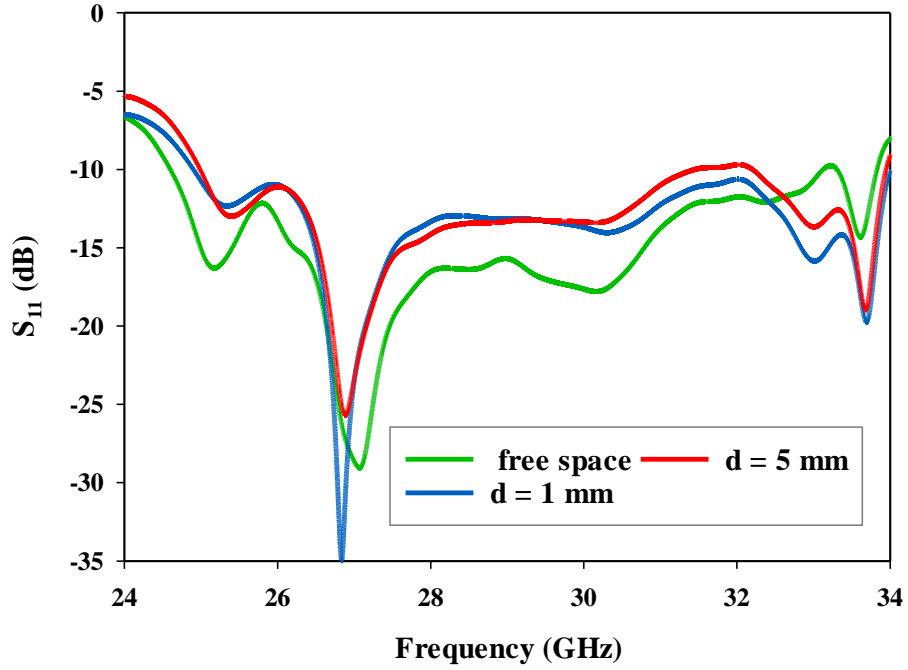


Figure 2-27 $|S_{11}|$ of CP DRA placed next to a phantom.

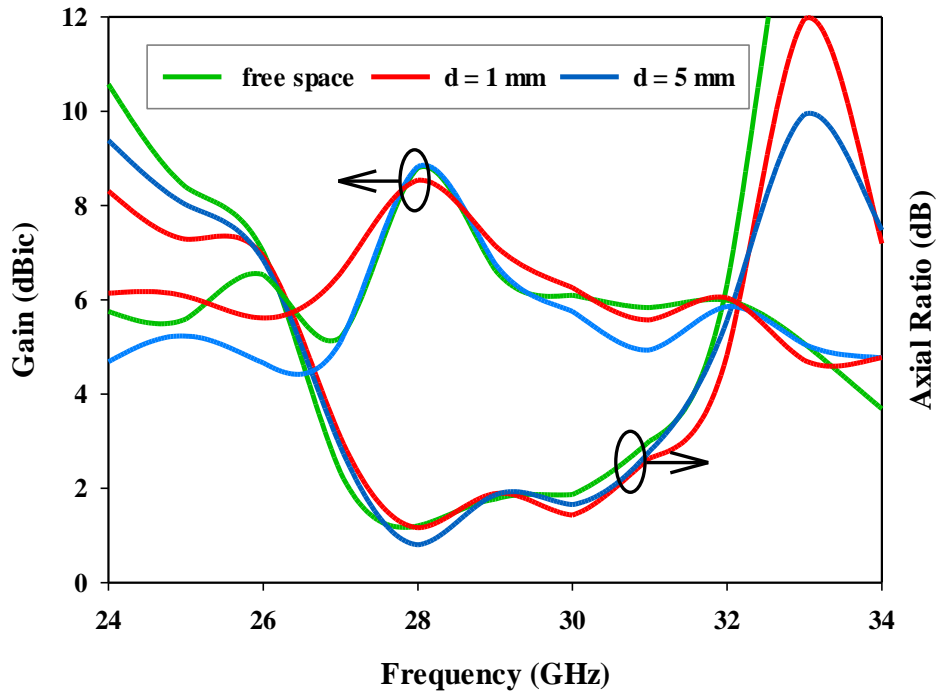


Figure 2-28 Gain and axial ratio of a CP DRA placed next to a body phantom.

Figure 2-27 illustrates the reflection coefficient when the proposed antenna is located above the tissue model at distances of 1mm and 5mm. In both cases the achieved impedance bandwidth is ~29%, which is close to that of free space. Once more, this demonstrates a marginal

impact of the human tissue on the DRA bandwidth, which can be explained as a result of the presence of a ground plane between the DRA and tissue that minimises the interaction between them. This has also been confirmed for the CP radiation, where it can be noted that the same AR bandwidth was achieved at various separation distances between the antenna and human tissue. The same is true for the gain as illustrated in Figure 2-28. The tested SAR of the proposed DRA has meet the requirement of both standers of 1.6 W/kg for (1) g of tissue and 2 W/kg for (10) g of tissue as illustrated in Figures 2-29 and 2-30.

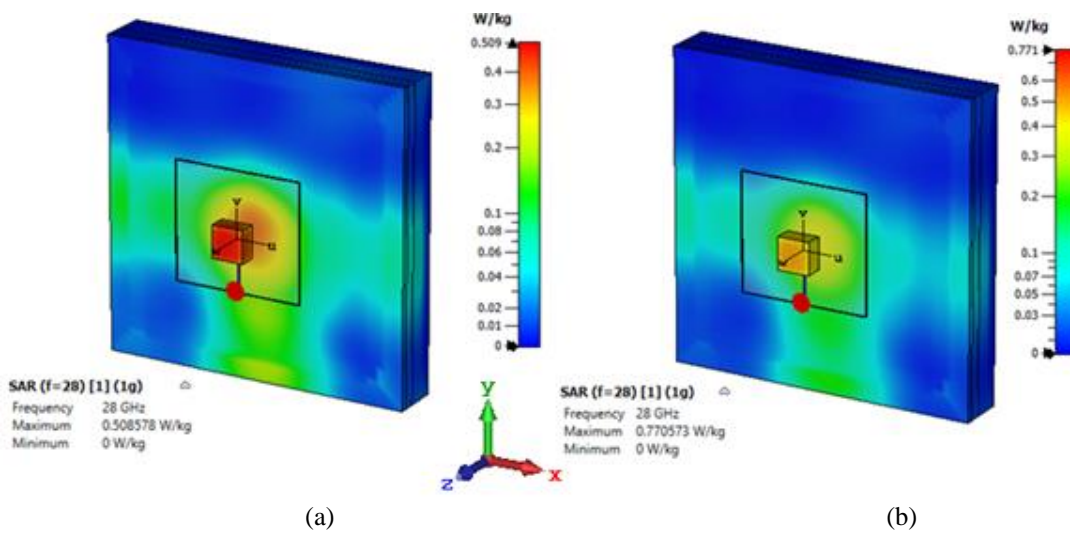


Figure 2-29 The SAR of the proposed DRA with various input power levels for a 1g tissue; (a) 15 dBm, (b) 18

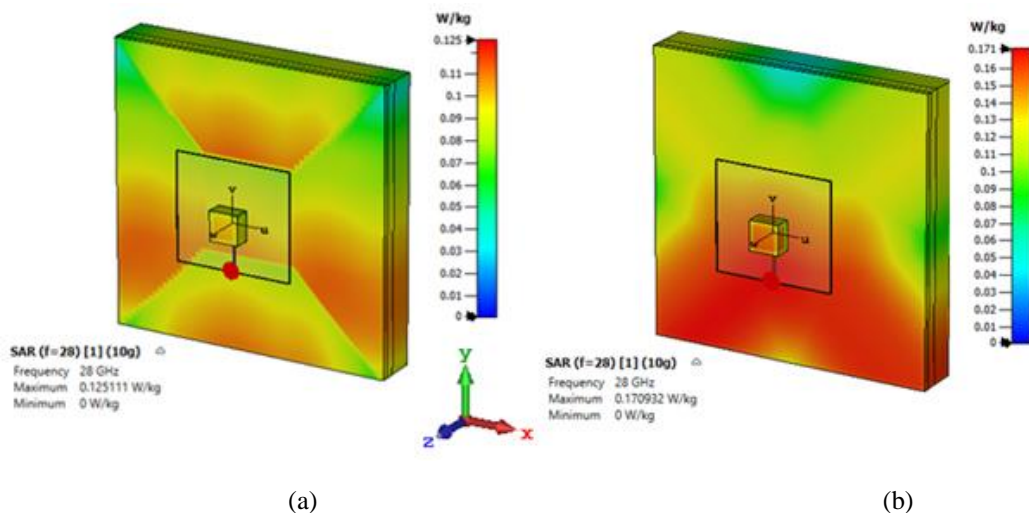


Figure 2-30 The SAR of the proposed DRA with various input power levels for a 10g tissue; (a) 15 dBm, (b) 18 dBm,

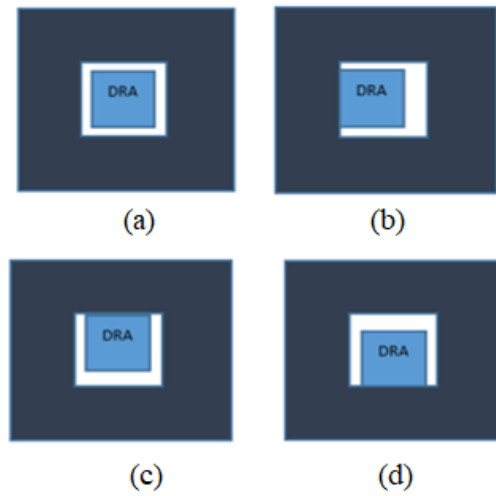


Figure 2-31 a) centered DRA, b) DRA shifted to the left by 25 μm . c) DRA shifted towards top by 25 μm , d) DRA shifted to the bottom by 25 μm .

Prior the fabrication, and to fix the alignment issue, a second ground plane with a hollow square cavity was utilized as illustrated in Figure 2-31, where it can be noted that the square cavity is bigger than the DRA by 25 μm along each side. This difference in size is needed to ensure that the DRA can be inserted easily in the created cavity. Hence more investigations were conducted in order to study the effects of any misalignment that can be caused if the DRA is shifted from the center as illustrated in Figures 2-31 b-e.

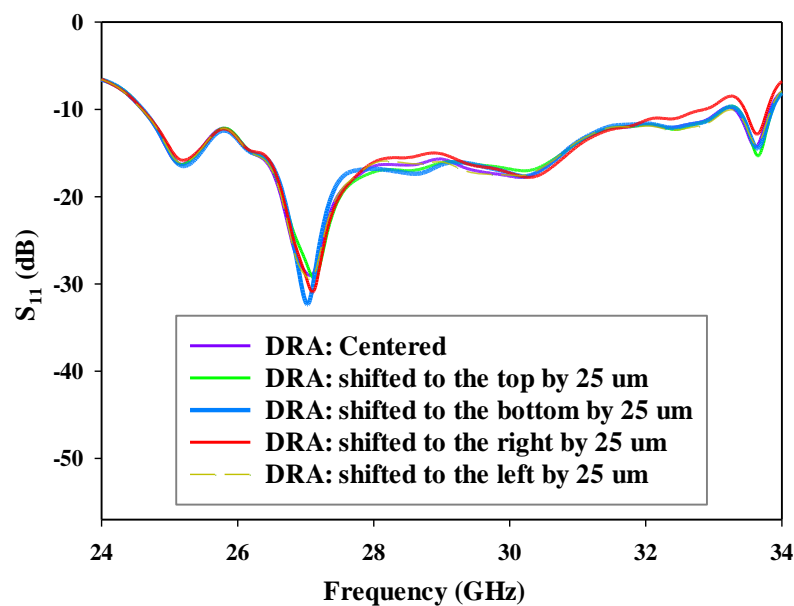


Figure 2-32 $|S_{11}|$ of DRA for various misaligned positions

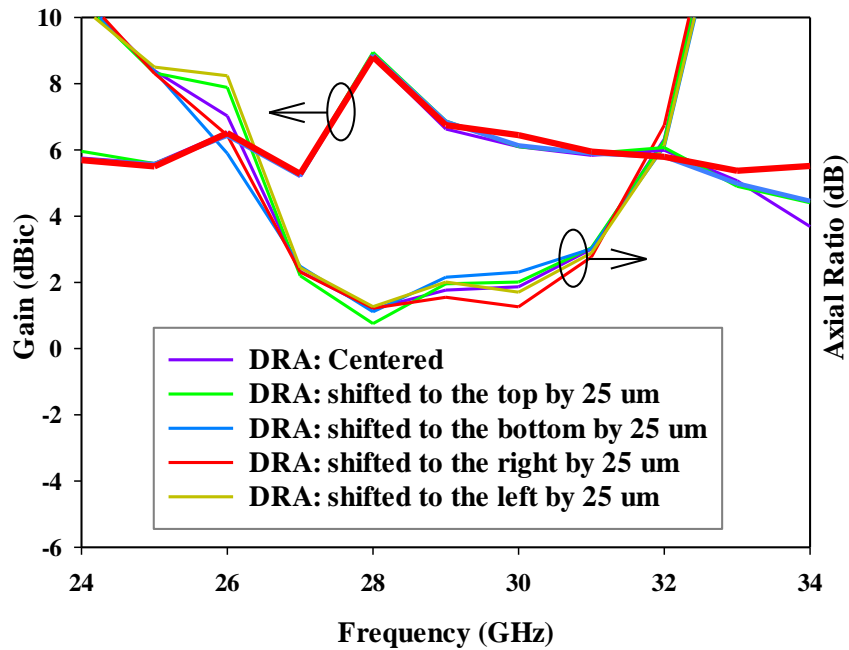


Figure 2-33 Gain and AR of DRA for various misaligned positions.

Figure 2-32 illustrates the simulated reflection coefficient when the DRA is precisely centered at the hollow cavity or shifted by 25 μm along either the x or y axes. However, from these results it can be noted that the archived impedance bandwidth of 29% was maintained in all scenarios with unnoticed variation. This has also been confirmed for the gain and axial ratio as illustrated in Figure 2-33, where the achieved gain of 8.7dBic at 28 GHz and CP bandwidth of 14% were maintained for the potential misaligned DRAs. The lower resonance mode of TE_{111} has been excited at 25 GHz together with two higher order modes of TE_{113} and TE_{133} at 27 and 30 GHz, respectively. The proposed ground plane groove was included in the simulations as illustrated in Figure 2-34. The thicknesses of the upper and lower ground planes were set to 0.1 and 0.018 mm, respectively. Additionally, the requisite DRA position was determined by etching a square hollow cavity in the top ground plane. The two ground planes were joined together by sandwiching a 63-micron-thick pre-preg layer in-between. Additionally, a similar square cavity slot was created in the pre-preg dielectric layer also so that the DRA can be placed directly above the cross-slot of the bottom ground plane.

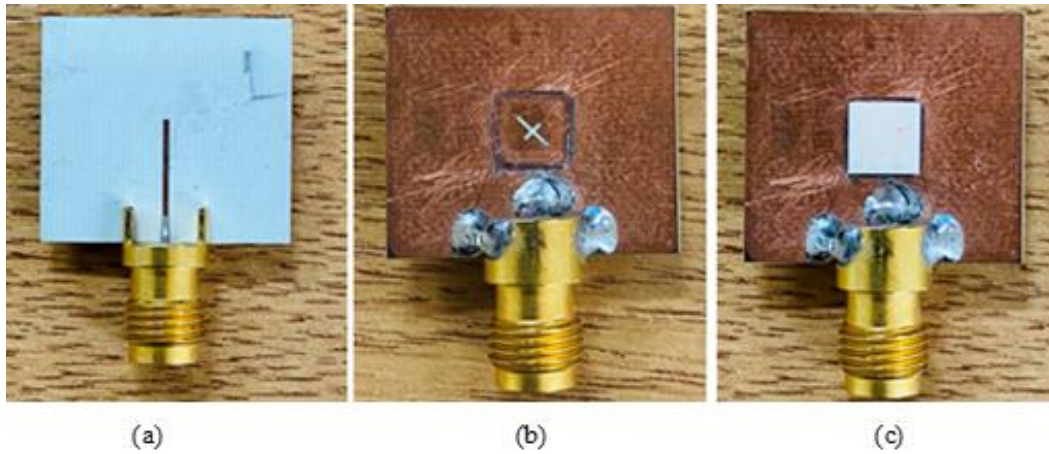


Figure 2-34 The prototyped DRA (a) back view (b) Top view of feed network with grooved ground plane (c) Assembled DRA.

The simulated and measured reflection coefficients are in close agreement as demonstrated in Figure 2-35, with impedance bandwidths of ~29% in both instances. The agreement between simulations and measurements demonstrates the effectiveness of the employed alignment technique.

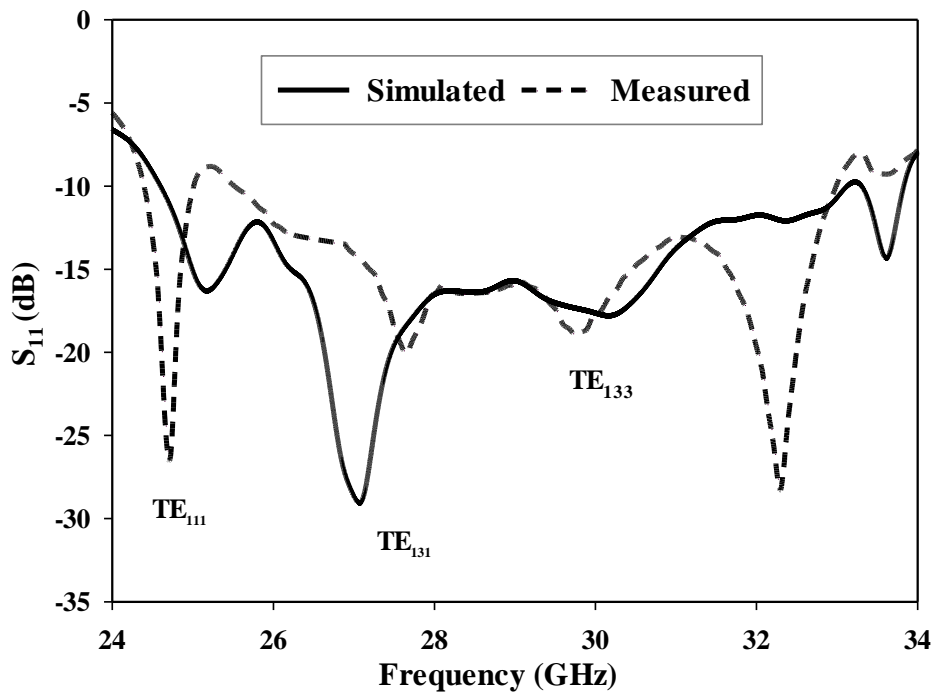


Figure 2-35 The measured and simulated $|S_{11}|$ of the CP DRA on a grooved ground plane.

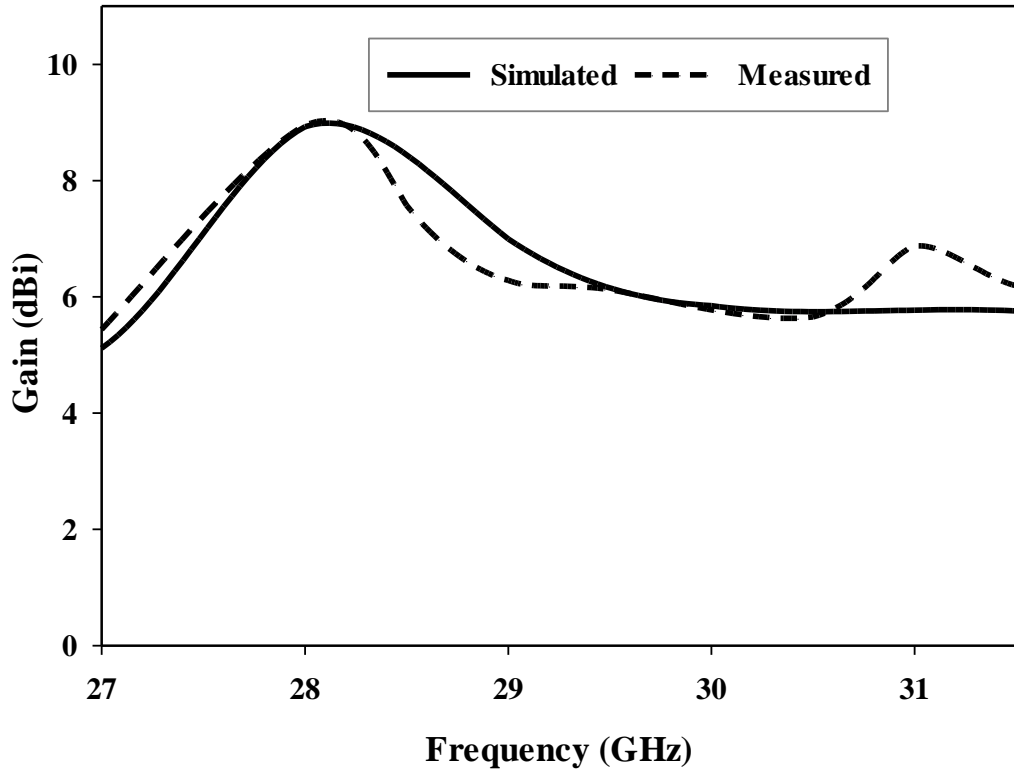


Figure 2-36 The measured gain of the CP DRA on a grooved ground plane.

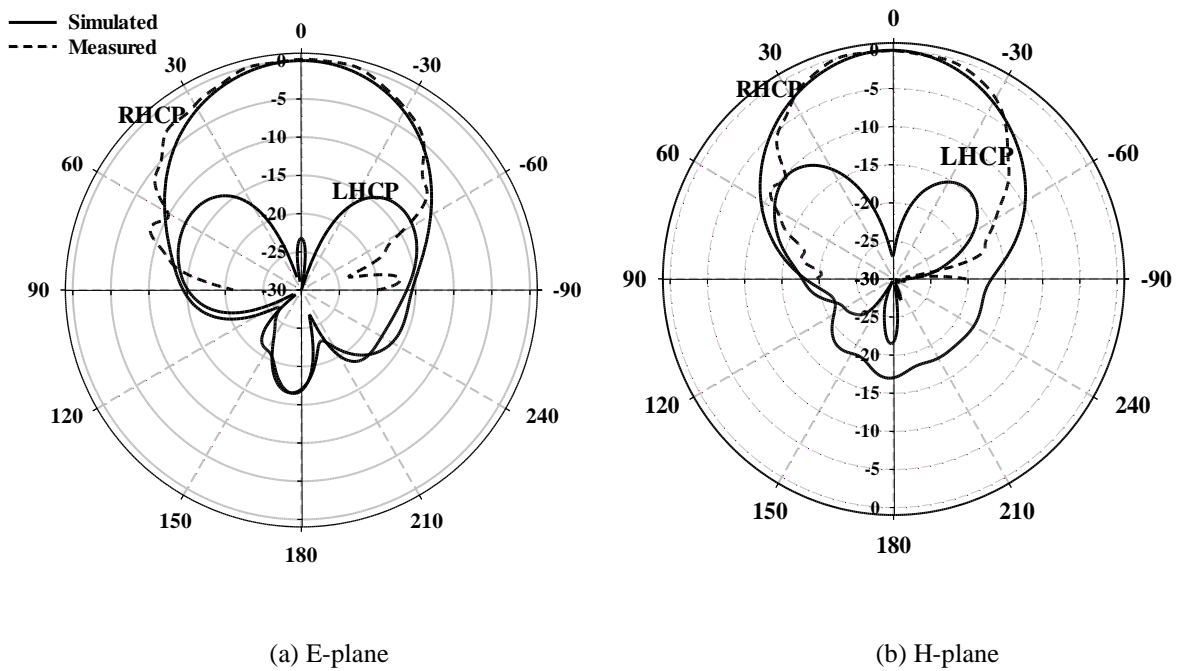


Figure 2-37 The simulated and measured Normalized radiation patterns at 28GHz for a CP DRA above a grooved ground plane.

Moreover, Figure 2.36 demonstrates a close agreement between the simulated and measured gains with a maximum simulated gain of 8.7 dBic at 28 GHz compared to a measured gain of 8.54 dBic. Figure 2-37 presents the simulated and measured E- and H-planes radiation patterns at 28 GHz with measured components that remain almost as in the simulation. The antenna radiates a RHCP wave.

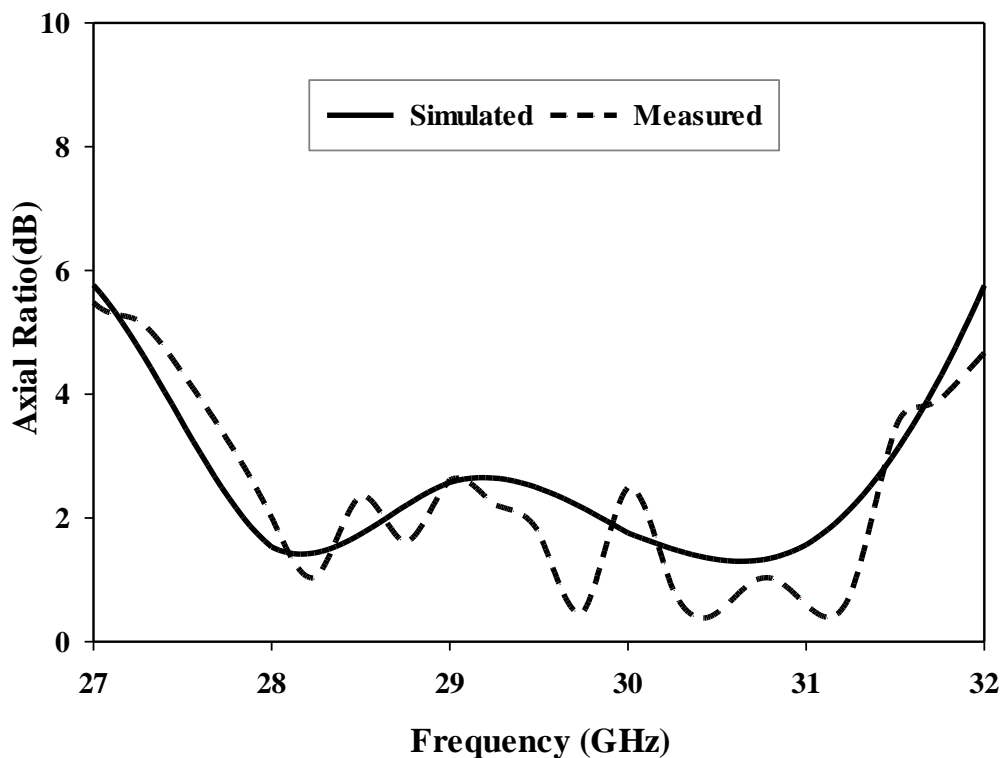


Figure 2-38 The measured axial ratio of the CP DRA on a grooved ground plane.

The measured and simulated CP Bandwidths accord with one another reasonably well, as illustrated in Figure 2-38, where it can be noted that the simulated and measured AR bandwidths are 14% and ~13.5%, respectively. From Table 2-5 it can be observed that, compared to the relevant literature, the proposed DRA offers the lowest profile together with improved radiation parameters. However, compared with the previous section, it will note that this design produces

the lowest profile and almost the same gain, nevertheless, the layered DRA offers wider bandwidth with the conjunction of AR, that due to the use of the dielectric coat [74].

Table 2-5 Comparison of the performance of a DRA on a grooved ground plane with published counterparts

Ref	DRA configuration	DRA dimension (mm)	S ₁₁ BW (%)	Gain (dBic)	AR BW (%)
This work	Rectangular	5.2 × 5.2 × 2.9	29	8.7	13.5
Pervious section	Layered Rectangular	8 × 8 × 5	75	8.91	26.7
[68]	Rectangular	8 × 12 × 15	20.7	5	9.6
[71]	Rectangular	5.85 × 5.85 × 4.8	11.7	8.5	3.9

2.6 A Wristwatch Dielectric Resonator Antenna

Another DRA configuration that is suitable for off-body communications is demonstrated in Figure 2-39 (a) with the top view of the configuration illustrated in Figure 2-39 (b). Once more, in order to achieve a CP radiation, the DRA was excited using a cross slot. The matching bandwidth was enhanced by utilizing a stub at the end of the 50Ω microstrip line that has respective width and length of $w_t = 0.4$ mm and $l_t = 10$ mm. The cross-slot width and lengths are $w_s = 0.43$ mm, $l_{s1} = 4$ mm and $l_{s2} = 2$ mm.

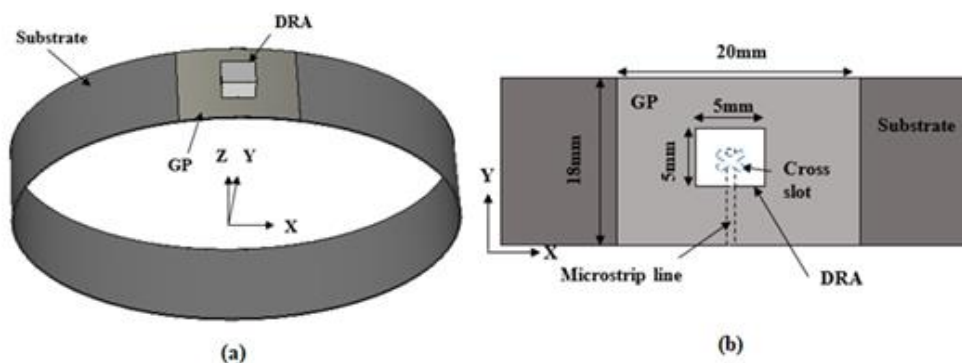


Figure 2-39 The proposed wristwatch DRA a) Oblique view b) Top view.

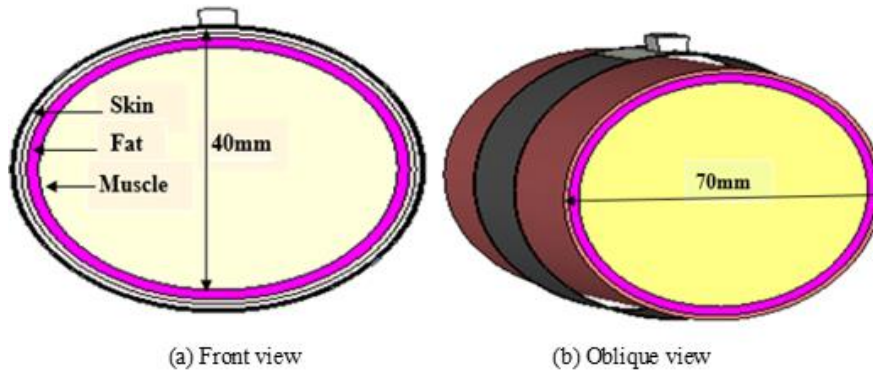


Figure 2-40 The wristwatch DRA on the equivalent wrist.

A curved DRA and substrate, with respective dielectric constants of $\epsilon_r = 9.9$ and $\epsilon_s = 3.5$ were utilized. The DRA size was chosen as $5 \times 5 \times 2.9$ mm with an 18×20 mm² conformal ground plane. The radii of the elliptical substrate are 20 mm and 35 mm with a thickness of 0.3 mm as shown in Figure 2-40. In order to study the human body's impact on the antenna performance, the ground plane width has been varied from 20-50 mm, in 10 mm steps. This was implemented in free space and on-wrist. Figure 2-41 illustrates the return losses of the wristwatch DRA for various sizes. It can be observed that -10 dB S_{11} bandwidth of $\sim 27\%$ was achieved for all ground plane sizes.

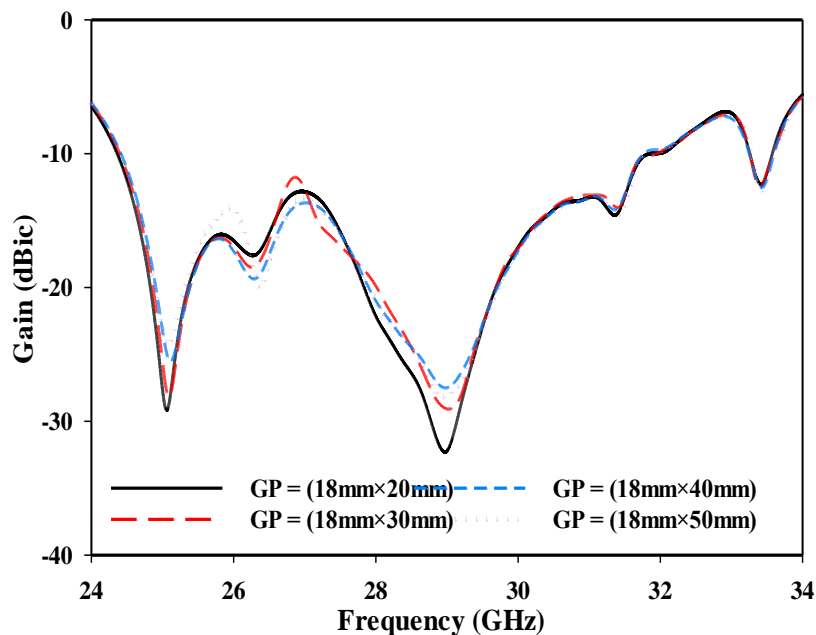


Figure 2-41 $|S_{11}|$ of a wristwatch DRA in free space with different ground plane sizes

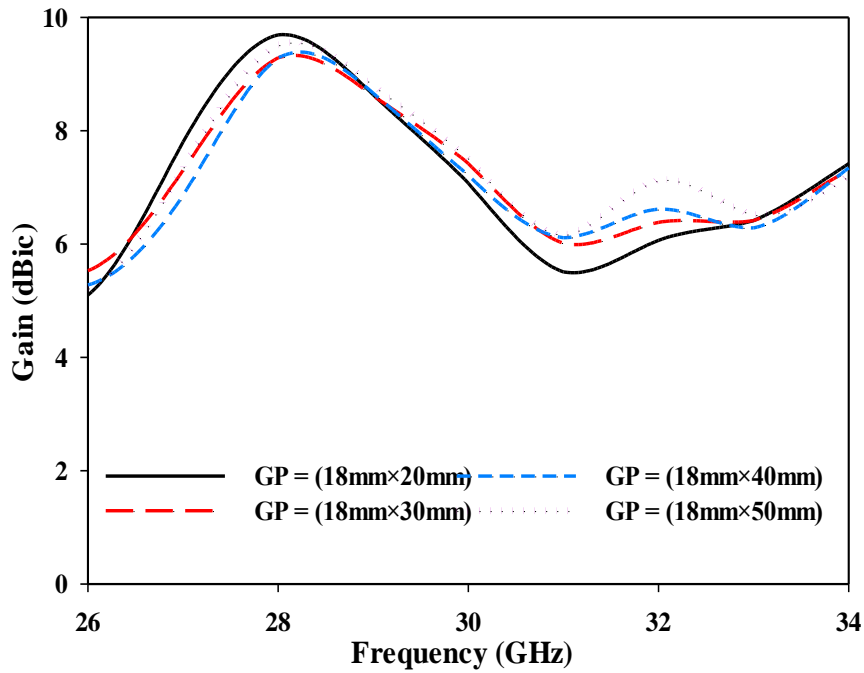


Figure 2-42 Gain of a wristwatch DRA in free space using different ground plane size

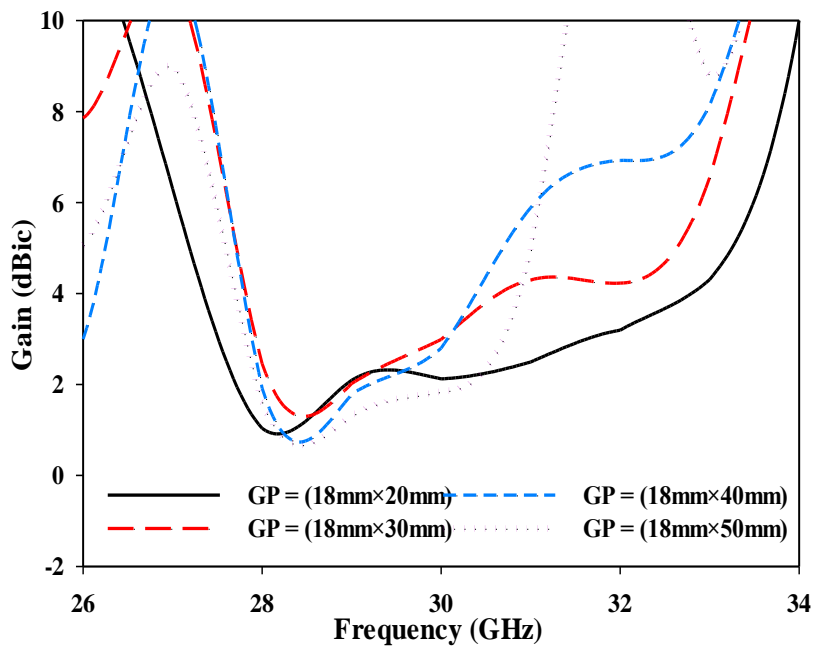


Figure 2-43 Axial Ratio of wristwatch DRA in free space with different ground plane sizes.

Figure 2-42 demonstrates a gain of more than 9 dBic in all scenarios. Moreover, Figure 2-43 presents the AR, where it can be noted that an AR bandwidth of ~14.7% was achieved using a ground plane size of 18 mm × 20 mm. The polar view of the far-field patterns is

illustrated in Figure 2-44, where it can be noted that the DRA radiates a RHCP wave since the E_R component is greater than the E_L counterpart by $\sim 20\text{dB}$. Additionally, the antenna offers a broadside radiation, which is suitable for off-body communication.

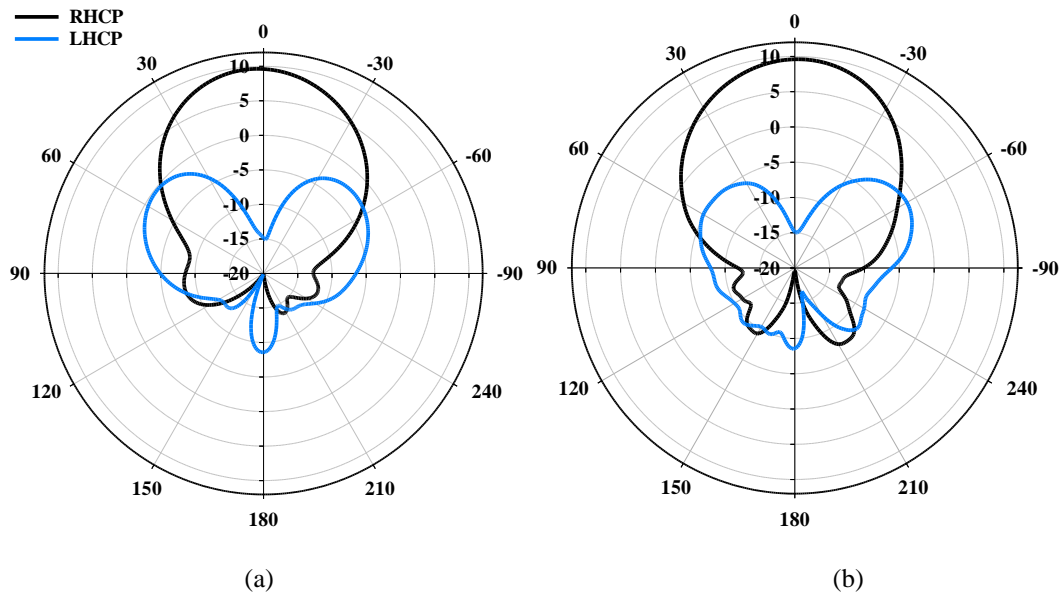


Figure 2-44 Far field pattern of wristwatch DRA in free space at 28GHz; a) E- plane and b) H- plane.

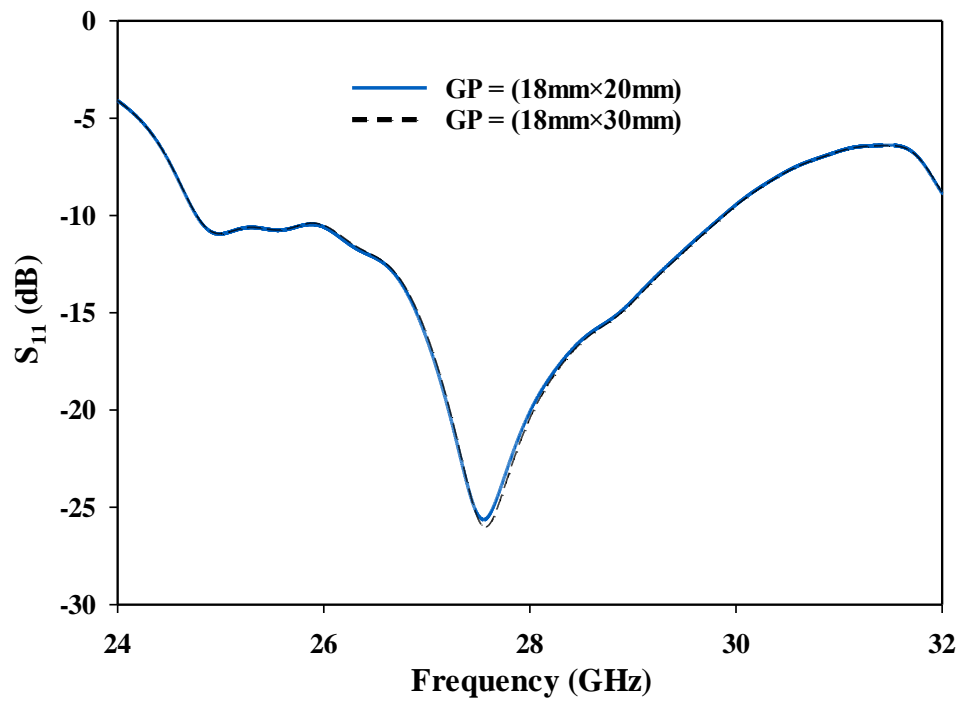


Figure 2-45 $|S_{11}|$ of DRA on-wrist with different ground plane sizes

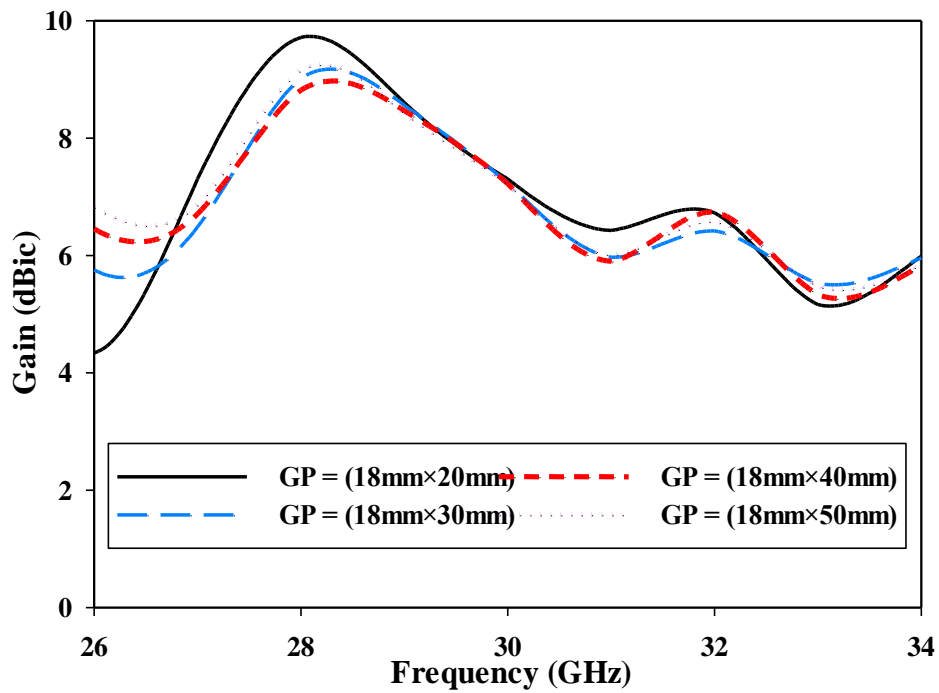


Figure 2-46 Gain of on-wrist DRA with different ground plane sizes.

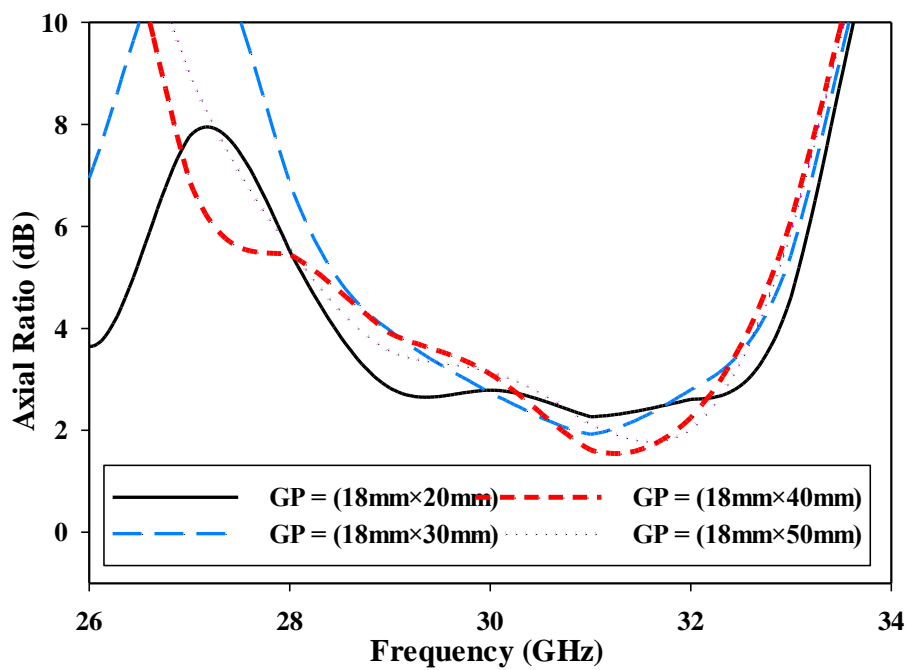


Figure 2-47 Axial ratio of on-wrist DRA with different ground plane sizes.

A three-layer elliptical cylinder was considered to model the wrist with the layers correspond to skin, fat and muscle Figure 2-40. The dielectric characteristics of the body

parameters at 28 GHz have been used according to those [136]. For the case of a DRA placed on the wrist, an impedance bandwidth of ~19% was achieved without any impact by the ground plane size as illustrated in Figure 2-45. The attained free space gains of over 9 dBic was sustained even in the presence of the wrist, as illustrated in Figure 2-46. Furthermore, Figure 2-47 depicts an axial ratio (AR) bandwidth of approximately 10.7% across the frequency span of 28.9-32.2 GHz, achieved with minimal deviations in relation to ground plane sizes. The inclusion of the wrist reduces the AR bandwidth, in contrast to earlier designs where the ground plane aimed to maintain consistent performance in free space and on the wrist. However, this approach doesn't apply in this case due to incomplete substrate coverage by the ground plane, as well as the curved ground plane and DRA. It should be noted that the proposed DRA offers the lowest profile compared to the reported on-wrists DRA designs reported in the literature as shown in the compared table 2-6, with a considerably wideband operation and a high gain. Figure 2-48 presents the E_R and the E_L components that remain almost as in free space where RHCP wave is radiated.

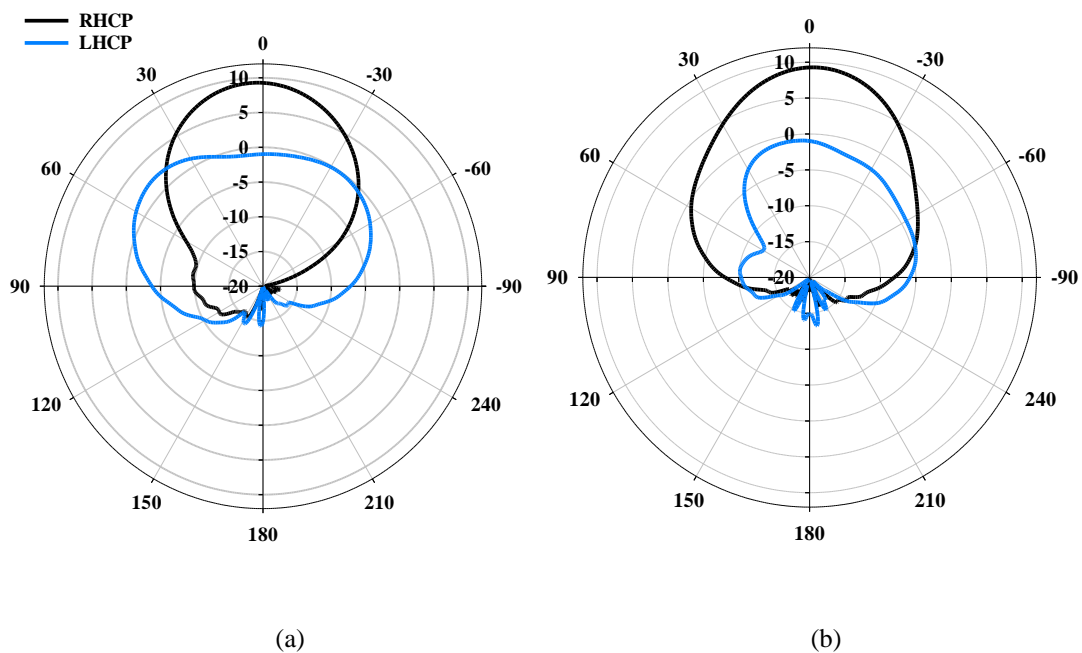


Figure 2-48 Far field pattern of the on-wrist DRA at 28GHz; a) E- plane and b) H- plane.

Table 2-6 Comparison of the performance of the wristwatch DRA against published counterparts

Ref	DRA size (mm)	ϵ_r	S_{11} BW (%)	Gain (dBi)	AR BW (%)
[78]	22 x 10 x 4	9.8	18.4	5	LP
[79]	55 x 27 x 10	12.3	19	5.15	LP
[139]	22 x 10 x 4	9.8	15.3	5.21	LP
This work	5 x 5 x 2.9	9.9	19	9.42	10.6

2.7 Conclusion

This Chapter proposed three low-profile configurations of mmWave DRAs for off-body communications, with close agreement between the measured and simulated results. The antennas exhibited impressive performance in terms of impedance bandwidth, axial ratio bandwidth, and maximum gain. The first DRA design achieved a 75% impedance bandwidth, 26.7% axial ratio bandwidth, and a maximum gain of approximately 8.9 dBic at 24 GHz. By incorporating an additional dielectric layer and a waterproof outer layer, the antenna's performance and robustness were improved. In the second design, an impedance bandwidth of 29% and an axial ratio bandwidth of 13.5% were achieved, with a maximum gain of 8.7 dBic at 28 GHz. The use of a second ground plane with a hollow square cavity provided a simple solution for DRA-feed misalignment. The third design presents a conformal wristwatch DRA that demonstrated an impedance bandwidth of approximately 27% in the frequency range of 24.4-31.8 GHz, with an axial ratio of around 14% and a gain of approximately 9.42 dBic in free space. The presence of the arm slightly reduced the impedance and axial ratio bandwidths to 19% and 10.6%, respectively. The circular polarization feature of this wearable device allows for flexible antenna alignment. The impact of the ground plane size on antenna performance was also carefully considered.

Overall, these DRA designs offer low-profile solutions with impressive radiation characteristics and circular polarization, which make them well-suited for wearable mmWave DRA. However, the maximum gain is only achieved at a specific frequency. To overcome this limitation, a DRA array will be considered in the next chapter. This array aims to achieve a stable high gain across most of both the impedance and axial ratio bandwidths.

Chapter 3

A Circularly Polarized mmWave Dielectric-Resonator-Antenna Array for Off-Body Communications

3.1 Introduction

Array antennas are used in wireless communication systems to enhance the gain in a particular direction. Phased array antennas, for example, can steer the beam electronically by adjusting the phase of the signals at each element, allowing for directional communication and interference rejection [140-142]. Moreover, the use of antenna arrays can also be achieved by implementing of beamforming techniques, which can further enhance the gain of the antenna system [143]. Therefore, array antennas offer significant advantages in terms of gain compared to a single- antenna element. By combining the outputs of multiple antenna elements, array antennas can achieve higher gain and improved radiation characteristics. This makes arrays well-suited for applications that require long-range communications or coverage over a wide area.

In this Chapter, a rectangular DRA element was used to design a 2×2 elements array. The design of the array involves careful consideration of the spacing between the DRA elements, as well as the feeding network that connects the individual elements to the source. The spacing between the elements affects the overall radiation pattern and beam width of the array. The feeding network ensures proper excitation of each element and enables control over the radiation properties of the array. Moreover, in order to overcome the misalignment issues, an automated process was followed to precisely outline the DRA positions on the utilized ground plane.

3.2 Design Methodology.

A single DRA element was developed first to operate at 28 GHz. The parameters of the proposed DRA array were set based on mmWave off-body communication requirements, such as low-profile, wideband, and high gain. The proposed antenna was simulated in free-space as well as on top of a three-layer model of a human tissue to investigate the effects of the human body on performance.

3.3 A Single DRA Element.

Figure 3-1 illustrates the antenna configuration, with respective dielectric constants and loss tangents of $\epsilon_r = 9.9$, $\tan\delta < 0.0001$ and $\epsilon_s = 3.66$, $\tan\delta < 0.0027$ for the DRA and substrate. The DRA dimensions were determined using the dielectric waveguide model (DWM), as well as CST Eigenmode solver for calculating the resonance frequencies of the TE_{mnp} resonance modes [138].

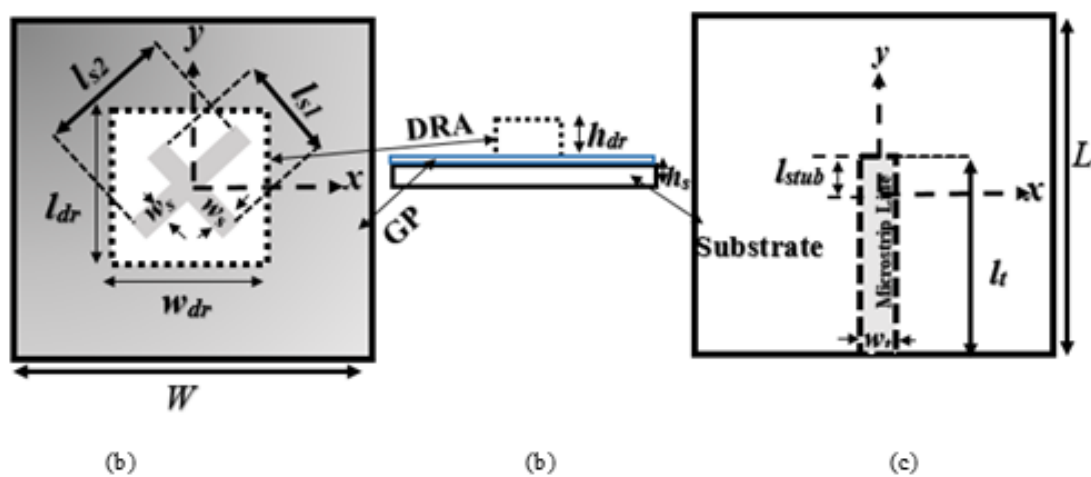


Figure 3-1 Antenna configuration a) top view b) front view c) back view.

In order to achieve the CP radiation, the single DRA element was excited by a cross slot while the energy coupling is controlled by a stub length extension (l_{stub}) with a recommended initial value of $0.25\lambda_g$, where λ_g is the guided wavelength. The cross-slot was fed using a 50Ω

microstrip line. The choice of the cross-slot arm lengths and widths are crucial for maximizing the impedance and AR bandwidths [144]. The lengths of the 1st and 2nd cross-slot arms were optimized as 1.7 mm and 3.2 mm, respectively, with an identical width of $w_s = 0.35$ mm for each arm. The formulas can be used to determine the starting lengths and widths of the slots.

$$l_s = \frac{0.4\lambda_0}{\sqrt{\varepsilon_e}} \quad (3.1)$$

$$\varepsilon_e = \frac{\varepsilon_r + \varepsilon_s}{2} \quad (3.2)$$

$$w_s = 0.2l_s \quad (3.3)$$

Where ε_r and ε_s are the dielectric constants of DRA and the substrate.

The best start points of the stub extension l_{stub} is:

$$l_{stub} = \frac{\lambda_g}{4} \quad (3.4)$$

In addition, the higher-order modes of TE_{113} , TE_{133} were simultaneously excited at 27 GHz and 30 GHz, respectively. Table 3-1 presents the resonance frequencies of the transverse electric (TE) modes that are supported by the designed DRA within the considered frequency range.

Table 3-1. Resonance frequencies of a number of TE modes supported by the used DRA.

Frequency (GHz)	Resonance Mode
25	TE ₁₁₁
27	TE ₁₁₃
30	TE ₁₃₃

3.3.1 The DRA Height

Special attention was given to choosing the smallest possible height of the DRA while maintaining reasonable radiation characteristics.

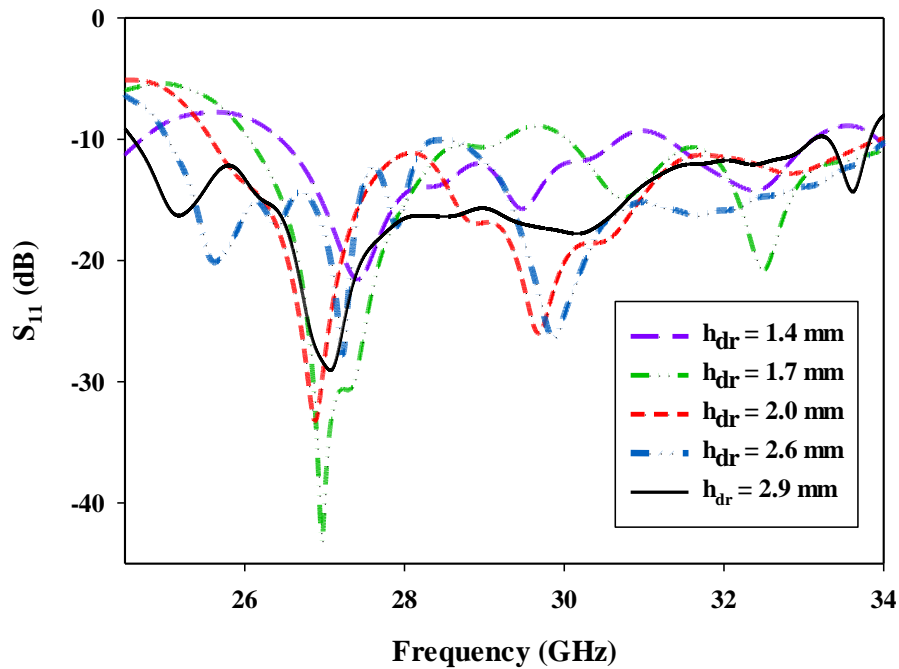


Figure 3-2. Reflection coefficient of various height of the DRA

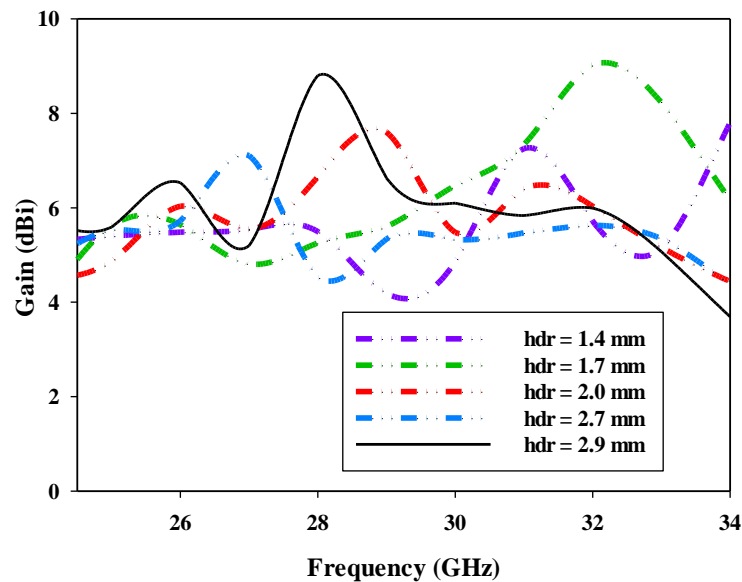


Figure 3-3. Gain of DRA with various heights.

Figure 3-2 shows the impedance bandwidth in different DRA heights, the impedance bandwidth of a rectangular dielectric resonator antenna (DRA) isn't directly dependent on its

height. Instead, it's influenced by various factors like the dielectric material properties, resonant frequency, and the resonator's dimensions. The impedance bandwidth is typically associated with the resonant frequency and the size of the resonator, rather than solely with its height. Validating the selected dimensions in the case study involves assessing whether the chosen dimensions align with the desired resonant frequency and the associated impedance bandwidth. If the dimensions lead to the intended resonant frequency and the desired impedance bandwidth, it would confirm the suitability of the chosen dimensions for the application. This validation ensures that the antenna meets the required performance criteria. The broadside gain is illustrated in Figure 3-3, where it can be observed that the maximum gain of ~9dBic was achieved at 28GHz with a height of 2.9mm. The axial ratio is introduced in Figure 3-4, where CP radiation was achieved with a 3dB AR bandwidth of 16% at a height of 2.9mm.

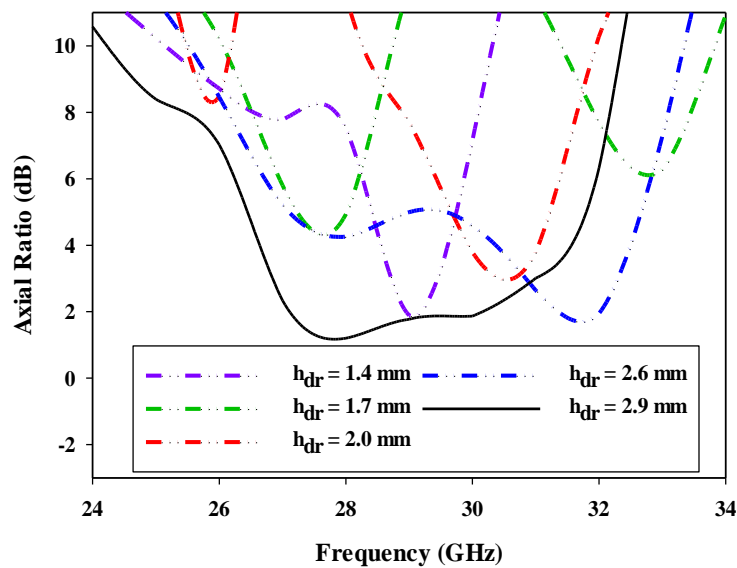


Figure 3-4. Axial ratio of DRA with various heights.

The far-field (polar view) patterns at the target frequency 28GHz at DRA height 2.9mm as clarified in Figure 3-5, where it can be noted that the DRA radiates a right-hand circular polarization (RHCP) wave since EL is greater than ER by ~20dB.

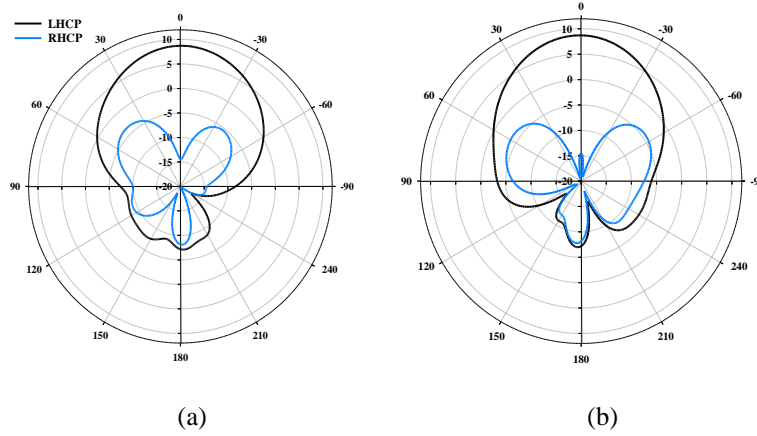


Figure 3-5. E- Plane and b) H- Plane radiation patterns of the proposed DRA at 28 GHz.

It should be noted that the proposed DRA offers the lowest profile compared to reported designs, albeit with a considerably wideband operation and a high gain. The final optimised antenna parameters are listed in Table 3-2.

Table 3-2. Parameters of the proposed single DRA element.

Parameters	Value (mm)	Description
w_{dr}	5.2	DRA width
l_{dr}	5.2	DRA length
h_{dr}	2.9	DRA height
L	19	Length of ground plane
W	21	Width of ground plane
h_s	0.254	Substrate height
l_t	10.5	Length of microstrip line
w_t	0.45	Width of microstrip line
l_{stub}	1	Stub length
l_{s1}	1.7	Length of the first slot
l_{s2}	3.2	Length of the second slot
w_s	0.35	Width of the cross slot

3.3.2 Single DRA Next to a Human Body.

To investigate the impact of human body on the antenna performance, the DRA was mounted on a three-layers tissue model.



Figure 3-6. A single DRA element above the body phantom.

Table 3-3. Human body tissue parameters at 28 GHz.

Tissue	Skin	Fat	Muscle
Relative Permittivity	16.55	6.09	24.43
Density [kg/m^3]	1109	911	1090
Conductivity[S/m]	25.82	6.58	33.6
Thickness (mm)	1	2	10

The modelled layers of the human body tissues of size $100 \times 45 \times 13 \text{ mm}^3$ are illustrated in Figure 3-6. Separation distances of 0 mm and 5 mm were considered between the DRA and the body phantom [37]. The characterizations of the body parameters are listed in Table 3-3 were [41].

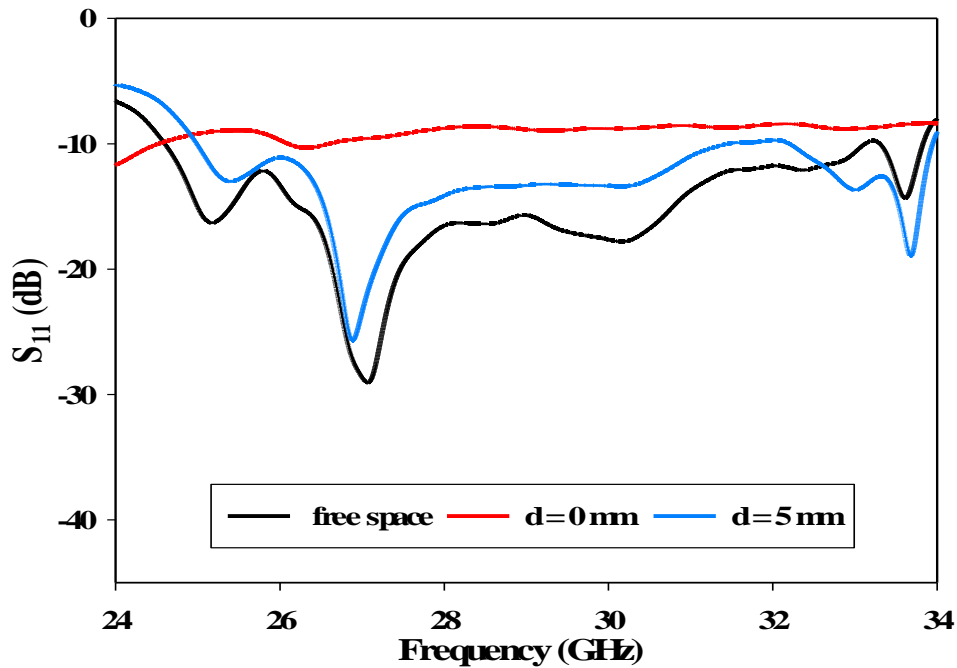


Figure 3-7. $|S_{11}|$ of a DRA in free space and placed next to a phantom.

Figure 3-7 illustrates the reflection coefficient when the DRA is positioned in free space as well as at distances of 0 mm and 5 mm above the phantom. For a 5mm distance, the achieved impedance bandwidth is ~31%, which is close to that of ~31.5% for a DRA in free space. This demonstrates a marginal impact of the human tissues on the impedance bandwidth, which can be explained as a result of the presence of a ground plane that minimizes the interaction between the DRA and tissues [72, 73]. Nevertheless, the reflection coefficient exhibits a substantial impact due to the proximity of the human body at a distance of 0 mm [37].

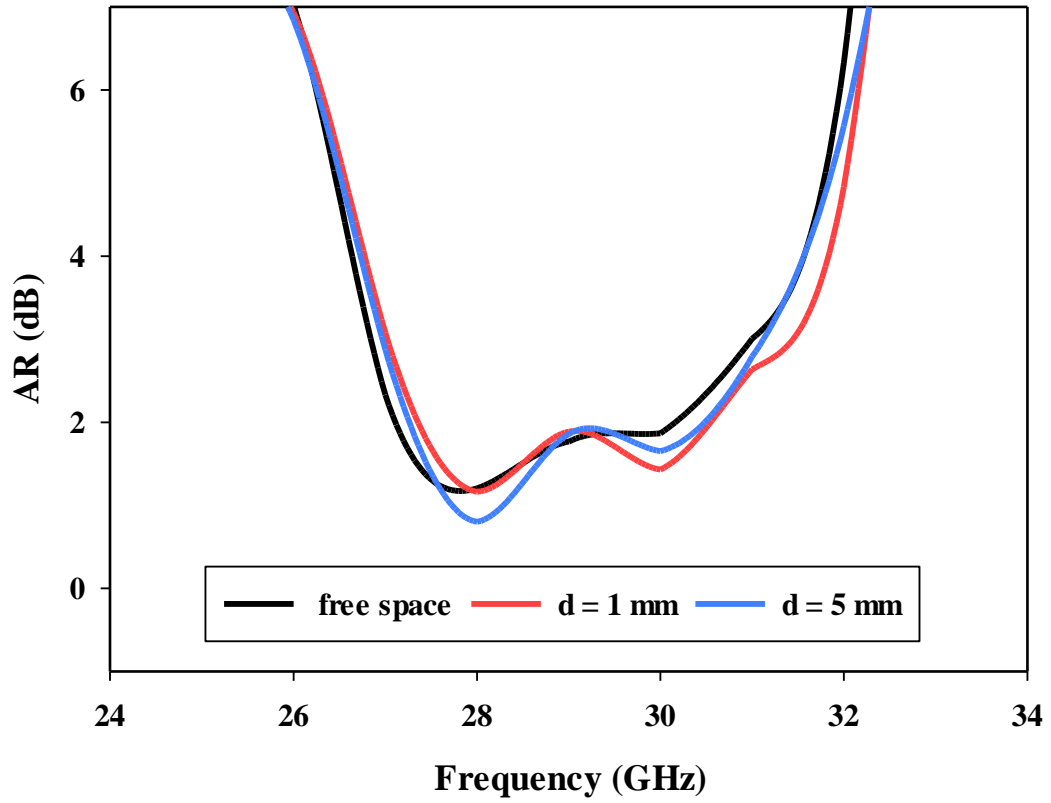


Figure 3-8. Axial ratio of a DRA placed in free space and next to a phantom.

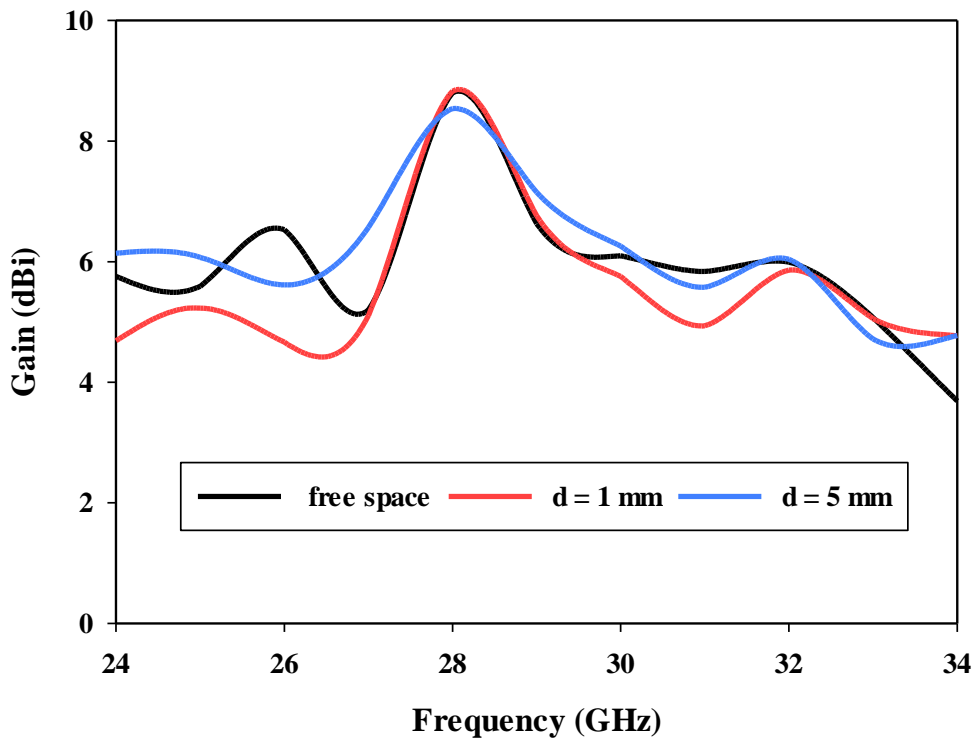


Figure 3-9. Gain of a DRA placed in free space and next to a phantom.

The same has also been confirmed for the CP radiation, where it can be noted from Figure 3-8 that almost the same AR bandwidth of 14% was achieved in free space as well at various separation distances between the antenna and the phantom. This is also the case for the achieved realized gain of ~8.7 dBic at 28 GHz as illustrated in Figure 3-9.

3.4 Broadside DRA Array

3.4.1 Array Factor

Suppose the array has N elements and that there is a d -space between each pair of adjacent elements. In addition, a complex current $I_o e^{jn\varphi}$, where $0 < n < N-1$, is used to drive each element. This indicates that the antennas are provided with linear phase shifts of φ between adjacent elements and equal current amplitudes. Thus, a phased array is the name given to this kind of antenna. However, if $\varphi = 0$, this means a uniform array is achieved. By considering an array of isotropic elements that are distributed along the z -axis, it is possible to derive the array factor as [145].

$$AF = 1 + e^{jY} + e^{j2Y} + \dots + e^{j(N-1)Y} \quad (3.2)$$

where

$$Y = (\beta d \cos\theta + \varphi) \quad (3.3)$$

The normalised AF form is:

$$(AR)_n = \frac{1}{N} \left[\frac{\sin\left(\frac{N}{2}Y\right)}{\sin\left(\frac{1}{2}Y\right)} \right] \quad (3.4)$$

When the main beam direction is perpendicular to the array axis, then a broadside array is achieved. It is clear from (3.2) that the maximum AF is achieved when $\gamma=0$. Consequently, when

the array axis is along the z direction, (3.3) becomes (3.5) when the maximum needs to be at $\theta=90^\circ$.

$$Y = (\beta d \cos \theta + \varphi)|_{\theta=90^\circ} = \varphi = 0 \quad (3.5)$$

Therefore, to satisfy the broadside radiation requirements, the array elements must be excited d by utilising uniform phase and amplitude. To determine the radiation pattern in a specific plane, the individual element pattern needs to be multiplied by the array's factor.

$$E_{array} = E_{single\ element} \times Array\ Factor \quad (3.6)$$

For example, to evaluate how the radiation pattern changes when two elements are used in an array configuration. Equations (3.5) and (3.6) were solved numerically using MATLAB to compute the array factor for a given antenna. The radiation pattern for one element was obtained from CST, and this data was utilized in conjunction with the MATLAB code to compare the results of two antenna elements. The parameters of the array factors were considered to be consistent with the simulation settings, where the inter-element spacing was set to 10mm.

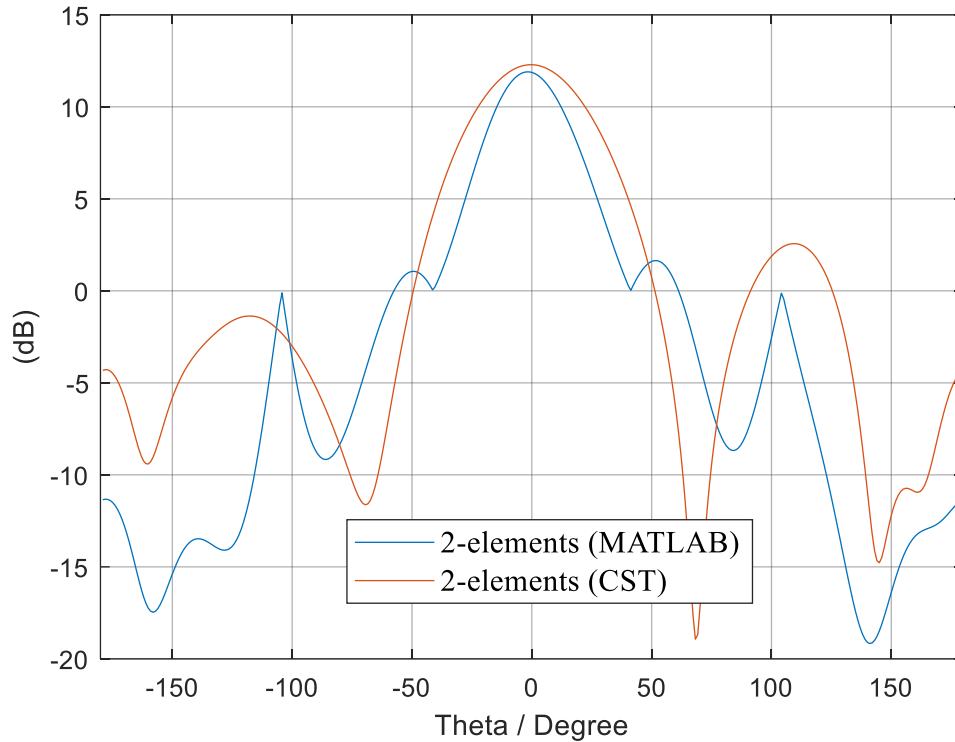


Figure 3-10. The radiation pattern for 2-elements at 28GHz

The radiation patterns for the two elements (from CST) and the array configuration (using MATLAB's array factor) were plotted on the same graph in Figure 3.-10. By comparing these patterns, it can be observed that the two shapes are quite similar. The differences, can be attributed to the fact that the MATLAB code does not take into account the feed network. Moreover, as mentioned earlier, antenna arrays are generally to enhance the gain. An array consists of two or more antenna elements that are spatially arranged and electrically interconnected to produce a directional radiation pattern. The radiation pattern of an antenna array can be altered by adjusting the spacing and phase shift between adjacent elements [146]. The single DRA element proposed in the last section will be utilized to create DRA arrays consisting of 2, 4, and 8 elements. These arrays will be thoroughly investigated to provide a clearer picture of the design process. As can be noted in Figure 3-11, the return losses of the single element in this instance has the largest bandwidth (31%), followed by the 4-element array (28.3%), the 2-element array (23%), and the 8-element array (18.7%). As a result, compared to

arrays with several elements, the single element may function across a larger range of frequencies.

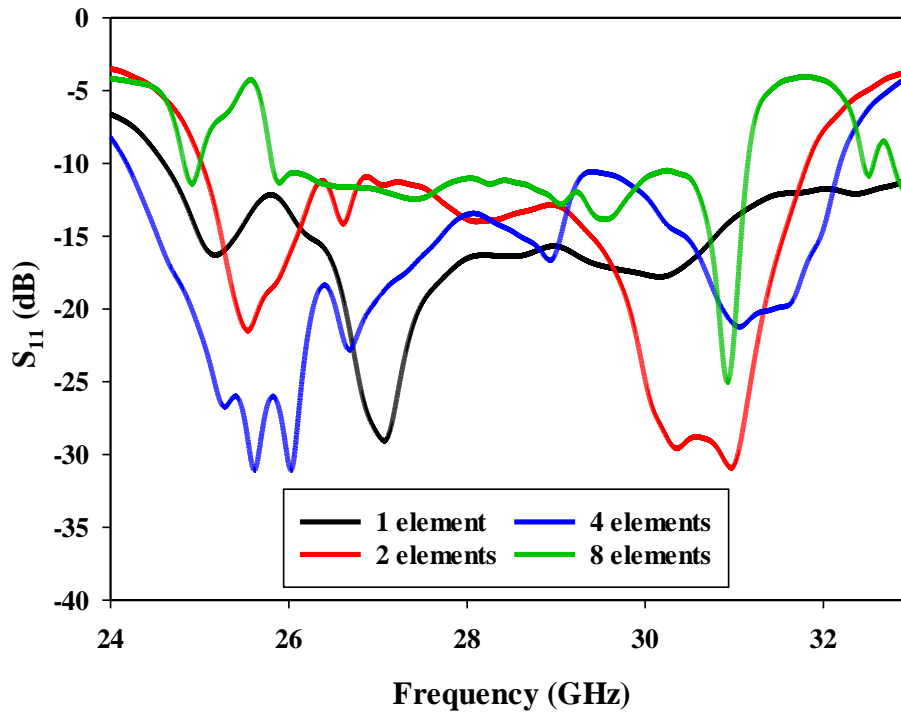


Figure 3-11. Reflection coefficients of various DRA arrays.

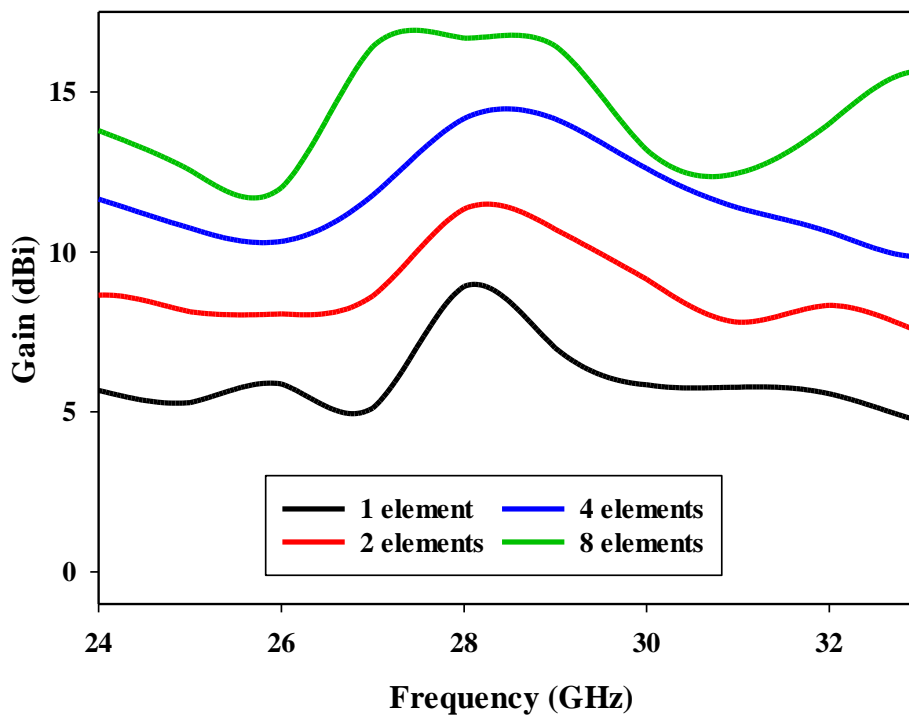


Figure 3-12. Gain of various DRA arrays.

Figure 3-12 illustrates the link between an antenna's gain, and the number of its elements. Particularly, the gain of the antenna grows along with the number of elements. A two-element antenna has a gain of 11.1 dBi compared to a single-element antenna's 8.71 dBi. An antenna with four elements has a gain of 14 dBi, whereas one with eight elements has a gain of 16.6 dBi. This is due to the fact that having more elements enables a radiation pattern that is more directed and focused, with less energy radiating in the undesirable directions.

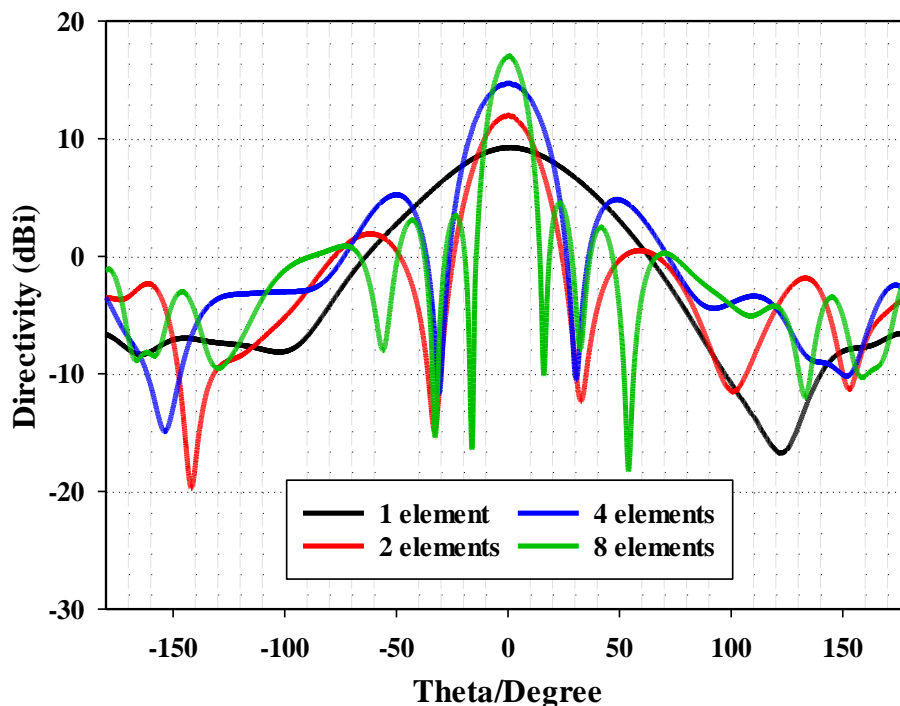


Figure 3-13. Directivity of various DRA arrays.

From, Figure 3-13. It can be seen that with a single DRA element $D = 9.25\text{dBi}$ was achieved, a 2-element array, have a directivity of 12 dBi, while a 4-element array would have a directivity of 14.7 dBi and an 8-element array would have a 17 dBi. This demonstrates that when the array's element count rises, the directivity rises as well, improving the ability to regulate the radiation's direction [147].

$$G = \eta \times D \quad (3.1)$$

where G , η and D == represent gain, efficiency and directivity, respectively.

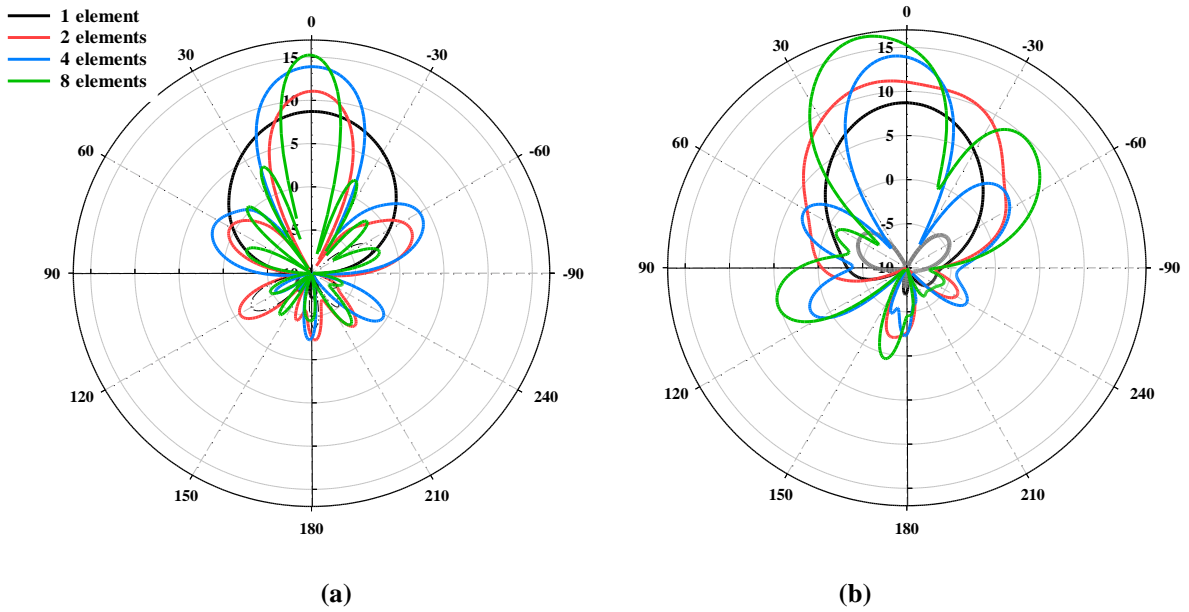


Figure 3-14. Radiation pattern of various DRA arrays at 28GHz. (a) E-plane. (b) H-plane

Figure 3- 14 illustrates the radiation pattern of the desired frequency of 28 GHz., where it can be noted that an antenna array with more elements produces a narrower beam with a higher gain (directivity). In general, the gain will be increased according to the number of the utilized antenna elements. However, this is not the case for the impedance bandwidth, which, can be noticed from Figure 3-15, where it is evident that the higher gain is associated by the array elements. Table 3-4 presents the results of the array analyses.

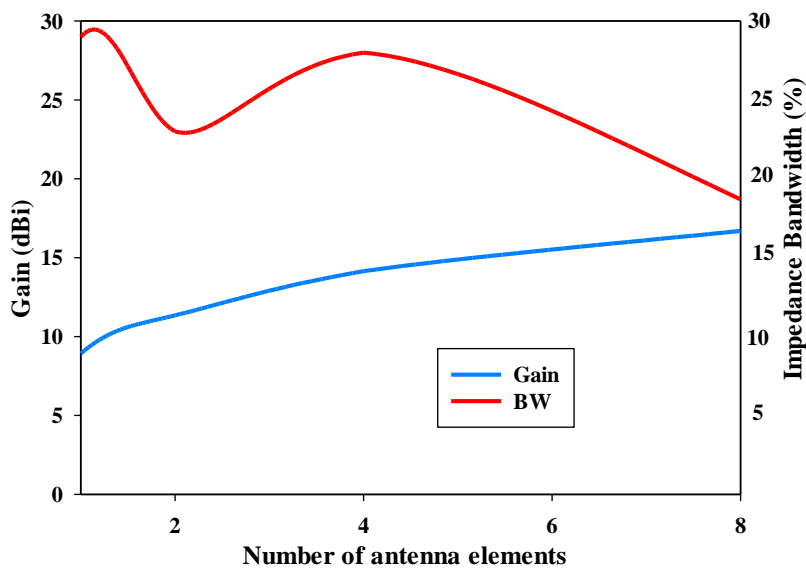


Figure 3-15. The array's gain and bandwidth as a function of the number of elements.

Table 3-4. Bandwidth, Gain, and size of various DRA arrays

	BW (%)	Gain (dBi)	Size (mm)
Single element	31	8.71	19×21×2.93
2 elements	23	11.1	35×35× 2.93
4 elements	28	14	36.5×36.5×2.93
8 elements	18.7	16.6	40×45×2.93

3.5 2 × 2 DRA Array

A 2 × 2 array antenna doesn't inherently signify MIMO (Multiple Input Multiple Output) by itself. However, it's commonly used in MIMO systems. For example, a four-element array antenna can be notated as 1 × 4 or 2 × 2. Typically, 1×4 indicates a linear array where the antennas are arranged linearly along one axis, while the 2×2 array features two rows and two columns of antennas, often arranged in a square or rectangular pattern [148, 149].

The presented single DRA element was utilised to design a compact broadside 4-element array that was positioned on a square ground plane with a size of 36.5 mm on which the cross-slots were etched as demonstrated in Figure 3-16(a). A square array geometry was chosen as illustrated in Figure 3-16(b) since it offers a more compact structure. The feed network is presented in Figure 3-16(c), where it can be observed that a four-way microstrip power divider line was utilized for the array feed network [150].

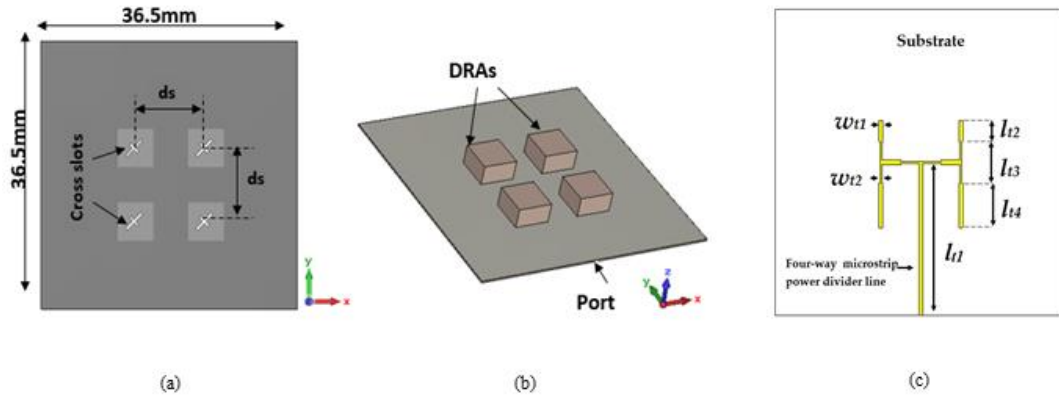


Figure 3-16. Configuration of the proposed DRA array antenna (a) Top view, (b) 3D view, and (c) Feed network

The dimensions were chosen to support the broadside array design criteria including uniform power division and phase distribution. In addition, two microstrip line widths were chosen; $w_{t1} = 0.5$ mm and $w_{t2} = 0.25$ mm for characteristic impedances of 50Ω and 100Ω , respectively. Furthermore, the lengths of the microstrip line sections were optimized as $l_{t1} = 18.13$ mm, $l_{t2} = 2.5$ mm, $l_{t3} = 5$ mm, and $l_{t4} = 5.3$ mm in order to achieve the widest impedance bandwidth. It should be noted that a Rogers substrate, RO4350B, was employed in the simulations based on the commercial availability. The spacing between the various antenna elements of an array is inversely correlated with mutual coupling [151].

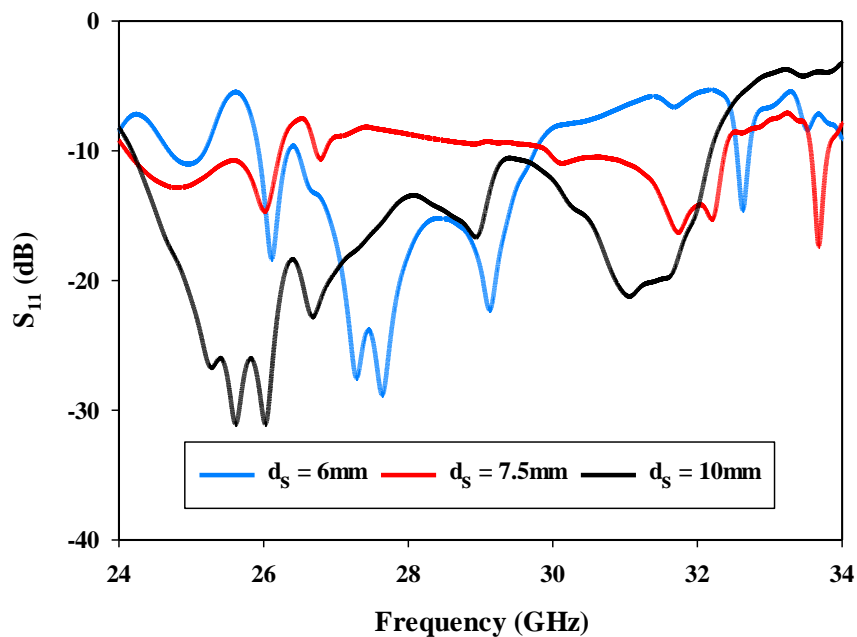


Figure 3-17. $|S_{11}|$ of the DRA arrays for various separation distances (d_s).

The impact of the separation distance (d_s) between the centres of adjacent DRA elements was investigated as demonstrated in Figure 3-16, where d_s was varied from 6 to 10 mm, which corresponds to a range of $0.558\lambda_0$ to $0.93\lambda_0$, where λ_0 is the free space wavelength at 28 GHz. As demonstrated in Figure 3-17, the widest impedance bandwidth was achieved when the antenna elements are separated by 10 mm, which can be understood as a result of the reduced mutual coupling at such distance. Noteworthy is the fact that the widest archived impedance bandwidth for the array is 28%, which is close to that of the single DRA element. Moreover, Figures 3-18 and 3-19 present the AR and gain as functions of (d_s), where the widest AR bandwidth of 13% and highest gain of ~ 14 dBic were achieved, again, when $d_s = 10$ mm due to the reduced mutual coupling.

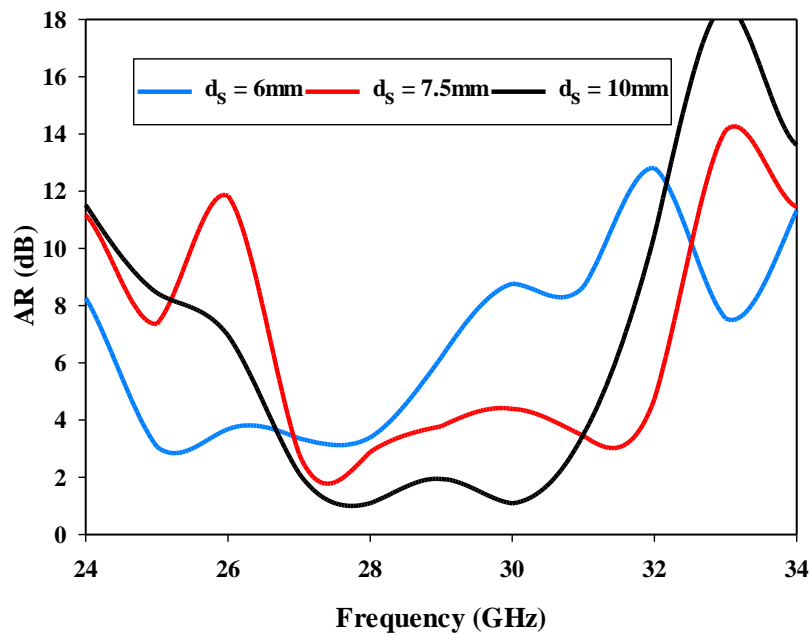


Figure 3-18. AR of the DRA arrays using various separation distances (d_s) between the DRAs.

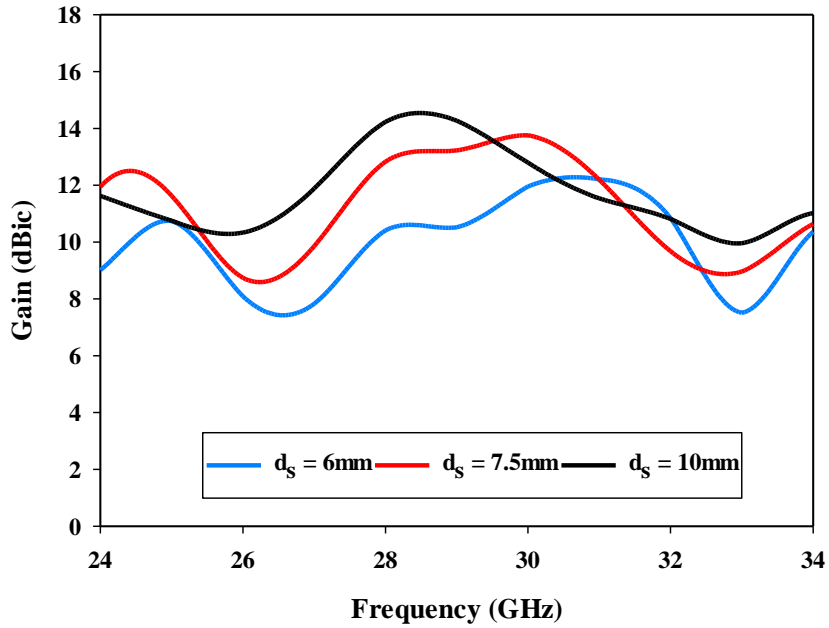


Figure 3-19. Gain of the DRA arrays using various separation distances (d_s) between the DRAs.

Figure 3-20 displays the radiation patterns of the E-field and H-field at various distances between adjacent elements. It is evident that the best results were achieved at a distance of 10 mm (d_s). Additionally, Figure 3-21 demonstrates that the directivity reached its peak at the 10 mm distance.

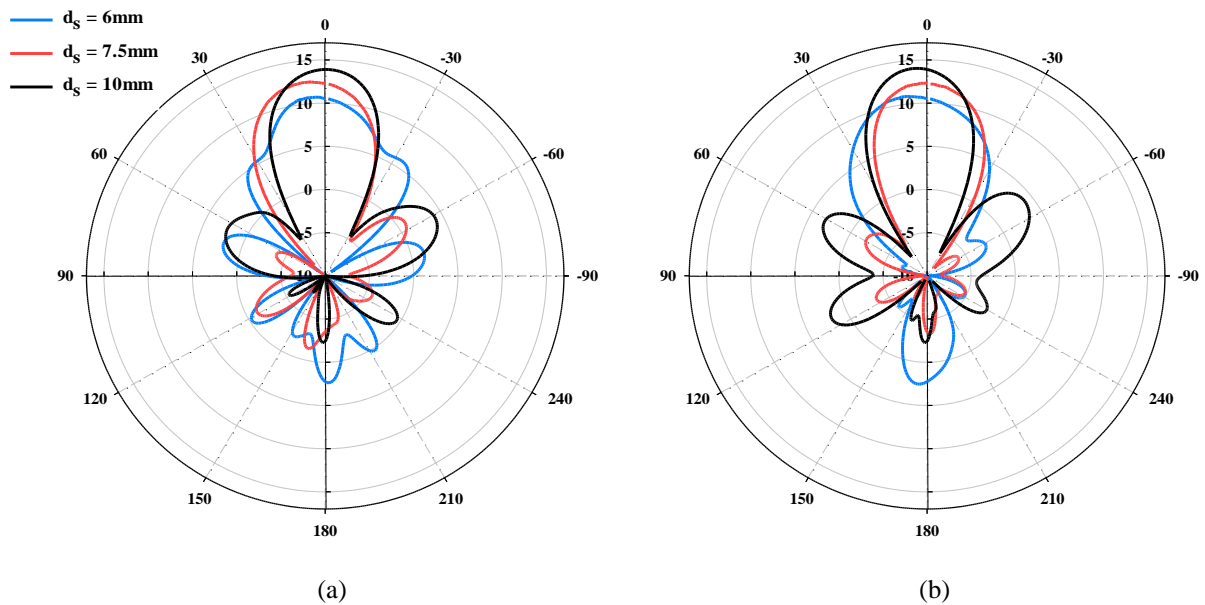


Figure 3-20. Radiation pattern of the DRA arrays using various separation distances (d_s) between the DRAs.

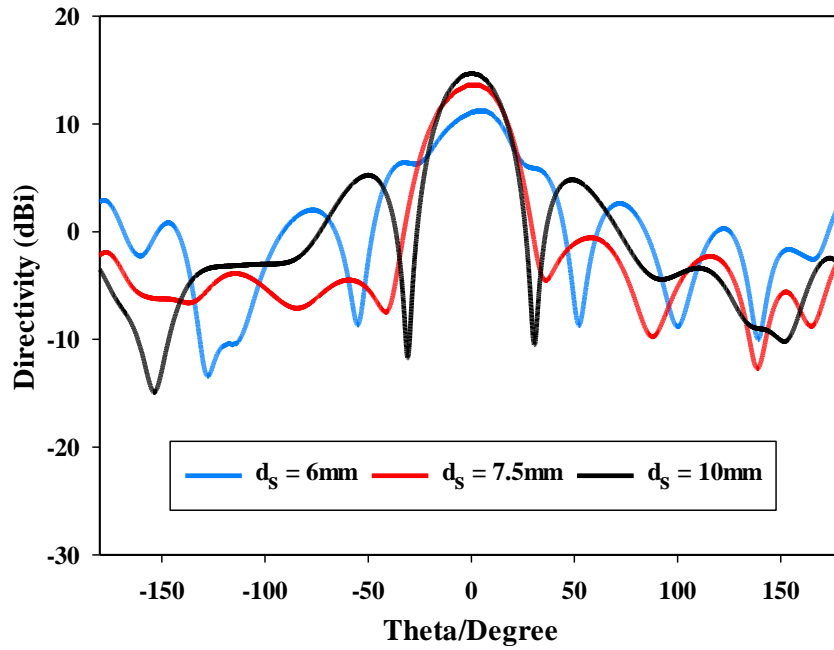
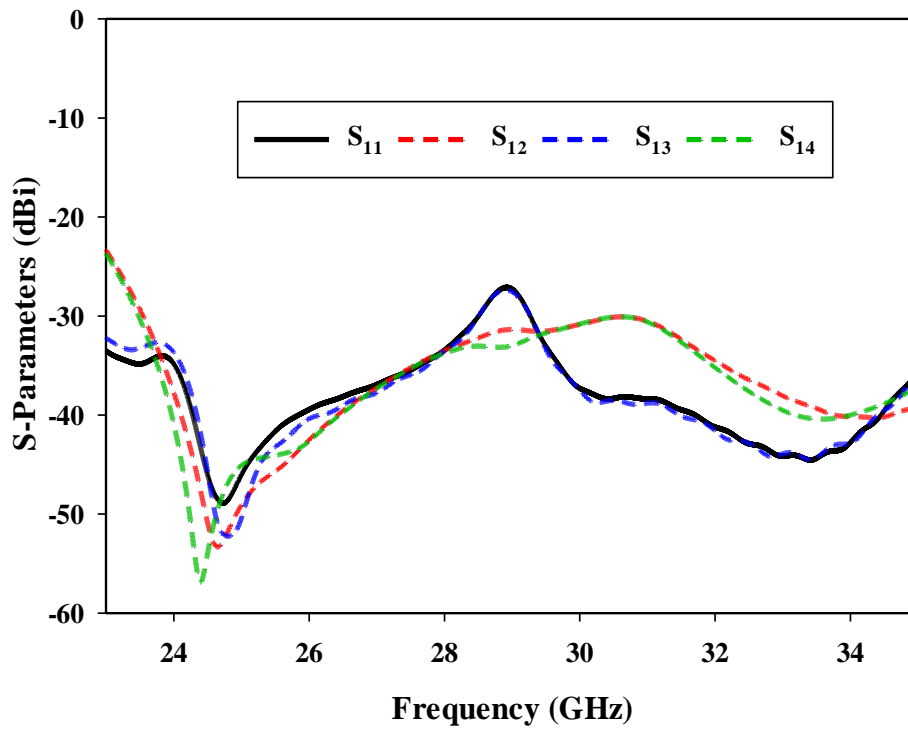


Figure 3-21. Directivity of the DRA arrays using various separation distances (d_s) between the DRAs.



(a)

Figure 3-22. S-parameter values of feeding network

The S-parameter performance of the four-way microstrip power divider is illustrated in Figure 3-22. The first port is designated as the input, and the subsequent ports are arranged in ascending order. Where S_{11} demonstrates a matching performance of less than -15 dB within

the desired frequency ranges. The reflection coefficient isolation all fall within an acceptable range. It should be mentioned that the phase shift between the output ports is 0.

3.5.1.1 28 GHz CP Rectangular DRA Array: Performance Metrics and Unique Attributes

- Impedance Bandwidth: Evaluation of the antenna's ability to operate efficiently over a range of frequencies around 28 GHz, indicating its versatility in accommodating different communication needs.
- Axial-Ratio Bandwidth: Analysis of the axial ratio bandwidth, highlighting the antenna's capacity to maintain circular polarization characteristics across a specific frequency range, crucial for reliable off-body communications.
- Gain at 28 GHz: Examination of the antenna's gain specifically at the critical frequency of 28 GHz, providing insights into its signal amplification capabilities and overall performance in the designated communication spectrum.

These key performance metrics underscore the array's suitability for off-body communications at millimeter-wave frequencies, with a focus on its impedance bandwidth, axial-ratio bandwidth, and gain at 28 GHz.

3.5.2 Array Next to a Human Body.

To learn more about the effects of the human body on the array performance, the same procedure used for a single DRA element was followed, i.e. the DRA array was placed at two various distances of 1 mm and 5 mm away from the three-layer human body model [37]. The modelled layers of the human body tissues of size $100 \times 45 \times 13 \text{ mm}^3$. as illustrated in Figure 3-23. The characterizations of the body parameters were used according to those given in [41].

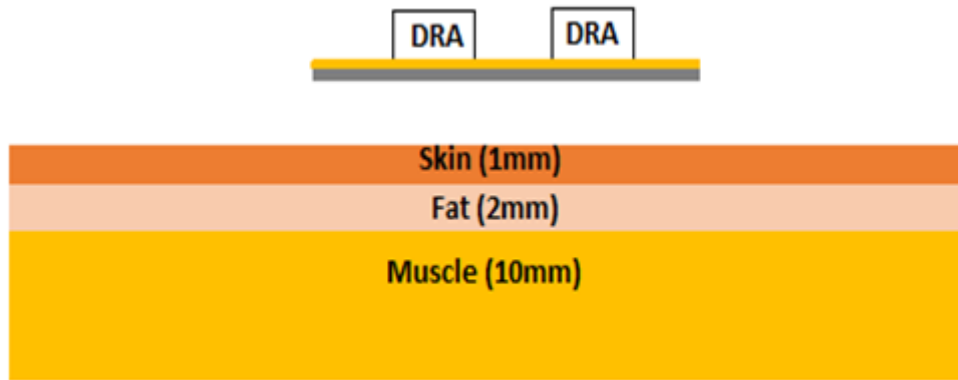


Figure 3-23. Cross section view of a DRA array next to the body phantom.

Figure 3-24 presents the reflection coefficient when the array is placed at free space and at distances of 1 mm and 5 mm from the phantom. These results confirm that the attained impedance bandwidth is approximately 28% at the two considered distances, which is comparable to that of a DRA array operating in free space. Owing to the presence of a ground plane between the antenna and the simulated tissue layers, the effect of the human tissue on the impedance bandwidth was minimized.

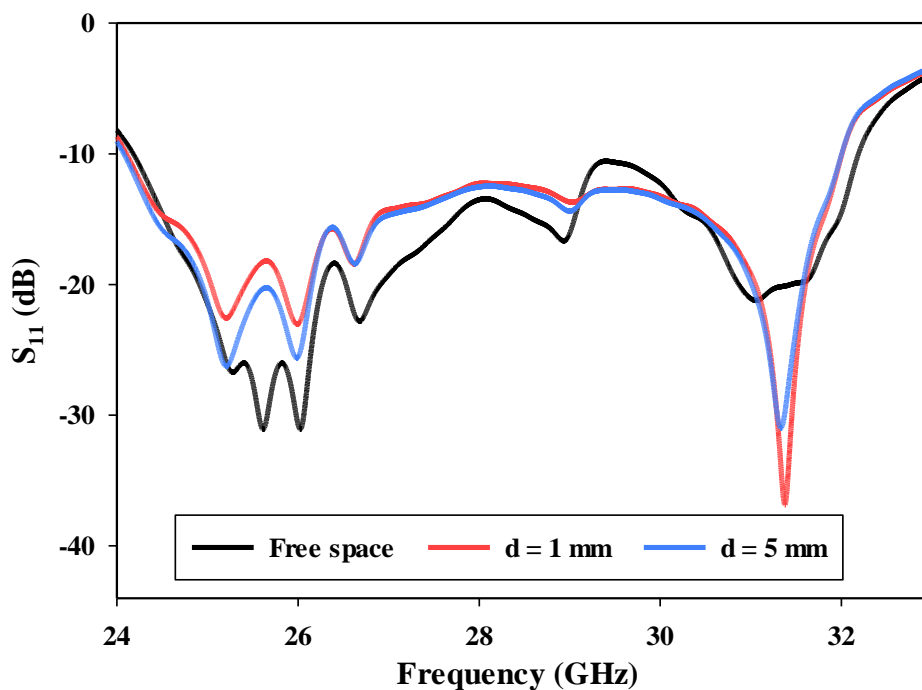


Figure 3-24. Reflection coefficient of a DRA array in free space and placed next to a phantom.

Similarly, the far field characteristics are not affected by the presence of the human tissue phantom layers as demonstrated in Figures 3-25 and 3-26, where it is evident that the achieved axial ratio bandwidth of 13% and gain of 14 dBic for an array is located at free space, are comparable to those when the array operates at the proximity of human tissues model. As was mentioned earlier, the chosen DRA element supports the following TE resonance modes across the considered frequency range of 24-31 GHz; TE_{111} , TE_{113} and TE_{133} . The excitation of the higher order modes provided a maximum gain of ~ 14 dBic at 28 GHz, which is considerably higher than those reported in the literature for 4 element DRA arrays. This is to be expected since the gain of the designed single dielectric resonator antenna is ~ 9 dBic compared to a typical gain of ~ 6 dBi for a DRA that operates in a lower order mode. In addition, all the excited modes support broadside radiation, which provided the required stability of the radiation patterns over the considered frequency range. Finally, merging the bandwidths of the excited adjacent resonance modes have provided considerably wider impedance and CP bandwidths.

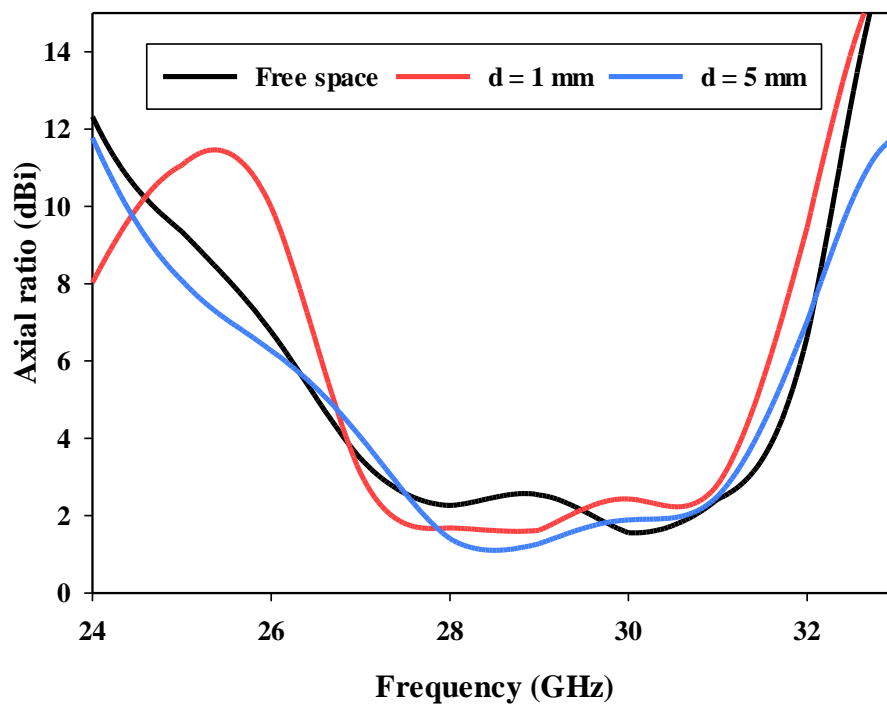


Figure 3-25. Axial ratio of a DRA array placed in free space and next to a body phantom.

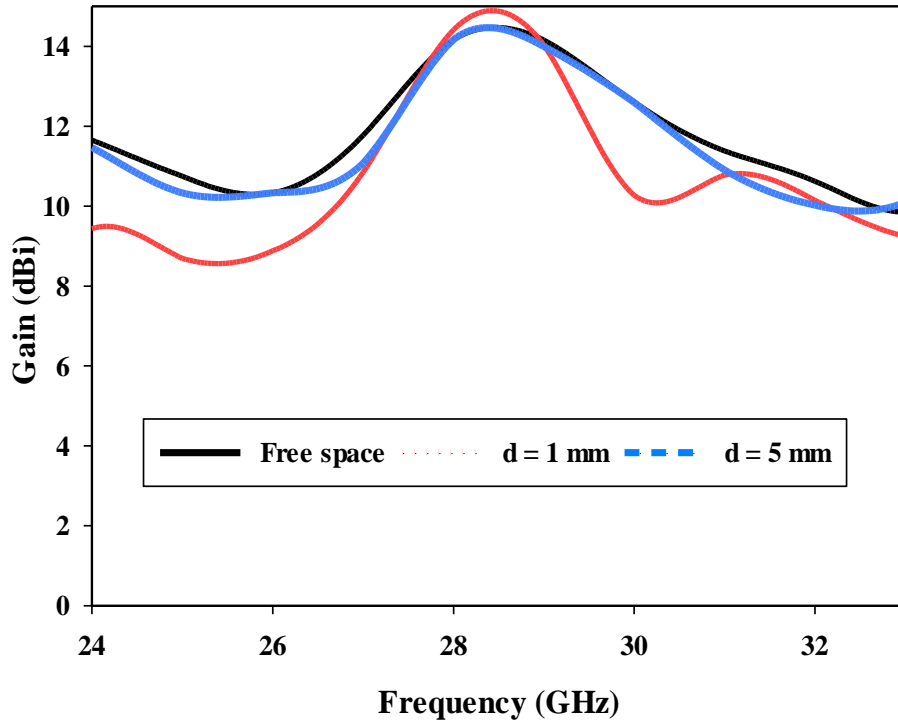


Figure 3-26. Gain of a DRA array operating in free space and next to a body phantom.

In addition, the surface current distribution at the resonant frequency of 28 GHz is depicted in Figure 3-27, where a clockwise rotation of the current vectors can be observed, which produces the left-hand circularly polarized radiation. It should be noted that the same current distribution was observed for the single circularly polarized DRA, which demonstrates an unnoticeable impact of the mutual coupling between the array elements on the current distribution.

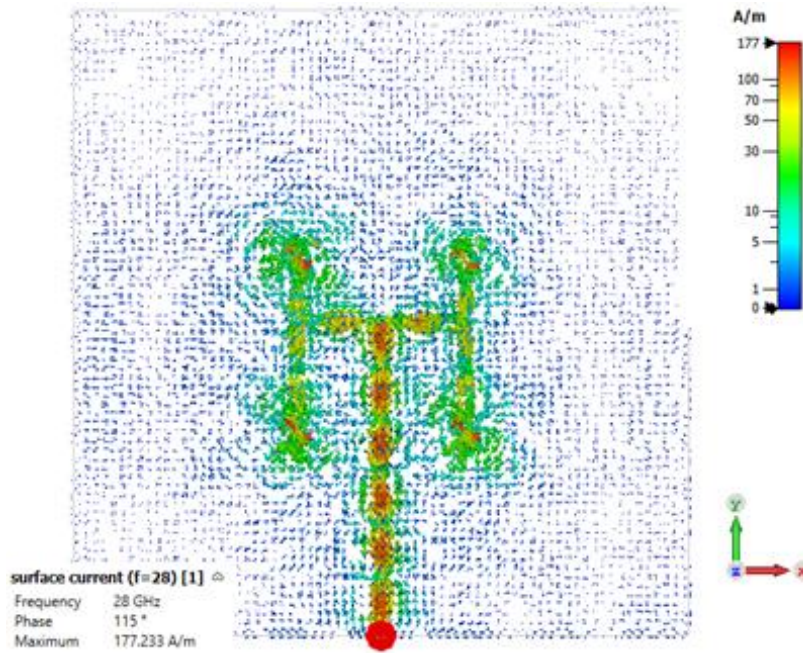


Figure 3-27. Surface current distribution on the DRA array's ground plane at 28 GHz.

3.5.3 Specific Absorption Rate (SAR) of the DRA Array

Figures 3-28 and 3-29 illustrate the SAR when the proposed DRA array is placed next to the equivalent three-layers tissue of the human body, where it can be noted that the SAR is well below the required safety threshold for different input power levels when 1 g and 10 g tissues are considered.

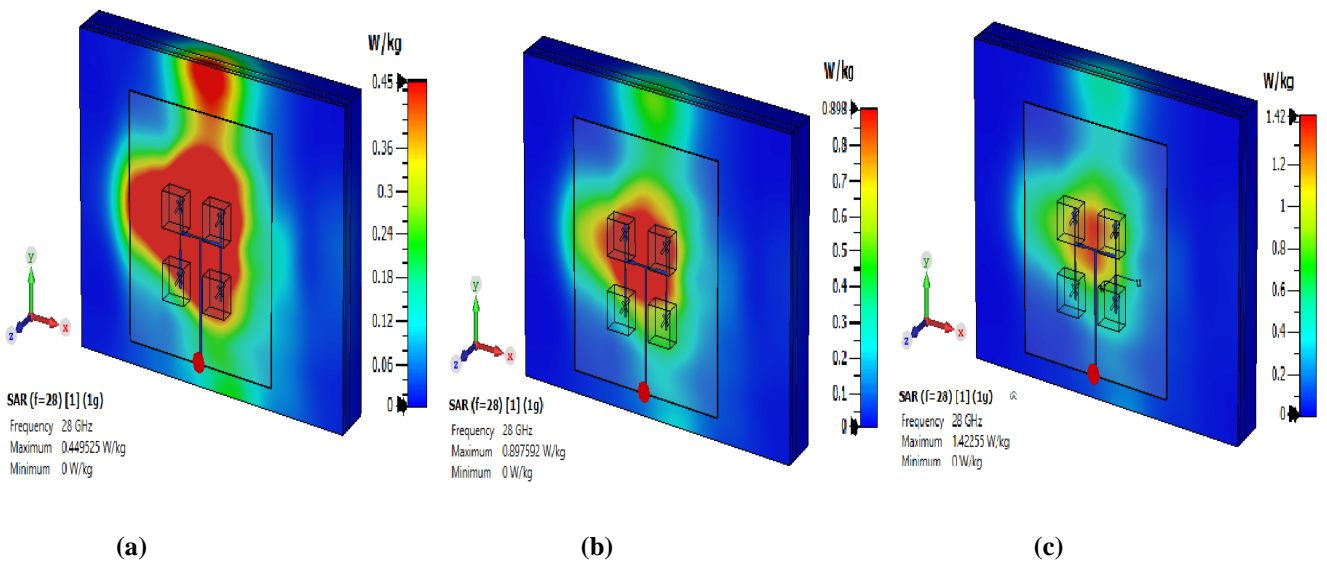


Figure 3-28. SAR of the DRA array for a 1 g tissue and input power of (a) 15 dBm, (b) 18 dBm, (c) 20 dBm

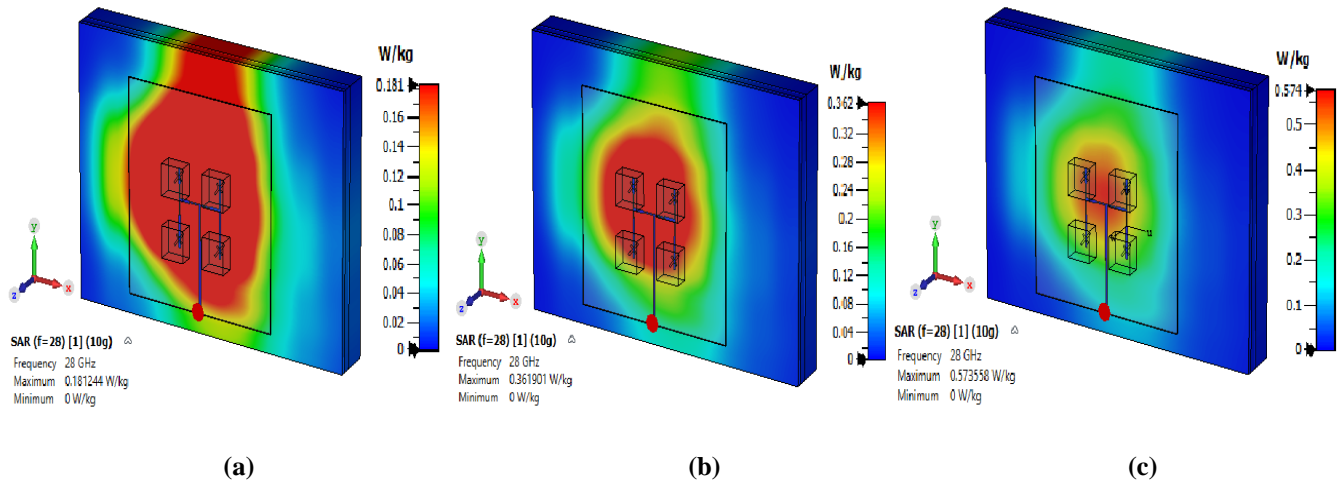


Figure 3-29. SAR of the DRA array for a 10 g tissue and input power of (a) 15 dBm, (b) 18 dBm, (c) 20 dBm.

Table 3-5. The average SAR for 1g and 10g tissues using input power of 15 dBm, 18 dBm, and 20 dBm.

Standard	Input power (dBm)	SAR(W/kg)	Distance (mm)
FCC/ANSI	15	0.4495	5
ICNIRP	15	0.18123	5
FCC/ANSI	18	0.8975	5
ICNIRP	18	0.3619	5
FCC/ANSI	20	1.4225	5
ICNIRP	20	0.5735	5

Table 3-5 summarizes the maximum achieved SAR levels to confirm that the recommended safety levels were maintained according to the FCC and ICNIRP standards.

3.6 Measurements.

At mmWave frequencies, the precise alignment and assembly of the DRA represent significant challenges that were addressed by outlining the DRA positions on the ground plane. The fabricated feed network is presented in Figures 3-30 (a) and (b), along with the outlined DRA positions. Once the DRA positions are outlined, the antennas were bonded to the ground plane using an extremely thin double-sided adhesive copper tape with a thickness of 0.08 mm.

The assembled DRA array prototype is presented in Figure 3-30 (c), which can be measured without any alignment and bonding concerns.

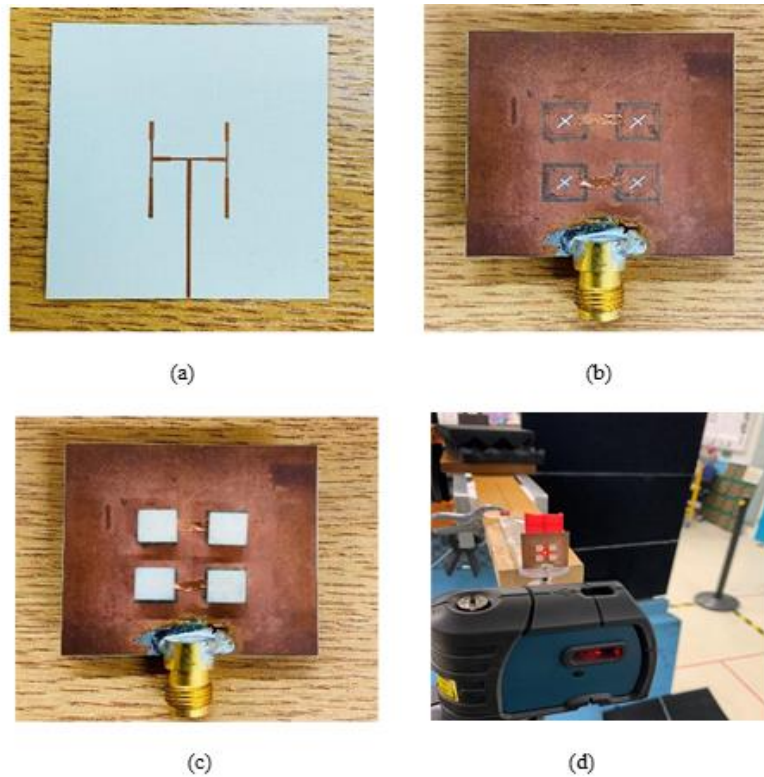


Figure 3-30. The array prototype a) Back view of the feed network b) Top view of the feed network c) Assembled DRA array d) Measurements system.

As per the previous investigation, the human body is observed to have negligible impact on the performance, therefore, all the measurements were conducted for the DRA array in free space. The measurement system is presented in Figure 3-30 (d). Figure 3-31 demonstrates the simulations and measurements for the array's reflection coefficient, where it can be noted that the measured -10 dB bandwidth is 8.16 GHz. In addition, good agreement was achieved between the measured and simulated impedance bandwidths of 29% and 28.4%, respectively. However, there is a slimily difference in the curves, which may be the result of marginal fabrication and experimental errors.

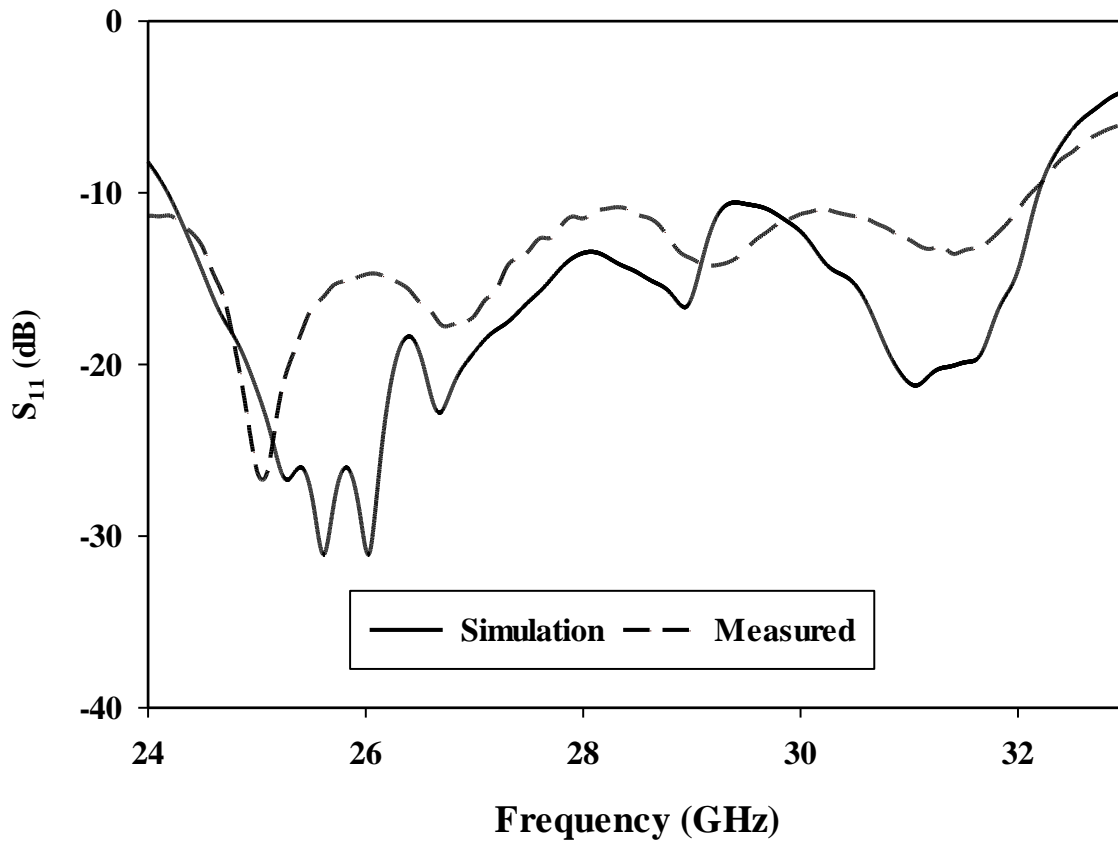


Figure 3-31. The simulated and measured $|S_{11}|$ of the DRA array.

The gain and axial ratio of the DRA array are presented in Figures 3-32 and 3-33, with close agreement between measurements and simulations. The measured gain, however, was marginally reduced to 13.7 dBic compared to a maximum simulated gain of 13.9 dBic at 28 GHz. This may be attributed to experimental errors as well as any slight variations in the dielectric constant of the utilized materials. On the other hand, the measured AR bandwidth is ~13%, which is similar to the simulated counterpart.

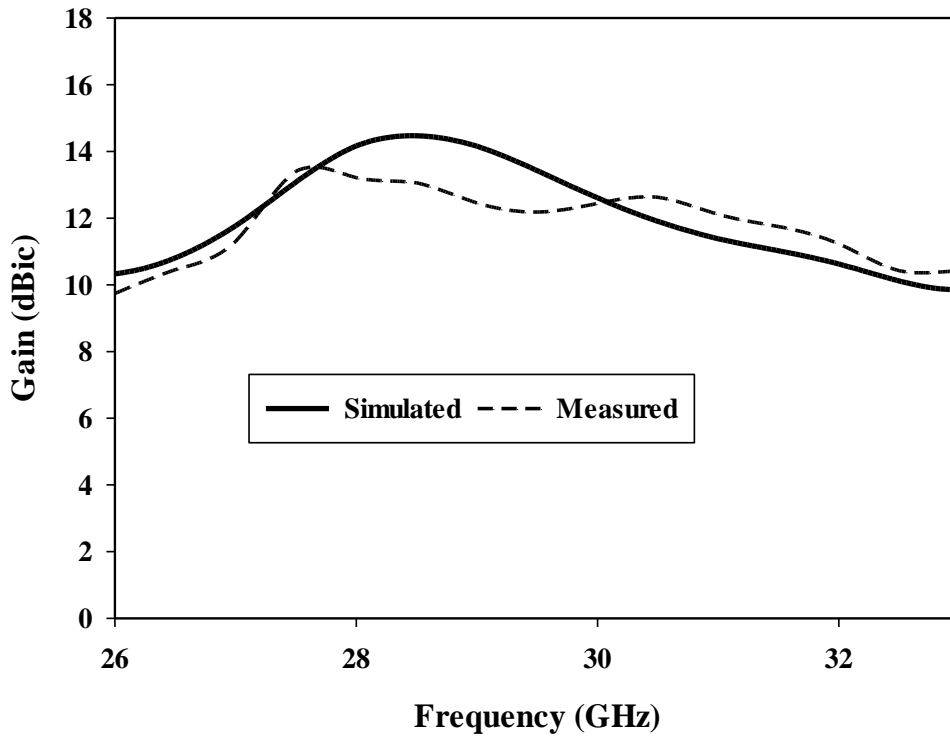


Figure 3-32. The simulated and measured gain of the DRA array.

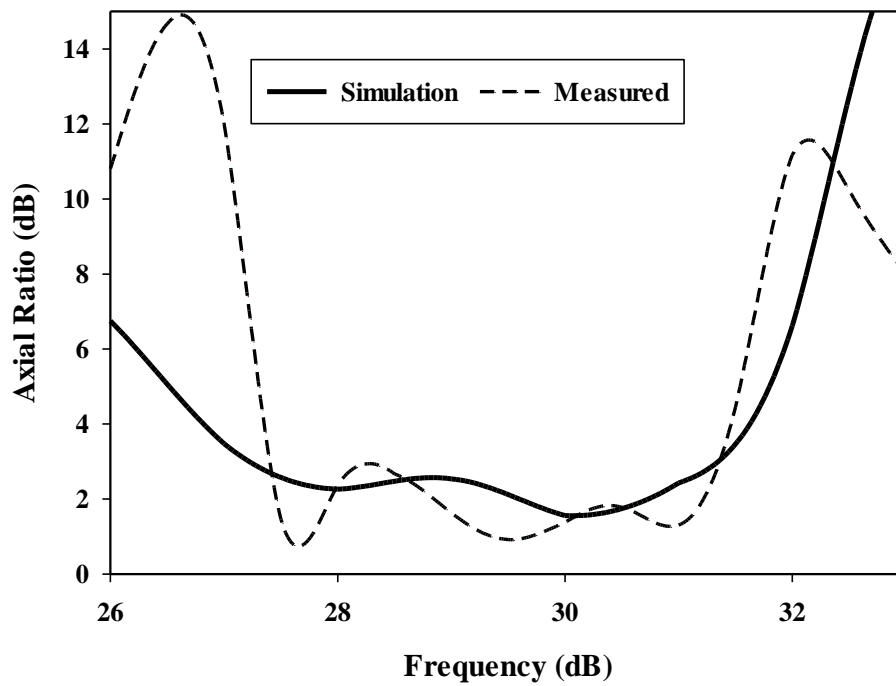
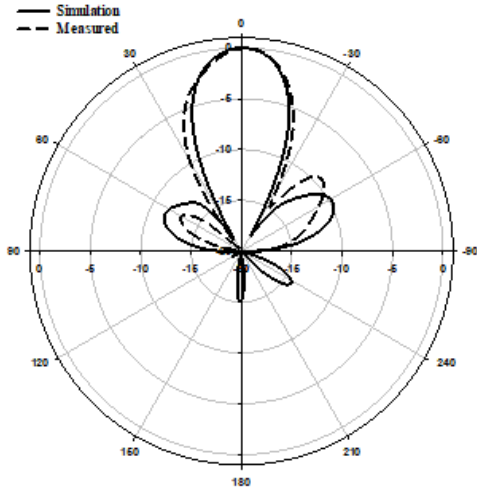
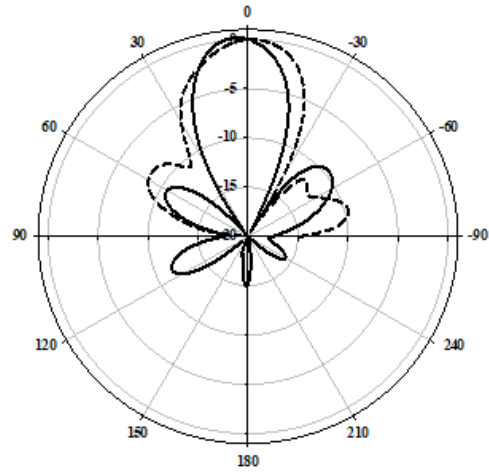


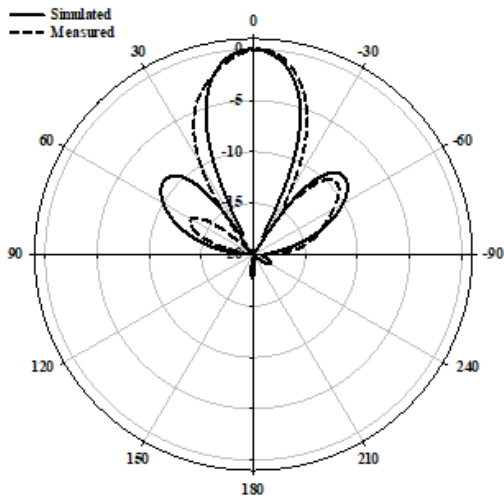
Figure 3-33. The simulated and measured gain of the DRA array.



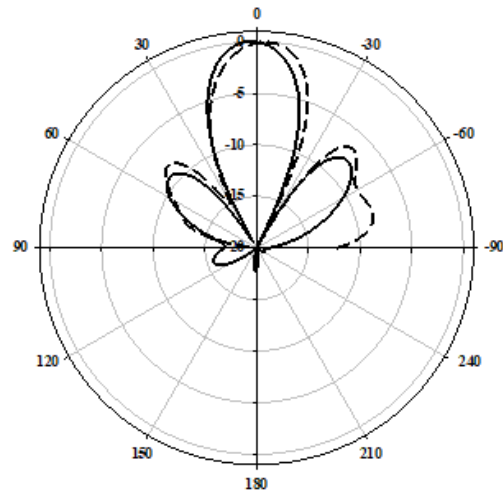
(a) E-plane at 28 GHz.



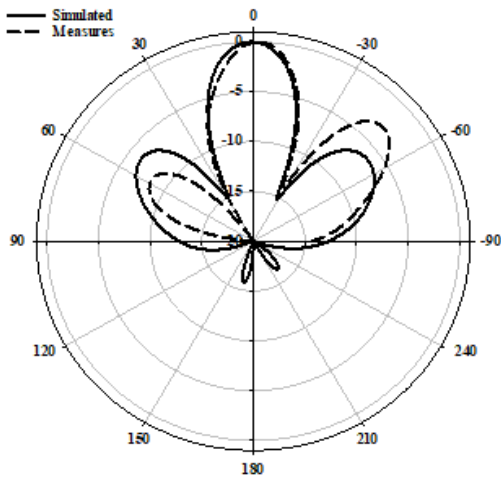
(b) H-plane at 28 GHz.



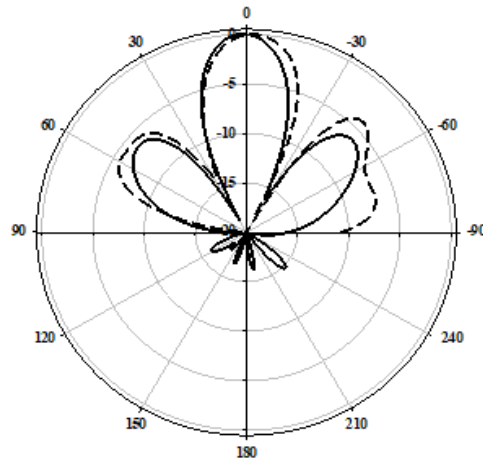
(c) E-plane at 29 GHz.



(d) H-plane at 29 GHz.



(e) E-plane at 30 GHz.



(f) H-plane at 30 GHz.

Figure 3-34. Simulated and measured radiation patterns across the CP bandwidth of the DRA array.

Figure 3-34 presents the simulated and measured E- and H-planes radiation patterns at 28 GHz, 29 GHz, and 30 GHz for the proposed antenna array in free space. Overall, a good agreement can be observed between measurements and simulations at these frequencies. For example, the respective measured and simulated gains are 13.7 dBic, 13.9 dBic at 28 GHz, 13.68 dBic, 14dBic at 29 GHz and 12.45 dBic, 12.6 dBic at 30 GHz. The presented 2 x 2 DRA array's performance parameters; Gain, AR, size, and bandwidths are listed in Table 3-6 as compared to those of various mmWave DRA array configurations that were reported in the literature. It can be observed that the proposed array, with only 4 DRA elements, provides a higher gain, as compared to the literature, and even outperforms that achieved using 8 elements [96] and only 2 dB less than that achieved using 16 elements [98], which illustrates higher performance at reduced complexity. As compared to circularly polarized designs in [92, 94, 97], this work provides a wider AR bandwidth combined with higher gain performance. Other designs in [95, 96, 98, 99] proposed LP antenna arrays. Therefore, this work offers improved performance as per measured gain of 13.7 dBic in combination with impedance and AR bandwidths of 28% and 13%, respectively, all overserved for a 4-element DRA array only.

Table 3-6. Comparison of the proposed antenna performance against previously published designs.

Ref	Elements number	f_c (GHz)	Gain	S_{11} BW (%)	AR BW (%)	Size (mm ³)
[92]	4	30	12.7dBic	16.4	1.1	-
[94]	4	60	11.4dBic	26	15.9	-
[95]	4	60	10.5dBi	12	LP	-
[96]	8	32	12dBi	18.29	LP	-
[97]	4	30	9.5dBic	33.8	5	20×20×1.52
[98]	16	28.7	15.68dBi	9.81	LP	46×46×1.5
[99]	4	27.5	9.8dBi	31.6	LP	47×8×1.084
This work	4	28	13.7dBic	29	13	36.5×36.5×2.9

3.7 Conclusion.

This study presented a four-element circularly polarized rectangular DRA array for mmWave off body applications. For the suggested antenna, cross-slot coupling together with a sequential parallel feeding network was utilized to achieve wide impedance bandwidth of 29% while maintaining a high radiation efficiency of 90%. The DRA offers a CP bandwidth improvement of more than 160% compared to reported counterparts that operate at the same frequency range. In addition, exciting a higher-order resonance mode provided a notably higher gain over a frequency range of 26-31 GHz. The SAR was investigated and it was demonstrated that the proposed array meets the required safety limits when placed at a distance of 5 mm from the human body tissue. The proposed antenna array was fabricated and measured with a gain of 13.7 dBic, which represents an enhancement of 5 dBi above that of a single DRA. The impact of human-body proximity was investigated and found to be negligible due to the presence of the ground plane. The results of simulations and measurements are in close agreement. The proposed antenna outperforms mmWave DRA arrays reported earlier in the literature in terms of gain and CP bandwidth and offers a promising potential for mmWave off-body communications.

Chapter 4

A Multi-Band Millimeter-Wave Rectangular Dielectric Resonator Antenna with Omnidirectional Radiation Using a Planar-Feed.

4.1 Introduction.

Throughout the previous chapters, the design and implementation of off-body antennas, which utilize a broadside radiation patterns, have been discussed intensively. However, it is equally imperative to explore the significance of on-body communications and introduce the concept of the omnidirectional radiation pattern, which plays a crucial role in on-body applications [152]. Unlike the broadside pattern, the omnidirectional radiation pattern radiates energy uniformly in all directions [153]. This point is of paramount importance in on-body applications as it ensures that the wireless signals are propagated over a 360-degree range around the body.

However, multi-band technology enables the adaptation to different communication needs and environments, while the specific radiation patterns address the challenges posed by the human body's proximity and the variability of device orientations. With the integration of dual-band technology, on-body, and off-body communication systems can unlock their full potential, paving the way for seamless wireless connectivity and empowering a wide range of applications across healthcare, sports, entertainment, and beyond. It should be noted that all the reported multi-band DRA designs radiate either broadside or omnidirectional patterns in both bands. As a result, the proposed DRA can be employed simultaneously for off-body and

on-body applications, for example, by utilizing the broadside and omnidirectional patterns, respectively.

This Chapter is organized as follows; first the proposed DRA configuration; the excitable DRA modes are then studied at a frequency range of 20- 30 GHz. This is followed by the design of the planar feed network and analysis of the performance of on-body mmWave DRA. Finally, the measured results are presented that agree closely with the CST simulations. All the simulations have been implemented using CST microwave studio.

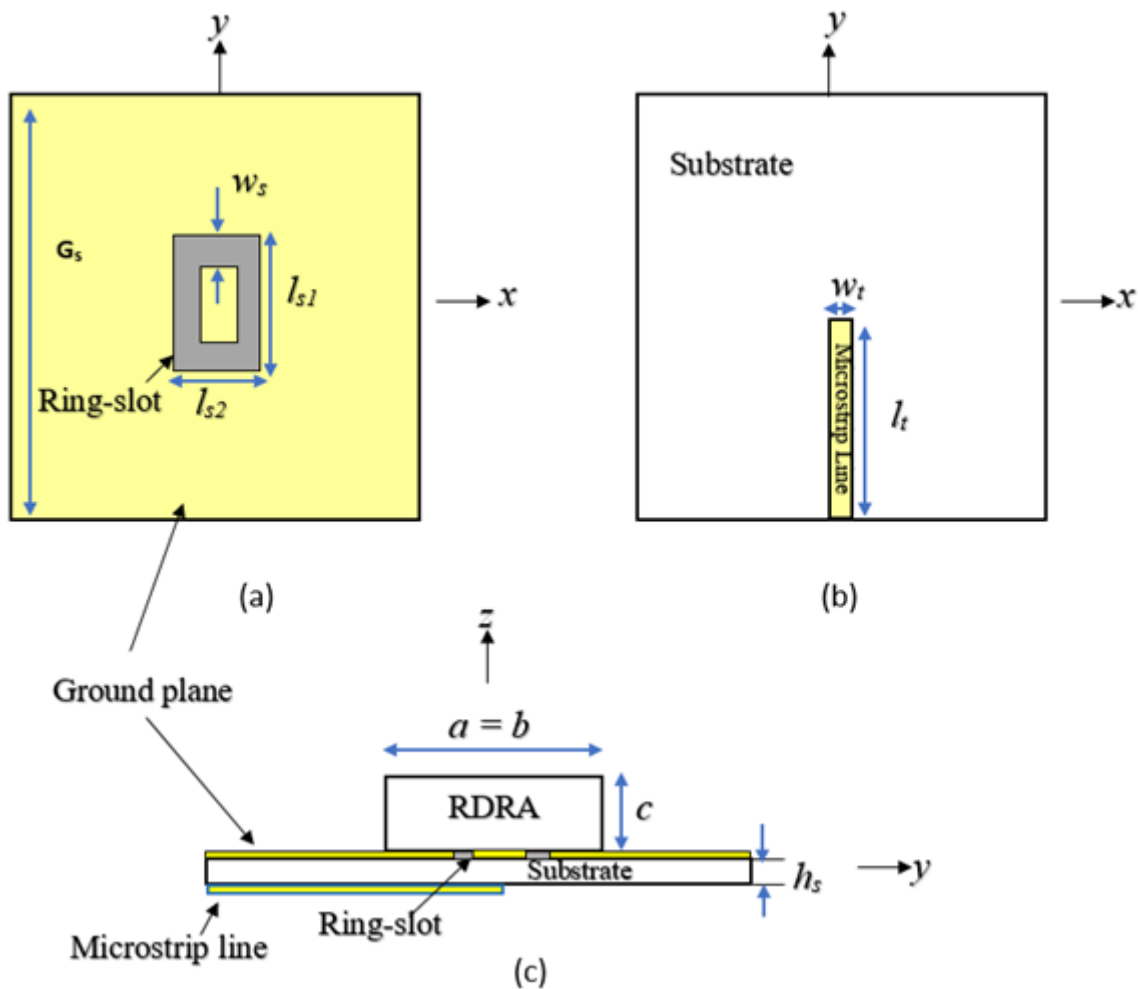


Figure 4-1. The proposed omnidirectional DRA; (a) Ground plane with an etched ring-slot, (b) Bottom view, (c) Side view

4.2 Antenna Configuration

The DRA has been designed using a square cross section to facilitate the excitation of the required degenerate modes for omnidirectional radiation. In addition, the DRA's material has been chosen as Alumina with a dielectric constant of $\epsilon_d = 9.9$ and a loss tangent of $\tan\delta = 0.0001$.

Figure 4-1 illustrates the utilized configuration in which the DRA is placed on a square ground plane with a size of $G_s = 12.5$ mm. The feed network also involves a square Rogers substrate, Ro4003, that is located at the lower side of the ground plane. The substrate has thickness of $h_s = 0.308$ mm, dielectric constant of $\epsilon_r = 3.5$ and loss tangent of 0.0027. Additionally, a 50Ω microstrip feedline has been printed on the substrate's lower surface with respective length and width of $l_t = 6.25$ mm and $w_t = 0.3$ mm.

It is well known that an electrically small vertical monopole and a ring-slot, which is etched in a metal ground plane, represent the duals of a planar loop antenna with equivalent size. Therefore, the small ring-slot provides the same fields as an electrically short vertical probe and can be used instead to create the required planar feeding network as can be observed from Figure 4-1. However, the ring-slot size may be increased depending on the field distribution of the required DRA mode. It should be noted that both square and rectangular ring-slot apertures have been investigated in this study. Furthermore, the utilized ring-slot consists of x - and y -directed slot arms with side lengths of l_{s1} and l_{s2} . These slots behave as magnetic currents that excite the required magnetic fields inside the DRA. Since the ring-slot is positioned at the interface between the Alumina DRA and the Rogers substrate, the circumference needs to be calculated in terms of the effective wavelength $\lambda_{eff} = \lambda_0 / \sqrt{\epsilon_{eff}}$, where λ_0 is the free space wavelength and ϵ_{eff} is defined as [154].

$$\epsilon_{eff} = \frac{\epsilon_d \epsilon_r (h + h_s)}{(\epsilon_d h + \epsilon_r h_s)} \quad (4.1)$$

4.3 Supported Modes of the Proposed DRA

Based on the dielectric waveguide model (DWM) [135], the DRA dimensions were chosen to support the required degenerate modes for omnidirectional radiation at ~28.5 GHz when the DRA is located above a metal ground plane. Therefore, the DRA's length, width, and height have been determined as $a = b = 3.8$ mm and $h = 1.7$ mm, respectively. These dimensions offer a compact DRA size that allows easy integration into various applications. The resonance frequencies of the TE_{mns}^y modes can be determined using the DWM as [135]:

$$k_x a = m\pi - 2 \tan^{-1}(k_x / (\varepsilon_d k_{x0}))$$

$$k_{x0} = [(\varepsilon_d - 1)k_0^2 - k_x^2]^{\frac{1}{2}} \quad (4.2)$$

$$k_y b = n\pi - 2 \tan^{-1}(k_y / k_{y0})$$

$$k_{y0} = [(\varepsilon_d - 1)k_0^2 - k_y^2]^{\frac{1}{2}} \quad (4.3)$$

$$2k_z h = m\pi - 2 \tan^{-1}(k_z / (\varepsilon_d k_{z0}))$$

$$k_{z0} = [(\varepsilon_d - 1)k_0^2 - k_z^2]^{\frac{1}{2}} \quad (4.5)$$

$$k_x^2 + k_y^2 + k_z^2 = \varepsilon_d k_0^2 \quad (4.6)$$

where k_0 is the free space wave number. Owing to the square cross section of the DRA, the resonance frequencies of the TE_{mns}^x and TE_{nms}^y modes are equal. Therefore, the required TE_{121}^x and TE_{211}^y higher order modes can be excited at the same frequency. This results in a total magnetic field distribution that is similar to that of the HEM_{218} mode of a cylindrical DRA that generates an omnidirectional pattern. Table 4-1 summarizes the supported resonance modes for the chosen DRA dimensions over a frequency range of 15-30 GHz based on the DWM.

Table 4-1. Resonance frequencies of the supported TE modes by the proposed DRA.

Frequency (GHz)	Resonance Mode
17.5	TE ₁₁₁
28.5	TE ₁₂₁ ^x , TE ₂₁₁ ^y

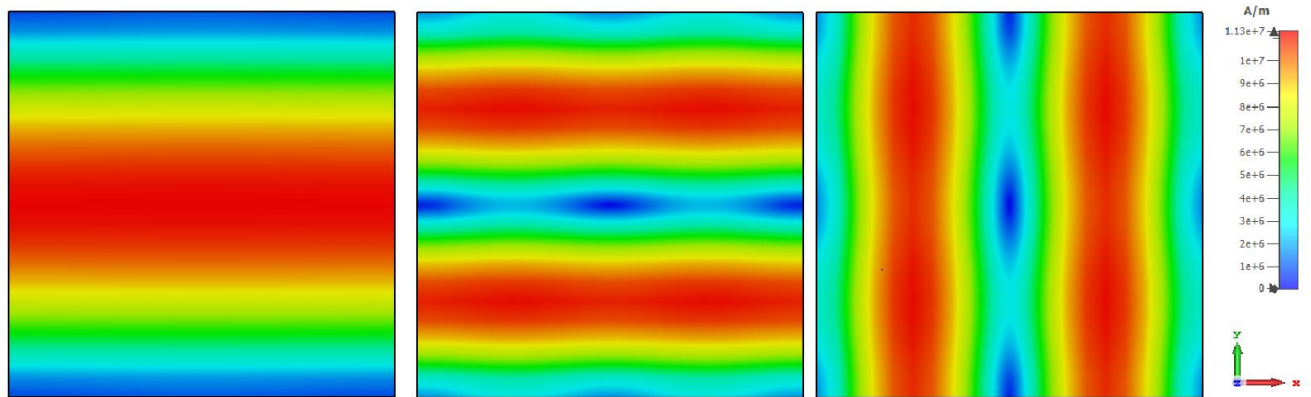


Figure 4-2. Magnetic field distributions inside the proposed isolated DRA at $z=0$ when $a = b = 3.8$ mm and $h = 1.7$ mm; (a) TE₁₁₁ mode at 17.5GHz, (b) TE₁₂₁^x mode at 28.5GHz, (c) TE₂₁₁^y mode at 28.5GHz.

The magnetic field distributions of the supported resonance modes inside an isolated DRA are illustrated in Figure 4-2. From the TE₁₂₁^x mode's magnetic field distribution, it can be observed that the H-field is null when $y = 0$. Therefore, the utilization of a centrally located x -directed slot aperture will suppress this mode. Hence, the slot needs to be shifted along the y -axis to a strong H-field point to excite this mode effectively. Similarly, for the TE₂₁₁^y mode, in which the H-field is null at $x = 0$, an off-set y -directed slot is needed at a strong H-field point for effective mode's excitation. However, for omnidirectional radiation, the degenerate modes need to be excited simultaneously. Therefore, a ring-slot aperture is utilized, which involves y and x -directed slot arms that act as magnetic current components exciting the aforementioned modes. Furthermore, the chosen DRA dimensions also support the fundamental broadside TE₁₁₁ mode at 17.5 GHz and hence it would be beneficial if the same ring-slot aperture excites the fundamental TE₁₁₁ mode as well as the TE₂₁₁^y and TE₁₂₁^x modes. As mentioned earlier, the interaction between these degenerate modes can result in a field distribution that is similar to

the cylindrical $\text{HEM}_{21\delta}$ mode [22]. For a rectangular DRA such mode is defined as a quasi- $\text{HEM}_{21\delta}$ mode, which offers the required omnidirectional radiation pattern.

4.4 Design of the Slot Aperture Feed

4.4.1 Square Ring-slot Feed

For simplicity, the special case of a square ring-slot is considered first by setting $l_{s1}=l_{s2}$. It is important to ensure that the first slot's resonances, which has a broadside radiation, is achieved at a frequency that is different from that of the TE_{211}^y and TE_{121}^x DRA modes to avoid any interference between the different radiation patterns. Subsequently, the separated slot resonance can be suppressed, or utilized as another operating frequency band, depending on the design requirements. The return losses are illustrated in Figure 4-3, where it can be noted that when $l_{s1} = l_{s2} = 2.1\text{mm}$, and $w_s = 0.5\text{ mm}$, the slot resonates at 27.7 GHz, when the slot circumference is $\sim 1.1\lambda_{\text{eff}}$, which is too close to that of the degenerate modes. This is also combined with a broadside radiation pattern instead of the expected DRA's omnidirectional pattern, which has not been observed initially at the expected frequency. Hence, the size of the slot has been adjusted to avoid the coexistence of the DRA and ring-slot resonances at the same frequency. As demonstrated in Figure 4-3, by increasing the slot size, the DRA modes and slot's resonance frequencies can be separated as the latter is achieved at 24 GHz when $l_{s1} = l_{s2} = 2.5\text{ mm}$. Hence, the required omnidirectional and fundamental DRA modes are effectively excited at $\sim 27.7\text{ GHz}$ and 16 GHz, respectively, using the same square ring-slot. In addition, the increased slot's size means the slot arms positions could have moved closer to stronger H-field points of the corresponding DRA's mode, which results in effective excitation of the required modes.

The excited degenerate modes provide an overall impedance bandwidth of 1.3%. Moreover, the TE_{111} broadside mode has been excited with a bandwidth of 3%. Besides, the

resonance of the ring-slot has been achieved with a bandwidth of 7.4%. It should be noted that the DRA modes are excited at resonance frequencies that are close to those listed in Table 4-1. Figure 4-4 presents the simulated magnetic field distribution inside the loaded DRA at 27.7 GHz, which is similar to that of the cylindrical $HEM_{21\delta}$ mode, and hence an omnidirectional radiation pattern has been achieved using the rectangular DRA.

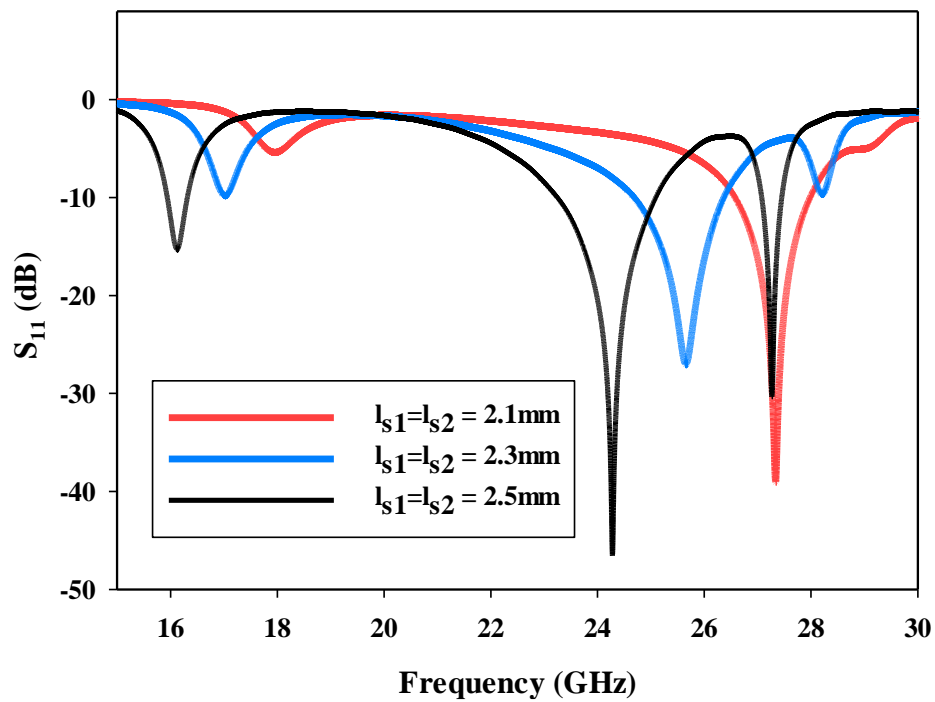


Figure 4-3. Return losses of the DRA using different sizes of the square-ring feeding slot.

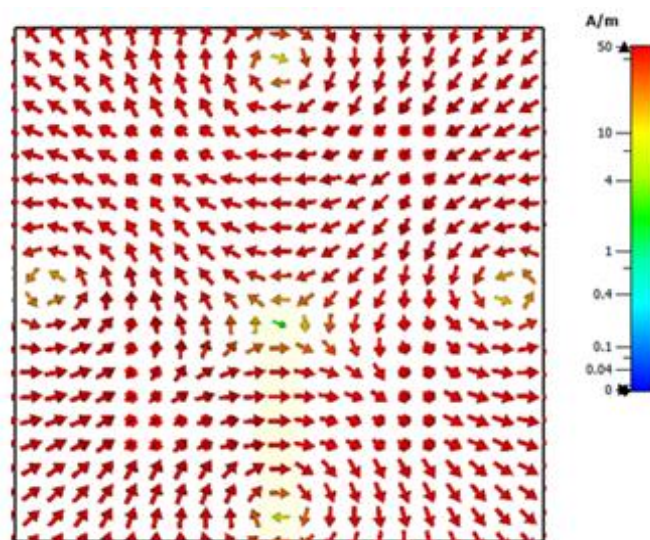


Figure 4-4. The xy plane view of the quasi $HEM_{21\delta}$ internal magnetic field distribution of a square ring-slot fed DRA at 27.7GHz.

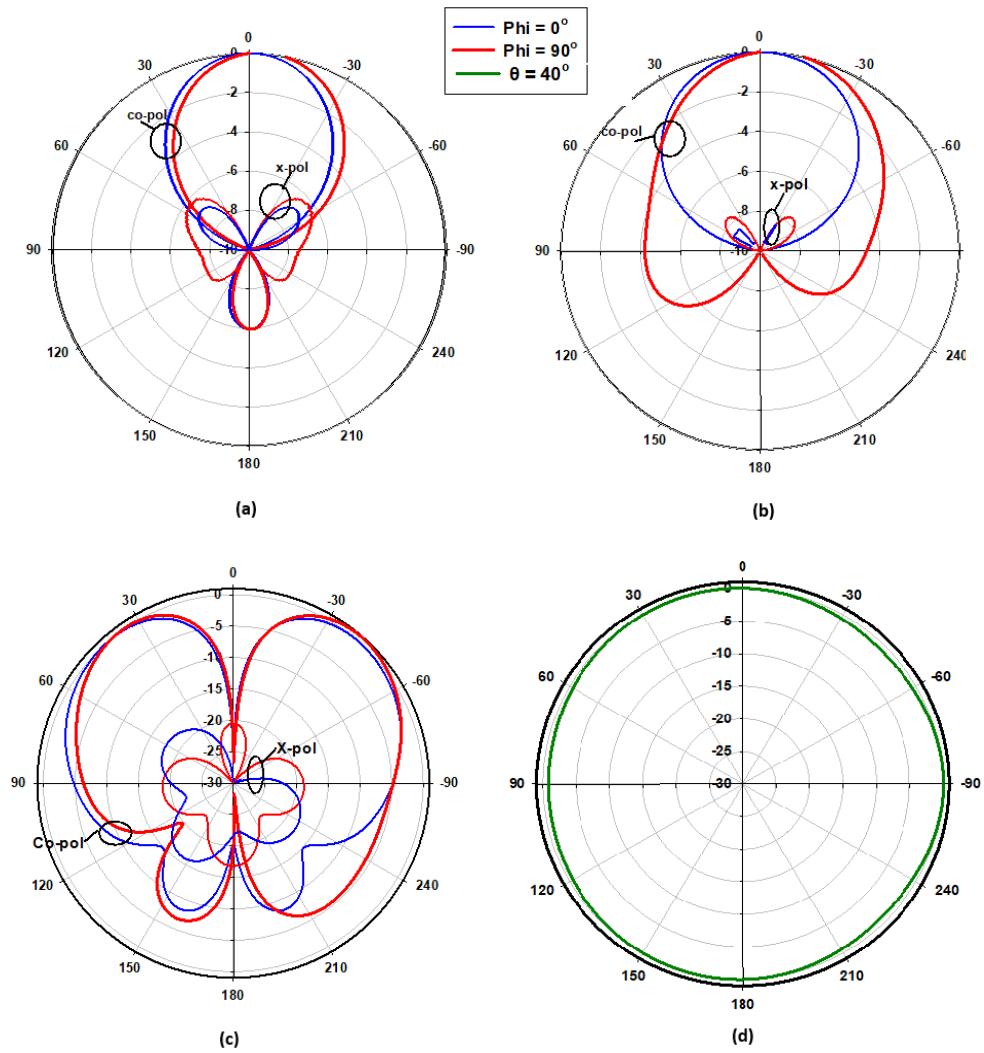


Figure 4-5. The radiation patterns of square ring-slot fed DRA with arm lengths of $l_1=l_2=2.5\text{mm}$, (a) 16 GHz, (b) 24 GHz (c) and (d) 27.7 GHz.

Figure 4-5 presents the achieved radiation patterns at the three resonance frequencies, where broadside radiation patterns have been achieved at 16 GHz and 24 GHz due to the excitation of the fundamental DRA mode, TE_{111} , and the ring-slot's resonance, respectively. As mentioned earlier, the quasi- HEM_{218} mode has been excited at 27.7 GHz when the size of the feeding square ring-slot is increased to 2.5 mm. As demonstrated in Figure 4-5 (c), an omnidirectional radiation has been attained with a maximum gain of 4.1 dBi at $\theta=40^\circ$. However, a slight asymmetry can be noted in the $\phi=90^\circ$ plane cut, which can be attributed to the asymmetrical feed point position compared to the traditionally used central coaxial probe that naturally enforces the fields' symmetry. Figure 4-5 (d) presents the azimuthal pattern at the $\theta=40^\circ$

plane, where it can be noted that an omnidirectional pattern has been achieved with a modest out-of-roundness. Therefore, a triple band operation has been attained with two different types of radiation patterns using a planar feed network. The variation of the omnidirectional gain at the $\theta = 40^\circ$ plane has been investigated as illustrated in Figure 4-6, where it can be noted that a maximum variation of ~ 1.5 dB exists, which results in a pattern that is not perfectly omnidirectional. This can be explained in terms of the limitations imposed by the centrally located square ring-slot since changing the slot's size is associated with a proportional shift in the position of each slot arm. This may result in having slot arms positioned at points with slightly different H-field strengths. It should be noted that this variation is slightly higher than that of 1.26 dB for an omnidirectional cylindrical DRA with a planar feed network [20].

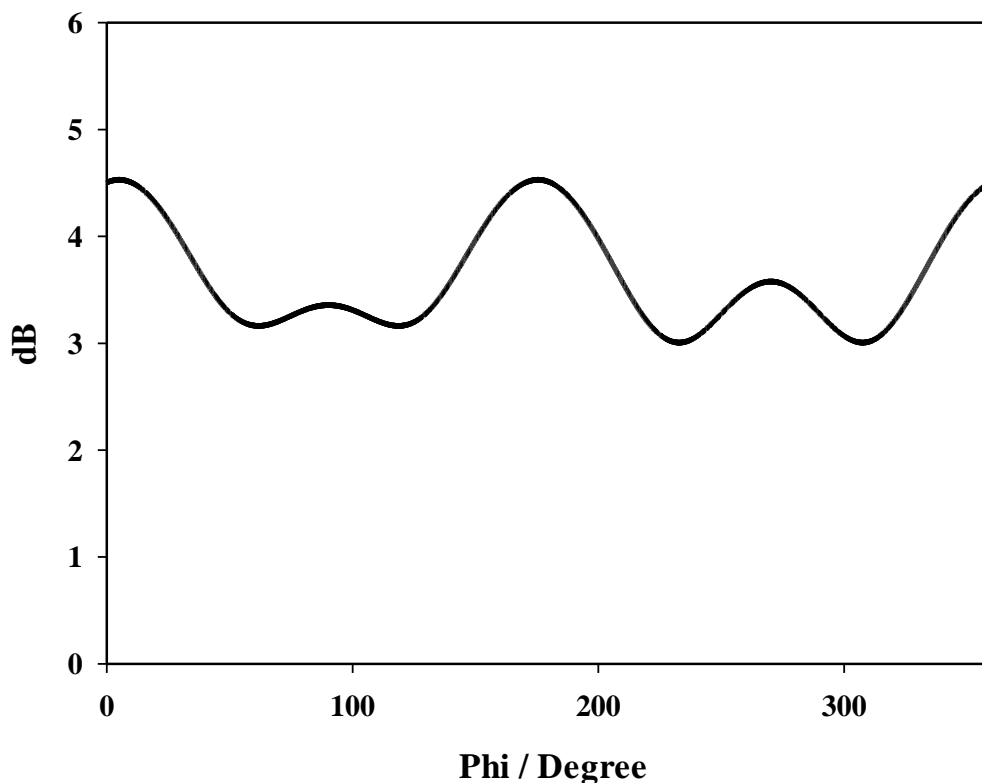


Figure 4-6. The omnidirectional gain variation at the $\theta=40^\circ$ azimuth plane when a square ring feeding slot is utilized.

An attempt to minimize the omnidirectional gain's variation is introduced in the next section. Figure 4-7 illustrates the realized gain at the main beam directions for the three bands.

For the two broadside patterns, it can be observed that realized gains of 6.5 dBi and 4.8 dBi are achieved at 16 GHz and 24 GHz, respectively. On the other hand, an omnidirectional gain of 4.1 dBi is achieved at 27.7 GHz at the main lobe direction of $\theta=40^\circ$. The simulated radiation efficiency is also illustrated in Figure 4-7, where it is evident that a high radiation efficiency of $\sim 90\%$ is achieved at all the operating frequency bands.

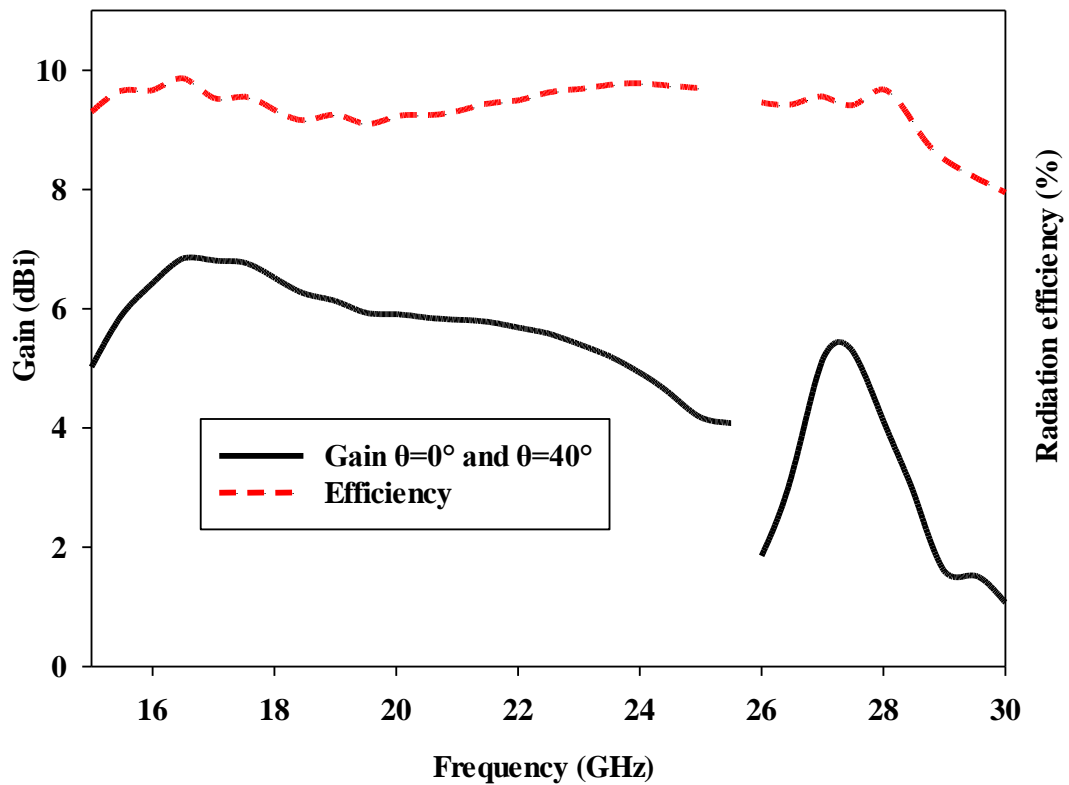


Figure 4-7. Realized gain and radiation efficiency of the square ring-slot fed DRA.

4.4.2 Rectangular Ring-slot Feed

To minimize the azimuthal gain variations at $\theta = 40^\circ$, a rectangular ring-slot aperture is considered as it offers the flexibility of changing the size of only one pair of the ring-slot arms at a time. The return losses are illustrated in Figure 4-8 when the longest slot arm's length, l_{s1} , varies from 2.7 to 3.2 while $l_{s2} = 2$ mm. It should be noted these dimensions' result in a slot circumference of $\sim 1.1\lambda_{\text{eff}}$ at 23 GHz. The results demonstrate that the proposed antenna

configuration exhibits three operating frequency bands at 17.5 GHz, 23 GHz, and 28.5 GHz for the TE₁₁₁ DRA mode, slot resonance, and quasi-HEM_{21δ} mode, respectively, when $l_{s1} = 2.7$ mm. The achieved respective bandwidths for the three resonance modes are 17.3 GHz to 17.9 GHz, 22.1 GHz to 24 GHz, and 28.3 GHz to 28.8 GHz, which correspond to percentage bandwidths of 3.4%, 7.7%, and 1.9%. It can be noted that these bandwidths are wider than those achieved when a square ring-slot is utilized to excite the same DRA modes, which demonstrates the effectiveness of the rectangular ring-slot. It can also be observed from these results that the strongest impact of varying l_{s1} is on the slot's resonance frequency, which is expected owing to the change in the circumference of the rectangular ring-slot. On the contrary, smaller variations can be noted in the resonance frequencies of the excited DRA modes as mainly depend on the DRA dimensions and permittivity.

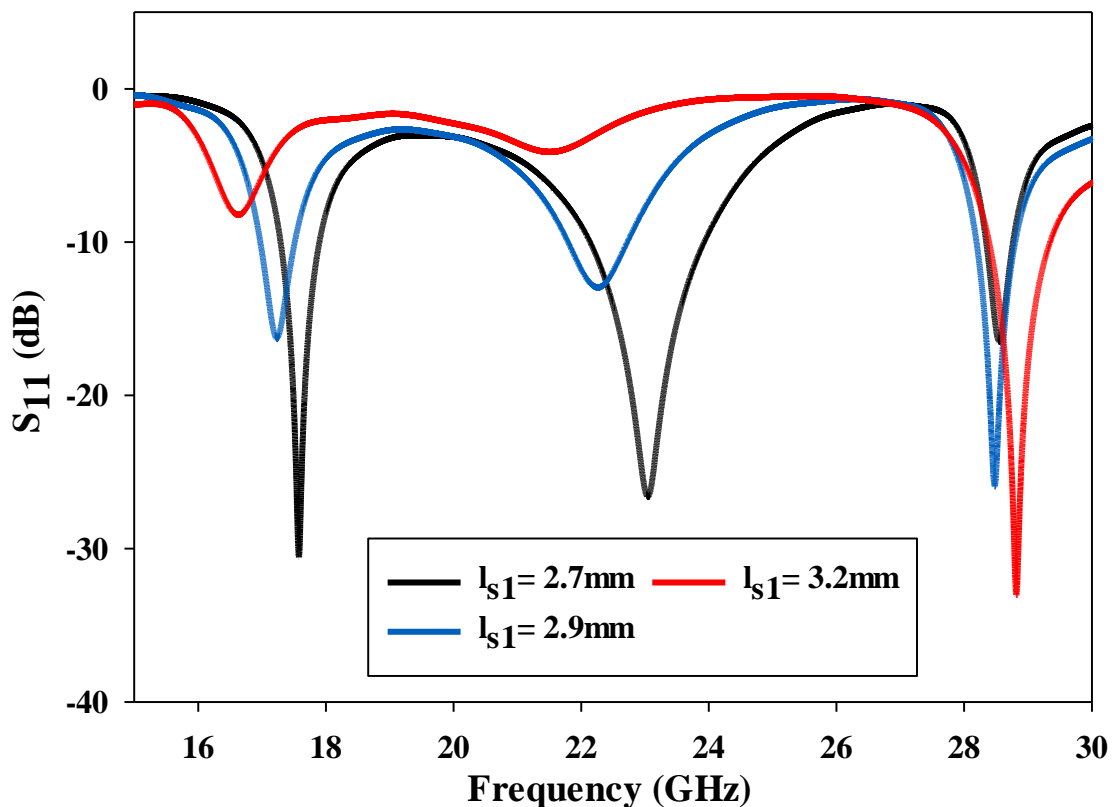


Figure 4-8. Simulated return losses of the rectangular ring-slot DRA when the longest slot arm's length, l_{s1} , is varied while $l_{s2} = 2$ mm.

The simultaneous excitation of the degenerate modes has been investigated by using y -directed arm slot only with a length of l_{s1} and an offset of $0.5l_{s2}$ from the x -axis, which has excited the TE_{211} resonance mode at 30 GHz. Similarly, the TE_{121} resonance mode has been individually excited at 30 GHz when an x -directed slot with a length of l_{s2} and an offset of $0.5l_{s1}$ from the y -axis. However, when the x and y -directed linear slots are combined to create the rectangular ring-slot, the resonance is achieved at a slightly lower frequency of 28.5 GHz with an overall field distribution that is similar to that of the cylindrical $HEM_{21\delta}$ mode as demonstrated in Figure 4-9. The 3D radiation patterns for the three operating frequency bands are illustrated in Figure 4-10, where it can be noted that an omnidirectional pattern has been achieved at 28.5 GHz with a maximum gain of 4.3 dBi

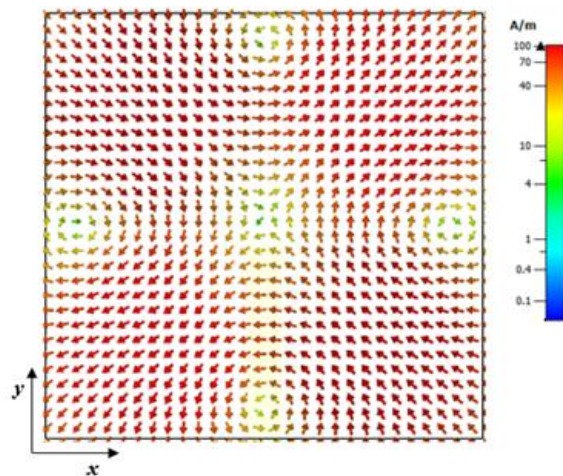


Figure 4-9. The xy plane view of the internal magnetic field distribution inside the rectangular ring-slot fed DRA, which corresponds to the quasi $HEM_{21\delta}$ at 28.5 GHz.

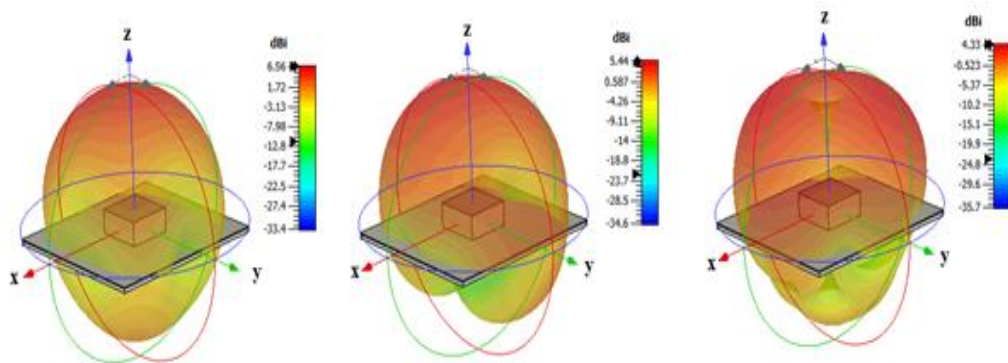
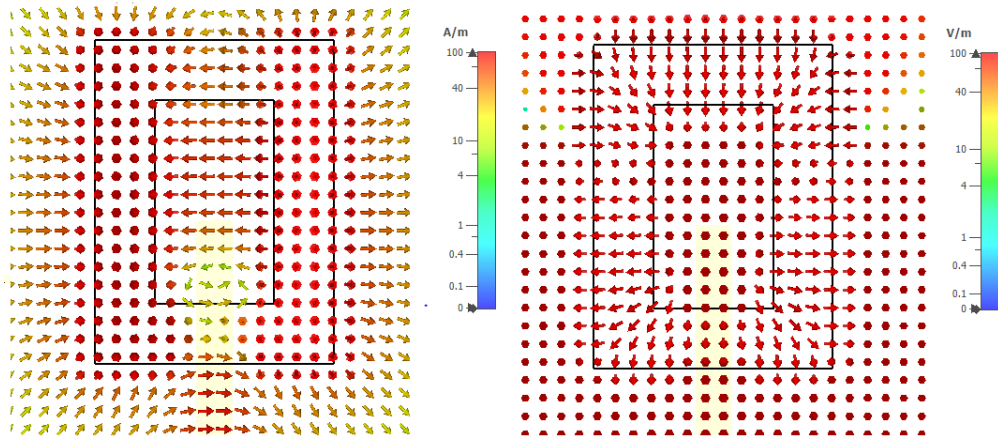


Figure 4-10. 3D radiation patterns at the three operating frequency bands; (a) 17.5 GHz, (b) 23 GHz, (c) 28.5 GHz.

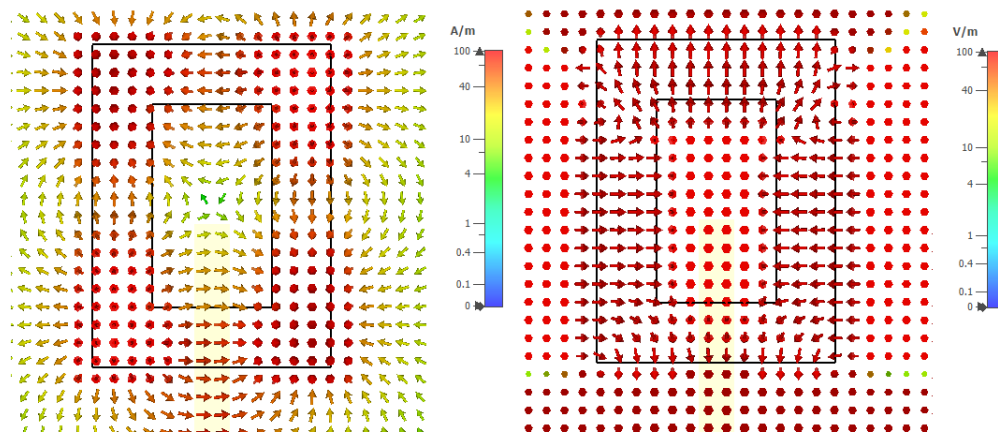
In addition, the electric and magnetic field distributions on the rectangular ring-slot are illustrated in Figures 4-11 and 4-12 at 17.5 GHz and 28.5 GHz, respectively.



(a) H-field

(b) E-field

Figure 4-11. The xy plane view of the electric and magnetic field distributions on the rectangular ring-slot feed structure at 17.5 GHz



(a) H-field

(b) E-field

Figure 4-12 The xy plane view of the magnetic and electric field distributions on the rectangular ring-slot feed at 28.5 GHz.

4.4.3 The Ground Plane Size and the Dielectric Constants

Figure 4-13 presents the variation of the return losses as a function of the ground plane size, where it can be observed that the slot's resonance is strongly dependent on the ground plane size [155]. As a result, there is also an impact on the excited DRA modes and the achieved resonance frequencies due to the variation in the performance of the feeding slot.

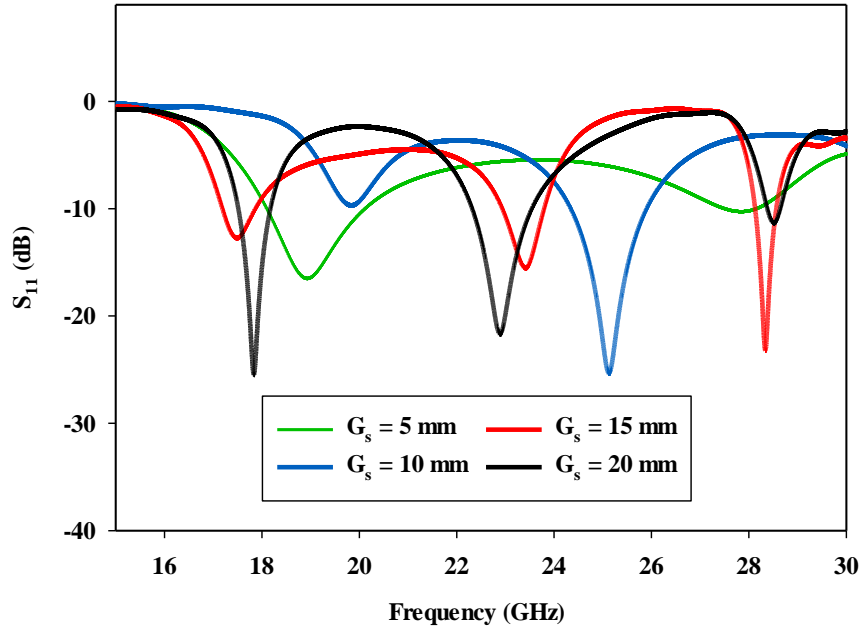


Figure 4-13. The variation of return losses as a function of the ground plane size.

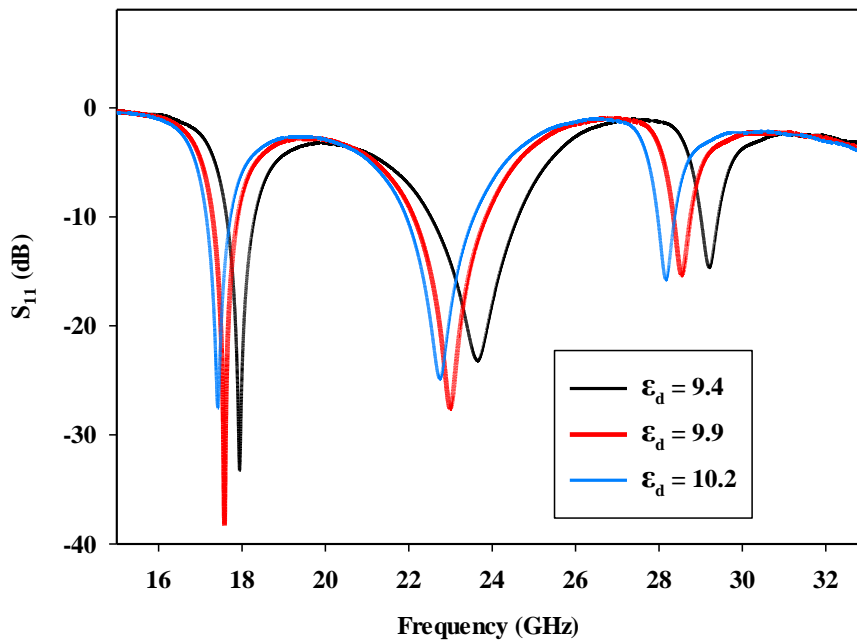


Figure 4-14. The variation of the return losses as a function of the dielectric constant of the DRA

As a result, there is also an impact on the excited DRA and the achieved resonance frequencies due to the variation in the performance of the feeding slot. Another key parameter that has been investigated is the sensitivity of the DRA performance to a range of Alumina's dielectric constants that have been used in the literature. The results of these investigations are

presented in Figure 4-14, which demonstrates a stable DRA performance when ϵ_d is varied from 9.4 to 10.2.

4.4.4 DRA Performance Next to a Human Body

The mmWave omnidirectional antennas are widely used for on-body applications. Therefore, it is important that the antenna's performance is assessed when the proposed antenna is placed next to the human body as illustrated in Figure 4-15, practical tests were conducted on three common body areas: the arm, chest, and stomach [35] where a three-layer phantom is utilized. The utilized parameters for the different tissue layers are illustrated in Table 4-2. The thickness of the three different body parts is according to [156].

Table 4-2. Human-body-tissue parameters at 28 GHz [157].

Tissue	Skin	Fat	Muscle
Relative Permittivity	16.55	6.09	25.43
Loss Tangent	0.2818	0.1454	0.242
Density (kg/m ³)	1109	911	1090

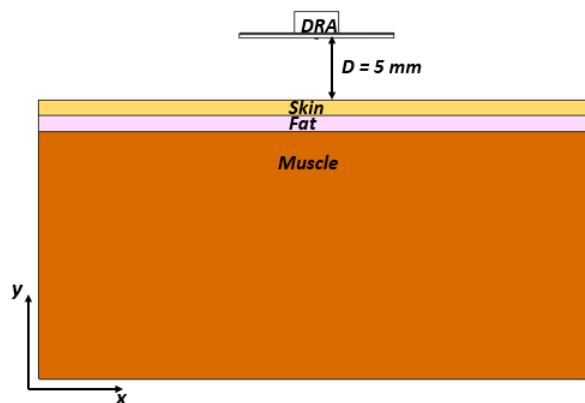


Figure 4-15. The proposed rectangular DRA in the proximity of a human body phantom (Chest).

The return losses of arm, chest, and stomach are presented in Figure 4-16, where it can be noted that the presence of the ground plane has minimized the impact of the human body on the resonance frequencies.

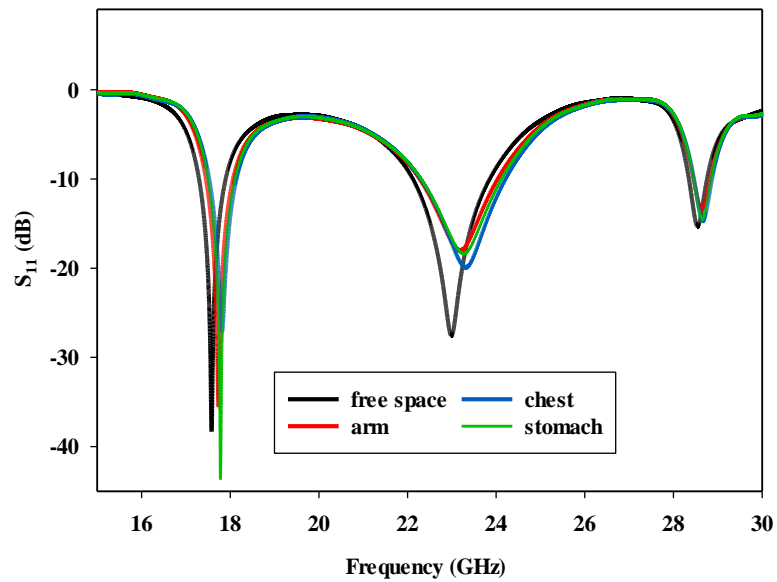


Figure 4-16. The variations in return losses when the antenna was placed on the arm, chest, and stomach

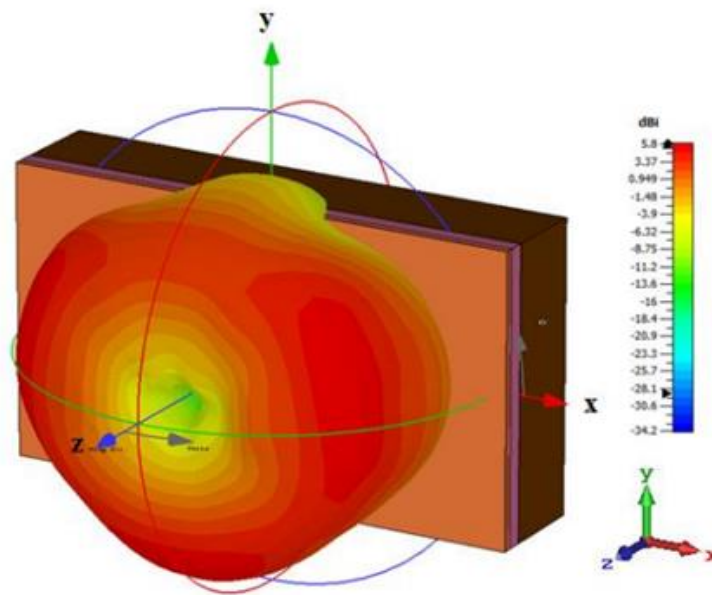


Figure 4-17. The 3D omnidirectional radiation pattern next to the equivalent tissue at 28.5 GHz when $d = 5$ mm.

In addition, the omnidirectional pattern is preserved at the presence human tissue as demonstrated in Figure 4-17, when $d = 5$ mm, which also can be attributed to the presence of the ground plane. However, reflections from the utilized phantom have reduced the back lobes

considerably and hence increased the omnidirectional realized gain from 4.33 dBi in free space to 5.8 dBi in the proximity of the human body tissue. On the hand the presence of the phantom has reduced the radiation efficiency from 95% to 84%. However, this did not impact the gain as the increased directivity has compensated for any loss due to the slightly reduced radiation efficiency.

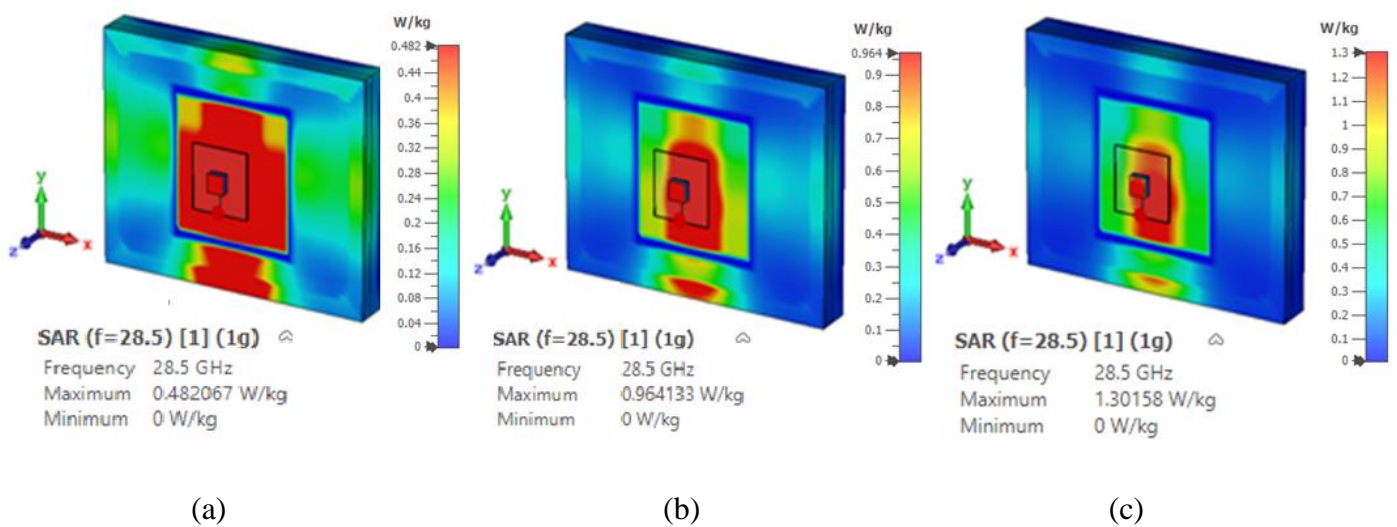


Figure 4-18. The SAR of the proposed DRA with various input power levels for a 1g tissue; (a) 15 dBm, (b) 18 dBm, and (c) 20 dBm.

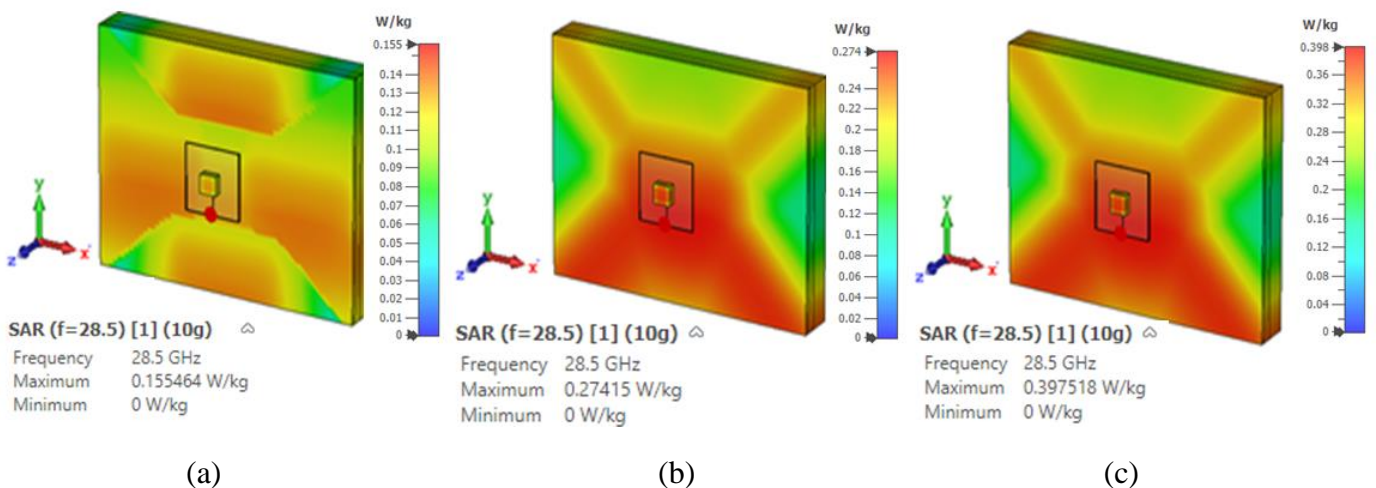


Figure 4-19. The SAR of the proposed DRA with various input power levels for a 10g tissue; (a) 15 dBm, (b) 18 dBm, and (c) 20 dBm.

The Specific Absorption Rate (SAR) indicates the safety threshold at which radio-frequency energy can be absorbed by human body tissue [41]. The SAR must be assessed to

ensure compliance with safety limits set by the Federal Communications Commission (FCC) and the International Commission for Non-Ionizing Radiation Protection (ICNIRP) standards. These standards define SAR thresholds of 1.6 and 2 W/kg for 1g and 10g tissues, respectively [41]. Unfortunately, the above guidelines do not offer dosimetric information or suggestions for mmWave frequencies [41, 42]. However, at 28 GHz, a 5 mm spacing is recommended between the antenna and the human body with input power levels of 15 dBm, 18 dBm, or 20 dBm at 28 GHz [42]. Subsequently, the proposed omnidirectional DRA has been simulated next to a layered phantom as demonstrated in Figure 4-15. The conducted SAR simulations has confirmed that the radiation from the proposed antenna meets the safety requirements as illustrated in Figures 4-18 and 4-19 for 1 g and 10 g tissues, respectively. It is worth noting that this SRA example is in the stomach scenario.

4.5 Measured Results

The Alumina DRA and planar feed network incorporating a rectangular ring-slot were fabricated by T-ceramics [128] and Wrekin [129], respectively. At the mmWave frequency range, a precise alignment between the DRA and the feeding slot poses significant challenges. To overcome these challenges, a solution involving mapping out the DRA position on the ground plane was implemented during the fabrication stage [59].

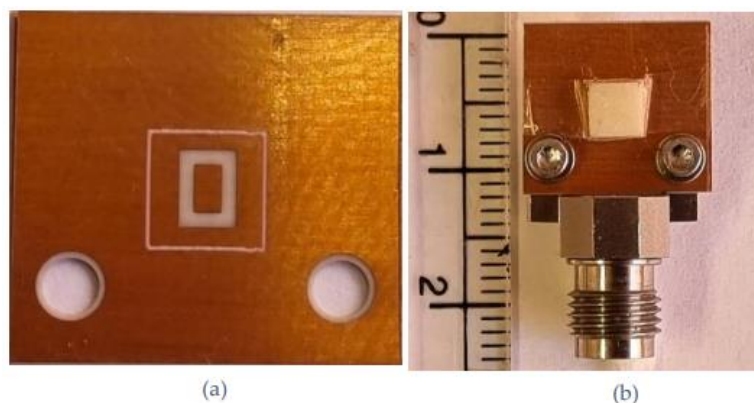


Figure 4-20. Prototype of the proposed antenna (a) Ground plane with a rectangular ring-slot and outlined DRA position, (b) Assembled prototype.

The resulting fabricated feed network, which includes the outlined DRA position, is presented in Figures 4-20 (a). Following the outlining of the DRA position, an ultra-thin double-sided adhesive copper tape with a thickness of 0.08mm was utilized to bond the antenna to the ground plane, ensuring secure assembly. The assembled DRA prototype is presented in Figure 4-20(b) including the utilized ELF50-002 SMA connector that has been attached using screws. In addition, the prototype was measured without experiencing any alignment or bonding issues. The implementation of this approach is critical in ensuring the mmWave measurements' accuracy, where even slight deviations can significantly affect the performance [80].

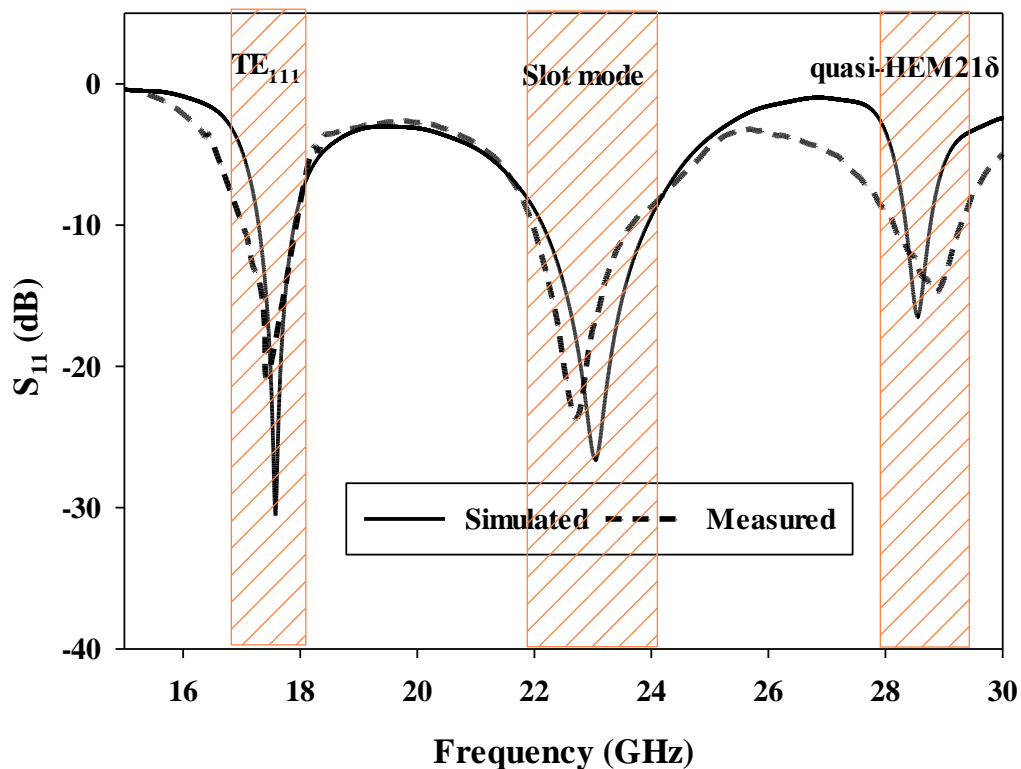


Figure 4-21. The measured and simulated return losses for the proposed DRA that is fed using a rectangular ring-slot.

As demonstrated in Figure 4-21, the measured and simulated return losses share almost the same resonance frequencies of 17.5 GHz, 23 GHz, and 28.5 GHz for the TE_{111} , ring-slot and quasi- $HEM_{21\delta}$ modes, respectively. In addition, the measured and simulated -10 dB impedance matching bandwidth of the lower band is 3.4%. In terms of middle band that corresponds to the

ring-slot resonance, the -10 dB impedance matching bandwidth is 1.8 GHz, demonstrating a good agreement between measured and simulated percentage impedance bandwidths of 7.7% and 7.5%, respectively. However, a slight discrepancy can be noted in the omnidirectional mode's simulated and measured bandwidths of 1.9% and 3%, respectively. This discrepancy can be attributed to measurement uncertainties, including measurement setup as well as fabrication and calibration errors. In addition, the utilization of bulky SMA and fittings could have contributed to the discrepancy between simulated and measured results. It should be noted that the achieved impedance bandwidth of the omnidirectional mode is narrower than that of a probe-fed omnidirectional rectangular DRA. For example, impedance bandwidths of 22% have been reported in [113] by merging the bandwidths of the DRA mode and that due to the feeding probe's resonance, which also offers an omnidirectional pattern. However, such hybrid operation is not possible in the proposed configuration since the feeding ring-slot has broadside radiation, i.e. different from that of the excited DRA mode. Therefore, a feeding ring slot with omnidirectional pattern needs to be utilized for bandwidth enhancement. Alternatively, a dielectric coat layer [108], or concentric rectangular ring-slots, can be utilized to achieve a wider bandwidth.

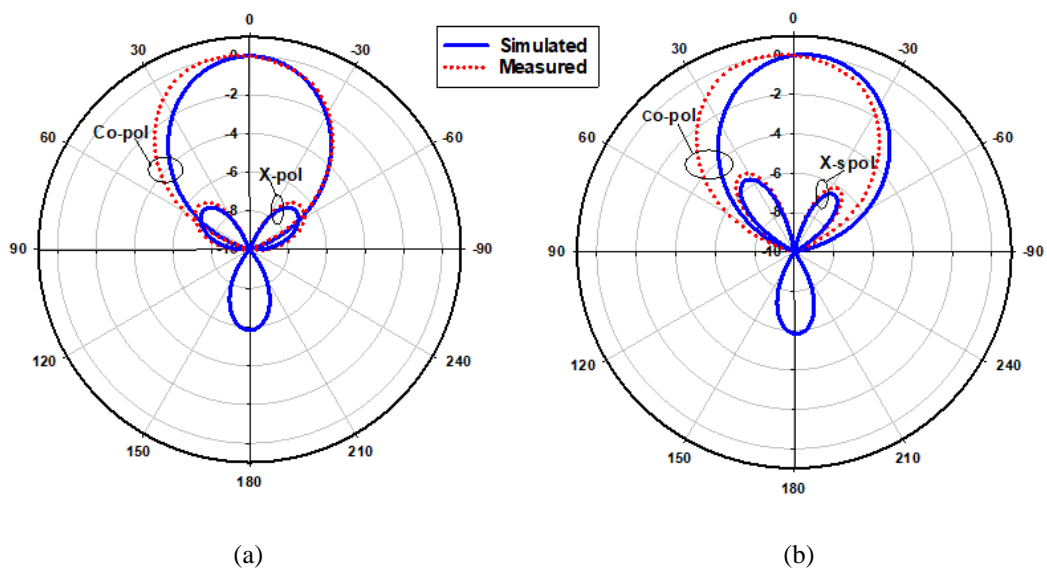


Figure 4-22. Normalized radiation patterns of the TE₁₁₁ mode at 17.5 GHz; (a) E-plane, (b) H-plane

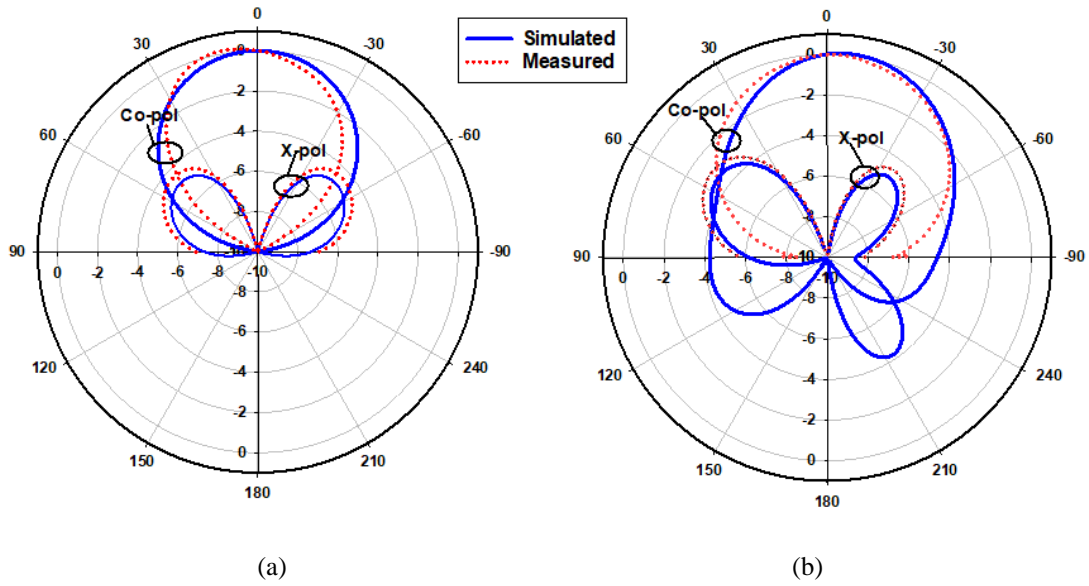


Figure 4-23. Normalized radiation patterns of the resonant slot at 23 GHz (a) E-plane, (b) H-plane

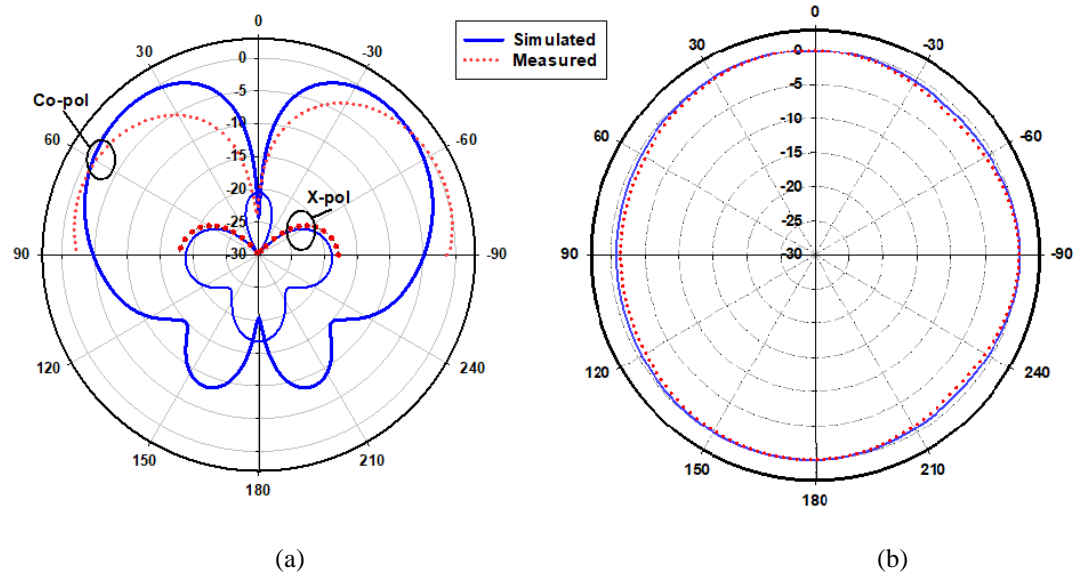


Figure 4-24. Normalized radiation patterns of the quasi-HEM_{21δ} mode at 28.5 GHz (a) $\phi=90^\circ$ plane, (b) $\theta=40^\circ$ plane.

Figure 4-22 presents the measured and simulated radiation patterns at 17.5 GHz, where the TE₁₁₁ broadside mode is excited. Close agreement can be observed between the simulated and measured broadside patterns. As mentioned earlier, the feeding slot's resonance is achieved at 23 GHz and the corresponding far field patterns are demonstrated in Figure 4-23 with reasonable agreement between measurements and simulations. For example, the respective measured beam widths are 88°, 108° in the E- and H- planes compared to 90° and 107° in the simulations. In addition, the simulated and measured omnidirectional radiation patterns are

presented in Figure 4-24 for both the elevation and azimuth planes at 28.5 GHz. The results demonstrate close agreement between simulated and measured radiation patterns, where an omnidirectional radiation pattern has been achieved with a main beam direction at $\theta=40^\circ$ as demonstrated in Figure 4-24 (a). The measured and simulated beamwidths of the omnidirectional patterns are 61.2° and 60.6° , respectively. However, a slight asymmetry can still be noted in the $\phi = 90^\circ$ plane cut of Figure 4-24 (a), owing to the asymmetrical feed point position. An improved roundness of the azimuthal plane pattern can be observed in Figure 4-24 (b), which suggests that the rectangular ring-slot arms are placed at equally strong magnetic field points, significant advancements in the design have effectively minimized the azimuthal plane gain variation, culminating in the establishment of a pattern that closely approximates omnidirectionality. This achievement denotes an enhanced uniformity in the antenna's radiation characteristics across the azimuthal plane, contributing to a more comprehensive and well-rounded coverage pattern. Furthermore, the co-polarized field component is considerably stronger than the cross-polarized component in all cases.

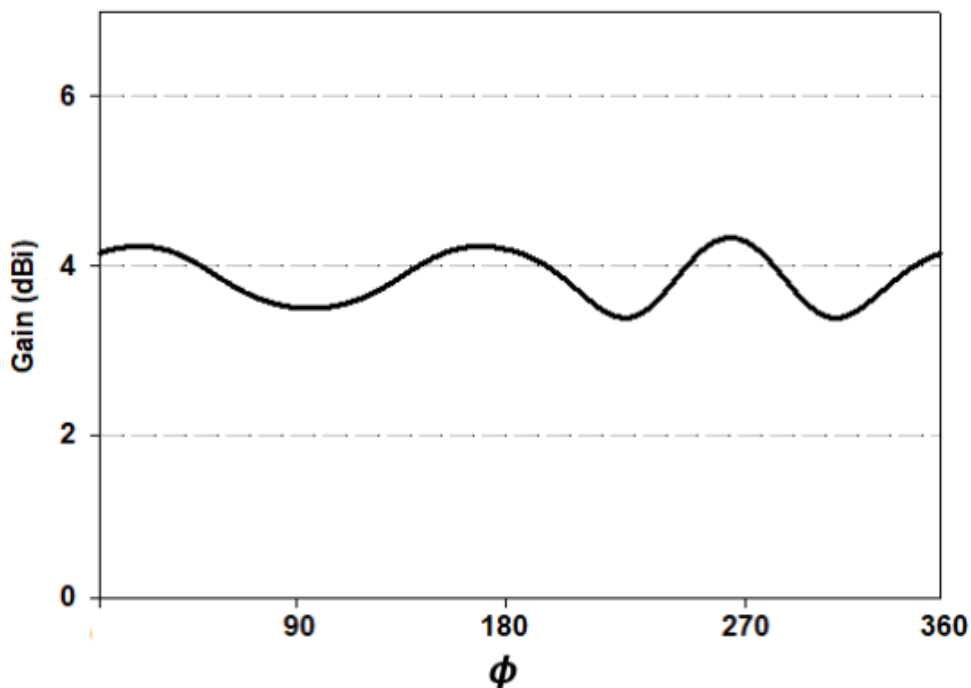


Figure 4-25. The azimuthal variation of the omnidirectional gain at the $\theta=40^\circ$ plane.

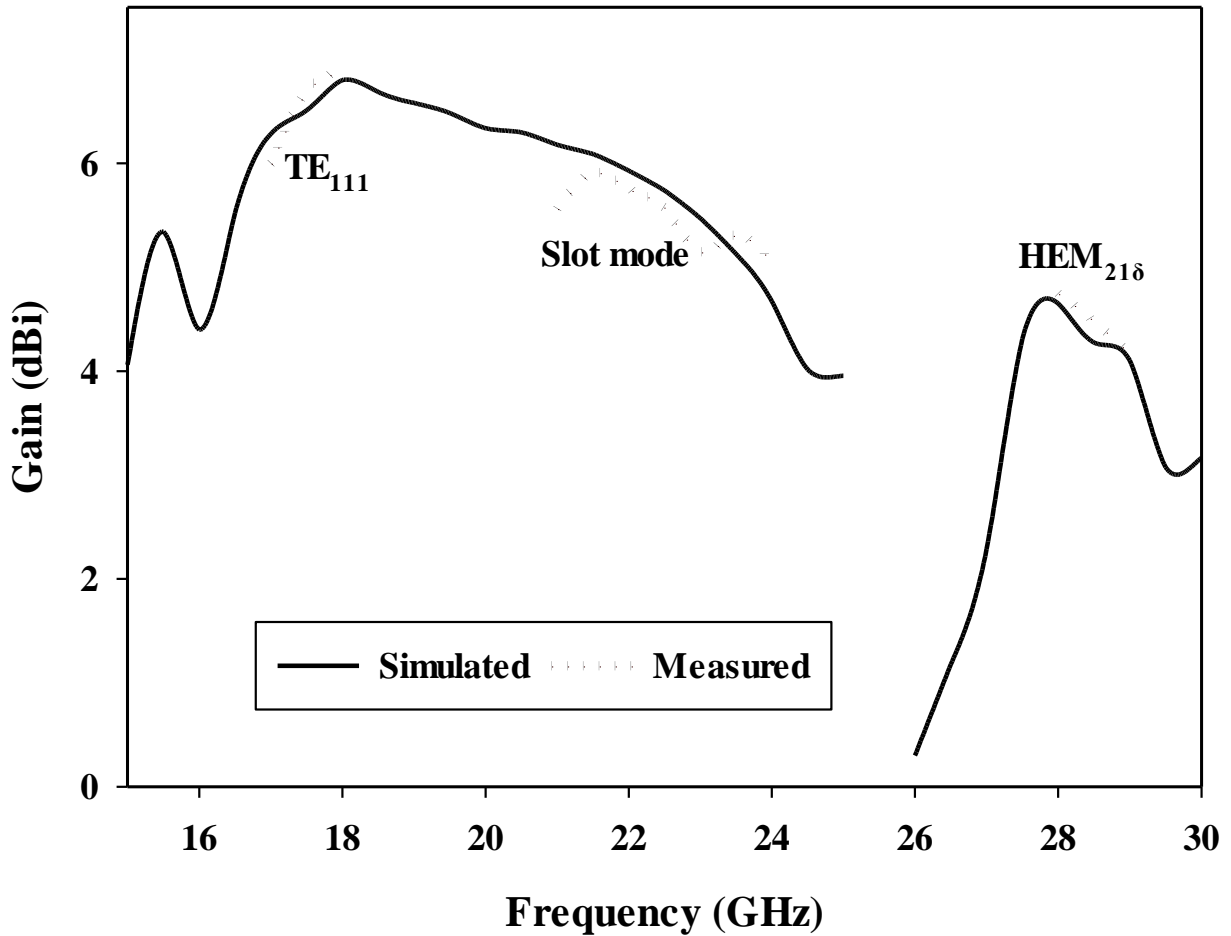


Figure 4-26. Measured and simulated gains at the main beam directions for the three resonance modes.

The azimuthal plane gain variation presented in Figure 4-25, where it is evident that the variation has been reduced considerably to ~ 0.85 dB, which results in a more stable omnidirectional pattern with close agreement between measurements and simulations. Additionally, the gain and radiation efficiency of the rectangular ring-slot fed DRA are illustrated in Figure 4-26, where it can be noted that the maximum achieved gains are 6.56 dBi, 5.2 dBi and 4.33 dBi for the TE₁₁₁ mode, ring-slot resonance and the quasi-HEM_{21δ} mode, respectively. Furthermore, a high radiation efficiency of $\sim 90\%$ has been attained in the three operating bands

Table 4-3. Comparison of the proposed on-body antenna's performance against cutting-edge mmWave counterparts

Ref	Antenna Type	Frequency GHz	Size (λ^3) ¹	S ₁₁ Bandwidth (%)	On-Body Gain dBi	On-Body η_{rad} (%)	3dB beam E-plane (degree)
[158]	Slotted patch	28, 38, 61	$1.04 \times 1.02 \times 0.052$	3, 1, 1.5	8.1, 8.3, 7	54, 60, 58	-
[47]	Yagi array	60	$3.2 \times 1.6 \times 0.04$	15	9	41	-
[37]	Patch-like	60	$2.8 \times 2.1 \times 0.23$	16.3	12	63	-
[159]	Textile	28	$1.89 \times 0.87 \times 0.147$	33	6.6	53.5	-
[160]	Q Slot	60	$2.58 \times 2.8 \times 0.32$	12	8	56.68	-
[161]	Patch-like	60	$1.6 \times 1.02 \times 0.23$	-	5.4	62.2	-
This work	RDRA	17.5, 23, 28.5	$1.19 \times 1.19 \times 0.16$	3.4, 7.7, 1.9	7.3, 6.8, 5.8	90, 87, 84	75,90,60,6

¹For [158] and this work, λ has been calculated at the highest mentioned frequency point.

A comparative analysis of the ring-slot-fed DRA performance with respect to the reported on-body mmWave antenna designs is presented in Table 4-3. As mentioned earlier, there is no reported study on the on-body mmWave DRA in the open literature; hence, a comparison was made with respect to different antenna types that are available in the literature. The comparison was conducted with respect to the size, bandwidth, gain, and radiation efficiency. It is evident from Table 4-3 that the electrical size of the proposed antenna was smaller than most of the reported designs, except that of [158]. In addition, the utilized simple geometry resulted in simple and low-cost fabrication. On the other hand, a triple-band operation was achieved, which was also the case in [158]. However, the individual bandwidths in the presented design were wider with higher gains compared to those in [158]. At the same time, the other antennas in Table 4-3 offer single-band operation, albeit with wider bandwidths. Furthermore, the proposed DRA outperformed the reported counterparts in terms of radiation efficiency.

4.6 Conclusion

A multiband millimeter-wave rectangular DRA with different types of radiation patterns was demonstrated. A key achievement was the utilization of a planar feed network to excite an

omnidirectional rectangular DRA instead of the traditionally used vertical coaxial probes. The dimensions of the feeding ring-slot were optimized to excite the required resonance modes, with improved performance in terms of the bandwidth and omnidirectional pattern quality. As a result, the quasi- HEM_{218} mode was excited for omnidirectional radiation. Moreover, broadside radiation was also achieved by exciting the fundamental TE_{111} mode and the ring-slot resonance mode. It should be noted that all the reported omnidirectional rectangular DRAs operate in the quasi- TM_{011} mode. Therefore, neither a planar feed network nor the excitation of the quasi- HEM_{218} mode were demonstrated earlier in the design of omnidirectional rectangular DRAs. Furthermore, an omnidirectional mmWave DRA of any shape has not been reported previously. The omnidirectional mode offers a gain of 4.33 dBi with a notably low azimuthal gain variation of 0.85 dB. The impact of different parts of the human body on the antenna performance was investigated and found to be marginal due to the presence of the ground plane. A comprehensive set of measurements was implemented with close agreement between the simulations and measurements. Overall, the proposed design offers considerable potential for a wide range of applications in the millimeter-wave frequency band. A comparison of the proposed DRA's performance against those of its earlier-reported counterparts showed that the DRA offers a smaller size and higher radiation efficiency, triple-band operation, and a low-cost, simple design.

Chapter 5

Dual Band mmWave Cylindrical and Hemispherical DRAs for Off & On Body Communications

5.1 Introduction

In the previous Chapters, rectangular DRAs were utilised for off-body and on-body applications. However, other DRA geometries such as cylindrical and hemispherical offer more diverse resonance modes a widely used in various applications. The design features of cylindrical and hemispherical Dielectric Resonator Antennas (DRAs), particularly with planar feed networks and strategically incorporated ring slots, are integral for achieving dual-band performance. The cylindrical shape offers simplicity, while the hemispherical shape provides symmetry, both supporting resonant modes contributing to desired radiation patterns. The planar feed network facilitates efficient energy transfer and simplified integration into planar systems. The inclusion of ring slots in the feed network allows for precise tuning of resonant frequencies, enabling independent control and optimization for dual-band operation. Together, these design elements play a critical role in realizing the antenna's flexibility, allowing it to operate efficiently in distinct frequency bands while maintaining desired radiation characteristics. Therefore, this Chapter aims to enhance the design by exploring the dual-band performance of cylindrical and hemispherical DRAs with a focus on achieving broadside and omnidirectional radiation patterns as potential candidates for off/on the body communications, similar to the approach taken in Chapter 4.

Dual-band technology is required for both on-body and off-body communications in the DRA. The integration of dual-band technology in the proposed Dielectric Resonator Antenna (DRA)

holds significance for both on-body and off-body communications. In on-body scenarios, where communication devices are near the human body, dual-band capability enhances adaptability to varying frequencies, optimizing signal transmission efficiency amidst dynamic environmental conditions. For off-body communications, the ability to operate in different frequency bands is essential for accommodating diverse communication protocols and standards. The proposed design's novelty lies in its capacity to seamlessly transition between distinct frequency bands, ensuring compatibility with a range of applications such as wearable devices, healthcare monitoring systems, and smart environments. This versatility enables the DRA to address the evolving landscape of wireless communication requirements, offering a novel solution that aligns with the multifaceted demands of contemporary on-body and off-body communication scenarios.

Cylindrical and hemispherical Dielectric Resonator Antennas (DRAs) offer distinct advantages over rectangular DRAs in terms of resonance modes and their applicability to diverse applications. The cylindrical and hemispherical shapes inherently support a broader range of resonant modes compared to rectangular geometries. This versatility allows for a more flexible and efficient tuning of the antenna to various operating frequencies. Cylindrical DRAs, for example, can support both TE and TM modes, providing additional degrees of freedom for optimization. The hemispherical shape, with its inherent symmetry, facilitates the excitation of specific modes beneficial for achieving desired radiation characteristics. These advantages make cylindrical and hemispherical DRAs well-suited for applications where a wide range of frequencies or specific resonance modes are crucial, such as in modern communication systems, satellite communication, and wireless sensor networks. The broader mode support and adaptable geometry enhance the antennas' versatility, making them suitable for diverse applications with varying frequency and performance requirements [23].

The primary objectives of investigating cylindrical and hemispherical Dielectric Resonator Antennas (DRAs) often revolve around optimizing their performance characteristics for specific applications. The choice of these particular shapes is driven by their inherent advantages, including versatile mode support and the ability to tailor radiation patterns. In the context of achieving dual-band performance, the investigation aims to design antennas that can efficiently operate in two distinct frequency bands. This dual-band capability is essential for adapting to the requirements of modern communication systems, where multiple frequency bands are often employed to accommodate different communication protocols and standards. The specific focus on dual-band performance signifies an intention to enhance the flexibility and versatility of cylindrical and hemispherical DRAs, making them suitable for a wide range of applications such as wearable devices, wireless sensor networks, and communication systems that demand adaptability to diverse frequency requirements. The research endeavors to explore and exploit the unique characteristics of these shapes to achieve optimal dual-band performance in line with the evolving needs of contemporary wireless communication technologies.

In this Chapter, the primary objective is to investigate the capabilities of cylindrical and hemispherical DRAs. Both of these antennas have been subjected to simulations in two scenarios: free space and in proximity to human tissue, mirroring the methodology employed for the rectangular DRAs. Both antennas have been measured in free space, where the effect on human tissue was negligible due to the presence of the ground plane.

5.2 Dual Band Cylindrical DRA

5.2.1 Theoretical Framework of CDRA

The CDRA mounted on a metal ground plane is illustrated in Figure 5-1. Three different mode types can be produced using this configuration: hybrid modes, HE or EH, TE ($E_z=0$), and TM ($H_z=0$). As shown in the electromagnetic fields, the TE and TM modes have axial symmetry

and lack azimuthal fluctuations along ϕ [162]. The hybrid modes, in contrast, exhibit azimuthal fluctuations and can be further divided into the HE and EH modes [163, 164].

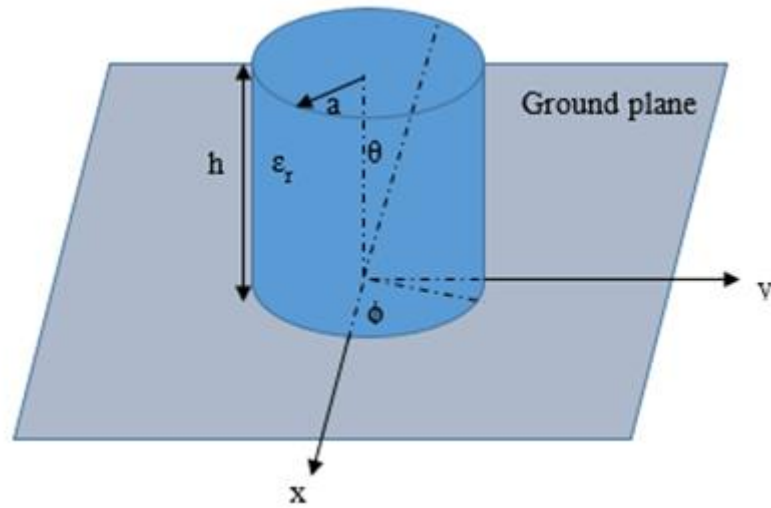


Figure 5-1 Cylindrical DRA placed on a ground plane.

A cylindrical DRA's resonant modes are divided into four groups: TE_{mnp} , TM_{mnp} , HE_{mnp} , and EH_{mnp} . The subscripts n and p denote the number of half-wavelength field variations along the radial (r) and axial (z) directions, respectively, whereas the subscript m denotes the number of full wavelength cycles in the azimuth direction. Unlike the rectangular DRA geometry, the sophisticated mathematical modelling make it difficult to determine the specific resonance frequencies for higher-order modes in a cylindrical DRA [165]. However, it is possible to ascertain the resonance frequencies of these modes using the CST MWS Eigenmode solver. In contrast, using the radius, height, and dielectric constant ϵ_r , one can approximately predict the resonance frequencies of lower-order modes. For instance, the resonance frequency of the $HEM_{11\delta}$ mode can be determined when the aspect ratio is $0.4 \leq a/h \leq 6$ [165, 166] as

$$k_0 a = \frac{6.324}{\sqrt{\epsilon_r + 2}} \left[0.27 + 0.36 \left(\frac{a}{2h} \right) - 0.02 \left(\frac{a}{2h} \right)^2 \right] \quad (5.1)$$

In which $0 \leq \delta \leq 1$, δ approaches 1 for higher dielectric constants. Similarly, in the range of $0.33 \leq \frac{a}{h} \leq 5$, the resonant frequency of the TE₀₁ δ mode can be calculated as [165, 167]. 82

$$k_0 a = \frac{2.327}{\sqrt{\epsilon_r + 1}} \left[1 + 0.02123 \left(\frac{a}{2h} \right) - 0.00898 \left(\frac{a}{h} \right)^2 \right] \quad (5.2)$$

The expression for the resonance frequency of the TM₀₁ δ mode is available when $0.33 \leq a/h \leq 5$ [165, 168]

$$k_0 a = \frac{2\pi f_0 a}{c} = \frac{\sqrt{3.83^2 + \left(\frac{\pi a}{2h} \right)^2}}{\sqrt{\epsilon_r + 2}} \quad (5.3)$$

5.2.2 Design of a Dual Band CDRA

The design of a dual-band CDRA configuration is presented in Figure 5-2. The ground plane is printed on the top of the substrate with dimensions of $G = 13 \text{ mm} \times 13 \text{ mm}$, while the microstrip line is printed on the lower side of an Ro4003 substrate with a thickness of $h_s = 0.308 \text{ mm}$ and a relative permittivity of 3.5. The cylindrical DRA has a respective radius and height of radius of $a = 2.3 \text{ mm}$ and $h = 1.7 \text{ mm}$ with a relative permittivity of 9.9. A 50-feeding line with dimensions of $l_t = 6.5 \text{ mm}$ in length and $wt = 0.3 \text{ mm}$ in width is employed, and the DRA is positioned above the center of the ring-slot that has been carved on the ground plane. The work suggests a novel strategy that experimentally explores the application of a ground plane-etched ring slot. Simulation software CST is used to guide the fabrication process and adjust the elliptical slot size to achieve a good impedance matching for the two operating frequency bands that offer broadside and omnidirectional radiations. This approach reduces the experimental design cycles required to optimize the antenna design.

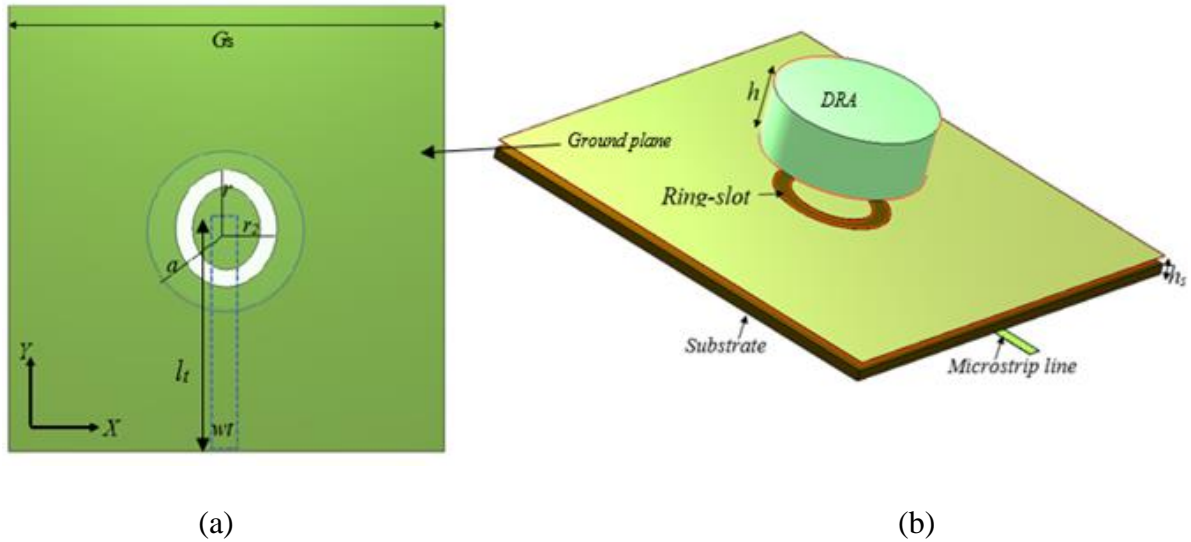


Figure 5-2 (a) Top view and (b) side view of the proposed CDRA configuration.

5.2.3 Shape of the Feeding Slot

To assess the dual-band broadside and omnidirectional performance of the proposed CDRA antenna, a comprehensive analysis was conducted using CST to investigate various design parameters, including the slot shape. The initial focus of the study was on the impact of different slot shapes on the antenna performance, with the results presented in Figures 5-3 to 5-5 for the simulated reflection coefficients.

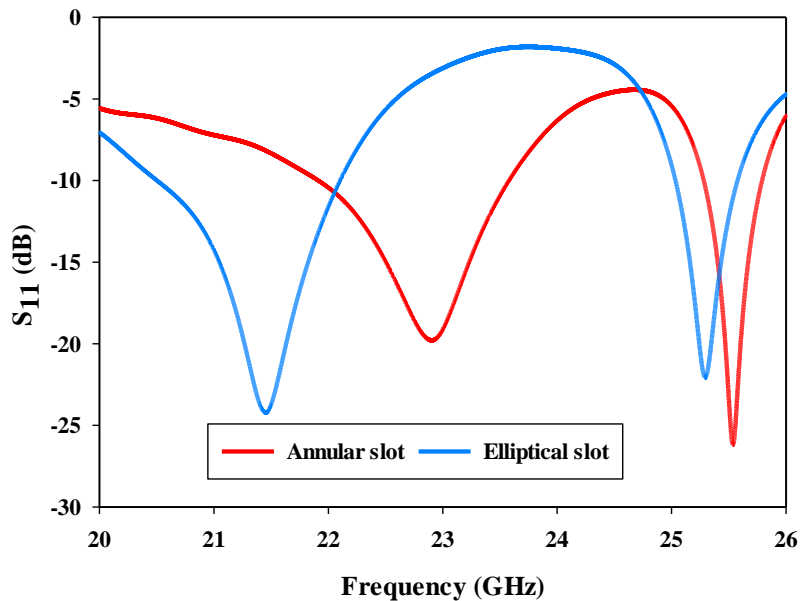
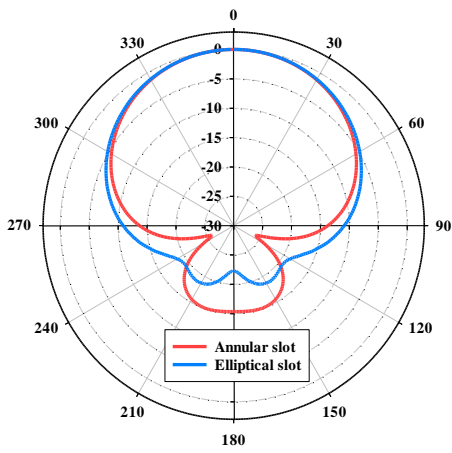
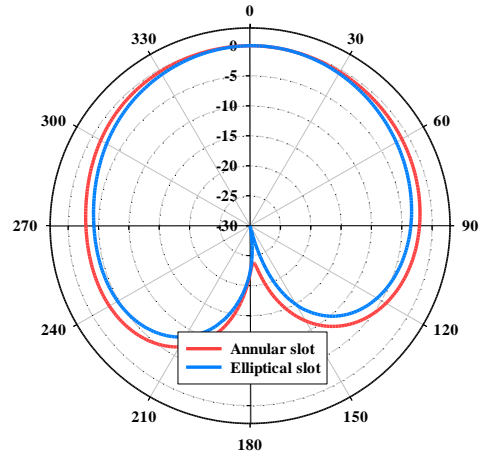


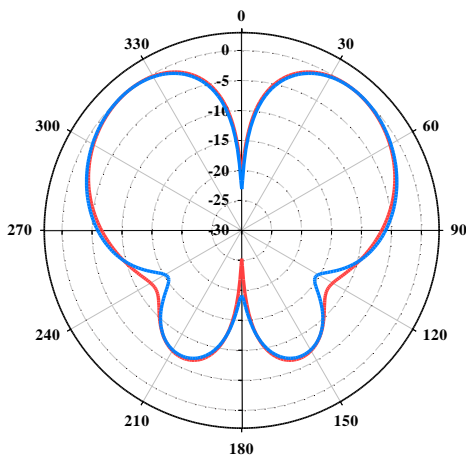
Figure 5-3 Simulated return loss of cylindrical DRA using elliptical and annular ring-slots



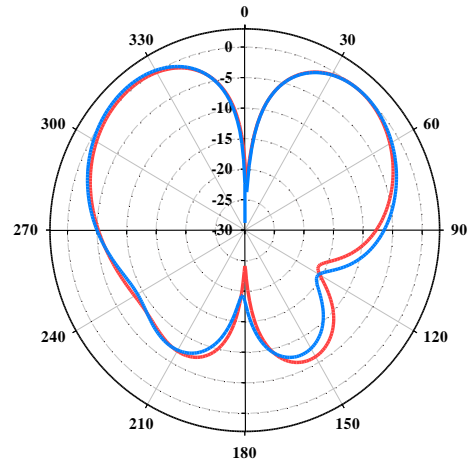
(a)



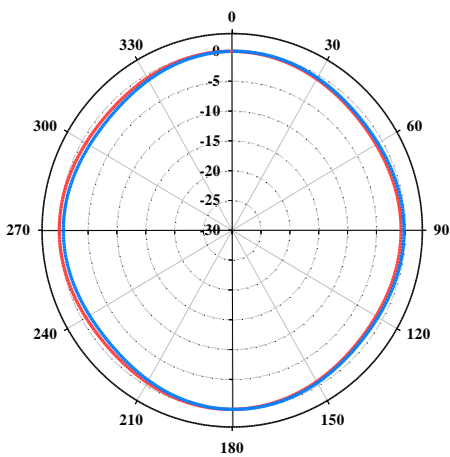
(b)



(c)



(d)



(e)

Figure 5-4 The Normalized radiation patterns of CDRA fed using annular and elliptical ring slots. (a) E-field (broadside), (b) H-field (broadside), (c) E-field (omnidirectional) (d) H-field (omnidirectional) (e) $\theta = 41^\circ$

The radii of the elliptical ring-slot are $r_1 = 1.7$ mm and $r_2 = 1.5$ mm with a thickness of 0.5 mm. On the other hand, the annular ring-slot radius has been chosen as 1.6 mm with a thickness of 0.5 mm. As shown in Figure 5-3, both elliptical and annular ring-slots produce desirable dual-band responses for practical applications. It should be noted that the achieved bandwidths are 7 % and 2 % in the case of annular ring slot compared to 7.5 % and 2.1% for the elliptical ring-slot. In both case the resonance modes of HEM_{111} and $HEM_{21\delta}$ have been excited at the lower and upper frequency bands. After analysing the simulated radiation patterns produced by a CDRA that is fed using elliptical and annular ring-slots, as shown in Figure 5-4, it becomes apparent that the elliptical ring-slot produces a slightly superior and nearly omnidirectional radiation pattern. This outcome is likely attributed to the elliptical shape, which provides a more uniform distribution of electromagnetic fields around the antenna, leading to a symmetrical radiation pattern. In contrast, the annular ring-slot exhibits a non-uniform distribution of fields, resulting in a radiation pattern that is less omnidirectional.

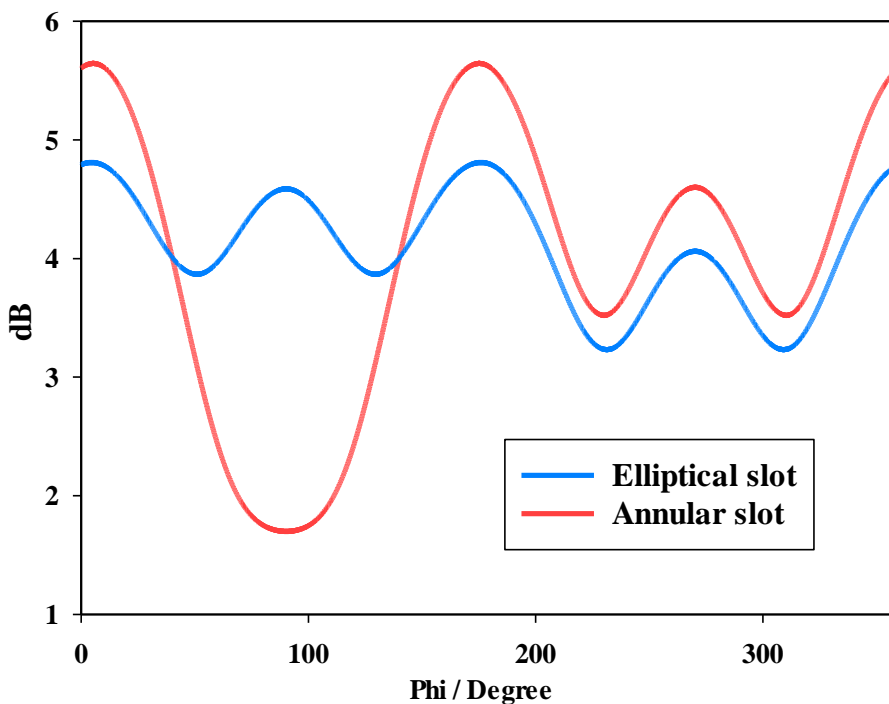


Figure 5-5 The omnidirectional gains' variation of CDRA fed using elliptical and annular ring-slots.

In Figure 5-5, the variation of the omnidirectional gain is investigated at the main beam direction of $\theta = 41^\circ$ plane. The results indicate that feeding the DRA using an annular ring-slot offers a maximum variation of approximately 3.9 dB, whereas feeding using the elliptical ring-slot offers a more modest variation of about 1.5 dB. As a result, the pattern of DRA fed using the elliptical ring-slot is nearly omnidirectional, making it a good choice in achieving more consistent gain across different azimuth angles. The required higher-order mode has been excited at the 25.5GHz frequency. This results in a total magnetic field distribution that corresponds to the HEM_{218} mode of a cylindrical DRA, which generates an omnidirectional pattern. The supported resonance modes for the chosen CDRA dimensions over a frequency range of 20-27 GHz based on the CST Eigen mode solver are presented in Figure 5-6.

Figure 5-7 illustrates the realized gain at the main beam directions for the two bands. For the two broadside patterns, it can be observed that a realized gain of 4.8 dBi is achieved at 21.5 GHz. On the other hand, an omnidirectional gain of 4.79 dBi is achieved at 25.5 GHz at the main lobe direction of $\theta=41^\circ$. The simulated radiation efficiency is also illustrated in Figure 7, where it is evident that a high radiation efficiency of $\sim 97\%$ is achieved at all the operating frequency bands.

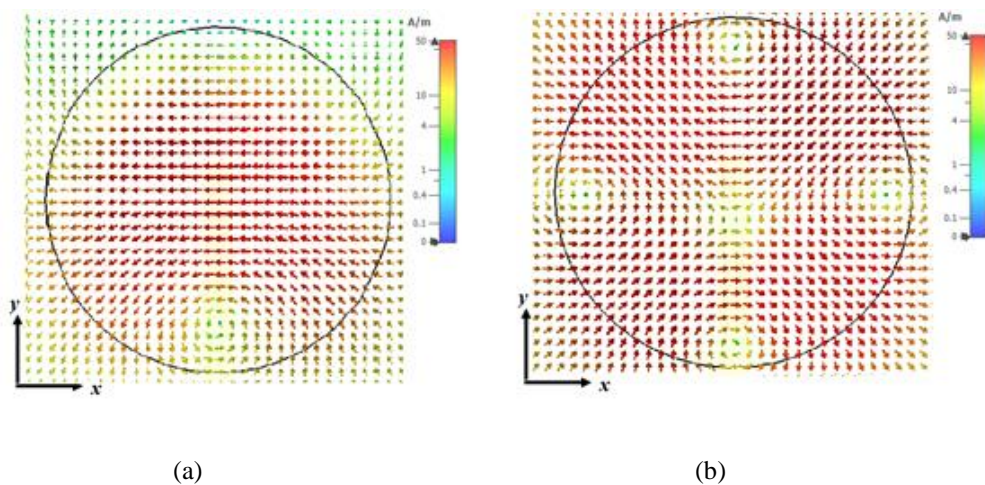


Figure 5-6 Field distributions of the CDRA a) HEM_{111} at 21.5GHz b) HEM_{218} at 25.5GHz.

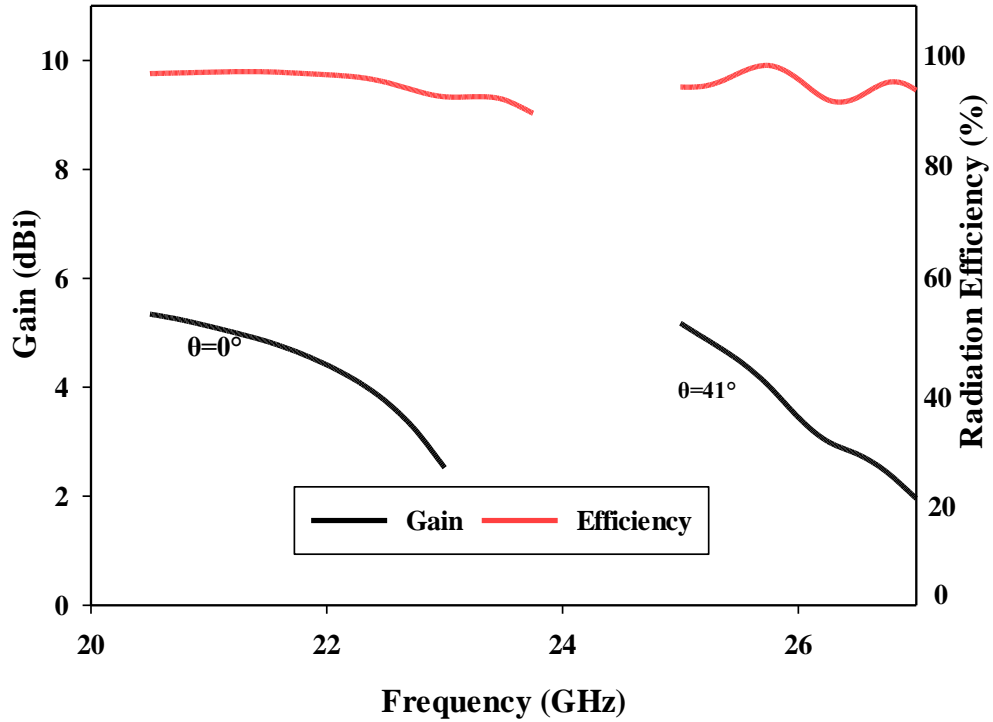


Figure 5-7 Realized gain and radiation efficiency of the ring-slot fed.

Table 5-1 compared results of annular and elliptical slots

	Annular slot	Elliptical slot
Broadside BW %	7	7.5
Omnidirectional BW%	2	2.1
Broadside gain (dB)	4.04	4.8
Omnidirectional gain (dB)	5	4.79
The omnidirectional gain's azimuthal variation in (dB)	3.9	1.5

It can be inferred that the elliptical ring slot offers superior performance compared to the annular ring-slot in both gain and bandwidth. The elliptical ring-slot provides a slightly wider bandwidth in both broadside and omnidirectional directions as compared to the annular ring-slot, along with a higher broadside and omnidirectional gain. In addition, the omnidirectional gain variation at $\theta = 41^\circ$ is ~ 1.5 dB in the case of elliptical ring-slot compared to ~ 3.9 dB for the annular counterpart. Thus, it can be concluded that the elliptical ring-slot is the preferred option to feed antenna in terms of performance as per the data presented in Table 5-1.

5.2.4 The Impact of the CDRA Height on Reflection Coefficient.

The height of the CDRA has been optimized to study its effect on the resonant frequency and impedance bandwidths of the dual bands. According to Figure 5-8, the simulation results illustrate the variations in these parameters for different heights, namely $h = 1.3\text{mm}$, $h = 1.5\text{mm}$, $h = 1.7\text{mm}$, and $h = 1.9\text{mm}$. Upon analysing the data, it becomes apparent that the most suitable height for achieving desirable resonant frequency and impedance bandwidth characteristics is $h = 1.7\text{mm}$. At this height, the CDRA antenna demonstrates an optimized performance. The selection of an optimal height is a critical aspect of the antenna design, as it directly influences the antenna's performance. Variation in the height can shift the resonant frequency, affecting the antenna's ability to efficiently operate within the desired frequency range. Additionally, the impedance bandwidth plays a crucial role in determining the frequency range over which the antenna can maintain acceptable performance and impedance matching.

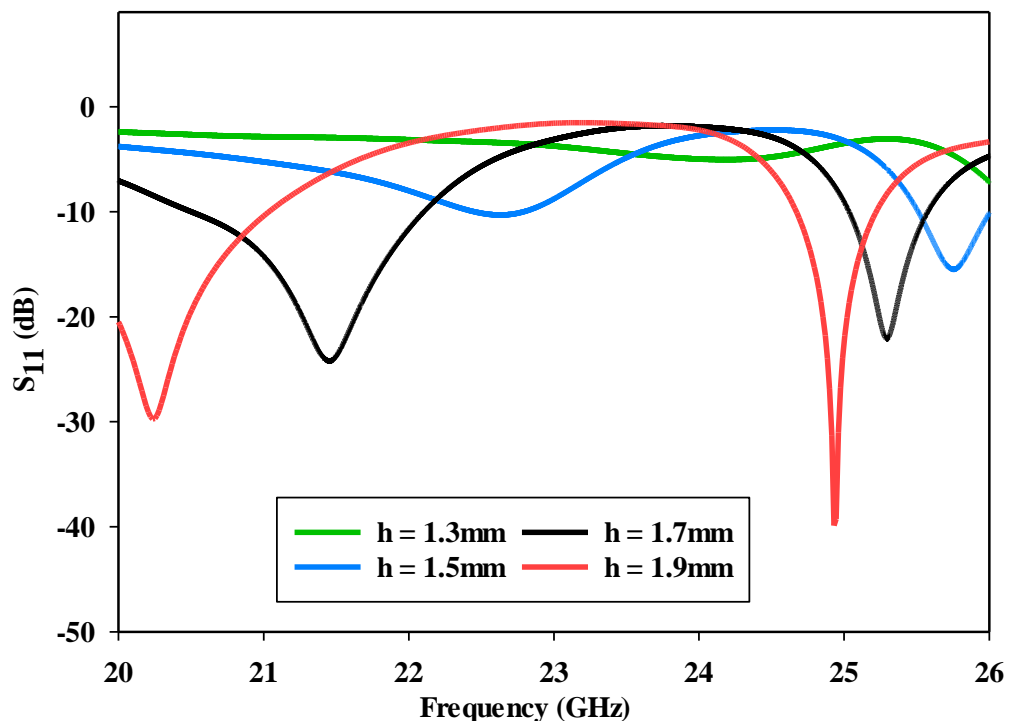


Figure 5-8 The variation of return losses as a function of the CDRA height.

5.2.5 Ground Plane Size and Effective Permittivity Impact on Reflection Coefficient

Figure 5-9 provides a visual representation of how the return losses vary with changes in the size of the ground plane. This figure illustrates that the resonance of the slot is greatly influenced by the size of the ground plane. In other words, the dimensions of the ground plane have a significant impact on the behavior of the slot and its ability to resonate effectively [169]. Furthermore, variations in the performance of the feeding slot have a direct effect on the excited DRA and the resulting resonance frequencies. The feeding slot is responsible for providing the necessary input to the DRA, and any changes in its performance will affect the overall behavior of the antenna system. This implies that the resonance frequencies achieved by the DRA can be altered based on how well the feeding slot is functioning.

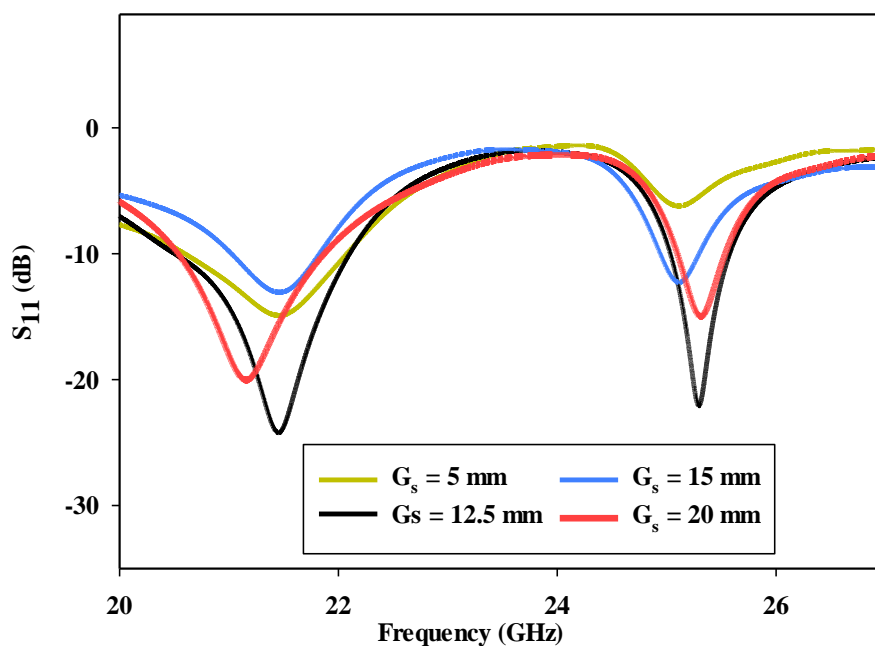


Figure 5-9. The variation of return losses as a function of the ground plane size.

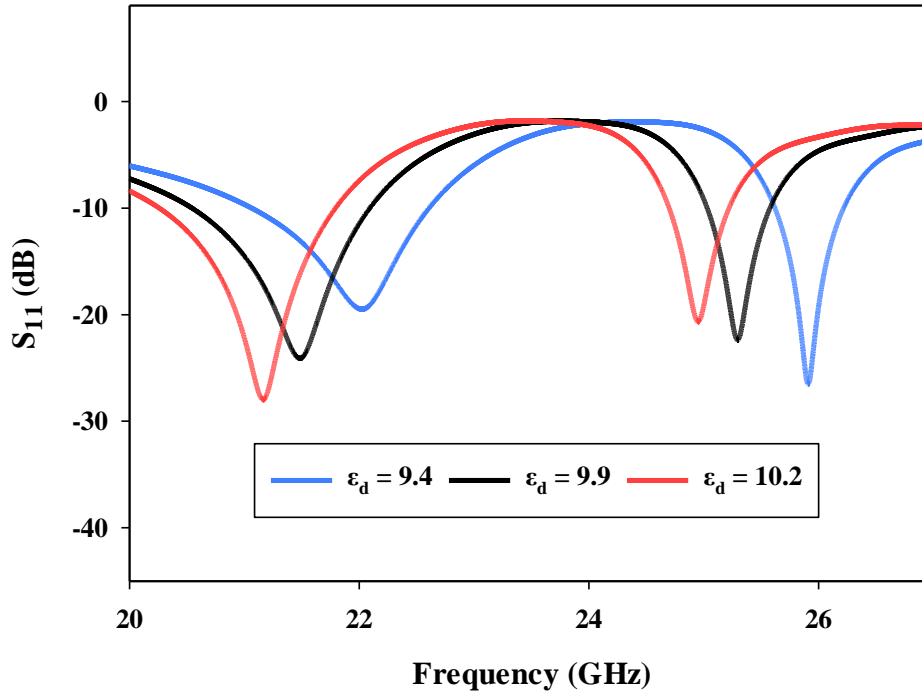


Figure 5-10 The variation of the return losses as a function of the dielectric constant of the CDRA.

Moreover, the research has also examined the sensitivity of the DRA performance to different Alumina dielectric constants. The dielectric constant of the material used in the DRA affects its electrical properties and, consequently, the overall performance. Figure 5-10 presents the DRA performance when the dielectric constant, ϵ_d , is varied between 9.4 and 10.2. This Figure presents the range of dielectric constants that result in consistent and reliable DRA performance, indicating its importance in achieving desired antenna conduct.

5.2.6 CDRA Next to a Human Tissue

In order to examine how the performance of the antenna is impacted by the presence of the human body, a three-layer model representing human body tissues was utilized to host a DRA that is fed using an elliptical ring-slot

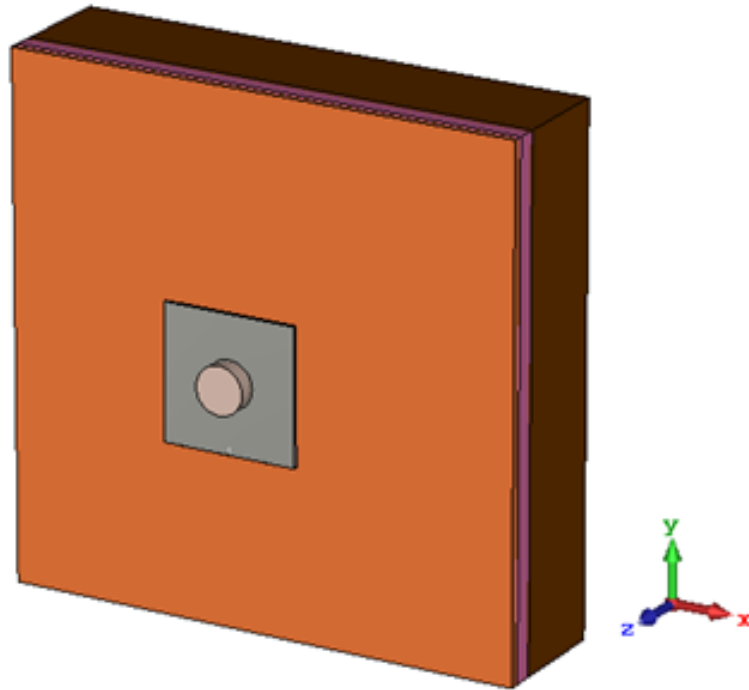


Figure 5-11. CDRA element above the body phantom.

Table 5-2. Human body tissue parameters at 25.5 GHz.

Tissue	Skin	Fat	Muscle
Relative Permittivity	18	6.34	26.2
Density (kg/m ³)	1109	911	1090
Conductivity [S/m]	24	4.66	31.1
Thickness (mm)	1	2	10

The dimensions of the simulated tissue layers were $90 \times 90 \times 13 \text{ mm}^3$ [68], as visually depicted in Figure 5-11. Various separation distances, namely 1 mm and 5 mm, were employed between the DRA and the body phantom [37]. The characterization of the body parameters was conducted by referring to the information provided in reference [136] and a concise summary of these parameters can be found in Table 5-2.

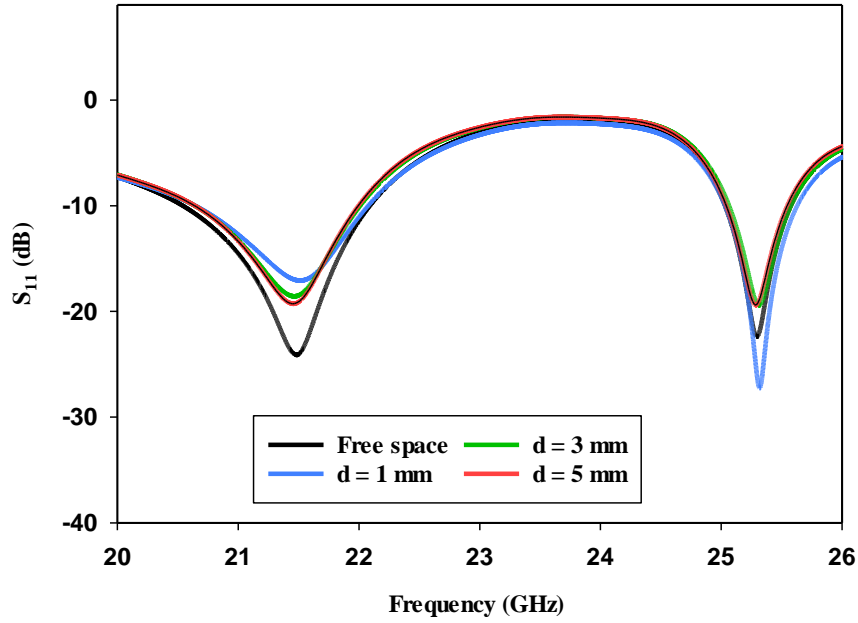


Figure 5-12. The variations of the return losses as a function of the distance between the DRA and human phantom

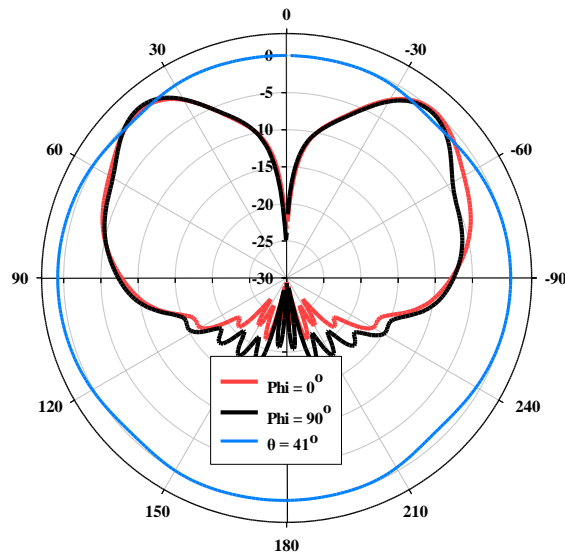


Figure 5-13 Normalized omnidirectional on body at $d = 5$ mm.

In this context, the distance between the DRA and the human phantom is being varied to understand how the proximity to the human body affects the antenna's impedance matching and, consequently, its return losses. As has been shown previously, the presence of the human tissue on the return losses is marginal, which is illustrated in Figure 5-12. Moreover, the radiation

pattern E-plane and H-plane, and the omnidirectional gain are still almost as in free space as demonstrated in Figure 5-13, where the main loop direction at $\theta = 41^\circ$

5.2.7 Analysis of the Specific Absorption Rate

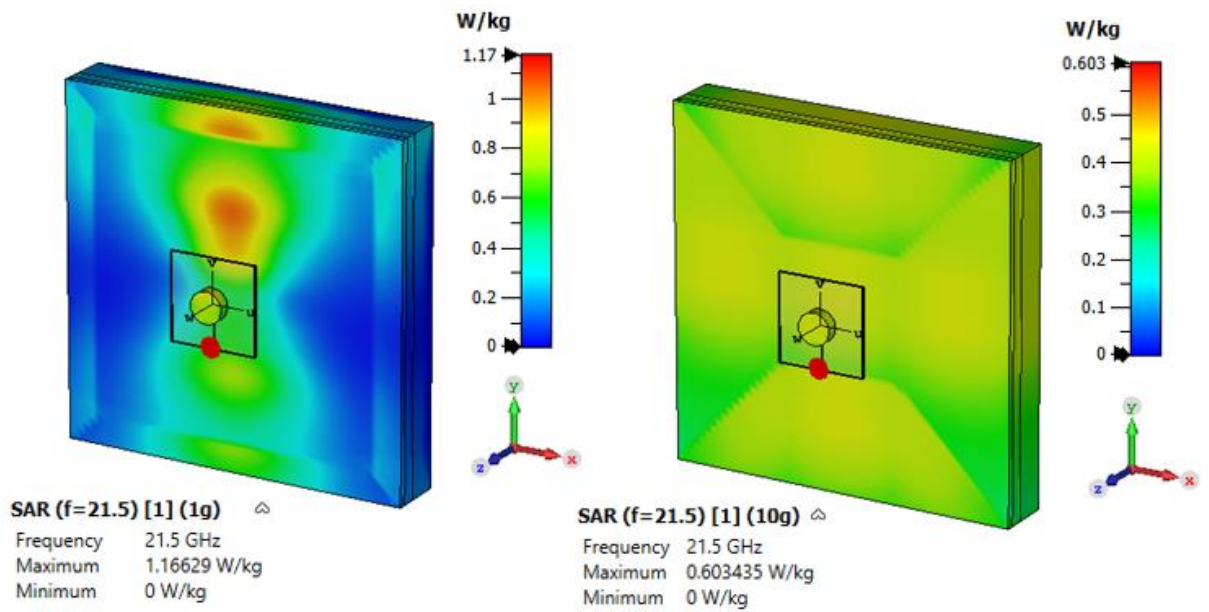
Figures 5-14 and 5-15 convey the specific absorption rate (SAR) with an input power of 18 dBm at 21.5 GHz and 25.5 GHz, respectively. The averaged SAR values for 1g and 10g tissues, using input powers of 15 dBm, 18 dBm, and 20 dBm, are listed in Tables 5-3 and 5-4 for the frequency bands 21.5 GHz and 25.5 GHz, respectively. As can be seen from the mentioned figures and tables all SAR results are below the recommended levels, for 1g or 10g.

Table 5-3 The averaged SAR for 1g and 10g tissues using input power of 15 dBm, 18 dBm, and 20 dBm at 21.5GHz.

Standard	Input power (dBm)	SAR(W/kg)	Distance (mm)
FCC/ANSI	15	0.58314	5
ICNIRP	15	0.30171	5
FCC/ANSI	18	1.16629	5
ICNIRP	18	0.60343	5
FCC/ANSI	20	1.5197	5
ICNIRP	20	0.78629	5

Table 5-4 The averaged SAR for 1g and 10g tissues using input power of 15 dBm, 18 dBm, and 20 dBm at 25.5GHz.

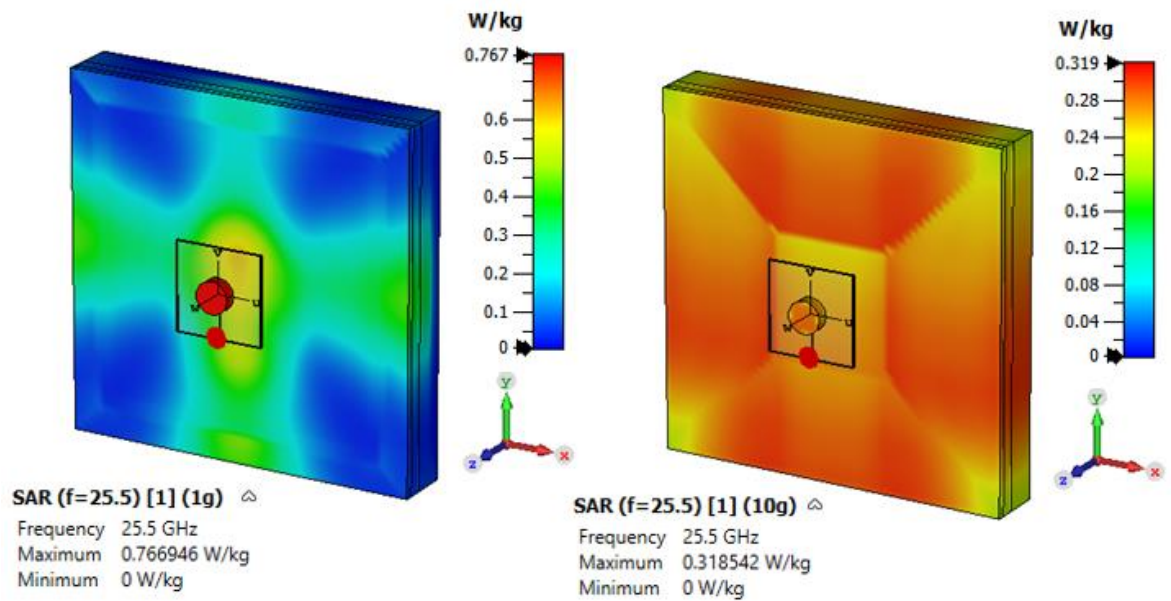
Standard	Input power (dBm)	SAR(W/kg)	Distance (mm)
FCC/ANSI	15	0.41833	5
ICNIRP	15	0.15927	5
FCC/ANSI	18	0.76694	5
ICNIRP	18	0.31854	5
FCC/ANSI	20	0.98773	5
ICNIRP	20	0.41024	5



(a) 1g

(b) 10g

Figure 5-14 The SAR with input power 18dBm at 21.5GHz



(a) 1g

(b) 10g

Figure 5-15 The SAR with input power 18dBm at 25.5GHz

Moreover, it can be observed that the FCC/ANSI standard generally yields higher SAR compared to the ICNIRP standard for the given input power levels. These results provide

insights into the potential rate of energy absorption by different tissues when exposed to electromagnetic fields at frequencies of 21.5GHz and 25.5GHz.

5.3 Measurements of the Cylindrical DRA

The fabrication and measurement procedures for the CDRA were conducted in a manner consistent with those employed for the Rectangular DRA. To ensure proper alignment during the process, the CDRA was positioned on the highlighted section of the ground plane as demonstrated in Figure 5-16. The placement of the CDRA in this specific location is critical for achieving optimal performance and accurate measured results. Proper alignment is essential for the accurate characterization and evaluation of the antenna's radiation properties and other relevant parameters.



Figure 5-16 CDRA prototype

As depicted in Figure 5-17 the -10 dB bandwidth of the lower band was measured as 7.5% is in excellent agreement with the simulated counterpart of 7.15%. Additionally, the measured and simulated bandwidths of the upper band are 2.1%. In addition, the gain of the elliptical ring-slot-fed DRA is illustrated in Figure 1-8, where it can be noted that the maximum simulated and measured gains are 4.8 dBi, 4.6 dBi, and 4.79 dBi, 4.53dBi for the HEM_{111} and the HEM_{218} modes, respectively.

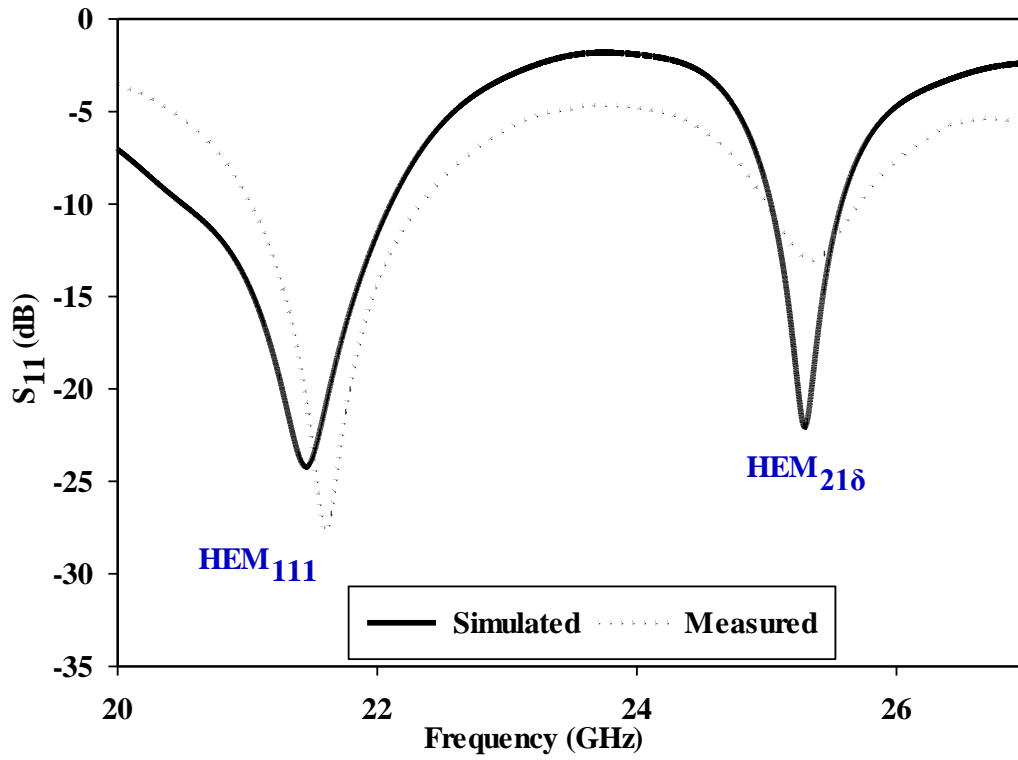


Figure 5-17 Simulated and measured $|S_{11}|$ of CDRA.

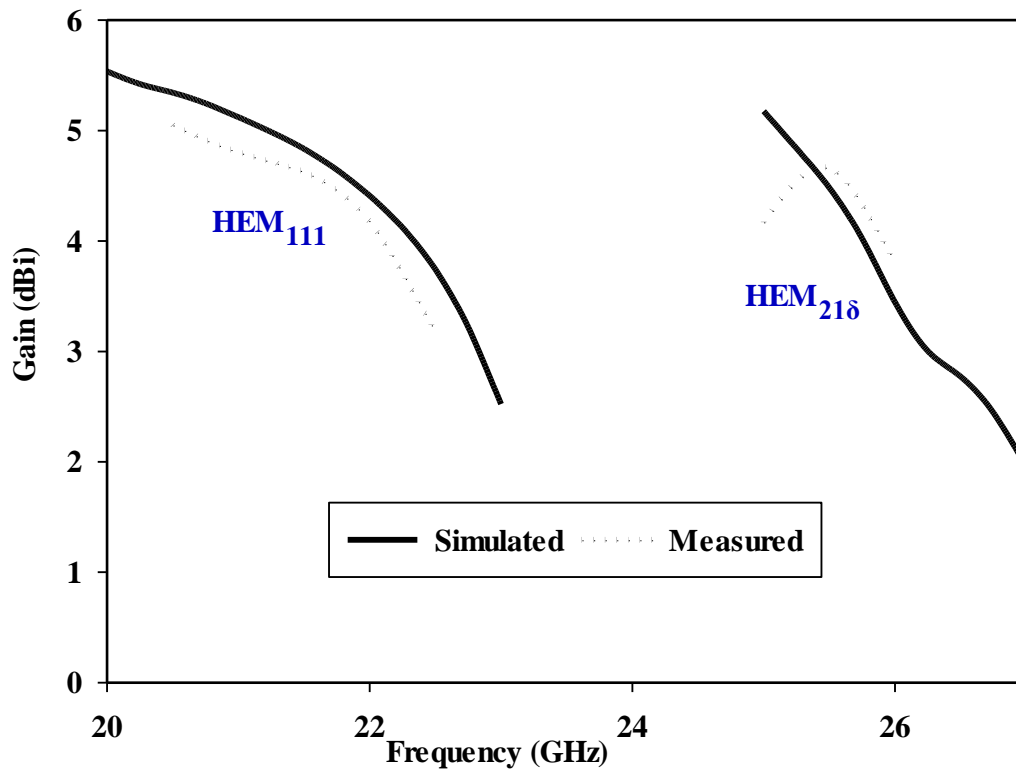


Figure 5-18 Measured and simulated gains at the main beam directions for the two resonance modes.

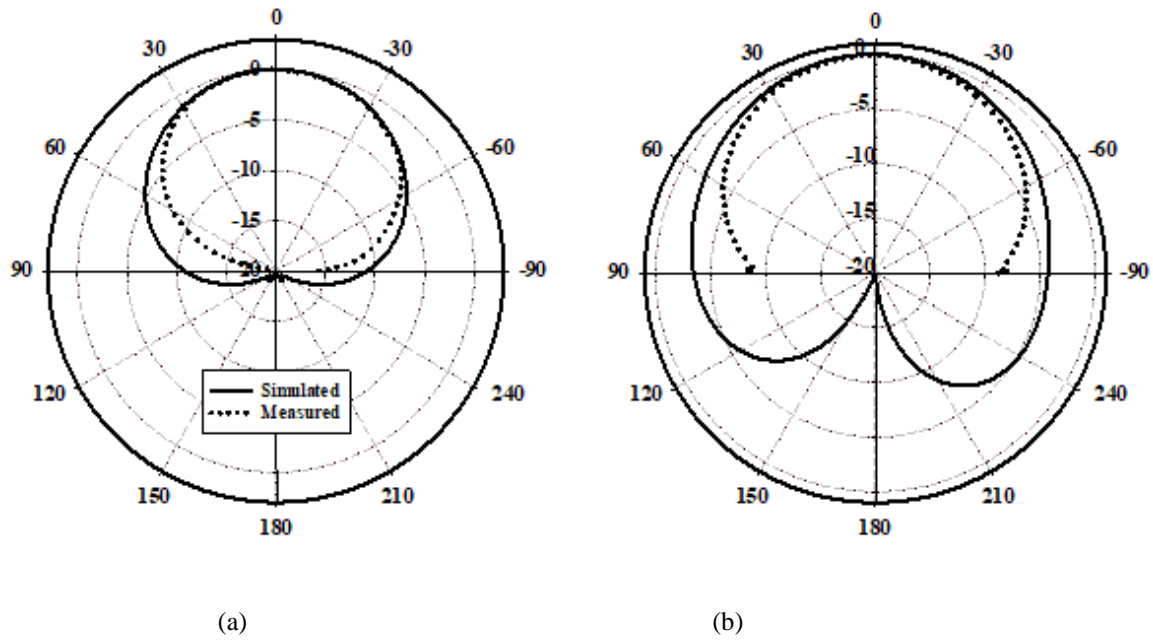


Figure 5-19 Normalised radiation patterns of the resonant slot at 21.5 GHz (a) E-plane, (b) H-plane

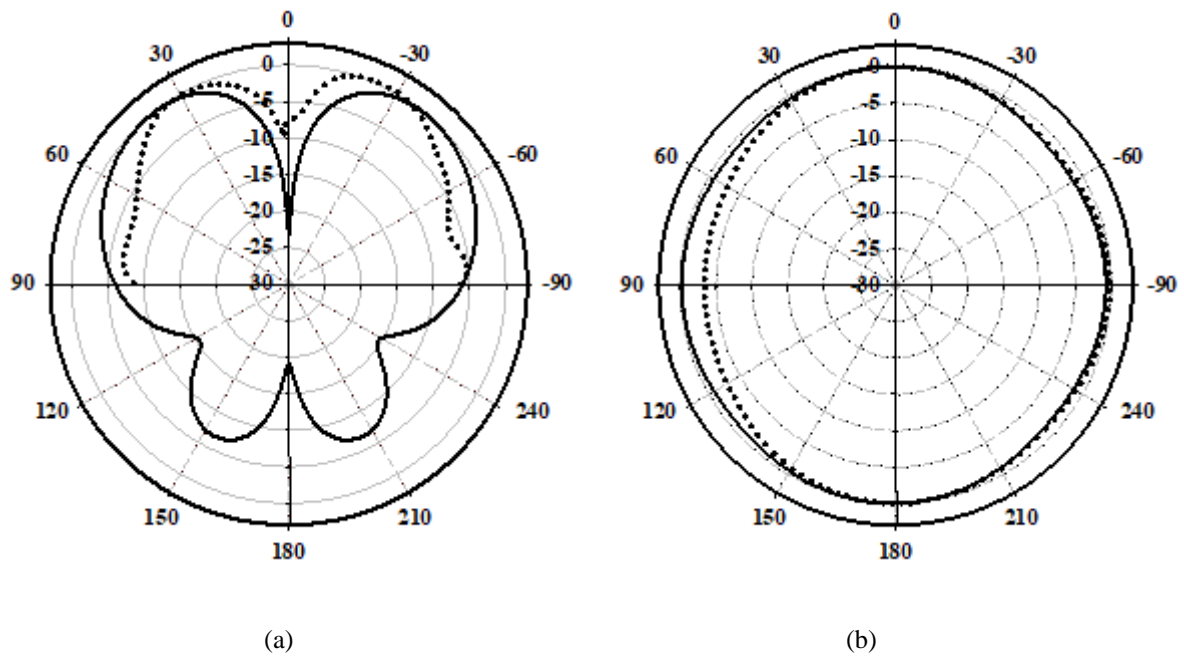


Figure 5-20 Normalised radiation pattern of CDRA at 25.5 GHz (a) E-plane and (b) $\theta = 41^\circ$

At 21.5 GHz, the antenna radiates the most energy in the broadside direction. Both E and H planes confirm this as shown in Figure 5-19 (a) and (b) in the simulated and the measured results. Figure 5-20 presents the measured and simulated radiation patterns of the proposed

CDRA at 25.25 GHz, revealing an omnidirectional radiation pattern peak at an azimuth angle of 41°.

5.4 Dual Band Hemispherical DRA

5.4.1 Geometry of the Hemispherical DRA

The hemispherical DRA can support both transverse electric TE_{nms} modes, with TE_{111} being the lowest-order TE mode, as well as transverse magnetic TM_{nms} modes, with TM_{101} as the lowest-order TM mode. The notations used in the mode characteristic equations for determining the resonance frequencies of supported TE modes in the dielectric resonator antenna have specific meanings:

- Subscript 'n' signifies the order of the Bessel function, aiding in understanding the elevation variations of the mode's fields within the antenna structure.
- Subscript 'm' represents the number of full-wave field variations along the azimuth axis, constrained within the range $0 \leq m \leq n$, offering insight into the azimuthal behavior of the fields.
- Subscript 's' refers to the number of half-wavelength field variations along the radius (r) axis, offering details about the radial variations of the antenna fields.
- The resonance frequencies crucial for the TE modes' operation are obtained from the roots of the mode characteristic equations.

The equation provided (5.4), aids in numerically determining these resonance frequencies for the supported TE modes in the dielectric resonator antenna. These frequencies are pivotal in understanding and characterizing the operational behavior of the antenna. [170].

$$\frac{j_n(ka)}{j'_n(ka)} = \epsilon_r^{1/2} \frac{h_n(k_0 a)}{h'_n(k_0 a)} \quad (5.4)$$

Where the dielectric wavenumber $k = k_0 \epsilon_r^{1/2}$, the symbols j_n and h_n denote the first and second kind of spherical Bessel and Hankel functions of order, respectively. Similarly, j'_n and h'_n represent the derivatives of these functions, respectively. Hence, from Equation 5.4 the roots ($k_0 a$) were derived numerically, allowing for the calculation of the first few mode's resonance frequency [171].

$$f_r = \frac{4.77 \times 10^7 \operatorname{Re}(k_0 a)}{\sqrt{\epsilon_r} R} \quad (5.5)$$

Hence the dimension of the dual-band HDRA can be accurately computed and the excited TE modes of the resonance frequency by applying the mathematical expression represented by Eq (5.4) and (5.5), for instance the TE₁₁₁ mode was excited at resonance frequency 21.5GHz

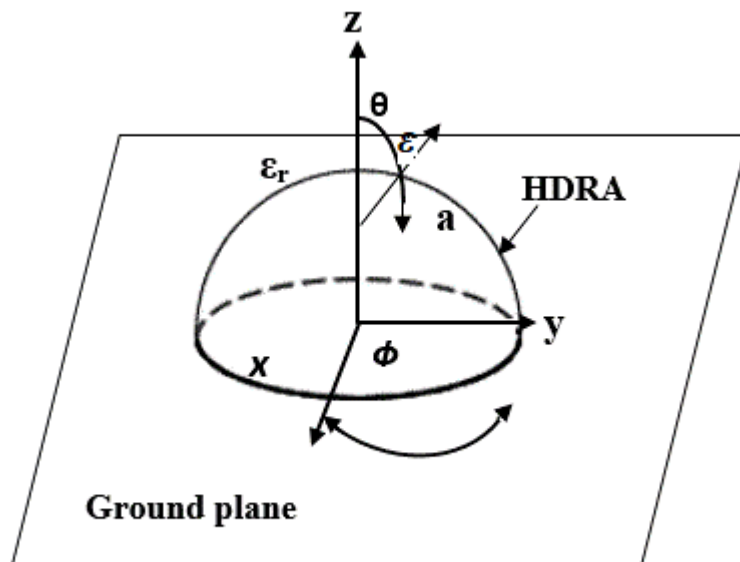


Figure 5-21 Geometry of Hemispherical DRA.

The geometry of the HDRA mounted on ground plane is shown in Figure 5-21. In this configuration, the radius and dielectric constant play a vital role in defining the resonance modes

of the DRA. Hemispherical DRAs have limited flexibility in selecting design parameters compared to other DRA shapes. This means that the choice of radius and dielectric constant has a significant impact on the antenna's performance. However, it's important to note that hemispherical DRAs come with certain drawbacks. Hemispherical DRAs are more expensive to manufacture and require additional effort compared to other conventional DRA shapes. These factors should be considered when deciding on the appropriate DRA design for a specific application. In terms of power connection, hemispherical DRAs can be excited through a probe, slot aperture, and conformal strip line, similar to how it is done with cylindrical and rectangular DRAs. This allows for the efficient transfer of power to the hemispherical DRA and facilitates its operation in practical systems [172-174].

5.5 HDRA Design.

To ensure consistency and facilitate direct assessments between designs, the feed network previously utilized with the CDRA has been repurposed for the hemispherical DRA, as illustrated in Figure 5-22.

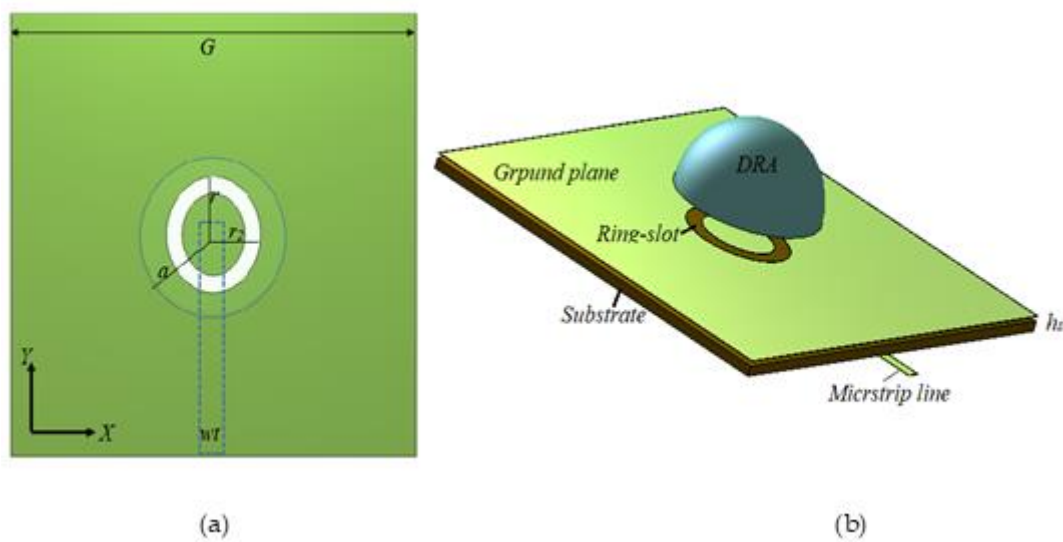


Figure 5-22 (a) Top view and (b) side view of the HDRA.

Hence, the hemispherical DRA shares the same radius of 2.3 mm as the CDRA and is strategically positioned above an elliptical ring-slot etched into the ground plane. This precise placement has been experimentally validated, establishing its effectiveness. This approach proves to be a dependable and efficient strategy for designing and optimizing the performance of hemispherical DRAs. The HDRA has been designed using an Alumina with a relative permittivity ϵ_r of 9.9.

5.5.1 Radius of the HDRA.

As the feed network is already optimized for the CDRA, the focus is shifted to optimize the HDRA itself. In this regard, the radius of the DRA varied within the range of 2.1mm to 2.5mm. Figure 5-23 displays the corresponding S_{11} results, revealing that the chosen radius of 2.3mm emerged as the most suitable in terms of achieving the desired impedance bandwidth for the dual-band operation. In addition, and as mentioned earlier, another aspect that affects the design of HDRA is the relative permittivity ϵ_r . Figure 5-24 demonstrates the impact of various relative permittivity values on the resonance frequencies.

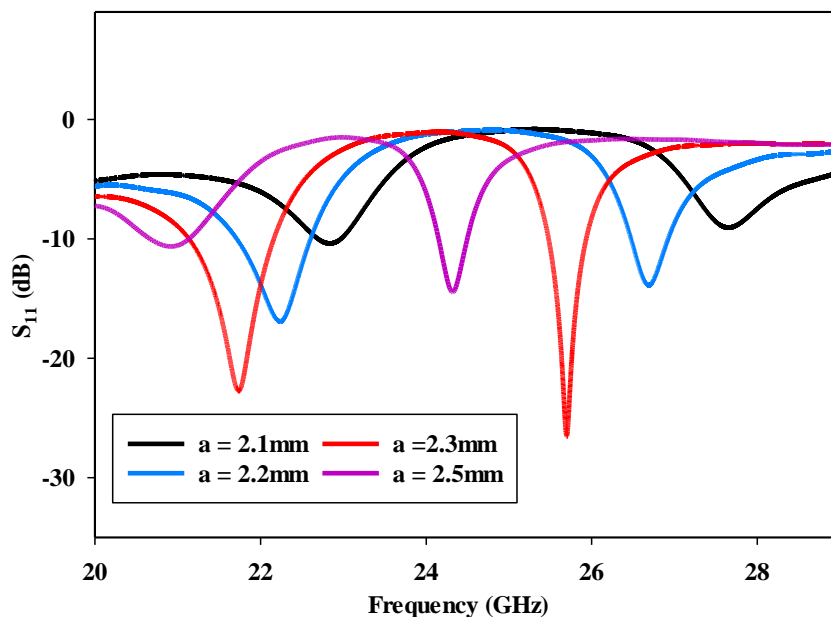


Figure 5-23 The variation of the return losses as a function of the radius of HDRA.

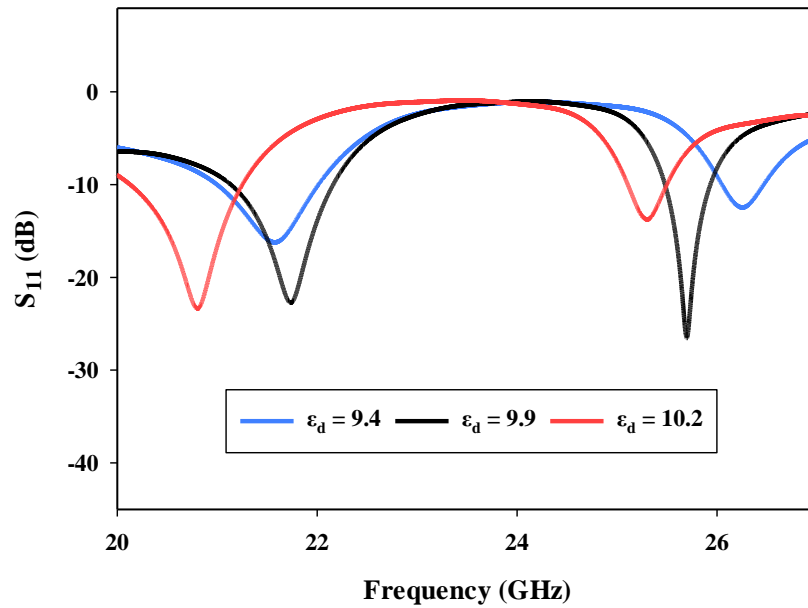


Figure 5-24 The variation of the return losses as a function of the dielectric constant of the HDRA.

At a radius of 2.3mm with the relative permittivity $\epsilon_r = 9.9$, the S_{11} results indicate a similarity in the dual-band performance of the HDRA and the CDRA. This resemblance can be attributed to the significant role played by the feed network in determining the frequency band of the antenna. Consequently, when the same feed network is employed, the resulting antenna, irrespective of the shape of the DRA geometry, will exhibit similar dual-band characteristics. This highlights the importance of the feed network in achieving and maintaining consistent dual-band performance across different DRA shapes.

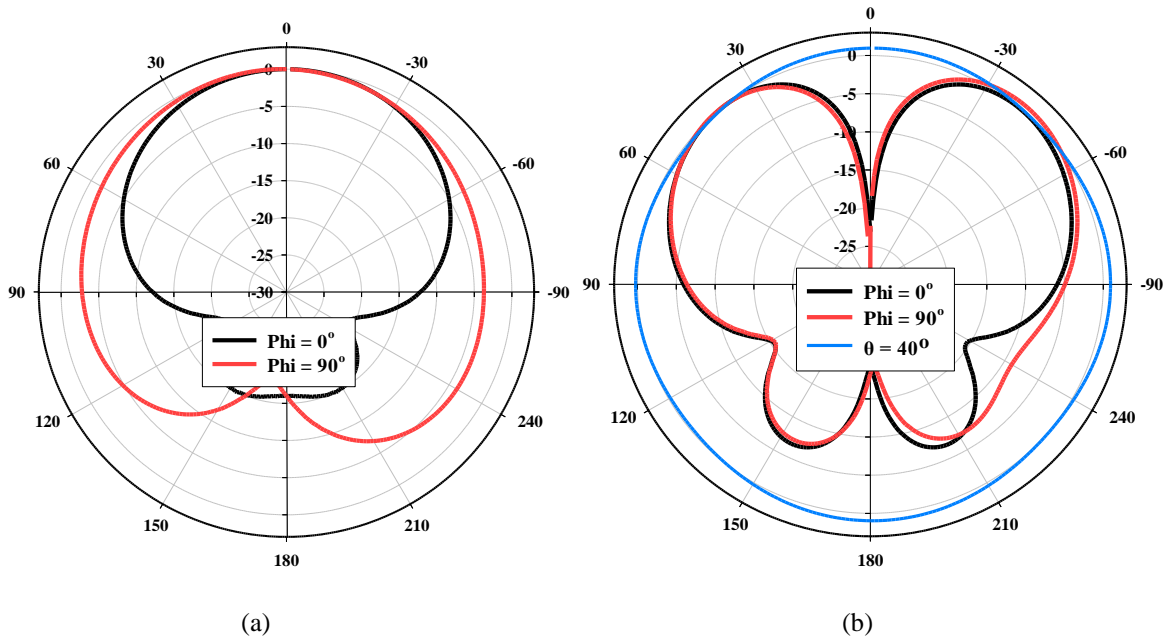


Figure 5-25 The Normalized radiation pattern of HDRA a) 21.5GHz, b) 25.7GHz

This dual-band behaviour demonstrates the antenna's capability to operate effectively in two frequency ranges with different radiation characteristics. The dual-band radiation pattern is illustrated in Figure 5-25. At the lower band of 21.5GHz, the antenna shows a broadside radiation, which is suitable for off-body communications. In contrast, at the upper band of 25.5GHz, the antenna demonstrates an omnidirectional radiation pattern, where it radiates energy uniformly in all directions around its horizontal plane, which is suitable for on-body communications.

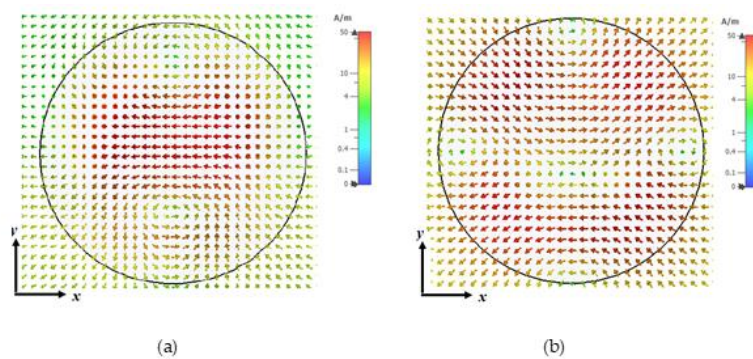


Figure 5-26 Field distributions of the HDRA a) TE_{111} at 21.5GHz b) TE_{218} 25.5GHz.

The simulated magnetic field distribution TE_{111} inside the loaded HDRA at 21.5 GHz is shown in Figure 5-26 (a), and the magnetic field distribution TE_{218} mode, at 25.5 in Figure 5-26 (b) which is enabling the use of the hemispherical DRA to produce an omnidirectional radiation pattern.

5.5.2 HDRA Next to the Human Tissue.

As has been done with the CDRA, the standard procedures followed and compared the simulated reflection coefficient in free space to that of a DRA that is adjacent to the human body at different distances. Figure 5-27, illustrates the antenna on the three layers of the human tissue [136].

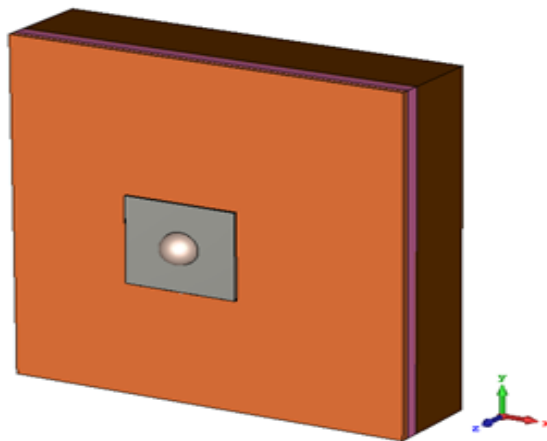


Figure 5-27 The proposed HDRA in the proximity of a human body phantom.

To better understand how the proximity to the human body impacts the antenna's impedance matching and, subsequently, its return losses, the distance between the DRA and the human phantom is changed in this context. The presence of human tissue on the return losses has previously been demonstrated to be minimal, as seen in Figure 5-28. As shown in Figure 5-29, the omnidirectional pattern is still almost as in free space, the E-plane and H-plane radiation patterns as well.

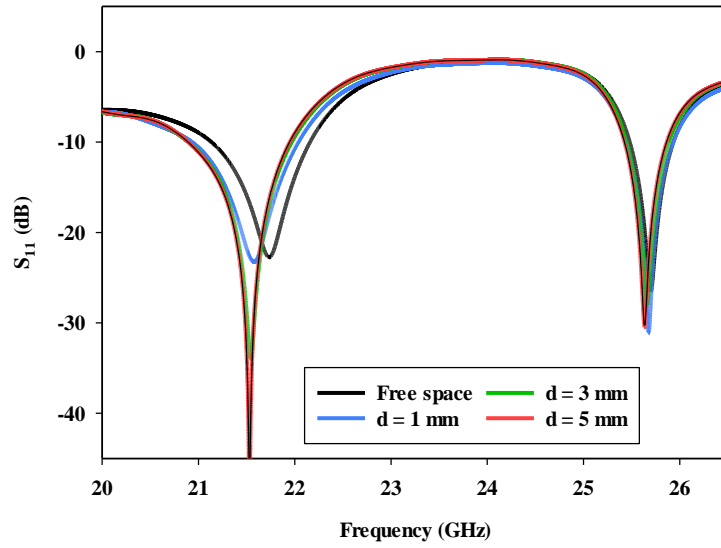


Figure 5-28 The variations of the return losses as a function of the distance between the DRA and human phantom

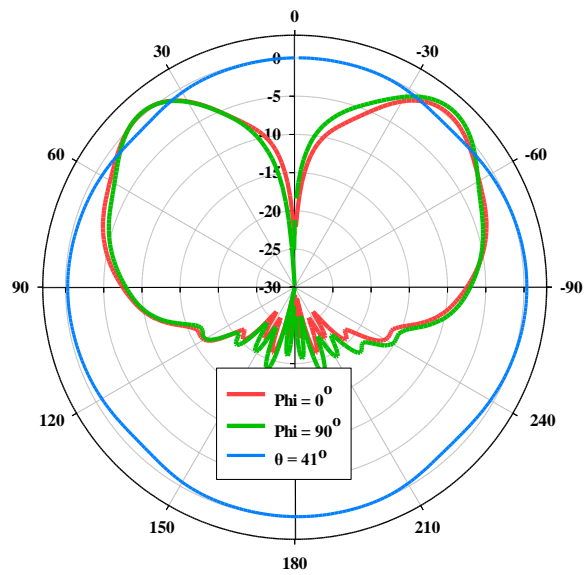


Figure 5-29 Normalized omnidirectional on body at d = 5mm.

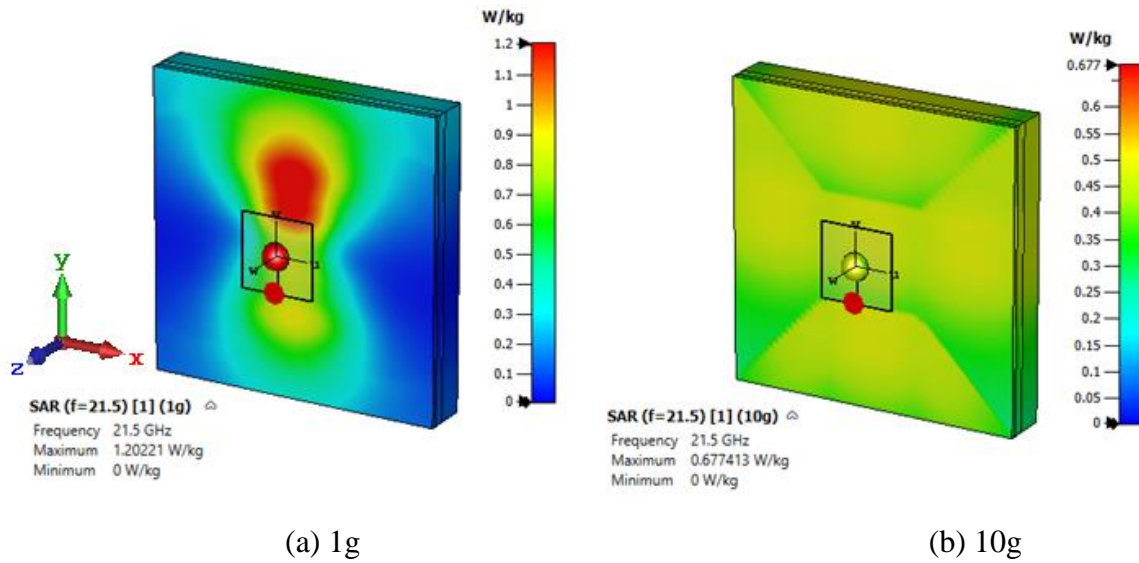


Figure 5-30 The SAR with input power 20dBm at 21.5GHz.

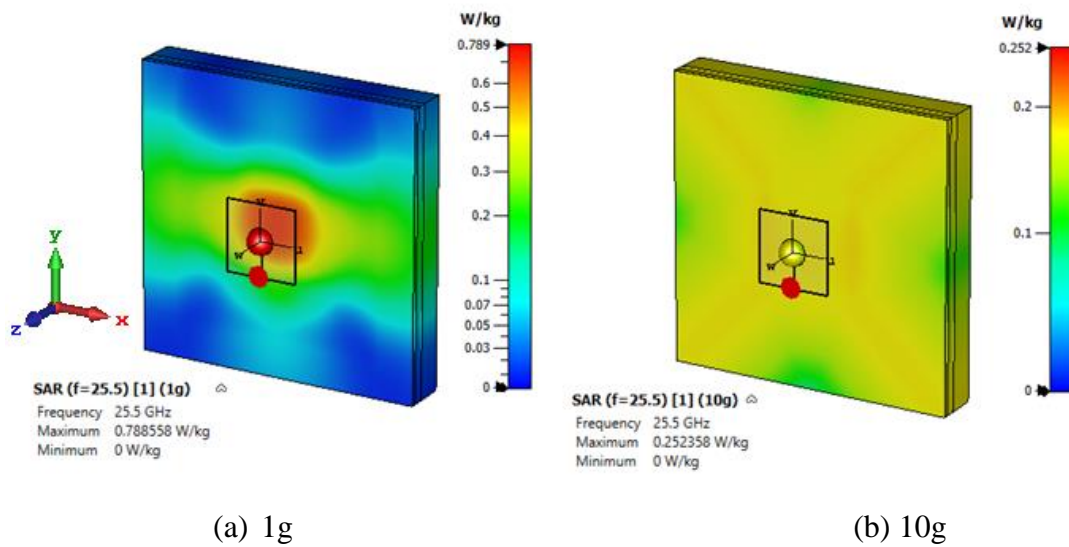


Figure 5-31 The SAR with input power 20dBm at 25.5GHz

The averaged SAR for 1g and 10g tissues using the input power of 15 dBm, 18 dBm, and 20 dBm, have been tested for both frequencies 21.5GHz and 25.5GHz, where the results indicated that the proposed antenna does not exceed the recommended average of the SAR for both standards FCC/ANSI and ICNIRP as listed in Tables 5-5 and 5-6. For example, SAR with input power of 20dBm at 21.5GHz and 25.5GHz are shown in Figures 5-30 and 5-31.

Table 5-5 The averaged SAR for 1g and 10g tissues using input power of 15dBm, 18 dBm, and 20 dBm at 21.5GHz.

Standard	Input power (dBm)	SAR(W/kg)	Distance (mm)
FCC/ANSI	15	0.477988	5
ICNIRP	15	0.185327	5
FCC/ANSI	18	0.95597	5
ICNIRP	18	0.37065	5
FCC/ANSI	20	1.20221	5
ICNIRP	20	0.67741	5

Table 5-6 The averaged SAR for 1g and 10g tissues using input power of 15 dBm, 18 dBm, and 20 dBm at 25.5GHz.

Standard	Input power (dBm)	SAR(W/kg)	Distance (mm)
FCC/ANSI	15	0.313523	5
ICNIRP	15	0.0935708	5
FCC/ANSI	18	0.62704	5
ICNIRP	18	0.14656	5
FCC/ANSI	20	0.788558	5
ICNIRP	20	0.25235	5

5.6 Hemispherical DRA Measurements

In accordance with the established protocols, the fabrication and measurement procedures for the (HDRA) were executed with meticulous attention to detail, ensuring that they were carried out in a manner that was similar to those employed for the (CDRA) and RDRA. Furthermore, it should be noted that the (HDRA) was positioned and integrated into the same

feed network utilized in the previous section of the experiment. This can be visually confirmed by referring to Figure 5-32, which provides a comprehensive illustration of the arrangement.

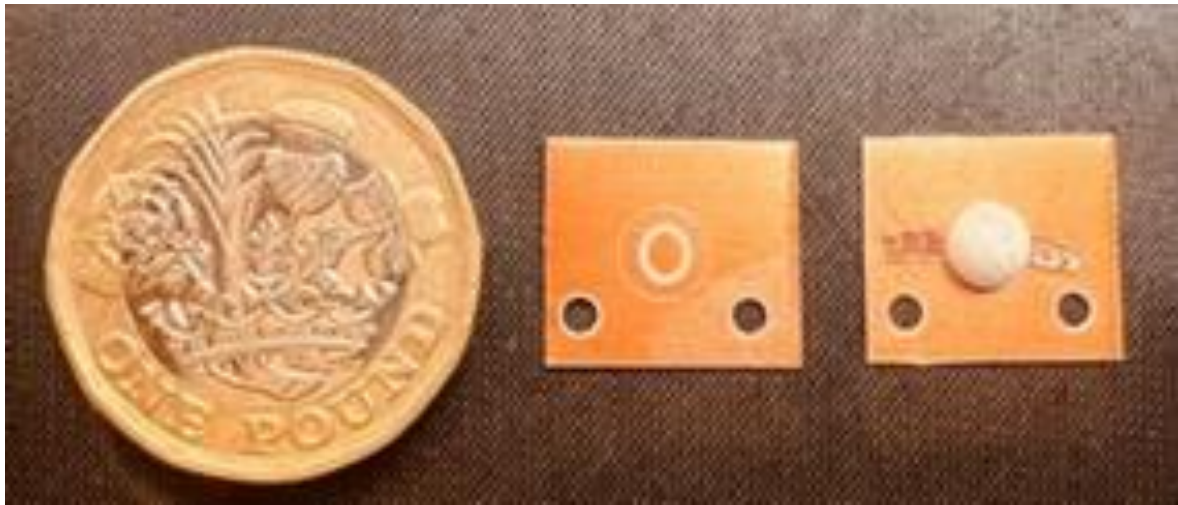


Figure 5-32 HDRA prototype

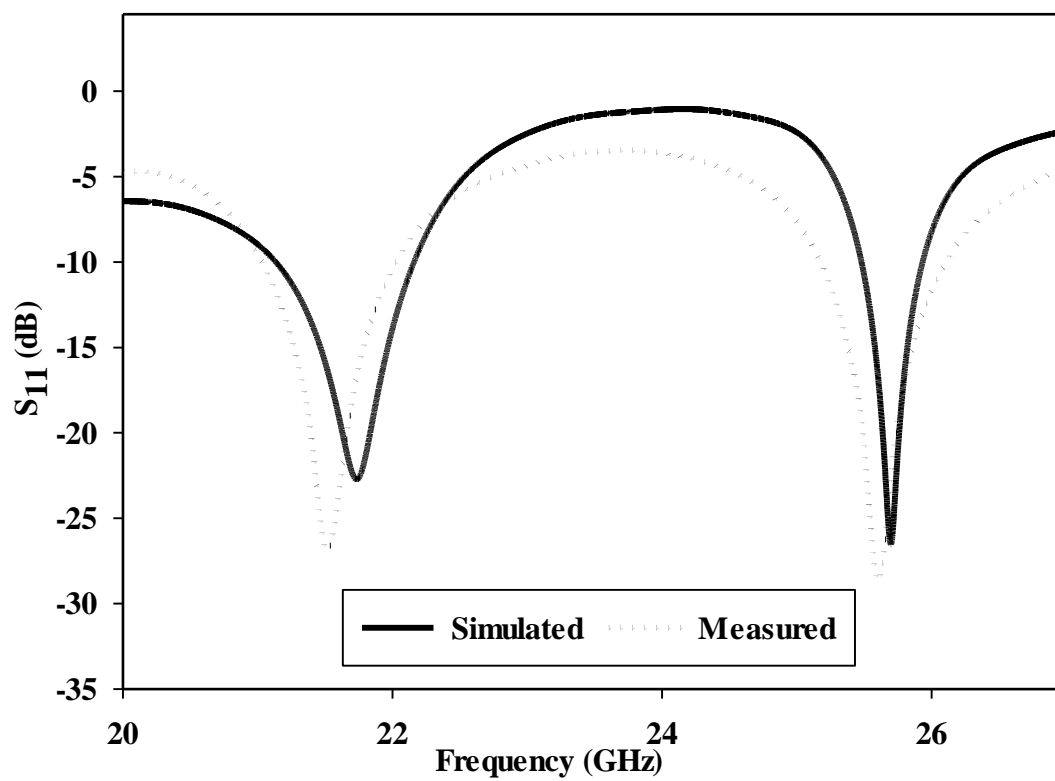


Figure 5-33 Simulated and measured $|S_{11}|$ of HDRA.

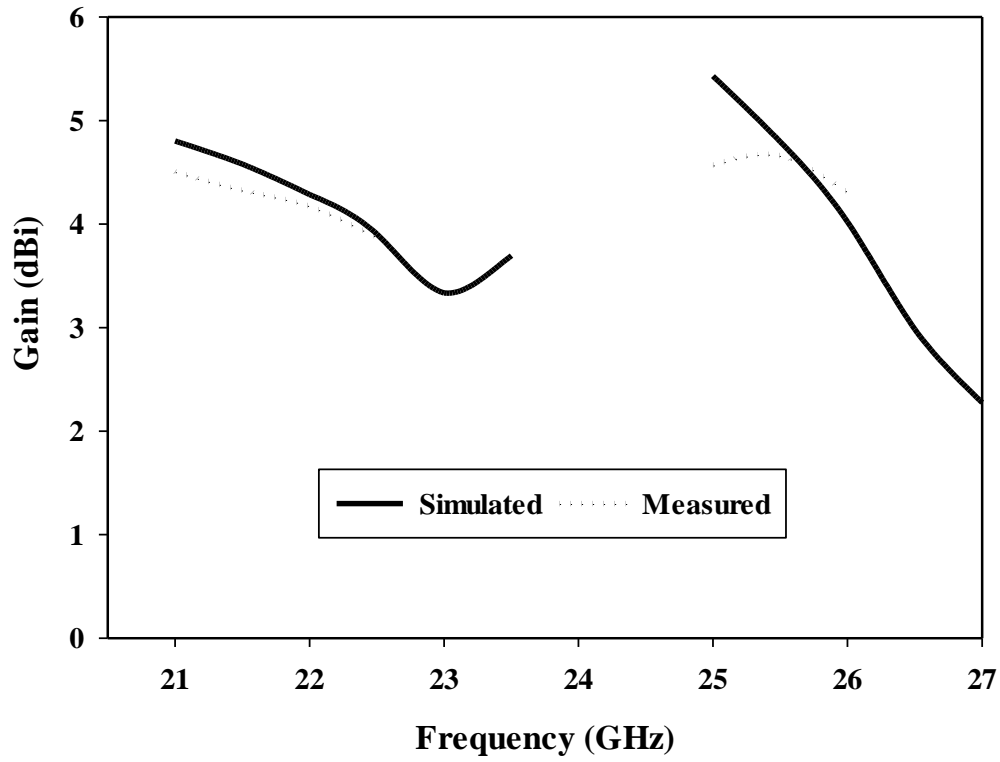


Figure 5-34 Simulated and measured Gain of HDRA. (you need to indicate θ for each case)

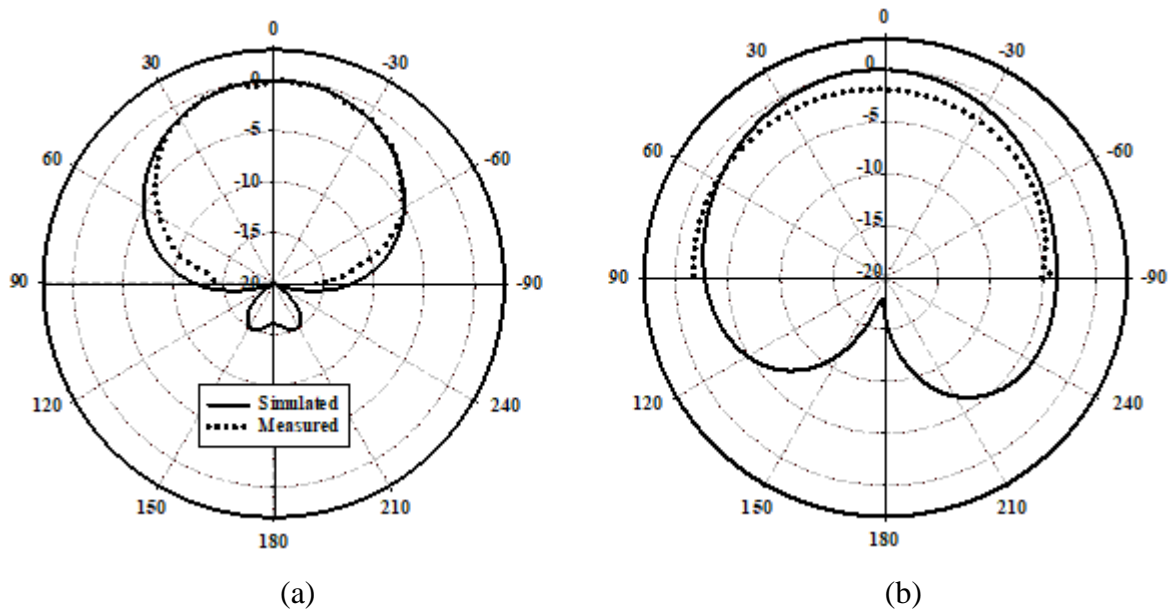


Figure 5-35 Normalised radiation patterns of the resonant slot at 21.5 GHz (a) E-plane, (b) H-plane.

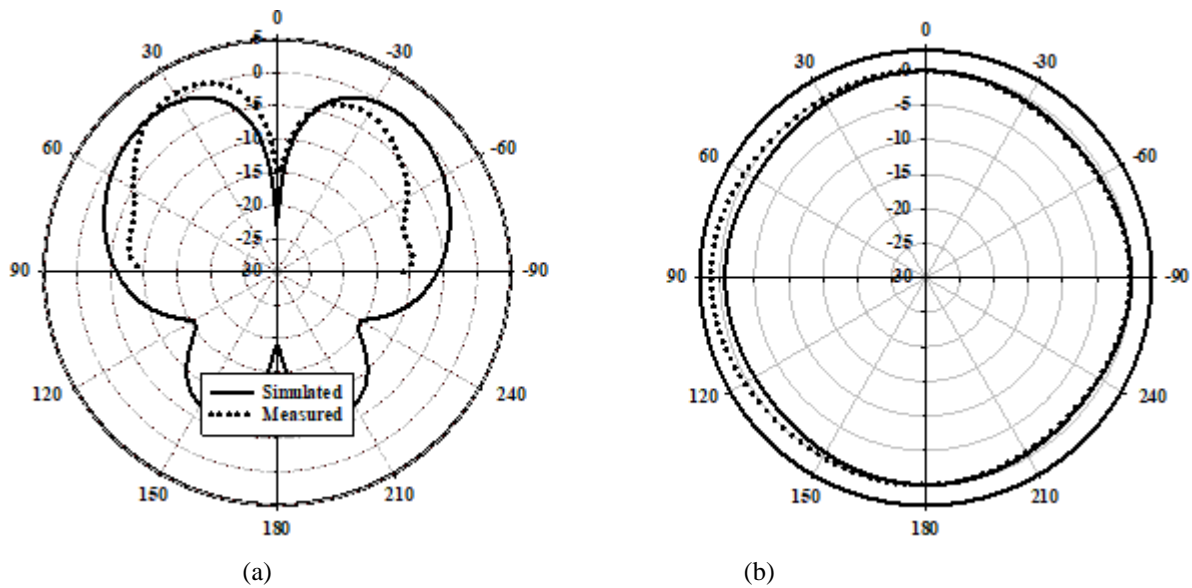


Figure 5-36 Normalized radiation pattern at 25.5GHz (a) x - z plane and (b) azimuth-plane.

The results obtained from the measurement of reflection coefficients for the (HDRA) are highly commendable as demonstrate a remarkable agreement with the simulation outcomes. Exactly, the degree of conformity between the two approaches is approximately 7.5% in the lower band broadsided, while in the upper band omnidirectional, it is 2.1%. These findings are represented in Figure 5-33, which provides a clear and comprehensive overview of the performance of the HDRA in both frequency ranges. The gain of the elliptical ring-slot-fed HDRA is depicted in Figure 5-34. The results reveal that the highest gains achieved for the lower band are 4.3dBi and 4.19dBi, respectively. Moreover, for the upper band, the gains are recorded at 4.39dBi and 4.25dBi in the simulated and measured scenarios, respectively.

The obtained radiation pattern from the simulations and measurements of HDRA are in good agreement, as demonstrated in Figures 5-35 and 5-36. In particular, Figure 5.36 (b) presents the radiation patterns of the HDRA at 25.5 GHz, with both the simulated and measured results indicating an omnidirectional radiation pattern peak at an $\theta = 40^\circ$. This signifies that the DRA is capable of radiating energy uniformly in all directions at this frequency, making it an

ideal choice for a wide range of applications that require broad coverage, especially for on-body communication.

The primary objectives of investigating cylindrical and hemispherical Dielectric Resonator Antennas (DRAs) with a specific focus on achieving dual-band performance include designing antennas that can operate effectively in two distinct frequency bands, achieving frequency reconfiguration, reducing overall size while maintaining or enhancing performance, improving efficiency, ensuring wideband impedance matching, exploring polarization diversity, and catering to applications in wireless communication. The goal is to develop multifunctional antennas that not only support dual-band operation but also offer versatility, compactness, and efficiency for various communication standards and services, for instance for off/on-body applications.

5.7 Conclusion.

CDRA and HDRA were designed with a planar feed network featuring a ring slot, offering excellent dual-band radiation performance, both broadside and omnidirectional. This approach provides a practical and effective solution for achieving desired radiation patterns, making these designs highly suitable for a wide range of applications. The two dual-band mmWave DRAs have been designed and fabricated successfully. Furthermore, a unidirectional and omnidirectional mm Wave of CDRA and HDRA has been tested, as potential candidates for off/on-body applications. The required modes have been excited using annular and elliptical ring-slots, where the latter demonstrated a more stable and improved performance. For both DRAs, the omnidirectional mode of the CDRA and HDRA offer a gain of 4.8 dBi and 4.39dBi, with a notably low azimuthal gain variation of ~ 0.85 dB and 1.5 dB respectively. A comprehensive set of measurements was implemented to validate the simulations. The SAR level was lower than the recommended level for both standards FCC and ICNIRP. Overall, the

proposed designs offer considerable potential for a wide range of applications in the millimetre-wave frequency band.

Chapter 6

Conclusion and future work

6.1 Conclusion

This study successfully simulated and measured low-profile mmWave Dielectric Resonator Antennas for off/on-body communications, with close agreement between the measured and simulated results. The proposed off-body DRAs showed impressive performance in terms of impedance bandwidth, axial ratio bandwidth, and maximum gain. As an example, the layered single DRA design achieved a 75% impedance bandwidth, 26.7% axial ratio bandwidth, and a maximum gain of approximately 8.9 dBic at 24 GHz. By incorporating an additional dielectric layer and a waterproof outer layer, the antenna's performance and robustness were improved.

Furthermore, a special attention has been given to the alignment and assembly of a mmWave DRA, where it has been demonstrated that the use of a second ground plane with a hollow square cavity, to accommodate the DRA, provided a simple solution for the DRA-feeding slots with an impedance bandwidth of 29% and an axial ratio bandwidth of 13.5% were achieved, with a maximum gain of 8.7 dBic at 28 GHz.

. The third design was focused on the conformal wristwatch DRA, which demonstrated an impedance bandwidth of approximately 27% in the frequency range of 24.4-31.8 GHz, with an axial ratio of around 14% and a gain of approximately 9.42 dBic in free space. The circular polarization feature of this wearable device allows for flexible antenna alignment. The impact of the ground plane size on the antenna performance was also carefully considered.

In Chapter 3, a single DRA element of dimensions of $(0.48\lambda_o \times 0.48\lambda_o \times 0.27\lambda_o)$ at 28 GHz has been used as the radiating element that was used in the design of a four-element

circularly polarized rectangular DRA array for mmWave off-body applications. For the suggested antenna, cross-slot coupling together with a sequential parallel feeding network has been utilized to achieve a wide impedance bandwidth of 29% while maintaining a high radiation efficiency of 90%. The proposed antenna array has been fabricated and measured with a gain of 13.7 dBic, which represents an enhancement of 5 dBi above that of a single DRA.

In Chapter 4, a multiband millimeter-wave rectangular DRA with different types of radiation patterns has been demonstrated. A key achievement is the utilization of a planar feed network to excite the quasi HEM_{218} mode for omnidirectional radiation from rectangular DRA. Besides, broadside radiation has also been achieved by exciting the fundamental TE_{111} mode and the ring-slot resonance mode. It should be noted that all the reported omnidirectional rectangular DRAs in the literature utilize a coaxial feeding probe to excite the quasi- TM_{011} mode. Therefore, neither a planar feed network nor the excitation of the quasi- HEM_{218} mode have been demonstrated earlier in the design of omnidirectional rectangular DRAs. Furthermore, an omnidirectional mmWave DRA of any shape has not been reported earlier. Finally, dual band mmWave DRAs with two different radiation patterns (broadside and omnidirectional) have been successfully developed and constructed.

Chapter 5 presents cylindrical and hemispherical DRAs for unidirectional and omnidirectional mmWave radiation have been put through testing as possible possibilities for off- and on-body applications. Both annular and elliptical ring-slots have been used to stimulate the necessary modes, with the latter showing improved and more stable performance. The CDRA and HDRA yield gains of 4.8 dBi and 4.39 dBi, respectively, with noticeably little azimuthal gain fluctuation of 0.85 dB and 1.5 dB, respectively. To verify the models, an extensive collection of measurements was put into practice. The SAR has been investigated

and it has been demonstrated that all proposed designs meet the required safety limits when placed at a distance of 5 mm from the human body tissue. The impact of human-body proximity has been investigated and found to be negligible due to the presence of the ground plane. The results of simulations and measurements are in close agreement. The proposed antennas offer a promising potential for mmWave off/on-body communications. Overall, a comparison of the proposed DRA's performance against those of earlier reported counterparts shows considerable potential for a wide range of applications in the millimeter-wave frequency band.

Table 6-1 The proposed mm wave DRA for of/ on-body applications

DRA configuration	Frequency GHz	Size (mm³)	S₁₁ BW (%)	Gain (dBi)	AR BW (%)	Application
Layered RDRA	24	25 × 27 × 5	75	8.91	26.7	Off-body
Grooved RDRA	28	19 × 21 × 2.9	29	8.7	13.5	Off-body
Wristwatch RDRA	28	18 × 18 × 2.9	19	9.42	10.6	Off-body
RDRA array	28	36.5 × 36.5 × 2.9	29	13.7	13	Off-body
RDRA	17.5, 23, 28.5	12.5 × 12.5 × 1.7	3.4, 7.7, 1.9	7.3, 6.8, 5.8	Linear	Off/On-body
CDRA	21.5, 25.5	13 × 13 × 2.3	7.15, 2.1	4.8, 4.79	Linear	Off/On-body
HDRA	21.5, 25.5	13 × 13 × 2.3	7.5, 2.1	4.19, 4.25	Linear	Off/On-body

Table 6-1 summarizes results from a study evaluating various Dielectric Resonator Antenna (DRA) designs, including Layered RDRA, Grooved RDRA, Wristwatch RDRA, RDRA array, RDRA, CDRA, and HDRA.

6.2 Future work

The extensive field testing to evaluate the antenna's performance in real-world of on/off-body communication scenarios, considering factors like user mobility, environmental conditions, and signal stability. Enhance the antenna's robustness against adverse weather conditions and physical wear and tear, ensuring its reliability in practical applications. In addition, exploring multi-band and multi-mode DRA designs, along with achieving frequency configurability and adaptability through innovative metamaterials, would enhance adaptability in dynamic communication environments. Moreover, optimizing antennas through advanced materials, including metamaterials, and manufacturing methods such as 3D printing or SIW-based structures to enhance antenna efficiency and robustness. Metamaterials offer a promising avenue for enhancing antenna performance by tailoring the dielectric properties to specific needs, enabling antennas to operate more efficiently across a range of frequencies and applications, where, leveraging the unique properties of metamaterials to push the boundaries of antenna design and functionality. Additionally, efforts can be directed toward increasing the antenna's gain directivity, and bandwidth, particularly for applications requiring extended communication ranges. This involves experimenting with novel excitation techniques and radiation patterns to elevate antenna performance. Furthermore, the integration of beamforming techniques with the multiband rectangular DRA can be explored to facilitate adaptive beam steering, enhancing communication quality and coverage in millimeter-wave systems. Investigating Multiple-Input Multiple-Output (MIMO) configurations using arrays of DRAs could improve communication capacity and reliability.

Evaluating on-body interactions, energy efficiency, realistic channel models, interoperability with existing standards, user studies, and field trials would further advance this field, ultimately leading to more efficient and practical antenna solutions for.

References

- [1] S. K. K. Dash, T. Khan, and Y. M. Antar, "A state-of-art review on performance improvement of dielectric resonator antennas," *International Journal of RF and Microwave Computer-Aided Engineering*, vol. 28, no. 6, p. e21270, 2018.
- [2] S. Keyrouz and D. Caratelli, "Dielectric resonator antennas: basic concepts, design guidelines, and recent developments at millimeter-wave frequencies," *International Journal of Antennas and propagation*, vol. 2016, 2016.
- [3] A. Petosa and A. Ittipiboon, "Dielectric resonator antennas: A historical review and the current state of the art," *IEEE antennas and Propagation Magazine*, vol. 52, no. 5, pp. 91-116, 2010.
- [4] A. Petosa and A. Ittipiboon, "Dielectric resonator antennas A historical review and the current state of the art," *IEEE antennas and Propagation Magazine*, vol. 52, no. 5, pp. 91-116, 2010.
- [5] D. Soren, R. Ghatak, R. K. Mishra, and D. Poddar, "Dielectric resonator antennas: Designs and advances," *Progress In Electromagnetics Research B*, vol. 60, pp. 195-213, 2014.
- [6] F. P. Chietera, R. Colella, and L. Catarinucci, "Dielectric resonators antennas potential unleashed by 3D printing technology: A practical application in the IoT framework," *Electronics*, vol. 11, no. 1, p. 64, 2021.
- [7] R. S. Yaduvanshi and H. Parthasarathy, *Rectangular dielectric resonator antennas*. Springer, 2016.
- [8] K. Leung, "Analysis of aperture-coupled hemispherical dielectric resonator antenna with a perpendicular feed," *IEEE Transactions on Antennas and Propagation*, vol. 48, no. 6, pp. 1005-1007, 2000.
- [9] M. Aras, M. Rahim, A. Asrokin, and M. A. Aziz, "Dielectric resonator antenna (DRA) for wireless application," in *2008 IEEE International RF and Microwave Conference*, 2008, pp. 454-458: IEEE.
- [10] S. Das, H. Islam, T. Bose, and N. Gupta, "Coplanar waveguide fed stacked dielectric resonator antenna on safety helmet for rescue workers," *Microwave and Optical Technology Letters*, vol. 61, no. 2, pp. 498-502, 2019.
- [11] P. Anoop and R. Bhattacharjee, "Design of dual band triangular DRA for WLAN application," in *2015 IEEE Applied Electromagnetics Conference (AEMC)*, 2015, pp. 1-2: IEEE.
- [12] K. Leung and K. So, "Rectangular waveguide excitation of dielectric resonator antenna," *IEEE Transactions on Antennas and Propagation*, vol. 51, no. 9, pp. 2477-2481, 2003.

- [13] A. Pellegrini *et al.*, "Antennas and propagation for body-centric wireless communications at millimeter-wave frequencies: A review [wireless corner]," *IEEE Antennas and Propagation Magazine*, vol. 55, no. 4, pp. 262-287, 2013.
- [14] K. N. Paracha, S. K. A. Rahim, P. J. Soh, and M. Khalily, "Wearable Antennas: A Review of Materials, Structures, and Innovative Features for Autonomous Communication and Sensing," *IEEE Access*, vol. 7, pp. 56694-56712, 2019.
- [15] P. S. Hall and Y. Hao, "Antennas and propagation for body centric communications," in *2006 First European Conference on Antennas and Propagation*, 2006, pp. 1-7: IEEE.
- [16] Z. G. Liu and Y. X. Guo, "Dual band low profile antenna for body centric communications," *IEEE transactions on antennas and propagation*, vol. 61, no. 4, pp. 2282-2285, 2012.
- [17] M. C. Kemp, "Millimetre wave and terahertz technology for detection of concealed threats-a review," in *2007 Joint 32nd International Conference on Infrared and Millimeter Waves and the 15th International Conference on Terahertz Electronics*, 2007, pp. 647-648: IEEE.
- [18] X. Wang *et al.*, "Millimeter wave communication: A comprehensive survey," *IEEE Communications Surveys & Tutorials*, vol. 20, no. 3, pp. 1616-1653, 2018.
- [19] J. Bang, H. Chung, J. Hong, H. Seo, J. Choi, and S. Kim, "Millimeter-wave communications: Recent developments and challenges of hardware and beam management algorithms," *IEEE Communications Magazine*, vol. 59, no. 8, pp. 86-92, 2021.
- [20] R. Salvado, C. Loss, R. Gonçalves, and P. Pinho, "Textile materials for the design of wearable antennas: A survey," *Sensors*, vol. 12, no. 11, pp. 15841-15857, 2012.
- [21] A. Sharma, Y. Saini, A. K. Singh, and A. Rathi, "Recent advancements and technological challenges in flexible electronics: mm wave wearable array for 5G networks," in *AIP conference proceedings*, 2020, vol. 2294, no. 1: AIP Publishing.
- [22] A. Iqbal *et al.*, "Electromagnetic bandgap backed millimeter-wave MIMO antenna for wearable applications," *IEEE Access*, vol. 7, pp. 111135-111144, 2019.
- [23] P. R. Meher, B. R. Behera, and S. K. Mishra, "Design and its state-of-the-art of different shaped dielectric resonator antennas at millimeter-wave frequency band," *International Journal of RF and Microwave Computer-Aided Engineering*, vol. 30, no. 7, p. e22221, 2020.

- [24] S. K. K. Dash, T. Khan, and A. De, "Dielectric resonator antennas: An application oriented survey," *International Journal of RF and Microwave Computer-Aided Engineering*, vol. 27, no. 3, p. e21069, 2017.
- [25] M. R. Akdeniz *et al.*, "Millimeter wave channel modeling and cellular capacity evaluation," *IEEE journal on selected areas in communications*, vol. 32, no. 6, pp. 1164-1179, 2014.
- [26] J. G. Andrews *et al.*, "What will 5G be," *IEEE Journal on selected areas in communications*, vol. 32, no. 6, pp. 1065-1082, 2014.
- [27] P. J. Soh, G. A. Vandenbosch, M. Mercuri, and D. M.-P. Schreurs, "Wearable wireless health monitoring Current developments, challenges, and future trends," *IEEE Microwave Magazine*, vol. 16, no. 4, pp. 55-70, 2015.
- [28] O. Boric-Lubecke, V. M. Lubecke, B. Jokanovic, A. Singh, E. Shahhaidar, and B. Padasdao, "Microwave and wearable technologies for 5G," in *2015 12th International Conference on Telecommunication in Modern Satellite, Cable and Broadcasting Services (TELSIKS)*, 2015, pp. 183-188: IEEE.
- [29] N. F. M. Aun, P. J. Soh, A. A. Al-Hadi, M. F. Jamlos, G. A. Vandenbosch, and D. Schreurs, "Revolutionizing wearables for 5G: 5G technologies: Recent developments and future perspectives for wearable devices and antennas," *IEEE Microwave Magazine*, vol. 18, no. 3, pp. 108-124, 2017.
- [30] Y. Niu, Y. Li, D. Jin, L. Su, and A. V. Vasilakos, "A survey of millimeter wave communications (mmWave) for 5G opportunities and challenges," *Wireless networks*, vol. 21, no. 8, pp. 2657-2676, 2015.
- [31] G. A. Conway and W. G. Scanlon, "Antennas for over-body-surface communication at 2.45 GHz," *IEEE transactions on antennas and propagation*, vol. 57, no. 4, pp. 844-855, 2009.
- [32] M. Ur-Rehman, Q. H. Abbasi, M. Akram, and C. Parini, "Design of band-notched ultra wideband antenna for indoor and wearable wireless communications," *IET Microwaves, Antennas & Propagation*, vol. 9, no. 3, pp. 243-251, 2014.
- [33] M. V. Varnoosfaderani, D. V. Thiel, and J. W. Lu, "A folded slot antenna with full ground plane for wearable waterproof wireless sensors," in *2014 IEEE Antennas and Propagation Society International Symposium (APSURSI)*, 2014, pp. 838-839: IEEE.
- [34] G. A. Casula, A. Michel, P. Nepa, G. Montisci, and G. Mazzarella, "Robustness of wearable UHF-band PIFAs to human-body proximity," *IEEE Transactions on Antennas and Propagation*, vol. 64, no. 5, pp. 2050-2055, 2016.

- [35] G. Gao, S. Wang, R. Zhang, C. Yang, and B. Hu, "Flexible EBG-backed PIFA based on conductive textile and PDMS for wearable applications," *Microwave and Optical Technology Letters*, vol. 62, no. 4, pp. 1733-1741, 2020.
- [36] S. Singh and S. Verma, "SAR reduction and gain enhancement of compact wideband stub loaded monopole antenna backed with electromagnetic band gap array," *International Journal of RF and Microwave Computer-Aided Engineering*, vol. 31, no. 10, p. e22813, 2021.
- [37] M. Ur-Rehman, N. A. Malik, X. Yang, Q. H. Abbasi, Z. Zhang, and N. Zhao, "A low profile antenna for millimeter-wave body-centric applications," *IEEE Transactions on Antennas and Propagation*, vol. 65, no. 12, pp. 6329-6337, 2017.
- [38] K. Y. Elwasife and M. R. Almassri, "Numerical study the dielectric properties and specific absorption rate of nerve human tissue at different frequencies," *Numerical Study The Dielectric Properties And Specific Absorption Rate Of Nerve Human Tissue At Different Frequencies*, vol. 4, no. 1, 2017.
- [39] N. Rais, P. J. Soh, F. Malek, S. Ahmad, N. Hashim, and P. Hall, "A review of wearable antenna," in *2009 Loughborough antennas & propagation conference*, 2009, pp. 225-228: IEEE.
- [40] J. Bang and J. Choi, "A SAR reduced mm-wave beam-steerable array antenna with dual-mode operation for fully metal-covered 5G cellular handsets," *IEEE Antennas and Wireless Propagation Letters*, vol. 17, no. 6, pp. 1118-1122, 2018.
- [41] T. Hamed and M. Maqsood, "SAR calculation & temperature response of human body exposure to electromagnetic radiations at 28, 40 and 60 GHz mmWave frequencies," *Progress In Electromagnetics Research M*, vol. 73, pp. 47-59, 2018.
- [42] A. Lak, Z. Adelpour, H. Oraizi, and N. Parhizgar, "Design and SAR assessment of three compact 5G antenna arrays," *Scientific Reports*, vol. 11, no. 1, pp. 1-9, 2021.
- [43] N. Chahat, M. Zhadobov, L. Le Coq, S. I. Alekseev, and R. Sauleau, "Characterization of the interactions between a 60-GHz antenna and the human body in an off-body scenario," *IEEE Transactions on Antennas and Propagation*, vol. 60, no. 12, pp. 5958-5965, 2012.
- [44] R. H. Elabd and A. J. A. Al-Gburi, "SAR assessment of miniaturized wideband MIMO antenna structure for millimeter wave 5G smartphones," *Microelectronic Engineering*, vol. 282, p. 112098, 2023.
- [45] S. Khan, V. Singh, and B. Naresh, "Textile antenna using jeans substrate for wireless communication application," *Int. J. Eng. Technol. Sci. Res.(IJETS)*, vol. 2, no. 11, pp. 176-181, 2015.

- [46] S. Sankaralingam and B. Gupta, "A circular disk microstrip WLAN antenna for wearable applications," in *2009 Annual IEEE India Conference*, 2009, pp. 1-4: IEEE.
- [47] N. Chahat, M. Zhadobov, L. Le Coq, and R. Sauleau, "Wearable endfire textile antenna for on-body communications at 60 GHz," *IEEE Antennas and Wireless Propagation Letters*, vol. 11, pp. 799-802, 2012.
- [48] M. Abdullah and A. Khan, "Multiband wearable textile antenna for ISM body center communication systems," in *2015 XXth IEEE International Seminar/Workshop on Direct and Inverse Problems of Electromagnetic and Acoustic Wave Theory (DIPED)*, 2015, pp. 90-96: IEEE.
- [49] S. Agneessens, S. Lemey, T. Vervust, and H. Rogier, "Wearable, small, and robust The circular quarter-mode textile antenna," *IEEE Antennas and Wireless Propagation Letters*, vol. 14, pp. 1482-1485, 2015.
- [50] H. Li, S. Sun, B. Wang, and F. Wu, "Design of compact single-layer textile MIMO antenna for wearable applications," *IEEE Transactions on Antennas and Propagation*, vol. 66, no. 6, pp. 3136-3141, 2018.
- [51] S. D. Murali, B. N. M. Muni, Y. D. Varma, and S. Chaitanya, "Development of wearable antennas with different cotton textiles," *Int. Journal of Engineering Research and Applications*, vol. 4, no. 7, pp. 08-14, 2014.
- [52] J. DicCbshfsE, M. K. Abd Rahim, N. A. Samsuri, H. A. M. Salim, and M. F. Ali, "Embroidered fully textile wearable antenna for medical monitoring applications," *Progress In Electromagnetics Research*, vol. 117, pp. 321-337, 2011.
- [53] M. Al-Haddad, N. Jamel, and A. N. Nordin, "Flexible antenna: a review of design, materials, fabrication, and applications," in *Journal of Physics: Conference Series*, 2021, vol. 1878, no. 1, p. 012068: IOP Publishing.
- [54] F. F. Hashim, W. N. L. B. Mahadi, T. B. Abdul Latef, and M. B. Othman, "Key Factors in the Implementation of Wearable Antennas for WBNs and ISM Applications: A Review WBNs and ISM Applications: A Review," *Electronics*, vol. 11, no. 15, p. 2470, 2022.
- [55] S. F. Jilani, S. M. Abbas, K. P. Esselle, and A. Alomainy, "Millimeter-wave frequency reconfigurable T-shaped antenna for 5G networks," in *2015 IEEE 11th International Conference on Wireless and Mobile Computing, Networking and Communications (WiMob)*, 2015, pp. 100-102: IEEE.
- [56] X. Lin, B.-C. Seet, F. Joseph, and E. Li, "Flexible fractal electromagnetic bandgap for millimeter-wave wearable antennas," *IEEE Antennas and Wireless Propagation Letters*, vol. 17, no. 7, pp. 1281-1285, 2018.

- [57] S. Y. Jun, A. Elibiary, B. Sanz-Izquierdo, L. Winchester, D. Bird, and A. McClelland, "3-D printing of conformal antennas for diversity wrist worn applications," *IEEE Transactions on Components, Packaging and Manufacturing Technology*, vol. 8, no. 12, pp. 2227-2235, 2018.
- [58] E. Kaivanto, E. Salonen, and H. Khaleel, "Circularly Polarized Wearable Antennas," *WIT Transactions on State-of-the-art in Science and Engineering*, vol. 82, pp. 145-161, 2014.
- [59] T. S. Abdou, R. Saad, and S. K. Khamas, "A Circularly Polarized mmWave Dielectric-Resonator-Antenna Array for Off-Body Communications," *Applied Sciences*, vol. 13, no. 3, p. 2002, 2023.
- [60] W. J. Yang, Y. M. Pan, and S. Y. Zheng, "A low-profile wideband circularly polarized crossed-dipole antenna with wide axial-ratio and gain beamwidths," *IEEE Transactions on Antennas and Propagation*, vol. 66, no. 7, pp. 3346-3353, 2018.
- [61] M. Klemm, I. Locher, and G. Troster, "A novel circularly polarized textile antenna for wearable applications," in *7th European Conference on Wireless Technology, 2004.*, 2004, pp. 285-288: IEEE.
- [62] H. Yang, X. Liu, and Y. Fan, "Design of broadband circularly polarized all-textile antenna and its conformal array for wearable devices," *IEEE Transactions on Antennas and Propagation*, vol. 70, no. 1, pp. 209-220, 2021.
- [63] Z. H. Jiang, M. D. Gregory, and D. H. Werner, "Design and experimental investigation of a compact circularly polarized integrated filtering antenna for wearable biotelemetric devices," *IEEE Transactions on Biomedical Circuits and Systems*, vol. 10, no. 2, pp. 328-338, 2015.
- [64] U. Ullah, I. B. Mabrouk, and S. Koziel, "A compact circularly polarized antenna with directional pattern for wearable off-body communications," *IEEE Antennas and Wireless Propagation Letters*, vol. 18, no. 12, pp. 2523-2527, 2019.
- [65] Z. H. Jiang and D. H. Werner, "A compact, wideband circularly polarized co-designed filtering antenna and its application for wearable devices with low SAR," *IEEE Transactions on Antennas and Propagation*, vol. 63, no. 9, pp. 3808-3818, 2015.
- [66] S. Mashhadi, Z. Wu, and L. Thamae, "Investigation of a wearable broadband textile dielectric resonator antenna," in *2010 Loughborough Antennas & Propagation Conference*, 2010, pp. 349-352: IEEE.
- [67] P. Hu, Y. Pan, X. Zhang, and S. Zheng, "A compact filtering dielectric resonator antenna with wide bandwidth and high gain," *IEEE Transactions on Antennas and Propagation*, vol. 64, no. 8, pp. 3645-3651, 2016.

- [68] U. Illahi *et al.*, "Design of New Circularly Polarized Wearable Dielectric Resonator Antenna for Off-Body Communication in WBAN Applications," *IEEE Access*, vol. 7, pp. 150573-150582, 2019.
- [69] S. Mashhadi, S. Abbas, Z. Wu, and L. Thamae, "Transmission characteristics of wearable broadband textile dielectric resonator antennas in body area network," in *Proceedings of 2012 9th International Bhurban Conference on Applied Sciences & Technology (IBCAST)*, 2012, pp. 336-339: IEEE.
- [70] A. Kiran and G. K. Mishra, "Wearable Dielectric Resonator Antenna for Bluetooth Applications," in *2022 First International Conference on Electrical, Electronics, Information and Communication Technologies (ICEEICT)*, 2022, pp. 1-6: IEEE.
- [71] S. S. Singhwal, B. K. Kanaujia, A. Singh, and J. Kishor, "Novel circularly polarized dielectric resonator antenna for microwave image sensing application," *Microwave and Optical Technology Letters*, vol. 61, no. 7, pp. 1821-1827, 2019.
- [72] P. R. M. R. B. K. M. A. Althuway, "Design and analysis of a compact circularly polarized DRA for off-body communications," 2021.
- [73] T. S. Abdou and S. K. Khamas, "A mm-wave Circularly Polarized Wristwatch Dielectric Resonator Antenna for Off-Body Communications," in *2022 International Workshop on Antenna Technology (iWAT)*, 2022, pp. 168-171: IEEE.
- [74] A. A. Abdulmajid, Y. Khalil, and S. Khamas, "Higher-order-mode circularly polarized two-layer rectangular dielectric resonator antenna," *IEEE Antennas and Wireless Propagation Letters*, vol. 17, no. 6, pp. 1114-1117, 2018.
- [75] A. Mersani, W. Bouamara, L. Osman, and J. M. Ribero, "Dielectric resonator antenna button textile antenna for off-body applications," *Microwave and Optical Technology Letters*, 2019.
- [76] M. S. Iqbal and K. P. Esselle, "A compact wideband dielectric resonator antenna for on-body applications," in *2014 IEEE MTT-S International Microwave Workshop Series on RF and Wireless Technologies for Biomedical and Healthcare Applications (IMWS-Bio2014)*, 2014, pp. 1-3: IEEE.
- [77] S. Agrawal, R. D. Gupta, M. S. Parihar, and P. N. Kondekar, "A wideband high gain dielectric resonator antenna for RF energy harvesting application," *AEU-International Journal of Electronics and Communications*, vol. 78, pp. 24-31, 2017.
- [78] M. Boyuan, J. Pan, E. Wang, and Y. Luo, "Conformal bent dielectric resonator antennas with curving ground plane," *IEEE Transactions on Antennas and Propagation*, vol. 67, no. 3, pp. 1931-1936, 2018.

- [79] M. Boyuan, J. Pan, E. Wang, and D. Yang, "Wristwatch-Style Wearable Dielectric Resonator Antennas for Applications on Limbs," *IEEE Access*, vol. 8, pp. 59837-59844, 2020.
- [80] M. D. Alanazi and S. K. Khamas, "Wideband mm-wave hemispherical dielectric resonator antenna with simple alignment and assembly procedures," *Electronics*, vol. 11, no. 18, p. 2917, 2022.
- [81] A. Meredov, K. Klionovski, and A. Shamim, "Screen-Printed, Flexible, Parasitic Beam-Switching Millimeter-Wave Antenna Array for Wearable Applications," *IEEE Open Journal of Antennas and Propagation*, vol. 1, pp. 2-10, 2019.
- [82] I. Syrytsin, S. Zhang, and G. F. Pedersen, "Finger ring phased antenna array for 5G IoT and sensor networks at 28 GHz," 2018.
- [83] A. J. A. Al-Gburi *et al.*, "Broadband Circular Polarised Printed Antennas for Indoor Wireless Communication Systems: A Comprehensive Review," *Micromachines*, vol. 13, no. 7, p. 1048, 2022.
- [84] Y. Qasaymeh, A. Almuhausen, and A. S. Alghamdi, "A Compact Sequentially Rotated Circularly Polarized Dielectric Resonator Antenna Array," *Applied Sciences*, vol. 11, no. 18, p. 8779, 2021.
- [85] S. Kumar, G. H. Lee, D. H. Kim, H. C. Choi, and K. W. Kim, "Dual circularly polarized planar four-port MIMO antenna with wide axial-ratio bandwidth," *Sensors*, vol. 20, no. 19, p. 5610, 2020.
- [86] J. Kulkarni, A. G. Alharbi, I. Elfergani, J. Anguera, C. Zebiri, and J. Rodriguez, "Dual Polarized, Multiband Four-Port Decagon Shaped Flexible MIMO Antenna for Next Generation Wireless Applications," *IEEE Access*, vol. 10, pp. 128132-128150, 2022.
- [87] J. Kulkarni, R. K. Gangwar, and J. Anguera, "Broadband and Compact Circularly Polarized MIMO Antenna With Concentric Rings and Oval Slots for 5G Application," *IEEE Access*, vol. 10, pp. 29925-29936, 2022.
- [88] Y. Liu, Y. C. Jiao, Z. Weng, C. Zhang, and G. Chen, "A novel millimeter-wave dual-band circularly polarized dielectric resonator antenna," *International Journal of RF and Microwave Computer-Aided Engineering*, vol. 29, no. 10, p. e21871, 2019.
- [89] A. A. Abdulmajid, S. Khamas, and S. Y. Zhang, "Wide Bandwidth High Gain Circularly Polarized Millimetre-Wave Rectangular Dielectric Resonator Antenna," (in English), *Progress in Electromagnetics Research M*, vol. 89, pp. 171-177, 2020.
- [90] A. Petosa, A. Ittipiboon, Y. Antar, D. Roscoe, and M. Cuhaci, "Recent advances in dielectric-resonator antenna technology," *IEEE Antennas and Propagation Magazine*, vol. 40, no. 3, pp. 35-48, 1998.

- [91] S. Yarga, K. Sertel, and J. L. Volakis, "Multilayer dielectric resonator antenna operating at degenerate band edge modes," *IEEE Antennas and Wireless Propagation Letters*, vol. 8, pp. 287-290, 2009.
- [92] H. Chu and Y.-X. Guo, "A novel approach for millimeter-wave dielectric resonator antenna array designs by using the substrate integrated technology," *IEEE Transactions on Antennas and Propagation*, vol. 65, no. 2, pp. 909-914, 2016.
- [93] A. Petosa, *Dielectric resonator antenna handbook*. Artech, 2007.
- [94] Y.-X. Sun and K. W. Leung, "Circularly polarized substrate-integrated cylindrical dielectric resonator antenna array for 60 GHz applications," *IEEE Antennas and Wireless Propagation Letters*, vol. 17, no. 8, pp. 1401-1405, 2018.
- [95] A. A. Qureshi, D. M. Klymyshyn, M. Tayfeh, W. Mazhar, M. Börner, and J. Mohr, "Template-based dielectric resonator antenna arrays for millimeter-wave applications," *IEEE Transactions on Antennas and Propagation*, vol. 65, no. 9, pp. 4576-4584, 2017.
- [96] W. Mazhar, D. M. Klymyshyn, G. Wells, A. A. Qureshi, M. Jacobs, and S. Achenbach, "Low-profile artificial grid dielectric resonator antenna arrays for mm-wave applications," *IEEE Transactions on Antennas and Propagation*, vol. 67, no. 7, pp. 4406-4417, 2019.
- [97] A. Kesavan, M. a. Al-Hassan, I. Ben Mabrouk, and T. A. Denidni, "Wideband circular polarized dielectric resonator antenna array for millimeter-wave applications," *Sensors*, vol. 21, no. 11, p. 3614, 2021.
- [98] M. Niayesh and A. Kouki, "LTCC-integrated dielectric resonant antenna array for 5G applications," *Sensors*, vol. 21, no. 11, p. 3801, 2021.
- [99] Y.-T. Liu, B. Ma, S. Huang, S. Wang, Z. J. Hou, and W. Wu, "Wideband Low-Profile Connected Rectangular Ring Dielectric Resonator Antenna Array for Millimeter-Wave Applications," *IEEE Transactions on Antennas and Propagation*, 2022.
- [100] M. Z. Chowdhury, M. Shahjalal, S. Ahmed, and Y. M. Jang, "6G wireless communication systems: Applications, requirements, technologies, challenges, and research directions," *IEEE Open Journal of the Communications Society*, vol. 1, pp. 957-975, 2020.
- [101] P. R. Meher, B. R. Behera, S. K. Mishra, and A. A. Althwayb, "A chronological review of circularly polarized dielectric resonator antenna: Design and developments," *International Journal of RF and Microwave Computer-Aided Engineering*, vol. 31, no. 5, p. e22589, 2021.

- [102] D. Guha, A. Banerjee, C. Kumar, and Y. M. Antar, "Higher order mode excitation for high-gain broadside radiation from cylindrical dielectric resonator antennas," *IEEE Transactions on Antennas and Propagation*, vol. 60, no. 1, pp. 71-77, 2011.
- [103] T. S. Rappaport, G. R. MacCartney, M. K. Samimi, and S. Sun, "Wideband millimeter-wave propagation measurements and channel models for future wireless communication system design," *IEEE transactions on Communications*, vol. 63, no. 9, pp. 3029-3056, 2015.
- [104] Y. Liu and M. C. Yagoub, "Compact, Broadband, and Omnidirectional Antenna Array for Millimeter-Wave Communication Systems," *Journal of Microwaves, Optoelectronics and Electromagnetic Applications*, vol. 20, pp. 297-306, 2021.
- [105] N. K. Maurya, M. J. Ammann, and P. Mcevoy, "Series-fed Omnidirectional mm-Wave Dipole Array," *IEEE Transactions on Antennas and Propagation*, 2023.
- [106] L. Zou, D. Abbott, and C. Fumeaux, "Omnidirectional cylindrical dielectric resonator antenna with dual polarization," *IEEE Antennas and Wireless Propagation Letters*, vol. 11, pp. 515-518, 2012.
- [107] Y. M. Pan, S. Y. Zheng, and W. Li, "Dual-band and dual-sense omnidirectional circularly polarized antenna," *IEEE antennas and wireless propagation letters*, vol. 13, pp. 706-709, 2014.
- [108] P. F. Hu, Y. M. Pan, K. W. Leung, and X. Y. Zhang, "Wide-/dual-band omnidirectional filtering dielectric resonator antennas," *IEEE Transactions on Antennas and Propagation*, vol. 66, no. 5, pp. 2622-2627, 2018.
- [109] X. S. Fang and K. W. Leung, "Design of wideband omnidirectional two-layer transparent hemispherical dielectric resonator antenna," *IEEE Transactions on Antennas and Propagation*, vol. 62, no. 10, pp. 5353-5357, 2014.
- [110] J. Lai *et al.*, "Design of a dual-polarized omnidirectional dielectric resonator antenna for capsule endoscopy system," *IEEE Access*, vol. 9, pp. 14779-14786, 2021.
- [111] Y. M. Pan, K. W. Leung, and K. Lu, "Omnidirectional linearly and circularly polarized rectangular dielectric resonator antennas," *Ieee transactions on antennas and propagation*, vol. 60, no. 2, pp. 751-759, 2011.
- [112] K. W. Leung, Y. M. Pan, X. S. Fang, E. H. Lim, K.-M. Luk, and H. P. Chan, "Dual-function radiating glass for antennas and light covers—Part I: Omnidirectional glass dielectric resonator antennas," *IEEE transactions on antennas and propagation*, vol. 61, no. 2, pp. 578-586, 2012.

- [113] M. Zou and J. Pan, "Investigation of resonant modes in wideband hybrid omnidirectional rectangular dielectric resonator antenna," *IEEE Transactions on Antennas and Propagation*, vol. 63, no. 7, pp. 3272-3275, 2015.
- [114] M. Zou, J. Pan, D. Yang, and G. Xiong, "Investigation of dual-band omnidirectional rectangular dielectric resonator antenna," *Journal of Electromagnetic Waves and Applications*, vol. 30, no. 11, pp. 1407-1416, 2016.
- [115] W. Li, K. W. Leung, and N. Yang, "Omnidirectional dielectric resonator antenna with a planar feed for circular polarization diversity design," *IEEE Transactions on Antennas and Propagation*, vol. 66, no. 3, pp. 1189-1197, 2018.
- [116] N. Yang and K. W. Leung, "Size reduction of omnidirectional cylindrical dielectric resonator antenna using a magnetic aperture source," *IEEE Transactions on Antennas and Propagation*, vol. 68, no. 4, pp. 3248-3253, 2019.
- [117] N. Yang and K. W. Leung, "Compact cylindrical pattern-diversity dielectric resonator antenna," *IEEE Antennas and Wireless Propagation Letters*, vol. 19, no. 1, pp. 19-23, 2019.
- [118] X. S. Fang, L. P. Weng, and Y.-X. Sun, "Slots-coupled omnidirectional circularly polarized cylindrical glass dielectric resonator antenna for 5.8-GHz WLAN application," *IEEE Access*, vol. 8, pp. 204718-204727, 2020.
- [119] X. S. Fang, L. P. Weng, and Z. Fan, "Design of the Wideband and Low-Height Omnidirectional Cylindrical Dielectric Resonator Antenna Using Arced-Apertures Feeding," *IEEE Access*, vol. 11, pp. 20128-20135, 2023.
- [120] S. G. Kirtania *et al.*, "Flexible antennas: A review," *Micromachines*, vol. 11, no. 9, p. 847, 2020.
- [121] R. S. Anwar, L. Mao, and H. Ning, "Frequency selective surfaces: A review," *Applied Sciences*, vol. 8, no. 9, p. 1689, 2018.
- [122] E. Kaivanto, E. Salonen, and H. Khaleel, "Circularly polarized wearable antennas," *Innovation in Wearable and Flexible Antennas*, vol. 82, pp. 145-161, 2014.
- [123] K. Lu, K. W. Leung, and Y. M. Pan, "Theory and experiment of the hollow rectangular dielectric resonator antenna," *IEEE Antennas and Wireless Propagation Letters*, vol. 10, pp. 631-634, 2011.
- [124] L. Zou, "Dielectric resonator antennas: from multifunction microwave devices to optical nano-antennas," 2013.

- [125] B. Mukherjee, P. Patel, and J. Mukherjee, "A review of the recent advances in dielectric resonator antennas," *Journal of Electromagnetic Waves and Applications*, vol. 34, no. 9, pp. 1095-1158, 2020.
- [126] S. Maity and B. Gupta, "Closed form expressions to find radiation patterns of rectangular dielectric resonator antennas for various modes," *IEEE transactions on antennas and propagation*, vol. 62, no. 12, pp. 6524-6527, 2014.
- [127] A. Mersani, W. Bouamara, L. Osman, and J. M. Ribero, "Dielectric resonator antenna button textile antenna for off-body applications," *Microwave and Optical Technology Letters*, vol. 62, no. 9, pp. 2910-2918, 2020.
- [128] "T-Ceram s.r.o. Available online: <http://www.t-ceram.com/>. (accessed on 03 January 2023).".
- [129] "Wrekin Circuits Ltd. Available online: <https://www.wrekin-circuits.co.uk/>. (accessed on 06 December2022)."
- ".
- [130] "UKRI National Millimetre Wave Facility. Available online: <https://www.sheffield.ac.uk/mm-wave/> (accessed on 06 October 2022)."
- [131] S. Gregson, J. McCormick, and C. Parini, *Principles of planar near-field antenna measurements*. IET, 2007.
- [132] T. S. Abdou and S. K. Khamas, "A Low-profile Wide Bandwidth Circularly Polarized Dielectric Resonator Antenna for mm-wave Off-Body Applications," in *2023 17th European Conference on Antennas and Propagation (EuCAP)*, 2023, pp. 1-5: IEEE.
- [133] A. Rashidian and D. M. Klymyshyn, "On the two segmented and high aspect ratio rectangular dielectric resonator antennas for bandwidth enhancement and miniaturization," *IEEE Transactions on Antennas and Propagation*, vol. 57, no. 9, pp. 2775-2780, 2009.
- [134] R. K. Mongia and P. Bhartia, "Dielectric resonator antennas—A review and general design relations for resonant frequency and bandwidth," *International Journal of Microwave and Millimeter-Wave Computer-Aided Engineering*, vol. 4, no. 3, pp. 230-247, 1994.
- [135] R. K. Mongia and A. Ittipiboon, "Theoretical and experimental investigations on rectangular dielectric resonator antennas," *IEEE Transactions on antennas and propagation*, vol. 45, no. 9, pp. 1348-1356, 1997.
- [136] P. Hasgall *et al.*, "IT'IS Database for thermal and electromagnetic parameters of biological tissues," *Version 3.0*, 2015.

- [137] P. R. Meher, B. R. Behera, S. K. Mishra, and A. A. Althuwayb, "Design and analysis of a compact circularly polarized DRA for off-body communications," *AEU-International Journal of Electronics and Communications*, vol. 138, p. 153880, 2021.
- [138] R. Mongia, "Theoretical and experimental resonant frequencies of rectangular dielectric resonators," in *IEE proceedings H (microwaves, antennas and propagation)*, 1992, vol. 139, no. 1, pp. 98-104: IET.
- [139] W. Liu, B. Ma, and J. Pan, "Investigation on arc dielectric resonator antenna and arc microstrip patch antenna," in *2018 IEEE 3rd Advanced Information Technology, Electronic and Automation Control Conference (IAEAC)*, 2018, pp. 211-214: IEEE.
- [140] D. H. Staelin, *Electromagnetics and applications*. Massachusetts Institute of Technology Cambridge, MA, USA, 2011.
- [141] R. C. Hansen, *Phased array antennas*. John Wiley & Sons, 2009.
- [142] A. K. Bhattacharyya, *Phased array antennas: Floquet analysis, synthesis, BFNs and active array systems*. John Wiley & Sons, 2006.
- [143] M. Nosrati, S. Shahsavari, S. Lee, H. Wang, and N. Tavassolian, "A concurrent dual-beam phased-array Doppler radar using MIMO beamforming techniques for short-range vital-signs monitoring," *IEEE Transactions on Antennas and Propagation*, vol. 67, no. 4, pp. 2390-2404, 2019.
- [144] R. D. Maknikar and V. G. Kasabegoudar, "Circularly polarized cross-slot-coupled stacked dielectric resonator antenna for wireless applications," *International Journal of Wireless Communications and Mobile Computing*, vol. 1, no. 2, pp. 68-73, 2013.
- [145] C. A. Balanis, *Antenna theory: analysis and design*. John wiley & sons, 2016.
- [146] D. Ehyae, "Novel approaches to the design of phased array antennas," University of Michigan, 2011.
- [147] N. M. Nor, M. H. Jamaluddin, M. R. Kamarudin, and M. Khalily, "Rectangular dielectric resonator antenna array for 28 GHz applications," *Progress In Electromagnetics Research C*, vol. 63, pp. 53-61, 2016.
- [148] P. Chowdhury, N. Chakma, A. H. Murshed, M. A. Hossain, and Q. D. Hossain, "An improved 2×2 array antenna using both-sided microwave integrated circuit technology for circular polarization," *International Journal of Electrical & Computer Engineering (2088-8708)*, vol. 13, no. 1, 2023.
- [149] N. Zainol, Z. Zakaria, M. Abu, M. M. Yunus, and E. Ruslan, "Design of 2×2 array antenna with harmonic suppression using T-shape DGS and spurline," in *2017 11th European Conference on Antennas and Propagation (EUCAP)*, 2017, pp. 1044-1048: IEEE.

- [150] A. Vahora and K. Pandya, "Implementation of cylindrical dielectric resonator antenna array for Wi-Fi/wireless LAN/satellite applications," *Progress In Electromagnetics Research M*, vol. 90, pp. 157-166, 2020.
- [151] J. He, L. Li, and T. Shu, "Sparse nested arrays with spatially spread orthogonal dipoles: high accuracy passive direction finding with less mutual coupling," *IEEE Transactions on Aerospace and Electronic Systems*, vol. 57, no. 4, pp. 2337-2345, 2021.
- [152] S. Bhattacharjee, S. Maity, S. R. B. Chaudhuri, and M. Mitra, "A compact dual-band dual-polarized omnidirectional antenna for on-body applications," *IEEE Transactions on Antennas and Propagation*, vol. 67, no. 8, pp. 5044-5053, 2019.
- [153] H. Yang and X. Liu, "Wearable dual-band and dual-polarized textile antenna for on-and off-body communications," *IEEE Antennas and Wireless Propagation Letters*, vol. 19, no. 12, pp. 2324-2328, 2020.
- [154] A. Petosa, N. Simons, R. Siushansian, A. Ittipiboon, and M. Cuhaci, "Design and analysis of multisegment dielectric resonator antennas," *IEEE Transactions on Antennas and Propagation*, vol. 48, no. 5, pp. 738-742, 2000.
- [155] J.-S. Row, "The design of a squarer-ring slot antenna for circular polarization," *IEEE Transactions on Antennas and Propagation*, vol. 53, no. 6, pp. 1967-1972, 2005.
- [156] R. Xu, H. Zhu, and J. Yuan, "Electric-field intrabody communication channel modeling with finite-element method," *IEEE transactions on biomedical engineering*, vol. 58, no. 3, pp. 705-712, 2010.
- [157] T. Hamed and M. Maqsood, "SAR Calculation & Temperature Response of Human Body Exposure to Electromagnetic Radiations at 28, 40 and 60 GHz mmWave Frequencies," *Progress In Electromagnetics Research*, vol. 73, pp. 47-59, 2018.
- [158] M. Ur-Rehman, M. Adekanye, and H. T. Chattha, "Tri-band millimetre-wave antenna for body-centric networks," *Nano communication networks*, vol. 18, pp. 72-81, 2018.
- [159] M. Wagih, A. S. Weddell, and S. Beeby, "Millimeter-wave textile antenna for on-body RF energy harvesting in future 5G networks," in *2019 IEEE Wireless Power Transfer Conference (WPTC)*, 2019, pp. 245-248: IEEE.
- [160] M. M. Khan, K. Islam, M. N. Alam Shovon, M. Baz, and M. Masud, "Design of a novel 60 GHz millimeter wave Q-slot antenna for body-centric communications," *International Journal of Antennas and Propagation*, vol. 2021, pp. 1-12, 2021.

- [161] H. A. Rahman, M. M. Khan, M. Baz, M. Masud, and M. A. AlZain, "Novel compact design and investigation of a super wideband millimeter wave antenna for body-centric communications," *International Journal of Antennas and Propagation*, vol. 2021, pp. 1-15, 2021.
- [162] A. Kapoor and G. Singh, "Mode classification in cylindrical dielectric waveguides," *Journal of lightwave technology*, vol. 18, no. 6, pp. 849-852, 2000.
- [163] K. M. Luk and K. W. Leung, "Dielectric resonator antennas," Research studies press 2003.
- [164] J. Sethares and S. Naumann, "Design of microwave dielectric resonators," *IEEE Transactions on Microwave Theory and Techniques*, vol. 14, no. 1, pp. 2-7, 1966.
- [165] A. Abdulmajid, "High Gain Wide Bandwidth Layered Dielectric Resonator Antennas," University of Sheffield, 2019.
- [166] S. Long, M. McAllister, and L. Shen, "The resonant cylindrical dielectric cavity antenna," *IEEE Transactions on Antennas and Propagation*, vol. 31, no. 3, pp. 406-412, 1983.
- [167] R. De Smedt, "Correction due to a finite permittivity for a ring resonator in free space," *IEEE transactions on microwave theory and techniques*, vol. 32, no. 10, pp. 1288-1293, 1984.
- [168] M. Tsuji, H. Shigesawa, and K. Takiyama, "Analytical and experimental investigations on several resonant modes in open dielectric resonators," *IEEE transactions on microwave theory and techniques*, vol. 32, no. 6, pp. 628-633, 1984.
- [169] N. M. Mohamed-Hicho, E. Antonino-Daviu, M. Cabedo-Fabres, and M. Ferrando-Bataller, "Designing slot antennas in finite platforms using characteristic modes," *IEEE Access*, vol. 6, pp. 41346-41355, 2018.
- [170] M. McAllister and S. A. Long, "Resonant hemispherical dielectric antenna," *Electronics Letters*, vol. 20, pp. 657-659, 1984.
- [171] G. A. Sarkar, S. Ballav, A. Chatterjee, S. Ranjit, and S. K. Parui, "Four element MIMO DRA with high isolation for WLAN applications," *Progress In Electromagnetics Research Letters*, vol. 84, pp. 99-106, 2019.
- [172] K. W. Leung, K. Lai, K. Luk, and D. Lin, "Input impedance of aperture coupled hemispherical dielectric resonator antenna," *Electronics Letters*, vol. 13, no. 29, pp. 1165-1167, 1993.
- [173] K.-W. Leung, K.-M. Luk, K. Y. Lai, and D. Lin, "Theory and experiment of an aperture-coupled hemispherical dielectric resonator antenna," *IEEE Transactions on Antennas and Propagation*, vol. 43, no. 11, pp. 1192-1198, 1995.

- [174] H. Ng and K. Leung, "Circular-polarized hemispherical dielectric resonator antenna excited by dual conformal-strip," in *IEEE Antennas and Propagation Society International Symposium (IEEE Cat. No. 02CH37313)*, 2002, vol. 3, pp. 442-445: IEEE.